**Pedro Emanuel
Santos Silva**

**Desenvolvimento de novas estruturas com
filamentos helicoidais**

**Development of new structures with helical
filaments**

**Pedro Emanuel
Santos Silva**

Desenvolvimento de novas estruturas com filamentos helicoidais

Development of new structures with helical filaments

Tese apresentada à Universidade de Aveiro para cumprimento dos requisitos necessários à obtenção do grau de Doutor em Nanociências e Nanotecnologia, realizada sob a orientação científica do Professor Doutor Fernão Vístulo de Abreu, Professor Auxiliar do Departamento de Física da Universidade de Aveiro e coorientação científica da Professora Doutora Maria Helena Godinho, Professora Auxiliar do Departamento de Ciência dos Materiais da Universidade de Nova de Lisboa

o júri / the jury

presidente / president   **Vítor Brás de Sequeira Amaral**

Professor Catedrático da Universidade de Aveiro (por delegação da Reitora da Universidade de Aveiro)

vogais / examiners committee   **Pawel Pieranski**

Directeur de Recherche da Université Paris-Sud

Pedro Manuel Alves Patrício da Silva

Professor Coordenador do Instituto Superior de Engenharia de Lisboa

Ricardo Guimarães Dias

Professor Auxiliar da Universidade de Aveiro

Fernão Vístulo de Abreu

Professor auxiliar da Universidade de Aveiro (orientador)

**agradecimentos /
acknowledgements**

agradecimentos (cont.)   À minha família que sempre acreditou nas minhas capacidades. Aos meus pais pela vida, por todas as oportunidades que me proporcionaram e pelos seus valores. Aos meus irmãos por serem especiais, únicos e me chatearem o juízo de vez em quando. À minha madrinha por ter-me recebido bem em sua casa sempre que precisei.

À Astrid por todo apoio incondicional. A escrita da tese foi por vezes muito frustrante e se não fosse compreensão e dedicação dela, muito provavelmente a conclusão da tese não teria sido possível.

palavras-chave   Filamentos helicoidais, Impressão 4D, microfibras, polímeros, electrofi-
açao, simulaoẽs de dinâmica molecular.

resumo   O entrelaçamento de estruturas filamentares marcou um passo impor-
tante na evolução da humanidade. Vários tipos de filamentos são usados
em tecidos, cordas e, mais recentemente em micro e nanoestruturas.
Esta tese oferece um contributo que pode ser relevante para as àreas
do têxtil, nanotecnologias e campos relacionados com a ciência dos
materiais.
Nesta tese, são descritos métodos para produzir micro e nanofibras com
diferentes propriedades físicas de acordo com formatos pré-estabelecidos
nas estruturas. Alguns destes métodos são inspirados em sistemas nat-
urais, onde as estruturas contêm topologias específicas para ultrapassar
diferentes tarefas. Em particular, fibras helicoidais são produzidas exper-
imentalmente usando a técnica de electrofiação. Em segundo lugar, é
introduzido uma generalização do conceito das perversões. Perversões
são ocorrências geométricas que invertem o sentido de rotação de estru-
turas helicoidais. As perversões aparecem quando filamentos, com as
extremidades constrangidas, enrolam e adoptam formas helicoidal mas
têm de conservar a torção total. Mostramos que é possível obter matem-
aticamente e experimentalmente uma variedade contínua de perversões
diferentes que apresentam diferentes geometrias. Experimentalmente,
diferentes perversões são geradas irradiando microfibras electrofiadas
com ciclos de irradiação de luz UV e máscaras opacas. Os resultados
experimentais confirmam também que os diferentes tipos de perversões
têm comportamentos distintos quando libertadas e adoptam config-
urações finais diferentes. Do mesmo modo, usando uma abordagem
experimental semelhante, são obtidas hélices com diferentes curvaturas
alternadamente. É observado que, durante o relaxamento das fibras, as
regiões com curvatura intrínseca maior, começam a enrolar primeiro,
enquanto as regiões com curvatura intrínseca menor permanecem alon-
gadas até a um ponto em que começam a enrolar depois. Todos os
efeitos observados experimentalmente estão em concordância com simu-
lações computacionais realizadas para modelar a dinâmica de filamentos
com curvatura intrínseca. Os resultados experimentais e computacionais
demonstram que é possível controlar com precisão a forma de microfila-
mentos modificando as propriedades mecânicas da superfície das fibras,
em vez de depender arranjos moleculares específicos.

resumo (cont.)   Por último, descrevemos duas abordagens para obter entrelaçamentos com fibras helicoidais usando exclusivamente interacções mecânicas. A ligação nos tecidos é gerada, no primeiro caso, fazendo enrolar as perversões entre os filamentos adjacentes e, no segundo caso, entrelaçando as voltas das hélices dos filamentos. Simulações computacionais mostram como tecidos podem ser gerados com sucesso usando cada uma das ideias para criar ligações entre as fibras.

keywords

Helical filaments, 4D printing, microfibres, polymers, electrospinning, molecular dynamics simulations.

abstract

The entanglement of filamentary structures marked an important step in mankind evolution. Filaments appear in fabrics, ropes and, more recently, in micro and nanostructures. This thesis offers a contribution that can be relevant to the fields of textiles, nanotechnologies and materials science in general.

In this thesis, we present methods for shaping micro and nanofibres on demand and with different physical properties. Some of these methods are inspired in natural systems, where structures have specific topologies to fulfil different tasks. In particular, it will be discussed how fibres with helical shape can be produced using the electrospinning technique.

Secondly, we introduce a generalization of the concept of perversions. Perversions are geometrical occurrences that reverse the handedness of connected helices. Perversions arise when clamped filaments coil into a helical shape but must conserve zero overall twist. We show mathematically and experimentally that a continuous range of different perversions can exist and present different geometries. Experimentally, different perversions are generated by using irradiated micro electrospun fibres with cycles of UV light and opaque masks. Experimental results also confirm that different types of perversions behave differently upon release and adopt different final configurations. We also produce filaments containing helices with alternating curvatures. It is observed that, upon release, the regions with higher curvature start to curl first, while regions with lower intrinsic curvature remain stretched until start to curl later. All the effects observed in experiments is in good agreement with computational simulations performed to model the dynamics of filaments with intrinsic curvature. The experimental and computational results showed that the precise control of the shape of microfilaments can be achieved by changing the properties of the fibres surface, instead of relying on material's molecular arrangements.

Finally, we describe two approaches to entangle helical filaments by using exclusively mechanical interactions. The linkage in fabrics is generated, in the first case, by winding perversions between neighbouring filaments and, in the second case, by intertwining helical loops of the filaments. Computational simulations show how fabrics can be generated by using both approaches to create links between the fibres.

Contents

Contents

Chapter 1

Introduction

Fibres, strands, threads, cords, strings, tendrils or fibrils are words commonly used to describe filamentary structures present in the everyday life. In fact, most of them are ubiquitously present since the existence of men. From learning how to knot a sharp stone into a rod for hunting, to produce carbon nanotubes for hydrogen storage, we could ask ourselves what is yet to know about filaments. Although it is true that there is already a good understanding about the processes involving the manipulation of filaments, in the last decades, the interest in micro and nanotechnology raised the demand for materials designed to improve or add new functionalities to the current technologies. For instance, even a well established industry as the textile one is studying new techniques to produce non-woven mats or to fabricate clothing incorporating electronic devices[1], [2] Moreover, many strategies to produce filaments have limitations at smaller length scales. This can happen simply due to the limitation of the technique to produce smaller filaments or because, at some point of the miniaturization, there are factors associated to the length scale that need to be considered, as the differences between the mechanical properties between the bulk and thin filaments or the limitations in handling and production rates[3]. Notwithstanding, several approaches are being taken

to solve some of the current challenges. One of them involves the inspiration from the solutions devised by nature. For instance, learning how some bacteria propel themselves in a medium, other than in a random way, might prove to be useful to produce nanorobots using similar approaches[4].

Nature developed numerous strategies to deal with different tasks. During the many million years of evolution, organisms and other types of organic structures refined a variety of ingenious mechanisms, like self-cleaning lotus leaves[5], the ability of octopus to change their body shape to mimic other animals[6] or how fireflies generate light to communicate[7] are just a few examples of the immense diversity of mechanisms. It is no wonder biomimicry, biomimetic and bioinspired terms are so commonly used to describe many scientific works. While the former term describes solely the imitation of a biological system, biomimetics attempts to copy the function into other systems. In the case of the research based in bioinspired functionalities, the original mechanisms are pushed beyond what is exhibited in the natural world[8]. Typically, works start from the biomimicry or biomimetic steps like, for instance, the studies from Leonardo da Vinci on trying to find why birds fly, during the the late fifteenth and early sixteenth centuries. Four centuries later, the Wright brothers were also inspired by flight of the birds to come forth with a early version of an aircraft. With the improvement and development of more better materials, powerful engines and efficient designs, man have created bioinspired aircrafts (and spacecrafts) that surpassed birds on how much higher and faster they can fly, with enough power to carry voluminous and heavy contents. Although learning and bringing forth the new concepts into real applications is not straightforward, as in the aircraft example, many unsuccessful strategies had a ill-fated outcome. Establishing a bridge between nature and the diverse engineering fields can be of the utmost importance to the development of the humankind technology. In the words of Leonardo da Vinci[9], "Nature is the source of all true knowledge; she has her own logic, her own laws, she has no effect without cause nor invention without necessity".

1.1 Helical shapes

In the specific case of filamentary structures, it is particularly important how they fold, propel and assemble. For instance, human hair besides of having a great social importance, it provided important functions for the survivability of the human beings over time. Hair protects our heads from the UV light, provides a good thermal insulation by entrapping air, helps waterproofing the scalp, with the production of a secreting oil, and protects from mechanical abrasion[10]. Furthermore, hair displays different

shapes, straight, wavy or curly, which allowed the human being to adapt to the different social customs or geographical implications. The curliness in hairs arises mainly to the existence of a retrocurvature of the hair follicles. This asymmetry further promotes an elliptical cortex, opposed to a circular cortex on straight hairs, and to an asymmetric distribution of a specific type of keratins, that is accumulated in the concave side of the curvature[11]. Another example is the case of the filaree seeds. This flowering plant uses a particular mechanism to disseminate its seeds. First, after the flowering, the plant stores enough elastic energy in the fruits, consisting in encapsulated seeds with a long straight tail, the awn, by creating a tension between the awns and a surrounding tissue. With the abrupt snap of the tissue, the release of the tension flings the seeds away from the plant. After reaching the ground, the awn starts a cycle of winding and unwinding with the variation of the humidity, it coils upon drying and straightens upon wetting. These motions help the seed moving across the surface until, eventually, find a hole to drill itself into the soil[12], [13].

Many organisms and other filamentary structures adopt the helical shape in nature. A well-known example is the molecular shape of the deoxyribonucleic acid, DNA, where two linear strands twist together forming a double helix structure. All the genetic information of a living organism is stored in this molecule. The helical configuration exposes less the bases, protecting them from mutations, and it has a more compact conformation. A human DNA would have a end-to-end extension of $\sim 2\,\mathrm{m}$ if stretched, but nucleus cells only have $6\,\mu\mathrm{m}$ of diameter[14]. Furthermore, helical shapes can be observed in a variety of situations on the everyday life, like in curly hairs, twisting staircases, *fusilli* pasta, screws or springs. Helices are everywhere, either by the advantages of their shape or as a consequence of the physical properties of materials.

A helix is a smooth curve in a three-dimensional space characterized by its tangent making a constant angle, different from zero, with a fixed line (centreline), Figure 1.1. A simple way to describe the helix shape is to think in a circular motion and add translation in the perpendicular direction (to the plane that contain the circular motion). Circumferences do not have handedness. But in the helix case, if the circular motion sense is kept, going up or down generates two helices with opposite handedness. Helices are the simplest non-trivial three-dimensional curves.

Mathematically, a helical curve, $\mathbf{r}(s)$, can be written parametrically by

$$x = R\cos\alpha, \tag{1.1a}$$

$$y = R\sin\alpha, \tag{1.1b}$$

$$z = h\alpha, \tag{1.1c}$$
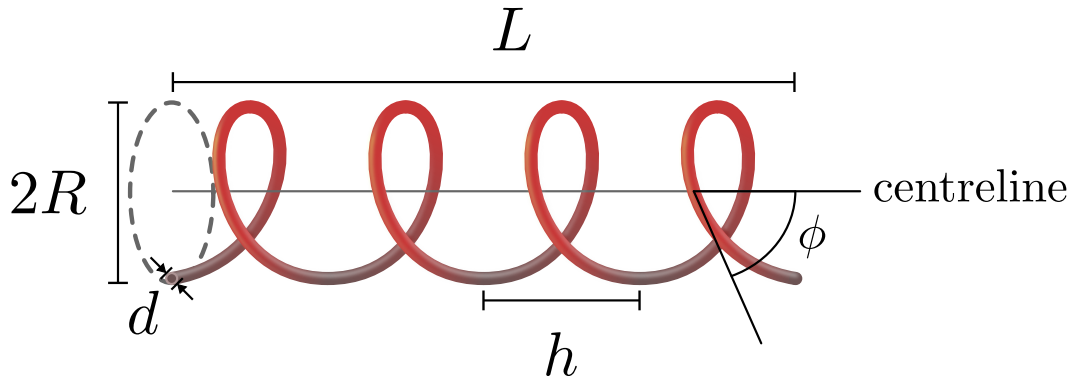
Figure 1.1: Depiction of a helix and its properties: R is the radius of the helix; d is the filamentary diameter; h is the pitch; L is the helical height.

where R is the radius of the helix, h is the pitch, given by the vertical separation between the helix loops and α is a point of the curve. This curve is regular, i.e. $\mathbf{r}' \neq 0$, then, the tangent vector $\mathbf{T}$ can be obtained by differentiating the curve equation,

$$\frac{d\mathbf{r}}{d\alpha} = (-R\sin\alpha, R\cos\alpha, h), \tag{1.2}$$

and dividing by its normalization,

$$ds = \sqrt{R^2 + h^2}\, d\alpha, \tag{1.3}$$

$$\mathbf{T} = \frac{\frac{d\mathbf{r}}{d\alpha}}{\|\frac{d\mathbf{r}}{d\alpha}\|} = \frac{1}{\sqrt{R^2 + h^2}}\left(-R\sin\alpha, R\cos\alpha, h\right). \tag{1.4}$$

The normal vector $\mathbf{N}$ is given by a second differentiation of the position vector and its normalization,

$$\mathbf{N} = \frac{\frac{d\mathbf{r}^2}{d^2\alpha}}{\|\frac{d\mathbf{r}^2}{d^2\alpha}\|} = \left(-\cos\alpha, -\sin\alpha, 0\right). \tag{1.5}$$

The curvature of a curve, κ, is defined by the amount it bends over the tangent:

$$\mathbf{T}' = \kappa\mathbf{N}. \tag{1.6}$$

This quantity assumes non-negative scalar values and zero for linear curves, despite the normal vector cannot be defined by the tangent. In the helical case, the curvature is given by:

$$\kappa = \frac{R}{R^2 + h^2}. \tag{1.7}$$

To complete the orthogonal triad of unit vectors, called the Frenet-Serret frame, the

binormal $\mathbf{B}$ is defined as the vector perpendicular to the tangent and normal vectors,

$$\mathbf{B} = \mathbf{T} \times \mathbf{N} \tag{1.8}$$

$$= \frac{1}{\sqrt{R^2 + h^2}} \left(h\sin\alpha, -h\cos\alpha, R \right). \tag{1.9}$$

The variation of the binormal vector gives the rate of rotation over the normal vector around the tangent,

$$\mathbf{B}' = -\tau\mathbf{N}. \tag{1.10}$$

This scalar value defines the torsion of a curve:

$$\tau = \frac{h}{R^2 + h^2}. \tag{1.11}$$

The sign of torsion has a geometrical meaning, which when τ is positive the helix is right-handed and when τ is negative the helix is left-handed. To complete the Frenet-Serret formulas, which describe the kinematics of the curve, it is required to calculate the missing derivative $\mathbf{N}'$. Since $\mathbf{N}' \cdot \mathbf{N} = 0$, $\mathbf{N}'$ is a combination of the tangent and the binormal vectors, $\mathbf{N}' = a\mathbf{T} + b\mathbf{B}$:

$$a = \mathbf{N}' \cdot \mathbf{T} = -\mathbf{N} \cdot \mathbf{T}' = -\kappa\mathbf{N} \cdot \mathbf{N} = -\kappa, \tag{1.12}$$

and

$$b = \mathbf{N}' \cdot \mathbf{B} = -\mathbf{N} \cdot \mathbf{B}' = \tau\mathbf{N} \cdot \mathbf{N} = \tau, \tag{1.13}$$

resulting in the following equation for $\mathbf{N}'$:

$$\mathbf{N}' = -\kappa\mathbf{T} + \tau\mathbf{B}. \tag{1.14}$$

Then, the complete set of the Frenet-Serret equations

$$\begin{aligned} \mathbf{T}' &= & \kappa\mathbf{N}, \\ \mathbf{N}' &= -\kappa\mathbf{T} & + \tau\mathbf{B}, \\ \mathbf{B}' &= & -\tau\mathbf{N}, \end{aligned} \tag{1.15}$$

and the tangent $\mathbf{T}$ define the frame along the curve[15]. These equation can also be written in terms of the Darboux vector,

$$\boldsymbol{\Omega} = \kappa\mathbf{B} + \tau\mathbf{T}, \tag{1.16}$$

and the Frenet-Serret equations can written in a compact notation as $Q_i' = \boldsymbol{\Omega} \times Q_i$,

where $Q = [\mathbf{T}, \mathbf{N}, \mathbf{B}]$ is the Frenet-Serret frame.

Moreover, from the equations 1.7 and 1.11 arises the following equalities:

$$\frac{\kappa}{\tau} = \frac{R}{h} = \tan\phi, \tag{1.17}$$

where ϕ is the pitch angle, the angle between the tangent vector and the centreline, and also

$$R = \frac{\kappa}{\kappa^2 + \tau^2}, \tag{1.18}$$

$$h = \frac{\tau}{\kappa^2 + \tau^2}. \tag{1.19}$$

Equation 1.17 puts in evidence the Lancret's theorem, which states that a constant curvature to torsion ratio is a necessary and sufficient condition for a curve to be a helix.

In nature or in man-made products, helicity can arise in different contexts. A common way to design helical compression springs involves the winding of a wire around a shaft. In some materials a heat treatment is required to accommodate the stresses caused by the deformations and, after cooling, the springs keep their shape. Another way to produce helical springs involves the application of a constant deformation to a straight wire by driving the wire toward a grooved head. The feed rate and the point of contact tune the helical shape[16]. The helicity arises in both processes by intrinsically creating a constant curvature and torsion along a linear wire.

By contrast, Snir and Kamien[17] suggested a purely entropic approach to understand the helical folding of molecular chains. The researchers started by considering long molecules as a solid and impenetrable tubes immersed in a solution of hard spheres. For specific ratios between the tube and spheres radii, the helical shape promotes the increasing of the entropy of the spheres, as some regions of the tube surroundings overlaps, decreasing the excluded volume. This model provides an explanation for the helical shape of many α helices and β sheets.

Furthermore, most coiled structures do not present a regular shape. However, even if Lancret's theorem is not verified for those structures, if their shape is close enough to the helical shape, they will be considered as helices. For instance, in the case of the DNA when the molecule opens for the replication process, as result from winding the molecule, it will generate an additional twisting called as supercoiling. This supercoiling effect makes the double twisted strands to adopt more complex shapes, like superhelices and plectonemes[18]. The supercoiling of the DNA can be measured by a topological quantity that defines the number of times that the the strands turns

in the original linear molecule: the linking number, Lk. When the DNA changes in response to the supercoiling, there is a change in the number of times strands revolve one another: the twist, Tw. Moreover, there is another quantity that describe how much the molecule coils and kinks in space: the writhe, Wr. All these quantities might not be straightforward calculated, or even hard to grasp the physical meaning in a 3D space. However, one important result from the study of the DNA supercoiling is that the sum of the twist and writhe numbers is equal to the linking number:

$$\text{Tw} + \text{Wr} = \text{Lk}. \tag{1.20}$$

In a closed molecule, like DNA rings, the linking number remains constant but twist and writhe may be converted one into another. Furthermore, despite the linking number is only defined in close curves, many types of DNA have anchorage points which constraint the rotation of the DNA. Therefore, these anchorage points can be regarded as if they are connected, holding the same properties of closed curves.

1.2 Perversions

A striking phenomenon that results from the conservation of the topological laws can be observed in plant tendrils, as reported by Darwin in his insightful work about climbing plants[19]. In one of his many observations, Darwin found that

"when an unattached tendril contracts spirally, the spire always runs in the same direction from tip to base. A tendril, on the other hand, which has caught a support by its extremity, although the same side is concave from end to end, invariably becomes twisted in one part in one direction, and in another part in the opposite direction; the oppositely turned spires being separated by a short straight portion. (...) Whether the spires turn once or more than once in opposite directions, there are as many turns in the one direction as in the other".

Besides observing the circumnutation of the tendrils and how it became twisted, Darwin also observed that the handedness of the tendrils swapped in some parts and that the number of turns was the same in both directions. This kind of behaviour can also be observed in gift ribbons. First, in order to the ribbon acquire a higher number of loops, the dull side of the stripe is swept with a scissor blade to the ribbon acquire a coiled shape, Figure 1.2. If the helix is stretched, at this point, with both ends fixed, it will tighten the loops until a maximum extension is reached. Upon release, the ribbon
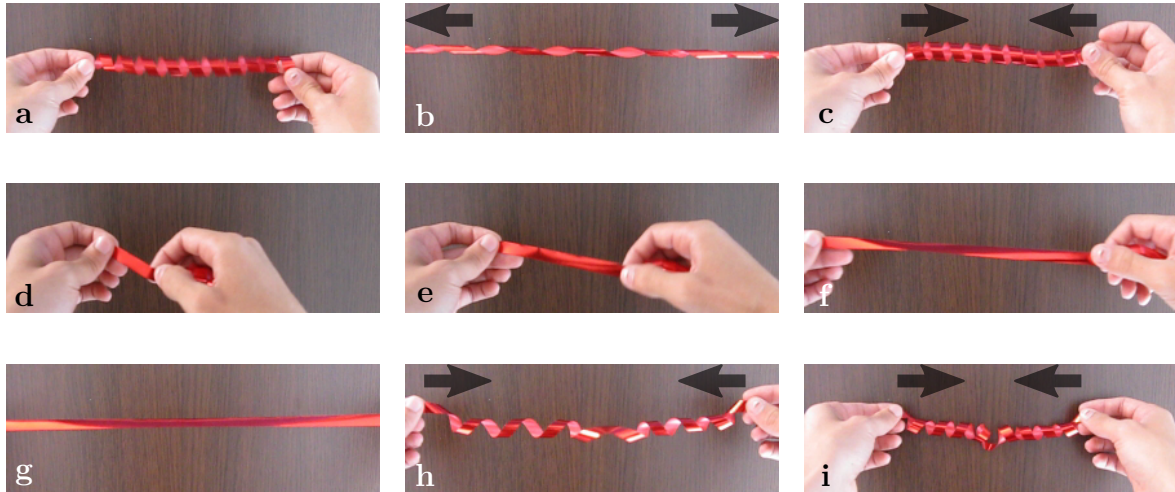
Figure 1.2: Formation of perversions in gift ribbons. **a** – **c** Pull and release of a helical gift ribbon, with both ends fixed; the loops get tighten and afterwards the ribbon recovers to the original shape. **d** – **f** Removal of the loops from the ribbon. **g** – **i** Due to the constraint imposed in the ends of the ribbon, when the stripe is let to relax, a perversion connecting two helices with opposite handedness, arises in the middle.

will return its original configuration. Stretching while removing the loops of the strip, will lead to a unlooped and straight configuration. The release of the ribbon, with both ends fixed, leads to a similar phenomenon observed on the plant tendrils: two helices with opposites handedness connected by hand reversal segment. Goriely and Tabor[20] associated this reversal to the term *perversion*, which was first used in the 19th century by Listing for describing the mirroring behaviour found on seashells.

Similarly to the invariant linking number on DNA, where it remains constant upon winding, the equation 1.20 is also verified during the curling of tendrils and gift ribbons. However, to calculate the linking number, two closed curves are required. Since both ends are clamped, the same approximation for DNA can be used by considering the fixed points being connected. In the case of the gift ribbon, the two borders can be used for describe the linking number between the two curves[21]. In the case of some tendrils, like the ones of passionflower, the cross-section is approximately circular, which makes it hard to define two curves along the filament. Some other tendrils have cross-sections where two curves can be easily defined, like in the case of the rectangular cross-section of cucumber tendrils. Nevertheless, the conservation law implies that the number of left- and right-handed loops must be the same during the curling of tendrils, ribbons or any winding filament constrained at two points, if there is no twist when they are initially released.

The mechanism underlying the curling behaviour in tendrils can be understood

with help of the step where the dull side of the ribbon is run over with a blade. This step changes the elastic properties of the dull side relatively to the bright side. This modification leads to an increase of the intrinsic curvature, which is related with the final number of loops. In case of the tendrils, it can be observed an increasing number of loops over the time, even if there is no significant alteration of the end-to-end distance. Therefore, the elastic properties must change also over the time. Indeed, observations performed by Mahadevan et al.[22] demonstrated the differences between straight and coiled cucumber tendrils. In the case of coiled tendrils, one of the sides of the tendrils had a layer with strong lignified fibrils.

Structures with asymmetric contraction have a non-vanishing curvature, an intrinsic curvature. If no others stresses along the filament exist, these structures are twistless filaments. In fact, on the gift ribbons cross-section, one of the directions is much smaller than the other, the ribbon can be folded into a looped ring, if the strand is not long enough. In the case of tendrils, or other filaments where both directions of the cross-section have comparable dimensions, self-contact avoids the helix collapsing into a ring. McMillen and Goriely[23] studied the mechanics of two semi-infinite helices with opposite handedness connected with a perversion by considering a rod with intrinsic curvature, K. After establishing the relation between the differential growth in different sides of the rod with the intrinsic curvature, they described the helices as solutions to the static Kirchhoff equations. From the solutions of the Kirchhoff equations, it is possible to define a set of helices that obey to the following ellipse in the curvature – torsion plane:

$$\left(\kappa - \frac{K}{2}\right) + \Gamma\tau^2 = \frac{K^2}{4} \tag{1.21}$$

where Γ is a ratio between bending and torsional stiffness in the normal direction.

Figure 1.3 shows a set of curves and their correspondence in curvature and torsion plane. The two extreme cases correspond to the unlooped straight filament, with zero curvature and torsion, and to the ring with curvature $\kappa = K$, ring radius is K^{-1}, and no torsion (self-contact effects not considered). The perversion is a heteroclinic orbit connecting any other two points with opposite torsion of the ellipse.

When the tension between the ends decreases, the filament twists to lower the stored elastic energy due to the intrinsic curvature, despite not having an intrinsic torsion. A first approach to calculate the transition from the straight to the helical configuration can be calculated by assuming a force F is applied in the ends in the direction of the filament centreline and the perversion introduces an increment on the energy function
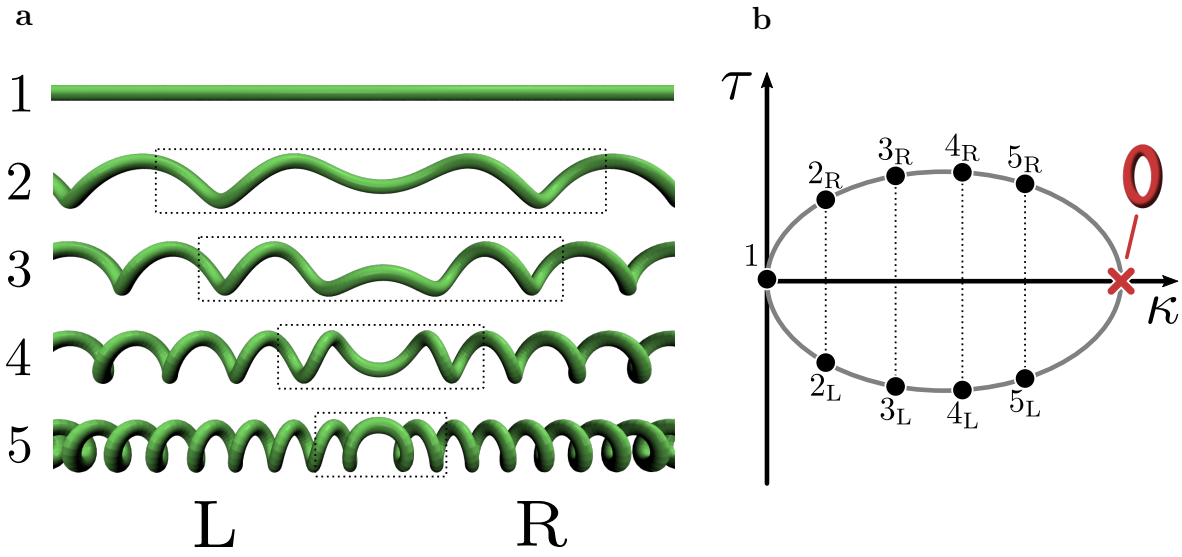
Figure 1.3: **a** Set of structures containing left- (L) and right-handedness (R) helices connected by perversions with different curvatures and torsions. **b** Each case is represented in the curvature – torsion plane. For each case number, when $\tau \neq 0$, left- and right-handed helices points only differ in the signal of the torsion and the perversion is an heteroclinic orbit joining the two points of the helices.

that can be ignored. The total energy density writes as[24]:

$$\varepsilon = \frac{1}{2}EI(\kappa - K)^2 + \frac{1}{2}GJ\tau^2 - \frac{F\tau}{\gamma},\tag{1.22}$$

where the three terms correspond to the bending, torsion and tension energies; E is the Young's modulus, I is the cross-sectional moment of inertia, J is the torsion constant and $\gamma = \sqrt{\kappa^2 + \tau^2}$. For stationary conditions, the minimization criteria requires that the derivative of energy is zero:

$$\frac{\partial \mathcal{E}}{\partial \kappa} = EI(\kappa - K) + \frac{F\kappa\tau}{\gamma^3} = 0\tag{1.23}$$

$$\frac{\partial \mathcal{E}}{\partial \tau} = GJ\tau - \frac{F\kappa^2}{\gamma^3} = 0.\tag{1.24}$$

By combining both equations, the applied force can be written in function of κ:

$$F = EI(K - \kappa)\frac{\left(\kappa^2 - \alpha\kappa(K - \kappa)\right)^{3/2}}{\kappa\left(\alpha\kappa(K - \kappa)\right)^{1/2}}, \quad \alpha = \frac{EI}{GJ}.\tag{1.25}$$

When the filament goes from the helical to the straight configuration, the critical force
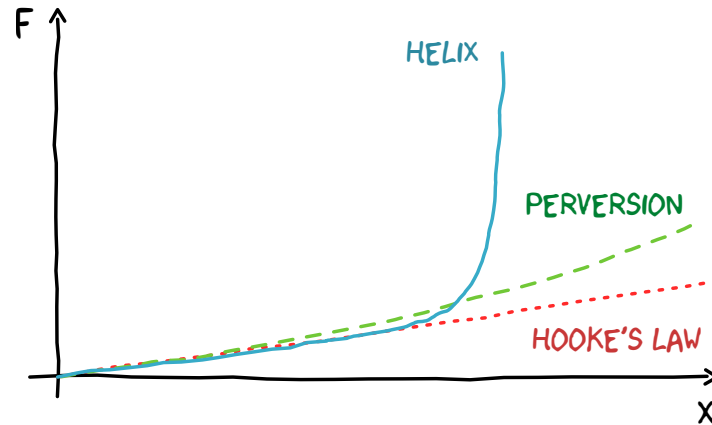
Figure 1.4: Comparison of typical force-extension profiles of helices and perversions. Adapted from [23].

can be obtained by taking the limit $\kappa \to 0$:

$$F_{\text{cr}} = \frac{E^2 I^2}{GJ} K^2. \tag{1.26}$$

Then, considering this simple approach, when $F < F_{\text{cr}}$ straight filaments with intrinsic curvature curl into helical structures.

Perversions in tendrils are a result of a topological constraint. Nevertheless, the fact of tendrils contain single or multiple perversions on their helical structures might have an impact on how the plant deals with imposing forces. For small displacements, x, helices without and with perversions have a similar Hookean behaviour. However, for higher displacements a helix without perversions have a stiffer behaviour than a helix with perversions[23], Figure 1.4. The differences of the force-extension behaviours between helices without and with perversion can be more easily understood by returning to the extension of the ribbon shown in Figure 1.2. After pulling a ribbon without perversions, Figure 1.2**b**, the loops become tighter and offer resistance to further extensions. The extension of the ribbon with a perversion is not shown in the Figure 1.2, but the behaviour is similar to the release but in a reverse order, from Figure 1.2**i** to **g**. In this case, after start pulling, the perversion unwinds until become unlooped. Then, for larger extensions, it is easier to strain helical ribbons with perversions than ribbon without any perversions.

The existence of perversions in plants can be of relative importance. But in the case of Spiroplasma, a helical bacteria that infects insects and plants, the perversions introduce an important advantage in the organism motility. At smaller scales, microorganisms cannot rely on the inertial forces and movement is mostly dependent on viscous forces of the surroundings. Therefore, reciprocal movements hardly promote some motility of

organisms. While some swimming bacterium use the rotation of large helical appendages to move, spiroplasmas invert the torsion in one of the ends and propagate that perversion along their body. Typically, the propagation of perversions come in pair which results in a zigzag-like movement. Thus, these bacterium have an advantage over other types of organisms on the movement in different mediums. Spiroplasma are known to have the ability to move in any directions and change their movement on gradients in chemical concentration or viscosity[25], [26].

It is still not clear how perversions might be useful for real life applications. Still, the physics behind perversions is useful for understanding problems where both handednesses exist in a single structure, like in proteins folding[27] or understanding cardiac looping[28]. The existence of perversions changes the force-extension profiles of helical structures and can also be looked as the introduction of a defect on the helical geometry, which can be useful for the movement of micro and nanostructures. Another example of structures with perversions are the double torsion springs, found for instance on clipboards. These wire springs consist on two springs with opposite handedness connected by a segment with a shape that, usually, does not resembles the perversions found in tendrils.

Up to this point, some of the properties of single filaments were presented. Besides the behaviour of single structures, many systems have more than one filament, which might originate different properties resulting from the interactions between them. For instance, depending on the characteristics of the fibres, a high number strands might become mechanically bonded and result in a fabric, even if strands are not knotted.

1.3 Entanglements

Knots and others types of entanglements have a huge importance in the history of humanity. An almost endless ways of knot usages can be found in the most diverse practices of civilizations, for instance in the construction of buildings like houses or bridges, in the manufacture of textiles and fishing nets, in the assembly of animal traps, suture of injuries or in everyday tasks like tying shoes. In fact, knots have assumed a essential role since the earliest technological developments of humankind. The simplest knot consists in forming a loop with some filament, pass one of the ends through it and then it can be tighten by pulling both ends. There are a countless number of other different knots topologies that can be created. But despite its usefulness and versatility in the everyday life, knots and braids only started to be mathematically formulated in the second half of nineteen century, originating to fields called as knot theory and braid theory[29].

Although knotting are a very smart way of trapping and attaching filaments, is

not much observed in nature to create links. There are many physical systems that resort to other kinds of entanglements. Pierre-Gilles de Gennes introduced the reptation theory in 1971 to explain the motion of entangled polymers[30]. Typically, dense polymer systems are very complex materials. Besides the chemical interactions, the global chains conformations play a decisive role in the material physical properties. Chains are entangled because they become intertwined and cannot pass through each others. This elastic and viscous chains with time eventually can flow through an allowed path by crawling along like reptiles[31]. A simple, but enlightening, example of this theory can be explained with uncooked and *al dente* spaghetti. Uncooked spaghetti is stiff and do not entangle at all. It is easy to select and separate strands from each other. On the other side, *al dente* spaghetti after being cooked and dried become intertwined. It is not easy to pull a strand without pulling others. By agitating the strand, eventually it comes away. The reptation theory received good agreement from rheological experiments, and found applications in electrophoresis. As a result of the widely acceptance of this theory, researchers started to believe that stable and localized links could only be formed through chemical interactions (crosslinking)[32].

The main motivation of this thesis started on a finding reported by one of the supervisors in 2008, in a rapid communication to Soft Matter: a new type of entanglement that is easily formed in helical structures[33]. This finding was innovative because it shows that physical interactions alone can produce stable and localized links in helical structures. These localized entanglements were called Physical PseudoKnots (PPKs). Physical since only physical interactions are required and pseudoknots because despite forming links in a specific region, structures are not knotted. These entanglements are formed easily on helices by intertwining their loops. In Figure 1.5 a possible way to
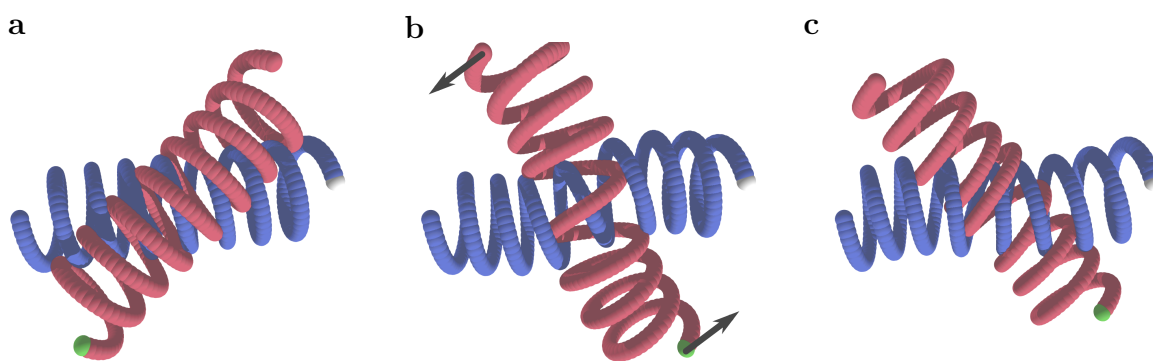

Figure 1.5: Physical Pseudoknot (PPK) formation illustration: **a** red helix gets inside the blue helix and rotates under a force (black arrows); **b** rotation forces blue helix loops to open; **c** after red helix slip into the blue, the two loop overstretch is restored trapping the red helix, making the previous path irreversible.

explain the formation of a PPK is shown. A red helix fits inside the blue helix, Figure 1.5**a**. The rotation of red helix relatively to the blue helix causes a displacement of two adjacent loops, 1.5**b**, until the red loop slip inside the blue helix, 1.5**c**. Afterwards, the displacement caused in the blue helix loops is restored and reversing the exact path would need to stretch the blue helix. Now, the previous path cannot be reversed unless the two loops are forced open. This asymmetry in the creation and destruction of PPKs resembles the ratchet effect. Moreover, the two helices are physically constrained, with properties that resembles with localized knots. However, PPKs are not true knots and they can still be dynamically untangled.

This finding was experimentally validated with mechanical springs [33], where it was shown that the energy required to form PPKs could be at least two orders of magnitude smaller than the energies required to destroy them. This result is impressive as the difference in magnitude between the energies involved in covalent and hydrogen bonding is of the order of one order of magnitude. In practical terms, this means that PPKs are very easy to make and much harder to destroy.

1.4 Organization of the thesis

This thesis contains modified versions of published peer-reviewed papers from Science Citation Index (SCI) journals (Chapters 4-6). The most obvious modification is the format. The content of the papers was adjusted to the rules of the thesis and the size of some figures was increased to a better readout. Also, some words followed a different spelling in different journals, therefore they might be changed to match the British English spelling of the thesis. The order chosen for the chapters does not follow a chronological order in which the work developed in this thesis was executed or the papers were published. Instead, after some insights about Molecular Dynamics, and details on the performed experimental work, putting in evidence the Electrospinning technique, strategies on how to model and produce helices and perversions in single filaments are first presented. Following the same route to describe new mechanisms in simulation and experimental helical filaments, the creation of helical structures with different topologies and the interactions of helical structures involving perversions and PPKs are then presented. This thesis includes both computational simulations and real experiments results.

In Chapter 2, the concepts of Molecular Dynamics (MD) algorithms are first introduced. In the simulations presented in this thesis, two different algorithms are used: the first is Filament Simulator (FS), an algorithm developed during my Master thesis[34], and the second is Large-scale Atomic/Molecular Massively Parallel Simulator

(LAMMPS)[35]. Afterwards, the operation and the main features of both algorithms are described by using pseudo-code, in the case of FS algorithm, and real input commands, in the case of LAMMPS algorithm.

Chapter 3 introduces some of the experimental considerations. First, we start by describing the properties of the used polymeric solutions and how their features could be used to obtain helical fibres. Then, a description of the apparatus used to produce microfibres, a homemade electrospinning equipment, is presented. To avoid splitting or modifying the next chapter, Chapter 4, where the electrospinning technique is reviewed, in Chapter 3 we include details not included in the review article, like the description of the equipment, the operation and used collectors. Also, further details on how multiple irradiation cycles using UV light and used characterization techniques are also described here.

Chapter 4 presents a review on producing helical fibres by using electrospinning technique. We start by discussing the role played by helical fibres in nature and how can helical structures be produced artificially. Then, the general principles of the electrospinning method are explained. Different approaches to obtain helical electrospun are classified in three categories: by buckling due to impingement on the collector; by twisting motion; and by buckling due to asymmetric contraction. A final remark on the specific tailoring of filaments with complex structures is offered in the end of the chapter.

P. E. S. Silva, F. Vistulo de Abreu, and M. H. Godinho, "Shaping helical electrospun filaments: A review," *Soft Matter*, 2017. DOI: 10.1039/C7SM01280B

Chapter 5 proposes a generalization of the concept of perversion by introducing a geometrical transformation at the centre of the perversion. Two extreme cases, symmetric and antisymmetric perversions, are further investigated through lab experiments by applying different irradiation schemes in electrospun fibres. The experimental results are then compared with computational simulations.

P. E. S. Silva, J. L. Trigueiros, A. C. Trindade, *et al.*, "Perversions with a twist," *Scientific Reports*, vol. 6, p. 23 413, Mar. 30, 2016. DOI: 10.1038/srep23413

In Chapter 6 we extend the shaping of the electrospun fibres and instead of applying the UV in different sides of the filament, fibres are irradiated in the same side, but in with different times in alternated regions. Moreover, we introduce an adaptation to the current strategy to produce helical fibres that allows to improve the fabrication time.

P. E. S. Silva and M. H. Godinho, "Helical Microfilaments with Alternating Imprinted Intrinsic Curvatures," *Macromolecular Rapid Communications*, vol. 38, no. 5, p. 1 600 700, Mar. 2017. DOI: `10.1002/marc.201600700`

Chapter 7 describes two approaches to obtain entanglements between helical filaments, using exclusively mechanical interactions. In the first, the linkage between the filaments is created by using the winding behaviour of the perversions. An introduction to braid theory will be presented to classify the types of obtained braids. In the second approach, fabrics are produced by using intertwining the helices and forming physical pseudoknots (PPKs).

Finally, a summary of the conclusions of all chapters and some perspectives are presented.

References

[1]   D. Filippini, *Autonomous Sensor Networks Collective Sensing Strategies for Analytical Purposes*. Berlin, Heidelberg: Springer, 2013.

[2]   G. Kellie, Ed., *Advances in Technical Nonwovens*, Woodhead Publishing series in textiles number 181, Amsterdam: Elsevier/Woodhead Publishing, 2016, 508 pp.

[3]   J. G. Cook and J. G. Cook, *Man-Made Fibres*, 5. ed, ser. Handbook of textile fibres. Cambridge: Woodhead Publishing, 2005, 723 pp.

[4]   L. Zhang, J. J. Abbott, L. Dong, B. E. Kratochvil, D. Bell, and B. J. Nelson, "Artificial bacterial flagella: Fabrication and magnetic control," *Applied Physics Letters*, vol. 94, no. 6, p. 064 107, Feb. 9, 2009. DOI: `10.1063/1.3079655`.

[5]   Y. T. Cheng, D. E. Rodak, C. A. Wong, and C. A. Hayden, "Effects of micro- and nano-structures on the self-cleaning behaviour of lotus leaves," *Nanotechnology*, vol. 17, no. 5, pp. 1359–1362, Mar. 14, 2006. DOI: `10.1088/0957-4484/17/5/032`.

[6]   S. Kim, C. Laschi, and B. Trimmer, "Soft robotics: A bioinspired evolution in robotics," *Trends in Biotechnology*, vol. 31, no. 5, pp. 287–294, May 2013. DOI: `10.1016/j.tibtech.2013.03.002`.

[7]   A. D. Carlson and J. Copeland, "Flash Communication in Fireflies," *The Quarterly Review of Biology*, vol. 60, no. 4, pp. 415–436, Dec. 1985. DOI: `10.1086/414564`.

[8]   V. I. Vullev, "From Biomimesis to Bioinspiration: What's the Benefit for Solar Energy Conversion Applications?" *The Journal of Physical Chemistry Letters*, vol. 2, no. 5, pp. 503–508, Mar. 3, 2011. DOI: `10.1021/jz1016069`.

[9]   A. Carruthers, *Writers on' Nature.* Read Books Ltd., 2016.

[10]   C. R. Robbins, *Chemical and Physical Behavior of Human Hair*, 5. ed. Berlin Heidelberg: Springer, 2012, 724 pp.

[11]   S. Thibaut, P. Barbarat, F. Leroy, and B. A. Bernard, "Human hair keratin network and curvature," *International Journal of Dermatology*, vol. 46, pp. 7–10, s1 Oct. 2007. DOI: 10.1111/j.1365-4632.2007.03454.x.

[12]   N. E. Stamp, "Self-Burial Behaviour of Erodium Cicutarium Seeds," *Journal of Ecology*, vol. 72, no. 2, pp. 611–620, 1984. DOI: 10.2307/2260070. JSTOR: 2260070.

[13]   D. Evangelista, S. Hotton, and J. Dumais, "The mechanics of explosive dispersal and self-burial in the seeds of the filaree, Erodium cicutarium (Geraniaceae)," *Journal of Experimental Biology*, vol. 214, no. 4, pp. 521–529, Feb. 15, 2011. DOI: 10.1242/jeb.050567. pmid: 21270299.

[14]   B. Alberts, Ed., *Molecular Biology of the Cell*, 4th ed, New York: Garland Science, 2002, 1548 pp.

[15]   D. J. Struik, *Lectures on Classical Differential Geometry*, 2nd ed. New York: Dover Publications, 1988, 232 pp.

[16]   J. L. Longe, *How Products Are Made. Vol. 6: An Illustrated Guide to Product Manufacturing.* Detroit, Mich.: Gale Group, 2001.

[17]   Y. Snir and R. D. Kamien, "Entropically Driven Helix Formation," *Science*, vol. 307, no. 5712, pp. 1067–1067, Feb. 18, 2005. DOI: 10.1126/science.1106243. pmid: 15718461.

[18]   A. D. Bates and A. Maxwell, *DNA Topology*, 2nd ed. Oxford ; New York: Oxford University Press, 2005, 198 pp.

[19]   C. Darwin, "On the Movements and Habits of Climbing Plants.," *Journal of the Linnean Society of London, Botany*, vol. 9, pp. 1–118, 33-34 Jun. 1865. DOI: 10.1111/j.1095-8339.1865.tb00011.x.

[20]   A. Goriely and M. Tabor, "Spontaneous Helix Hand Reversal and Tendril Perversion in Climbing Plants," *Physical Review Letters*, vol. 80, no. 7, pp. 1564–1567, Feb. 16, 1998. DOI: 10.1103/PhysRevLett.80.1564.

[21]   P. Pieranski, J. Baranska, and A. Skjeltorp, "Tendril perversion—a physical implication of the topological conservation law," *European Journal of Physics*, vol. 25, no. 5, p. 613, 2004. DOI: 10.1088/0143-0807/25/5/004.

References

[22] S. J. Gerbode, J. R. Puzey, A. G. McCormick, and L. Mahadevan, "How the Cucumber Tendril Coils and Overwinds," *Science*, vol. 337, no. 6098, pp. 1087–1091, Aug. 31, 2012. DOI: 10.1126/science.1223304. pmid: 22936777.

[23] McMillen and Goriely, "Tendril Perversion in Intrinsically Curved Rods," *Journal of Nonlinear Science*, vol. 12, no. 3, pp. 241–281, 2002. DOI: 10.1007/s00332-002-0493-1.

[24] J. Liu, J. Huang, T. Su, K. Bertoldi, and D. R. Clarke, "Structural Transition from Helices to Hemihelices," *PLOS ONE*, vol. 9, no. 4, e93183, 2014. DOI: 10.1371/journal.pone.0093183.

[25] R. Gilad, A. Porat, and S. Trachtenberg, "Motility modes of Spiroplasma melliferum BC3: A helical, wall-less bacterium driven by a linear motor," *Molecular Microbiology*, vol. 47, no. 3, pp. 657–669, Feb. 1, 2003. DOI: 10.1046/j.1365-2958.2003.03200.x.

[26] J. W. Shaevitz, J. Y. Lee, and D. A. Fletcher, "Spiroplasma Swim by a Processive Change in Body Helicity," *Cell*, vol. 122, no. 6, pp. 941–945, Sep. 23, 2005. DOI: 10.1016/j.cell.2005.07.004. pmid: 16179261.

[27] A. Krokhotin, A. Liwo, G. G. Maisuradze, A. J. Niemi, and H. A. Scheraga, "Kinks, loops, and protein folding, with protein A as an example," *The Journal of Chemical Physics*, vol. 140, no. 2, p. 025 101, Jan. 14, 2014. DOI: 10.1063/1.4855735.

[28] J. Männer, "On the form problem of embryonic heart loops, its geometrical solutions, and a new biophysical concept of cardiac looping," *Annals of Anatomy - Anatomischer Anzeiger*, vol. 195, no. 4, pp. 312–323, Jul. 2013. DOI: 10.1016/j.aanat.2013.02.008.

[29] J. C. Turner and P. van de Griend, *History and Science of Knots*, ser. Series on Knots and Everything. WORLD SCIENTIFIC, May 1996, vol. 11.

[30] P.-G. Gennes, *Scaling Concepts in Polymer Physics*. Ithaca, NY: Cornell University Press, Nov. 30, 1979, 319 pp.

[31] M. Doi, *Introduction to Polymer Physics*. Clarendon Press, 1996, 148 pp.

[32] R. A. L. Jones, *Soft Condensed Matter*. OUP Oxford, Jun. 20, 2002, 213 pp.

[33] F. Vistulo de Abreu, R. G. Dias, and C. von Ferber, "Pseudo-knots in helical structures," *Soft Matter*, vol. 4, no. 4, p. 731, 2008. DOI: 10.1039/b719234g.

[34] P. E. S. Silva, "Modelling the dynamics of elastic filaments," Msc, University of Aveiro, 2010.

[35] S. Plimpton, "Fast Parallel Algorithms for Short-Range Molecular Dynamics," *Journal of Computational Physics*, vol. 117, no. 1, pp. 1–19, Mar. 1995. DOI: 10.1006/jcph.1995.1039.

[36] P. E. S. Silva, F. Vistulo de Abreu, and M. H. Godinho, "Shaping helical electrospun filaments: A review," *Soft Matter*, 2017. DOI: 10.1039/C7SM01280B.

[37] P. E. S. Silva, J. L. Trigueiros, A. C. Trindade, R. Simoes, R. G. Dias, M. H. Godinho, and F. V. de Abreu, "Perversions with a twist," *Scientific Reports*, vol. 6, p. 23 413, Mar. 30, 2016. DOI: 10.1038/srep23413.

[38] P. E. S. Silva and M. H. Godinho, "Helical Microfilaments with Alternating Imprinted Intrinsic Curvatures," *Macromolecular Rapid Communications*, vol. 38, no. 5, p. 1 600 700, Mar. 2017. DOI: 10.1002/marc.201600700.

Chapter

2

Molecular Dynamics simulations

Computer simulations are an extraordinary tool to investigate any physical phenomenon. The main purpose of simulations is to imitate a real system and to reinforce or invalidate the mechanisms behind the properties of real systems. Moreover, there are cases where is not feasible to conduct experiments, whether be unethical, tedious or time consuming. Computer simulations act as a link between theories and experiments: theory assumptions can be inserted in a simulation model and further compared with the experimental results. If experimental and computational results disagree then the model is inadequate to predict the physical properties of the tested system. In the case of computational and theory results disagree, probably there is a flaw in the theory. This way of doing experiments using a computer changed how investigation was made since the appearance of first computer simulations and is rare nowadays having a theory applied to the reality that is not tested first by computers simulations[1].

Ultimately it is desirable to have simulations that return the maximum information and exactly predict the experiments. However, in most of cases, due to the computer processing cost and amount of data, is better to use more efficient and approximate methods. In most of cases, introducing the essential physical considerations may be enough to predict good results. The level of detail can be adjusted depending on the observation variables. For instance, considering a polymer chain as a set of beads connected by springs might seem as realistic as considering a spherical cow. However, it is still possible to describe some behaviours of polymers, to some extent, by using this kind of approaches[2], [3].

Computer simulations can also be used as an exploratory tool. On the one hand, if the algorithm was developed to have a broad usage in studying a given problem, exploring multiple possibilities might be as easy as overriding a set of numbers. Results might reveal some interesting phase transitions or a new molecule conformation. On the other hand, instead of imitating a laboratory result, computer experiments can be used with the perspective of creating new possibilities. In the work developed during this thesis we have modelled the dynamics of helical structures. Although the simulated filaments behaviour matched with observed experiments, we questioned if the perversions placement could be controlled. Instead of resorting to the manipulation of experimentally obtained fibres, some exploratory experiments were carried out with the computer. Instead of applying a constant modification along the filament, the modification had a switch in the middle of the filament that would result in a local half twist. Obtained structure dynamics appeared to be, at first glance, very similar to the helical structures obtained without the switch and, therefore, not very interesting of studying for our purposes. Notwithstanding, putting the two different types of structures side by side some intriguing differences were observed. This observation instigated ourselves to question about a longtime observed phenomenon as tendril perversions, how it could be changed and what new properties would arise from the inserted modifications. Still, conditions used in simulations are often optimal and the effects under consideration observed in real experiments might not be as clear observed as in simulations (which was not the case, as it is presented in Chapters 5 and 6).

To study the dynamics of elastic filaments in the work developed in this thesis, two different approaches of Molecular Dynamics (MD) algorithms were used. The first, uses an algorithm developed during my Master thesis for modelling the dynamical behaviour of helices, which will be named, for convenience, as filament simulator (FS). However, the algorithm could not model filaments with heterogeneous cross-sections as the experimental fibres possess and had some stability issues for simulating structures with vanishing curvatures. To solve those points another tool based in MD simulations was

used, named Large-scale Atomic/Molecular Massively Parallel Simulator (LAMMPS).

MD simulations provide a simple approach to study the dynamics of a many-body system. The concept behind the MD simulations is similar to real experiments: a sample is prepared and a given phenomenon is studied with a measuring instrument for an interval of time. In a MD simulation a system of particles model is chosen to mimic the behaviour of a real system. Each particle has a set of variables that specify the interactions with the surrounding environment and the Newton's equation of motion are solved to calculate the particles position, for each time step.

2.1 Force Calculation

The calculation of forces acting on each particle is given by the fundamental relation between forces and potentials in conservative systems,

$$\mathbf{f}_i = -\nabla U(\mathbf{r}_i) \tag{2.1}$$

where $\mathbf{r}_i$ is the position vector of the particle i. The particles behaviour in a MD simulation depends on which interaction are considered and how potentials are defined. Typically, for a molecular system model, two types of interaction are considered, bonded and non-bonded. Bonded interactions involve the calculation of quantities that depend on the coordinates of adjacent particles. However, the potential energies are not usually written explicitly as a function of the particles coordinates, but instead as a function of local coordinates. For instance, in a spring-like chain model, particles are bonded through elastic potentials that depend on the displacement between consecutive particles, $s_i = \|\mathbf{r}_{i+1} - \mathbf{r}_i\|$. A more complex model considers also the angle variation between two consecutive segments, the bending angle,

$$\theta_i = \arccos(\hat{\mathbf{s}}_{i-1} \cdot \hat{\mathbf{s}}_i), \tag{2.2}$$

where $\hat{\mathbf{s}} = \mathbf{s}/s$ and $\mathbf{s}_i = \mathbf{r}_{i+1} - \mathbf{r}_i$. Another often considered quantity is the torsion angle,

$$\tau_i = \arccos\left(\hat{\mathbf{t}}_i \cdot \hat{\mathbf{t}}_{i+1}\right), \tag{2.3}$$

where $\mathbf{t}_i = \mathbf{s}_{i-1} \times \mathbf{s}_i$. In Figure 2.1 a representation of the three bonded interactions quantities can be visually better understood. The torsional angle is defined by the variation between the plane that contains particles $i-1, i, i+1$ and the plane that contains $i, i+1, i+2$.

The contribution to the potential energy due to stretching, bending and torsion can be written as:

$$U_{bonded} = U_{str} + U_{bend} + U_{tors} \tag{2.4a}$$

$$= \frac{1}{2} \sum_i K_i^s \left(s_i - s_i^{eq}\right)^2 \tag{2.4b}$$

$$+ \frac{1}{2} \sum_i K_i^b \left(\theta_i - \theta_i^{eq}\right)^2 \tag{2.4c}$$

$$+ \frac{1}{2} \sum_i K_i^t \left(\tau_i - \tau_i^{eq}\right)^2 \tag{2.4d}$$

where K_i^s, K_i^b and K_i^t are the stretching constant, bending stiffness and torsion stiffness, respectively. Other potentials can be used to describe the variation of these intrinsic properties. For instance, the potential energy associated to the torsion mode in molecular models is a periodic function instead of quadratic[4].

Non-bonded interactions consider effects between particles of the same structure, when they are not bonded, or with particles from other structures. Two common types of non-bonded interaction potential are the Coulomb potential,

$$U_{i,j}^{\mathrm{Coul}} = K^{\mathrm{Coul}} \frac{q_i q_{i+1}}{s_{i,j}}, \tag{2.5}$$

and the Lennard-Jones potential,

$$U_{i,j}^{\mathrm{L-S}} = 4\varepsilon_{\mathrm{L-S}} \left[\left(\frac{\sigma_{\mathrm{L-S}}}{s_{i,j}}\right)^{12} - \left(\frac{\sigma_{\mathrm{L-S}}}{s_{i,j}}\right)^6 \right], \tag{2.6}$$

where K^{Coul} is Coulomb's constants, q_i and q_j are signed magnitudes of the charges, $s_{i,j}$ is the distance between particles i and j, $\varepsilon_{\mathrm{L-S}}$ gives the depth of the potential well and $\sigma_{\mathrm{L-S}}$ determines the diameter of the particle.

The modelling of structures in molecular dynamics usually starts by considering first which potentials are applied upon the particles of a system. Simulations performed with the FS algorithm considered the potential energy arising from the bonded interactions. Structures consisted in linear chains constrained by stretching, bending and torsion interactions. In the case of the simulations performed with LAMMPS algorithm, only stretching potentials were used. Filaments in LAMMPS were modelled by arranging beads in hexagonal close packed and simple cubic lattices constrained only by stretching potentials. The representation of the structures considered on FS and LAMMPS algorithms are shown in Figure 2.1.
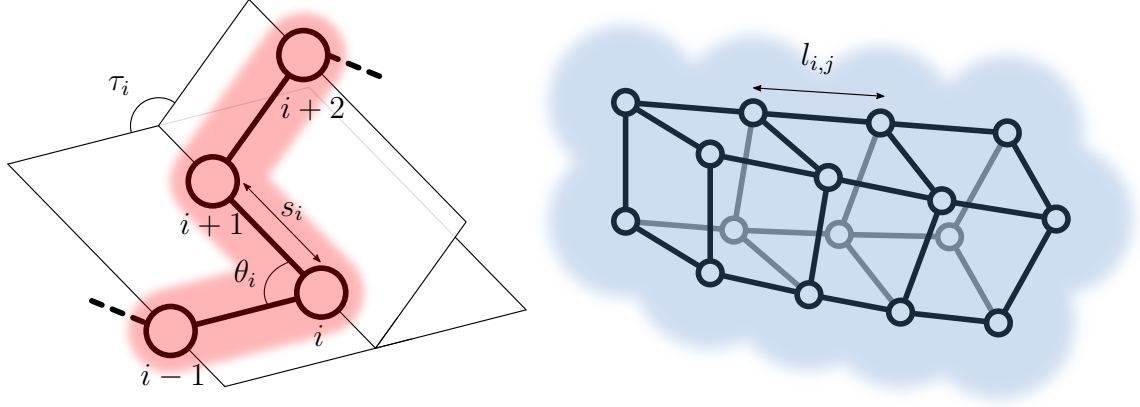
Figure 2.1: Different molecular dynamics models of chains considered in **a** Filament Simulator and in (**b** LAMMPS).

After the definition of each potential function, the next step involves the calculation of Eq. 2.1 in terms of the local coordinates:

$$\mathbf{f}_i = - \sum_j \frac{\partial U_{str}}{\partial s_j} \frac{\partial s_j}{\partial \mathbf{r}_i} \tag{2.7a}$$

$$- \sum_j \frac{\partial U_{bend}}{\partial \theta_j} \frac{\partial \theta_j}{\partial \mathbf{r}_i} \tag{2.7b}$$

$$- \sum_j \frac{\partial U_{tors}}{\partial \tau_j} \frac{\partial \tau_j}{\partial \mathbf{r}_i}. \tag{2.7c}$$

The complete derivation of the solutions of Eq. 2.7 is described in my master thesis[5]. Calculations for the stretching components is rather straightforward, while for bending and torsion components, their derivations involve more complicated calculations. The forces due to bonding interactions resulting from the displacement of the particles have the following equations:

$$\mathbf{F}_i^{str} = - k_{i-1} \Delta s_{i-1} \frac{\mathbf{s}_{i-1}}{s_{i-1}}$$

$$+ k_i \Delta s_i \frac{\mathbf{s}_i}{s_i}, \tag{2.8}$$

$$\mathbf{F}_i^{bend} = + \alpha_{i-1}^{bend} \Delta\theta_{i-1} \frac{\mathbf{s}_{i-1} \times \mathbf{t}_{i-1}}{s_{i-1}^2 t_{i-1}}$$

$$- \alpha_i^{bend} \Delta\theta_i \left(\frac{\mathbf{s}_{i-1}}{s_{i-1}^2} + \frac{\mathbf{s}_i}{s_i^2} \right) \times \frac{\mathbf{t}_i}{t_i^2}$$

$$+ \alpha_{i+1}^{bend} \Delta\theta_{i+1} \frac{\mathbf{s}_i \times \mathbf{t}_{i+1}}{s_i^2 t_{i+1}}, \tag{2.9}$$

$$\mathbf{F}_i^{tors} = - C_{i-2} \Delta\tau_{i-2} \frac{s_{i-2} \mathbf{t}_{i-1}}{t_{i-1}^2}$$

$$+ C_{i-1} \Delta\tau_{i-1} \left[\frac{(\mathbf{s}_{i-2} \cdot \mathbf{s}_{i-1}) \mathbf{t}_{i-1}}{s_{i-1} t_{i-1}^2} + \frac{\left(s_{i-1}^2 + \mathbf{s}_{i-1} \cdot \mathbf{s}_i\right) \mathbf{t}_i}{s_{i-1} t_i^2} \right]$$

$$- C_{i-1} \Delta\tau_i \left[\frac{\left(\mathbf{s}_{i-1} \cdot \mathbf{s}_i + s_i^2\right) \mathbf{t}_i}{s_i t_i^2} + \frac{(\mathbf{s}_i \cdot \mathbf{s}_{i+1}) \mathbf{t}_{i+1}}{s_{i-1} t_{i+1}^2} \right]$$

$$+ C_{i+1} \Delta\tau_{i+1} \frac{s_{i+1} \mathbf{t}_{i+1}}{t_{i+1}^2}. \tag{2.10}$$

2.2 Time integration

After the calculation of the force in each particles of the system, it is possible to determine the velocity and position of particles by integrating the equations of motion

$$m \frac{d\mathbf{v}_i}{dt} = \mathbf{f}_i \tag{2.11}$$

and

$$\frac{d\mathbf{r}_i}{dt} = \mathbf{v}_i, \tag{2.12}$$

where $\mathbf{v}$ is the particle velocity. There are several numerical methods available to solve the equation of motion. However, methods that require more than one calculation per timestep are computationally expensive and not usually not considered. Both algorithms, FS and LAMMPS, use the Velocity-Verlet method to integrate the equations of motions. The Velocity-Verlet method can be written as:

$$\mathbf{r}_i(t + \delta t) = \mathbf{r}_i(t) + \mathbf{v}_i(t)\delta t + \frac{1}{2} \frac{\mathbf{f}_i(t)}{m} (\delta t)^2 \tag{2.13a}$$

$$\mathbf{v}_i(t + \delta t) = \mathbf{v}_i(t) + \frac{1}{2m} [\mathbf{f}_i(t) + \mathbf{f}_i(t + \delta t)\delta t] \tag{2.13b}$$

One cycle of this method consists in updating first the position according with the equations of motion. Then, the next timestep acceleration, $\mathbf{f}(t + \delta t)/m$, is calculated computed with the new coordinates and the velocity is updated from the average of the

two accelerations. This method is accurate for computing the positions of systems from the atomic to the macroscopic scales, since no errors are introduced in the algorithm calculations. In comparison with other simple methods, as the Verlet or Leap-Frog methods, the Velocity-Verlet method allows to take larger steps of δt to update positions without losing the stability of the simulation, which means faster simulation times. However, due to the fact that the last computation of the acceleration needs to be stored, it requires four dimensional arrays instead of three.

2.3 Simulation of helices using FS algorithm

In this subsection a basic description of the implementation of the FS algorithm will be shown. For generality purposes, since the algorithm was first implemented in MATLAB and afterwards in C and in CUDA, pseudo programming language will be used and some steps ignored, typical from each programming language, for instance like memory allocation declarations and punctuation marks. For the sake of simplicity some parts of the implementation are only briefly described while other parts are given in more detail.

Like in a typical algorithm, in the Filament Simulator, the constants and variables are set up for a given simulation:

Algorithm 1 Filament Simulator

1: **procedure** DECLARE CONSTANTS
2:     Load and Save filenames
3:     Simulation times (TotIter, Dt, TempSave)
4:     Structures quantities (NumP, NumF)
5:     Potentials constants (Kstr, Kbend, Ktors)
6:     Collision constants (Kcoll, FilThick, TimeList, IntD)
7: **end procedure**
8: **procedure** INITIAL CONFIGURATION
9:     **if** Load previous simulation==**True then**
10:         LOAD(r, v, f)
11:     **else**
12:         SETNEW(r, v, f)
13:     **end if**
14:     t← 1   ▷ Start timer iterator
15: **end procedure**

Here, constants use, at least, one capital letter. The time of the simulation is given by the multiplication between the total number of iterations, TotIter, and the timestep, Dt. The number of particles per structure, NumP, was usually chosen in function of the number of particles in a loop. The higher the number of particles in a simulation,

the more computationally expensive the simulation becomes and, in the opposite, the lower the number, the less a circular loop it becomes. The number of filaments is given by NumF and the stretching, bending and torsion constants, of the bonded potentials, are given by Kstr, Kbend and Ktors, respectively. For the collision between filaments or from non-neighbours particles, a capsule-capsule collision algorithm was implemented, where a hard spring with constant KColl only applies when the distance between segments is lower than a filament thickness defined by FilThick.

The next procedure involves loading a state with a previous simulation or generate a new set of positions, velocities and forces of particles.

Since the collision between particles is usually the most expensive part of a MD algorithm and since in considered simulations, particles changed little their position in a low number of iterations we have implemented a list of possible collisions that is only updated after a number of iteration, TimeList. The considered possible collisions have a diameter of interaction defined by IntD+FilThick, where IntD is the additional interaction diameter. Then, next the collision list is updated:

16: **procedure** COLLISION LIST$(t, clist, r)$
17:     $c \leftarrow 1$
18:     **for** $i \leftarrow 0, \mathrm{NumF} * \mathrm{NumP} - 2$ **do**
19:         **for** $j \leftarrow i + 1, \mathrm{NumF} * \mathrm{NumP} - 1$ **do**
20:             $p_1 \leftarrow r[t, i]$
21:             $p_2 \leftarrow r[t, i + 1]$
22:             $p_3 \leftarrow r[t, j]$
23:             $p_4 \leftarrow r[t, j + 1]$
24:             $pvec \leftarrow$ SEGM2SEGM(p_1, p_2, p_3, p_4)
25:                                 ▷ Vector with lowest distance between two segments
26:             **if** $\|pvec\| < (\mathrm{IntD} + \mathrm{FilThick})$ **then**
27:                 $clist[c, 1] \leftarrow i$
28:                 $clist[c, 2] \leftarrow j$
29:                 $c \leftarrow c + 1$
30:             **end if**
31:         **end for**
32:     **end for**
33: **end procedure**

The function SEGM2SEGM calculates a tridimensional vector given by the minimum distance between two segments, with extremities points p_1, p_2 and p_3, p_4. After collecting the information of segments close to each other, the collision between particles is calculated next:

Using the list of possible collisions in the previous procedure, the distance between segments is now calculated and compared to the limit value of FilThick. If segments are

---

34: **procedure** $\textsc{Collisions}(t, clist, r, f)$
35:     **for** $c \leftarrow 0, \textsc{LengthOf}(clist)$ **do**
36:         $i \leftarrow clist[c, 1]$
37:         $j \leftarrow clist[c, 2]$
38:         $p_1 \leftarrow r[t, i]$
39:         $p_2 \leftarrow r[t, i + 1]$
40:         $p_3 \leftarrow r[t, j]$
41:         $p_4 \leftarrow r[t, j + 1]$
42:         $pvec \leftarrow \textsc{Segm2Segm}(p_1, p_2, p_3, p_4)$
43: $\triangleright$ Vector with lowest distance between two segments
44:         **if** $\|pvec\| <$ FilThick **then**
45:             $f[t, i] \leftarrow f[t, i] - \text{Kcoll} * (1 - \text{FilThick}) * pvec$
46:             $f[t, i + 1] \leftarrow f[t, i + 1] - \text{Kcoll} * (1 - \text{FilThick}) * pvec$
47:             $f[t, j] \leftarrow f[t, j] + \text{Kcoll} * (1 - \text{FilThick}) * pvec$
48:             $f[t, j + 1] \leftarrow f[t, j + 1] + \text{Kcoll} * (1 - \text{FilThick}) * pvec$
49:         **end if**
50:     **end for**
51: **end procedure**

---

intersecting, a repulsive force is added to the total force of the particles in the direction of the vector given by the minimum distance. Next, the first cycle of the Velocity-Verlet method is updated, the position and the first part of the velocity:

52: **procedure** $\textsc{Verlet Part I}(t, r, v, f, \text{Dt}, \text{M})$
53:     **for** $i \leftarrow 0, \text{NumF} * \text{NumP} - 1$ **do**
54:         $r[t + 1, i] \leftarrow r[t, i] + v[t, i] * \text{Dt} + 1/(2\text{M}) * f[t, i] * (\text{Dt})^2$
55:         $v[t + 1, i] \leftarrow v[t, i](1 - \text{DampF} * \text{Dt}) + 1/(2\text{M})f[t, i] * \text{Dt}$
56:     **end for**
57:     Move a set of particles
58: **end procedure**

A damping factor, DampF, is added to the velocity equation to ensure stability of the algorithm. This factor is also common in MD simulations and is chosen low enough so that the simulation does not get a viscous behaviour. If the damping factor is too low, the simulation becomes unstable and it will blow-up computationally.

After the update of new positions, the next step involves to calculate the bonded quantities, as the length of the segments l, the bending angle θ and the torsion angle τ. In a typical simulation, the particles are initially in an equilibrium position and, then, the equilibrium quantities can be set in the first iteration, $t = 1$. However, these quantities can be set up with amounts different from the ones of the initial configuration. The vectors that describe the direction of the segments, s, and the cross vector between adjacent segments, t, are also updated:

59: **procedure** NEW DISPLACEMENTS AND ANGLE VARIATIONS(t, r, v, f)
60:     **for** $i \leftarrow 0, \text{NumF} * \text{NumP} - 1$ **do**
61:         **if** All particles belong to the same molecule **then**
62:             $s[i] \leftarrow r[t+1, i+1] - r[t+1, i]$
63:             $l[i] \leftarrow \|s[i]\|$
64:             $\theta[i] \leftarrow \text{ArcCos}(s(i-1) \cdot s[i])/(l(i-1) * l[i])$
65:             $t[i] \leftarrow s(i-1) \times s[i]$
66:             $modt[i] \leftarrow \|t[i]\|$
67:             $\tau(i-1) \leftarrow \text{ArcCos}(t(i-1) \cdot t[i]/(modt(i-1) * modt[i]))$
68:         **end if**
69:         **if** t==1 **then**   ▷ Initial configuration can be set at equilibrium
70:             $l_0[i] \leftarrow l[i]$
71:             $\theta_0[i] \leftarrow \theta[i]$
72:             $\tau_0[i] \leftarrow \tau[i]$
73:         **end if**
74:     **end for**
75: **end procedure**

The condition "All particles belong to the same molecule" is to ensure no interactions due to bonded potentials occurs between different molecules. For instance, if no boundaries conditions were not used in this procedure, the last particle of a structure would be bonded to the first particle of another structure.

After updating the simulation variables, the force acting on each particle is calculated. Since all contributions due to stretching, bending and torsion are provided already in Equations 2.8, 2.9 and 2.10, for benefit of the description of the algorithm, the calculation of all components will be comprised in the FORCECALC function:

76: **procedure** FORCE CALCULATION$(t, r, v, f, \text{Dt}, \text{M})$
77:     **for** $i \leftarrow 0, \text{NumF} * \text{NumP} - 1$ **do**
78:         $f[i, t+1] \leftarrow \text{FORCECALC}(\text{Kstr}, \text{Kbend}, \text{Ktors}, l, l0, modt, \theta, \theta_0, \tau, \tau_0, s, t)$
79:         ▷ Calculation of all components of the force, see Equations 2.8, 2.9 and 2.10
80:     **end for**
81: **end procedure**

The next timestep velocity, in the Velocity-Verlet, is completely updated by adding the part due the calculation of the next timestep force:

82: **procedure** VERLET PART II$(t, r, v, f, \text{Dt}, \text{M})$
83:     **for** $i \leftarrow 0, \text{NumF} * \text{NumP} - 1$ **do**
84:         $v[t+1, i] \leftarrow v[t+1, i] + 1/(2\text{M})f[t+1, i] * \text{Dt}$
85:     **end for**
86: **end procedure**

The final part of an iteration ends by saving the new dynamics of the filaments. Not

all iterations are saved, since usually there is no major difference between close steps
and to avoid data files too big. Moreover, it was set to save some frame from time to
time, TempSave, to allow a preview of the dynamics during a runtime of a simulation.
This part is particularly useful if a simulation takes place during several hours or even
days.

87: **procedure** TEMPORARY SAVE AND AND CYCLE
88:     **if** MOD(t, TempSave) $== 0$ **then**
89:         SAVE(r,v,F)
90:     **end if**
91:     **if** MOD(t, TimeList) $== 0$ **then**
92:         **go to** COLLISION LIST
93:     **end if**
94:     **if** $t <$ TotIter **then**
95:         **go to** COLLISIONS
96:     **else**
97:         SAVE(r,v,F)
98:     **end if**
99: **end procedure**

Finally, the collision list does not require to be updated in every step, but, instead,
updated in a TimeList number of steps. The higher the number of steps the better
in terms of computational cost. However, if it set too high, some collisions might be
missed.

After reaching the total number of iterations, TotIter, the simulation makes a final
save of the filament dynamics and stops the iteration.

2.4 Simulations of filaments with intrinsic curvature using LAMMPS

FS is a simple but effective algorithm designed to model the dynamics of elastic
filaments. However, it was not adapted to have the functionality to allow heterogeneous
cross-sections. LAMMPS (Large-scale Atomic / Molecular Massively Parallel Simulator)
tool was used to perform these specific kind of simulations. LAMMPS is a classical
molecular dynamics open-source code developed by Sandia National Laboratories [6]
designed to run on parallel computers. It has many functionalities that allow to model
atomic, polyatomic, biological, metallic or granular molecules using a variety of force
fields and boundary conditions.

A typical input script consists in one or several text files containing several lines

that will be executed one line at a time. The first part of any LAMMPS script starts by defining the units, the dimensions and boundaries of the simulation box and the atom style, which types of atomic interactions are considered in the simulation:

Algorithm 2 LAMMPS

1: units lj   ▷ Determines the units of all quantities
2: boundary s s s   ▷ Boundaries non-periodic and shrink-wrapped
3: atom_style bond   ▷ Bead-spring polymers

Here, dimensionless quantities were used for simplification of the simulations and also for generalization of the observed effects, since they do not depend on the used units. Non-periodic boundaries were used since simulations involved the release and extension of filaments, which do not require periodic boundaries. For the atom style, only bonds were considered, which is the only attribute a bead-spring model requires. Next, a file containing the information of one or more structures (for instance, the particles positions, velocities, accelerations, bonds, name and other variables important for the dynamics and identification of particles) is loaded with a read data command:

4: read_data inputfile.txt   ▷ Read in a data file containing structure information
5: timestep tVAL   ▷ value between 1×10^{-4} to 2.5×10^{-3}
6: neighbor SKIN bin
7: neigh_modify every M

Filaments were modelled as rods with hexagonal close packing and simple cubic packing lattices. In the first type of packing, atoms were only connected to the first neighbours while in the latter the second neighbours were also considered, for bonded interactions. Additional neighbours were considered in structures with the simple cubic packing because the filaments generated with this disposition, and containing only the first neighbours, were not stable enough during the release and had their lattice deformed into a cubic close packing one. The "neighbor" and "neigh_modify" commands sets the parameters that are considered for building the pairwise neighbour lists and the frequency, M, the lists are updated, respectively.

Depending on the side that was initially strained, particles were identified with different names for further identification, atom type 1 for non pre-strained and atom type 2 for pre-strained. Other names were also used to designate regions with different pre-strains, neighbours distance or with other physical quantities. Bonds followed a harmonic potential, with equilibrium bond equal to the pre-set distance of the filament for bonds between non pre-strained atoms (atom type 1 – atom type 1) and smaller equilibrium bond values for bonds between atoms that had, at least, one atom type 2

(atom type 1 – atom type 2 and atom type 2 – atom type 2). The initial velocities and accelerations of the particles were set as zero, as by default:

```
 8: bond_style harmonic
 9: bond_coeff 1 Kstr1 X01
10: bond_coeff 2 Kstr2 X02
11: pair_style lj/cut CUT
12: pair_coeff * * ARG1 ARG2
```

The "pair" commands computes the non-bonded interactions. In simulations, the lj/cut style computes the standard Lennard-Jones potential with a cutting distance. The first two terms of the "pair_coeff" specify the atom types considered in the pairwise force field coefficients. By using the asterisk, all atom types are considered. The remaining terms are the epsilon, sigma and cutoff distance. The latter is optional, if not specified it considers the cutoff of the "pair_style" command.

Simulations were deterministic and did not include temperature effects, so the integration of the equations of motion used a NVE integrator (Verlet/Leap-frog method) to update beads positions and velocities on each timestep. The stepsize of ranged from $2.5 \times 10^{-3}\,\tau$ to $1 \times 10^{-4}\,\tau$. Fixed points were not updated during the simulations, but their positions were updated in a number of steps. The kinetic energy, potential energy, position, applied force and other quantities can be saved for individual particles and as well other properties for a group of particles.

```
13: compute THERMO all temp
14: thermo_style custom step temp vol lz pe ke
15: thermo Dumpfreq
16: thermo_modify norm yes flush yes
17: dump INFO all custom Dumpfreq name.lammpstrj id type mol x y z fx fy fz
    c_PEperatom c_KEperatom
18: fix INTEG all nve
19: fix DRAG all viscous 0.01
20: read_dump oldsimulation.lammpstrj FRAME x y z
```

The "compute" commands define a computation to be performed in a group of atoms. It can calculate global, local or per-atom quantities in a given iteration of the simulation. These commands do not perform the computation but they are required to set the quantities to be calculated or for a dump file output. The "dump" command saves the quantities of an instant of the simulation. The following "fix" commands set the integrator, NVE uses Velocity-Verlet by default, and a small dissipative damping force to all particles, respectively. Previous simulations can also be loaded for restarting a particular snapshot.

Typically in the release of filaments with intrinsic curvature, instead of applying the "nve fix" to all particles, the ends were left out of the integration (but all quantities for all particles were still computed). This way, both ends were set to be constrained and by gradually updating the positions the release speed was controlled.

The trajectories of the particles were afterwards observed by using the VMD (Visual Molecular Dynamics) open-source tool[7]. The LAMMPS output files can be simply loaded in VMD or by using a script to specify the bonds, set up the atom colours, representations and visualization properties, like resolution, camera position and type of perspective, lights and other graphical attributes.

Visualization frames were then saved in POV-Ray format to be read with a ray tracing program which generates images from a text based interface and produces high quality images[8].

2.4.1 Reduced units

The physical quantities used and measured in the simulations performed with LAMMPS are expressed as reduced, or dimensionless, units. Lennard-Jones reduced units, dimensionless physical quantities, are used for convenience and to ease the scale-up of the system. Without loss of generality, fundamental quantities are set equal to one, avoiding working with numbers that are neither too large or too small. Besides the simplification of some quantities and equations, the same model considerations can be scaled for different problems by adjusting the appropriate quantities.

The following quantities were used in the LAMMPS simulations:

$$\text{time}: \quad t^* = t/\tau \tag{2.14a}$$

$$\text{energy}: \quad U^* = U/\varepsilon \tag{2.14b}$$

$$\text{mass}: \quad m^* = m \tag{2.14c}$$

$$\text{length}: \quad \mathbf{r}^* = \mathbf{r}/\sigma \tag{2.14d}$$

$$\text{velocity}: \quad \mathbf{v}^* = \mathbf{v}\tau/\sigma \tag{2.14e}$$

$$\text{force}: \quad \mathbf{f}^* = \mathbf{f}\sigma/\varepsilon \tag{2.14f}$$

References

[1] D. Frenkel and B. Smit, *Understanding Molecular Simulation*, 2nd. Orlando, FL, USA: Academic Press, Inc., 2001.

[2] J. W. Hatfield and S. R. Quake, "Dynamic Properties of an Extended Polymer in Solution," *Physical Review Letters*, vol. 82, no. 17, pp. 3548–3551, Apr. 26, 1999. DOI: 10.1103/PhysRevLett.82.3548.

[3] B. Liu, J. Wang, X. Fan, Y. Kong, and H. Gao, "An effective bead–spring model for polymer simulation," *Journal of Computational Physics*, vol. 227, no. 5, pp. 2794–2807, Feb. 20, 2008. DOI: 10.1016/j.jcp.2007.11.012.

[4] M. P. Allen, "Introduction to molecular dynamics simulation," *Computational Soft Matter - From Synthetic Polymers to Proteins*, NIC Series, vol. 23, 2004.

[5] P. E. S. Silva, "Modelling the dynamics of elastic filaments," Msc, University of Aveiro, 2010.

[6] S. Plimpton, "Fast Parallel Algorithms for Short-Range Molecular Dynamics," *Journal of Computational Physics*, vol. 117, no. 1, pp. 1–19, Mar. 1995. DOI: 10.1006/jcph.1995.1039.

[7] W. Humphrey, A. Dalke, and K. Schulten, "VMD: Visual molecular dynamics," *Journal of Molecular Graphics*, vol. 14, no. 1, pp. 33–38, Feb. 1996. DOI: 10.1016/0263-7855(96)00018-5.

[8] *Persistence of Vision Raytracer (Version 3.6 - http://www.povray.org/)*, Williamstown, Victoria, Australia.

3

Experimental considerations

In the work developed in this thesis, fibres with helical shapes were produced by using different polymers and strategies. Micro and nanofibres can be produced with many different manufacturing methods, however, the conventional mechanical methods for fibre-spinning have robustness limitations for fibres with diameters smaller than about the order of the micrometer. Current commercial fibres have diameters with larger size, due to technological and economical reasons. The path to the production of fabrics containing fibres with smaller diameters offers the perspective of self-cleaning[1], [2], durability[3], [4], hydrophoby[5], [6], antimicrobially[7], [8], anti-static[9], [10], flame-retardancy[11], [12] and many other improvements to current textile technology. Nanomaterials are sized, at least in one dimension, 1 nm to 100 nm. However, in the context of textiles, nanofibres are often considered when filaments have a diameter with a size below the micrometer for practical reasons[13].

There are many spinning techniques to produce sub-micro and nanofibres, with smaller diameters to the ones produced by the conventional mechanical methods. For instance, melt-blowing techniques

consist in extruding a polymer melt through small nozzles, ejected at high speed through a blowing gas.[14] In bicomponent spinning, two solutions are spun together into different cross-sections arrangements, like islands-in-the-sea approach in which the "sea" part is further removed.[15] Produced fibres studied in this thesis used another common method to obtain thin fibres, the electrospinning technique. Instead of using high speed gases, in electrospinning experiments, as induced by the name, a solution is accelerated by the action of high-tension electrical fields. Due to the fact of the ease of use, namely on the wide variety of polymers and materials that can be used, the possibility of fibre functionalization, the production parameters can be controlled by adjusting the electrical fields and, a basic apparatus, only requires a high-tension power source, electrospinning is commonly used to produce micro and nanofibres[16], [17].

In this chapter, it will be first presented the properties of the materials used to obtain electrospun fibres. Then, some considerations of the used electrospinning apparatus and operation will be described. For the sake of not repeating the description of the electrospinning technique, addressed in Chapter 4, the details about electrospinning provided here will mainly focus on the homemade apparatus, operation, used collectors and UV irradiation schemes. Furthermore, the details about the major characterization techniques used in this thesis, polarizing optical microscopy (POM) and scanning electron microscopy (SEM), will be given in the end of this chapter.

3.1 Materials

From natural to synthetic polymers, approximately one hundred different polymers can be electrospun[16]. Usually, polymers or composites are dissolved with specific solvents. Then, the solution is inserted on a syringe, that is pumped at constant rate, and ejected through the action of an electrical force. A good solvent needs to evaporate during the flight of the fibre. During the flight, the jet may undergo in a bending instability due to the change of the shape and the accumulation of electric charges, which causes the jet to do a coiling movement. Although bending instabilities can induce coiling, the radius of curvature is much greater, by many orders of magnitude, than the diameter of the fibre, which makes the instability not suitable to use it as a mechanism to produce helical fibres. Electrospun helical fibres can be obtained by using different intrinsic mechanical properties of the filaments. For instance, the helicity in electrospun fibres can arise when the jet lands in the target or when the fibres have an anisotropic distribution of strains.

In this thesis, two different strategies to obtain helical fibres were used. The first is based in a method reported by Godinho et al.[18] in which the electrospun cellulose
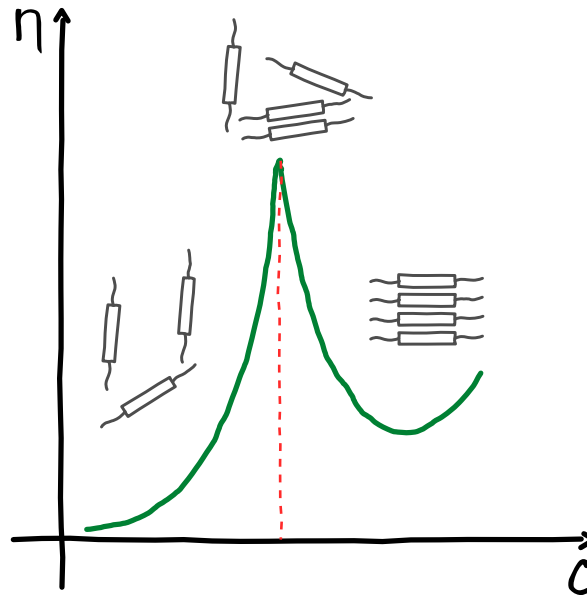
Figure 3.1: Variation of the viscosity, η, with the concentration of the solution, C, of a typical lyotropic liquid crystalline polymeric system, for a certain shear rate[23].

liquid crystal fibres possess a core of disclination formed off-axis. With the contraction of the electrospun mesh, some fibres acquire a helical shape. The second strategy also uses the asymmetric contraction to create helical structures, but instead arising from the chirality of the polymer it appears from further crosslinking when collected fibres are irradiated with UV light[19].

3.1.1 Cellulosic fibres

Formhals is widely attributed as being the inventor of electrospinning due to the contributions to development of the technique. In 1934, Formhals submitted a patent claiming a novel procedure to obtain textile yarns from a solution of cellulose acetate, acetone and alcohol. There was a clear intention of producing fibres and process the fibres into yarns or staples. Since then, cellulose and derivatives solutions, using many different solvents, have been reported to produce electrospun fibres[20], [21].

Cellulose is one of the most abundant polymer in nature. It can be extracted from many different sources, since it is the main constituent of plant cells walls, which provides a great advantage in terms of available resources for industrial purposes. Cellulosic fibres are renewable and environmentally friendly, offering a green alternative route to the manufacture of some currently produced materials. Electrospun cellulosic fibres can be used for a wide variety of applications such as filters, tissue scaffolds, biosensors, wound dressing materials and drug delivery systems[20]–[22].

Many cellulose derivatives can display both lyotropic and thermotropic cholesteric

liquid crystalline (LC) phases[24], [25]. In the specific case of the acetoxypropylcellulose (APC), when electrospun from the LC phase in dimethylacetamide (DMAc), the fibres adopt a helical shape[26]. The liquid crystalline phase can be quickly recognized by the change of the optical features and by the variation of the viscosity of the solution. A characteristic curve of the viscosity dependence on the concentration for a lyotropic system is shown in Figure 3.1. As the concentration of the polymer solution increases, the viscosity increases until a critical point, like an isotropic solution. This critical point is mainly dependant on the molecular weight of the polymer and the temperature of the solution[23]. Afterwards, with the formation of a nematic phase, the viscosity drops until reach a minimum point. A solid phase will appears for higher concentrations[27].

The critical concentration for the APC is near 50%w/w, at room temperature, for which both isotropic and nematic phases coexist. Using a higher concentration allows not only to obtain fibres in the nematic phase but also have a viscosity of the solution low enough to be electrospun.

Preparation of the acetoxypropylcellulose (APC) solutions

The APC (acetoxypropylcellulose) used in this work was obtained by the acetylation reaction of HPC (hydroxypropyl cellulose), as described in the literature[28]–[30]. The chemical structure and reaction can be seen in Figure 3.2. The free hydroxyl groups existing along the HPC ether are substituted by acetoxy groups, which induce mobility to the cellulose main chains allowing the existence of a cholesteric liquid crystalline phase at room temperature.

More precisely, the reaction was performed in a reactor where 50 g of HPC, purchased from Sigma-Aldrich ($\bar{M}_w = 100000$; $\bar{M}S = 3.5$), were dissolved in 150 mL of acetic anhydride. In order to start the esterification, 13.5 ml of acetic acid were added to the solution, under stirring, until a viscous solution is obtained. Afterwards, the mixture was left to rest for a week, being in every day warmed up to 60 °C and stirring for periods of 4 h. After this period, the reaction medium, at room temperature, was poured into a large excess of water for promoting the precipitation of a white gummy polymer. The separated soft solid was washed multiple times with distilled water, to remove the excess of acetic anhydride and acetic acid, and then dried upon 17 °C and in vacuum, for several days. A bluish translucid soft solid is obtained at room temperature.

One of the main difficulties of electrospinning cellulose is to find a good solvent. Cellulose can be hardly dissolved with commonly used solvents and some of the solvents known to dissolve cellulose, such as *N*-methyl-morpholine *N*-oxide/water, have evaporation rates not suitable for producing electrospun fibres. To overcome this difficulty, cellulose derivatives are used instead. DMAc is one of the most commonly used solvents to dissolve cellulose derivatives[31].
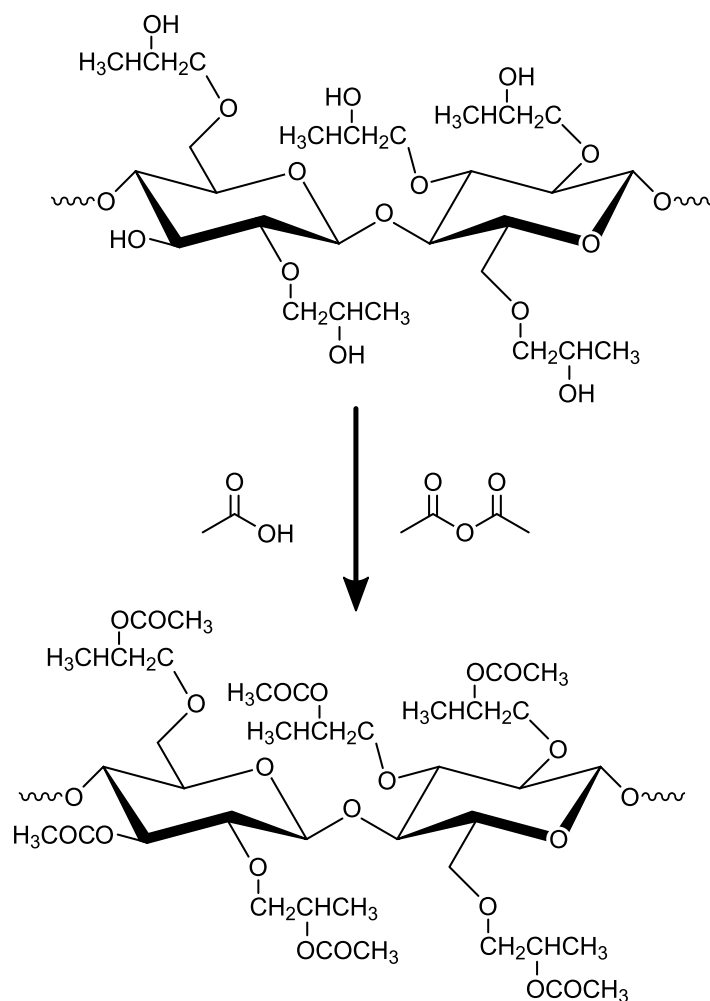
Figure 3.2: Schematic representation of the acetylation reaction of HPC (hydroxypropyl cellulose) to obtain APC (acetoxypropylcellulose). The average degree of esterification is equal three.

The cellulosic solution used in electrospinning was prepared by mixing 2.1 g of APC with 1.4 g of anhydrous DMAc and allowed to homogenize for two weeks, with brief stirring after one week, Figure 3.3.

Fibres of APC

The cellulosic solution was then electrospun to form APC micro and nanofibres. Electrospinning apparatus consisted in a 5 ml syringe fitted with a 18-gauge needle controlled by a syringe pump, a high DC voltage power supply and a grounded target. The APC solution was pumped at a constant feeding of $0.04\,\mathrm{ml\,h^{-1}}$, applied voltage on the needle was of 15 kV, temperature and humidity was about 20 °C and between 45 and 55%, correspondingly.

Resulting APC mats had both aligned and randomly distributed fibres between the two electrodes. The fibres were dried over vacuum, at room temperature, for 48 h.
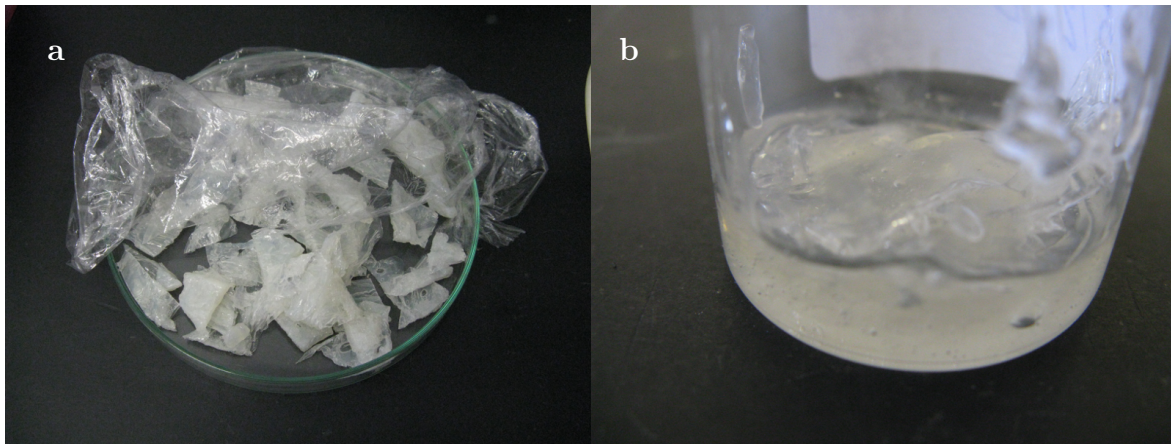
Figure 3.3: **(a)** APC chunks. **(b)** Solution of APC in DMAc after one week.

Using polarized optical microscopy (POM) it was possible to verify that the fibres were bonded to each other before coiling and only the thinnest filaments exhibited a helical shape. Figure 3.4 shows a example of a mat with low times of experiment run, about 1 min.

Since the number of helical fibres was low and it was hard to control the properties of the helical fibres by using this system, a different approach was considered.

3.1.2 Polyurethanes

Polyurethanes are plastics polymers created by combining polyols and isocyanates. Early researches started in the 1930s by Otto Bayer and, since then, polyurethanes were investigated due to the great mechanical and thermal properties, namely solvent resistance, abrasion resistance, high tear strength, good load-bearing capacity and low temperature flexibility. Different types of polyurethanes can be produced by changing the polymeric chains flexibility and the crosslinkings between them and used in products ranging from coatings, adhesives, mattresses to foam insulation[32].

Zhao et al.[33] reported the synthesis of elastomers composed by hard segments, the urethane/urea polymers, intercalated with two soft segments, polypropylene oxide and polybutadiene, Figure 3.6, to make pervaporation membranes with better permeation function. Produced membranes were found to display different optical states[34] and wrinkling patterns in the surface[35] resulting from the action of a mechanical stress. In a subsequent finding, Godinho et al.[36] also found that the exposition of the PU/PBDO to UV promoted a second crosslinking of the polymeric chains.

Several works reporting the fabrication of elastomeric janus structures, with a dual distinct physical properties behaviour, arose from this response of the PU/PBDO
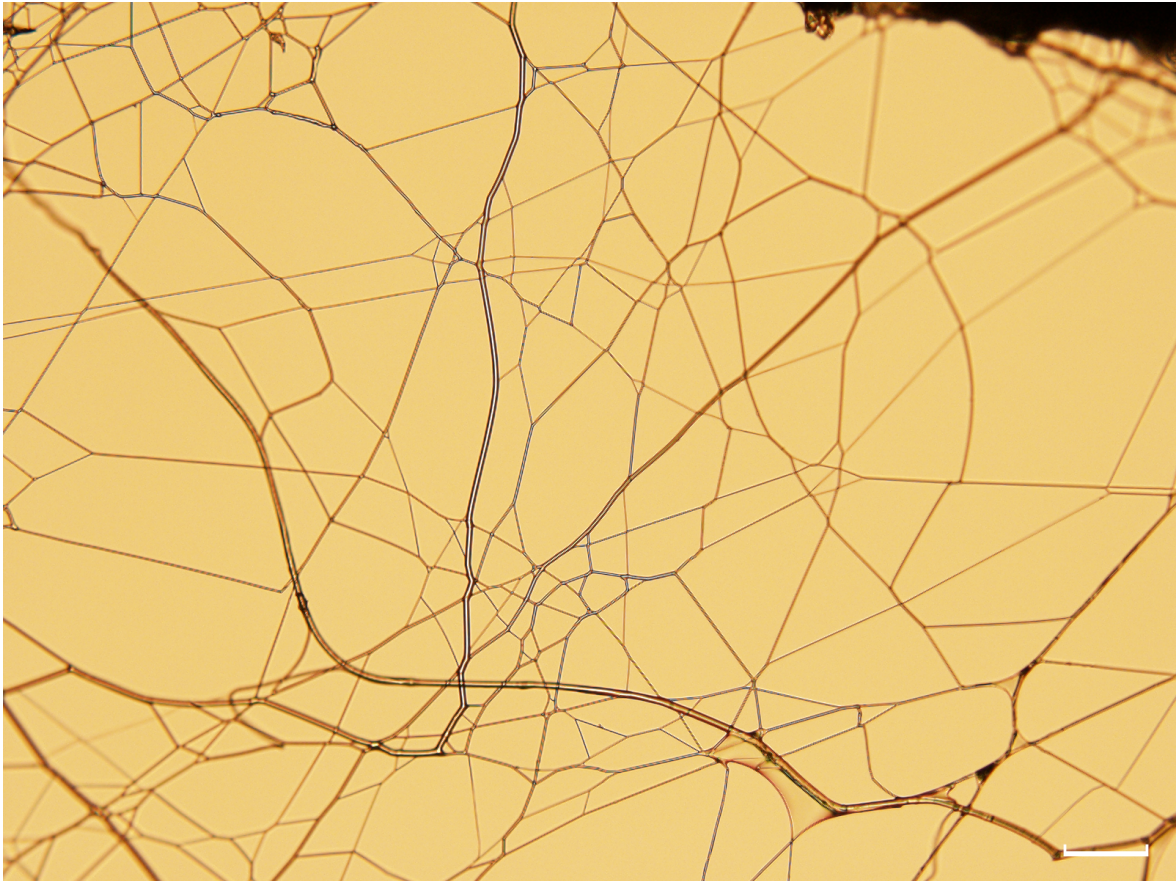
Figure 3.4: Electrospun APC fibres.

chemical structure to the UV light, for instance membranes[36]–[38], spheres[39], [40] and filaments[19]. Specifically in filaments, the creation of a half-layer with different mechanical properties generated asymmetric displacements within the fibres when stretched or contracted by the action of mechanical forces. This asymmetry creates an intrinsic curvature that makes filaments to coil upon contraction, adopting a helical shape for high enough asymmetry. Figure 3.5 shows an example of PU/PBDO fibres displaying little, or no curvature, when contracted (**a** to **b**). After being stretched, as shown in Figure 3.5**c**, and then contracted again, filaments display helical shapes, Figure 3.5**d**–**e**. Therefore, the main strategy to obtain helical structures from PU/PBDO solutions was first collect aligned fibres, that were not crossed or bonded, and then apply UV light in one of the sides of the filaments.
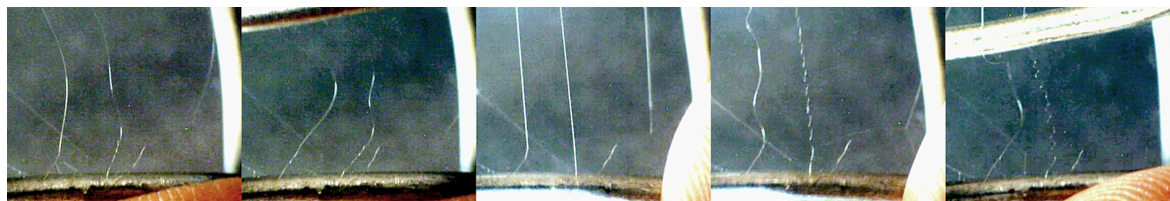
Figure 3.5: Schematic representation of the shrinkage of cellulosic membranes. **(a)** Fibres are aligned between two electrodes. **(b)** Bringing the two substrates together, **(c)** the fibres reduce the internal energy by coiling.

Preparation of the polyurethane/polybutadienediol (PU/PBDO) solutions

The PU was acquired from a Portuguese petrochemical industry and the PBDO was supplied by Sigma-Aldrich. Used procedure to obtain PU/PBDO solutions follows the protocol described by Trindade et al.[19]. The elastic behaviour of the filaments was controlled by the relative amount of the pre-polymers used for preparing the starting solution. The PU and PBDO prepolymers, with a 40%/60% w/w ratio, were dissolved in toluene, solid content 40% w/w. One drop of dibutyltin dilauryate catalyst was added, and the chemical reaction was allowed to occur during 1 h before inserting the reactive mixture in the syringe. The first network is formed by the reaction of PU with the PBDO, Figure 3.6.

A second crosslinking of the polymeric chains occurs when the fibres are irradiated with UV light. The photoinitiated crosslinking in the polymeric chains is represented schematically in Figure 3.7. At the molecular level, the UV light breaks the carbon double bonds and, in the presence of oxygen, a new link is created between the polymeric chains.

Fibres of PU/PBDO

PU/PBDO fibres were obtained by electrospinning and collected in two parallel electrodes. First, the PU/PBDO was dissolved in toluene and poured into a 1 mL syringe fitted with a 25-gauge needle and an infusion syringe pump (model KDS100) was used to control the solution feed rate, $0.8\,\mathrm{mL\,h^{-1}}$. A conducting ring of 15 cm diameter was held coaxially with the needle tip at its centre, and electrically connected to it and to the positive output of a high-voltage power supply (Glassman EL 30 kV) to control. The solution was electrospun onto a collector, by the action of an electric field applied between the syringe tip and the target. Different collectors were used, but all of them had a common feature: parallel electrodes. In general, electrospun filaments require tight gaps between the electrodes to achieve a high alignment between
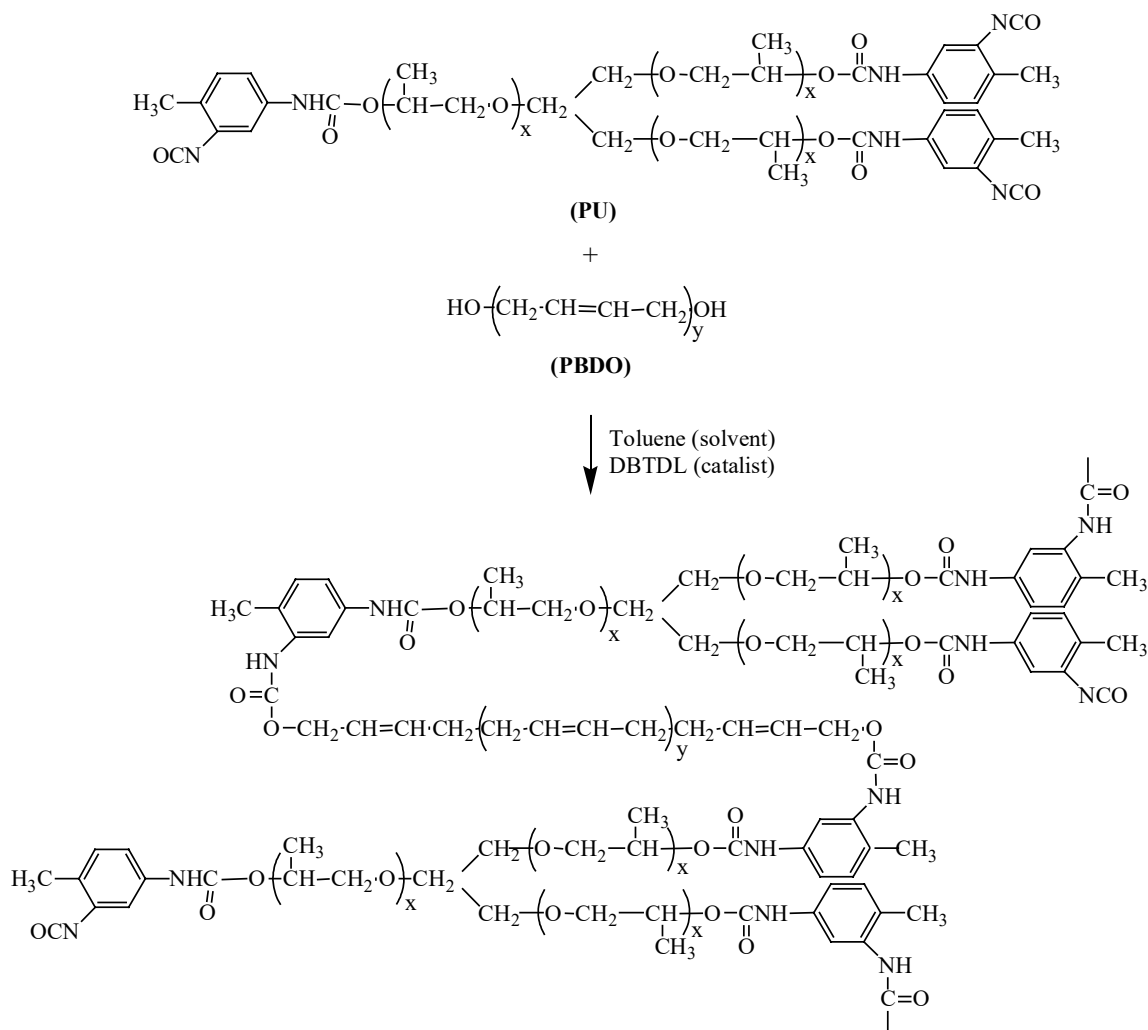
Figure 3.6: Synthesis of polypropylene oxide/polybutadiene urethane/urea reaction.

the fibres to overcome the instabilities caused during the flight. Moreover, due to the high viscosity of the electrospun solution, it was easy to obtain aligned fibres only by the action of rotation of the target. Also, considering that in a first stage, the properties of single fibres were studied, using a single target would have a low yielding of obtained fibres. Then, a sample holder containing multiple individual cells for fibre collection, made using acetate sheets cut with a precision cutting machine (Silhouette Portrait), was placed between the metallic bars. Optimal electrospinning conditions for this system were found to be: voltage at $14\,\mathrm{kV}$ for a syringe tip-target separation of $15\,\mathrm{cm}$, relative humidity 70%. From this point, two different approaches were used. The initial approach followed the same procedure that included a UV irradiation stage during $24\,\mathrm{h}$ and followed by the extraction of the toluene for $24\,\mathrm{h}$ (Soxhlet extractor). Then, fibres were dried in an oven for $48\,\mathrm{h}$ at 50°. However, many fibres were lost in the extraction of the stage, reducing the number of obtained fibres which was already
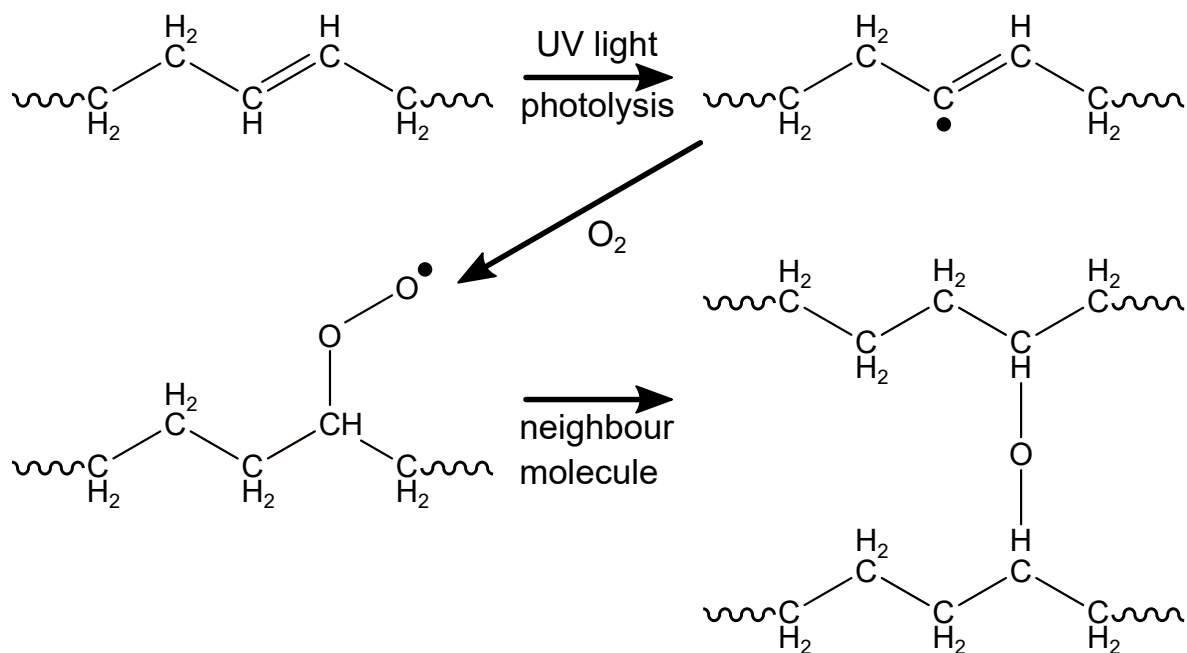
Figure 3.7: UV-curing of the PU/PBDO polymeric chains.

low. Then, a different approach was devised. Fibres after being spun could be stretched up to four times their length. Before the UV irradiation, fibres were stretched and only then irradiated with UV light. Afterwards, fibres adopted helical shapes upon release. It was found that required UV irradiation times were far shorter than previously used, from 24 h to less than 1 h and obtained helices had a stable helical configuration without requiring the toluene stage.

Figure 3.8 shows an example of a typical cell sample containing between one or a few more filaments being released. Upon release, fibres undergoes a buckling instability and starts to coil.
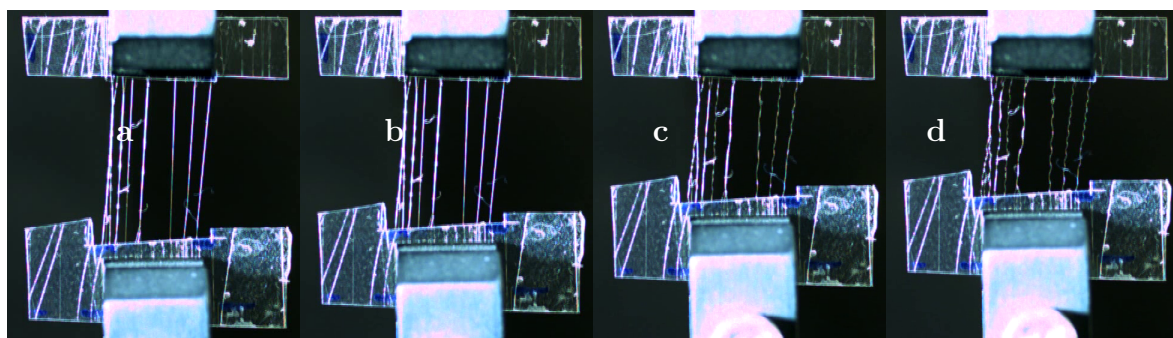

Figure 3.8: Release of PU/PBDO fibres. In frame **(a)** elastomers are overstretched and become increasingly relaxed, from **a** to **d**. During the relaxation fibres start to coil.

3.2 Electrospinning

The electrospinning apparatus is really simple, allowing a broad range of polymers to be spun. Several parts can be adjusted depending on which materials are used and the features desired in the final fabrics. To obtain helical fibres, it is required, at least, the existence of an intrinsic curvature that induces coiling in fibres. Strategies that involve the spinning jets with two different components may generate strains along the filament, due to the mismatch of the physical properties, like different viscosities or evaporation rates, and give rise to the coiling of the spun structures. Therefore, emulsion and bicomponent electrospinning are, in theory, good approaches to obtain helical fibres. Nevertheless, it is also possible to produce hollow and core-shell fibres with direct electrospinning method.

Jing et al. [41] produced hollow titania fibres by using a direct electrospinning method followed by a calcination step. During the calcination process, the release of gases pushed the TiO_2 nanoparticles into the fibre surface and formed a hollow structure after the complete melt, gasification and decomposition of the polymer part.

The emulsion electrospinning method requires the use of immiscible solutions to create micro or nano droplets in a suspension, Figure 3.9(a). When the emulsion is electrospun, the spherical droplets are stretched in the axial direction of the jet and move towards its centre. Afterwards, the subsequent squeezing and solvent evaporation make the droplets to agglomerate and form an inner core[42]. Although emulsion electrospinning is rather a simple approach to produce core-shell fibres, it can be difficult to produce stable emulsions and only a limited number of polymers can be emulsified.

In coaxial electrospinning the typical single-core needles are replaced by a coaxial needles and two solutions are pumped independently through them, Figure 3.9(b). Despite the experimental set up becomes considerably more complex because parameters like the interaction between the two solution surfaces (miscibility and stress) and the physical properties of the different phases (conductivity and solvent evaporation) need to be considered additionally, coaxial electrospinning can be used as a more general technique to produce multicore fibres. During the spinning stage, the outer layer can be used as a container to control a slower reaction of the inner solution or ensure smooth mass transfer. Another possibility is the encapsulation of materials that cannot be electrospun[43]–[45]. Hollow fibres can be obtained using coaxial electrospinning by selectively removing the fibre's inner core with a chemical extraction method[46] or with thermal treatment[47].

3.2.1 Electrospinning apparatus and operation

Figure 3.10 shows the homemade electrospinning equipment used to produce the fibres reported in this thesis. As the main components of a basic electrospinning setup, it includes a syringe pump, a high voltage power supply and a collector. Additionally, our laboratory equipment has an acrylic box connected to a air system, to control the humidity, temperature and extraction of the solvent. A computer controls the movements of a collector holder when system is operating. Controlling the collector movement allows to obtain nonwoven fabrics with higher dimensions if a flat collector is used moving along the axis plane. Besides the 3-axis translation, the setup also allows the target to rotate, which may modify the fibres alignment when deposited in the collector.

The initialization of a electrospinning experiment is shown in Figure 3.11. With no application of an electric potential, the solution is pumped through the needle and forms a semi-spherical droplet, Figure 3.11 (**b**). Turning on the electric field causes the droplet to deform until releasing a thin jet of solution, Figure 3.11 **c**. The deformation of the droplet has a conical shape that is know by Taylor's cone. The ejection of solution is made at the very end of the tip, so the diameter of the jet is smaller than the diameter of the needles orifice. Since the diameter of the jet is so reduced, it is hard to record and observe the initial path of the jet. After some distance, the jet undergoes into a bending instability which promotes a broader trajectory of the jet. In Figure 3.11 **c** it is possible to observe the region where the jet adopted a more disperse trajectory.
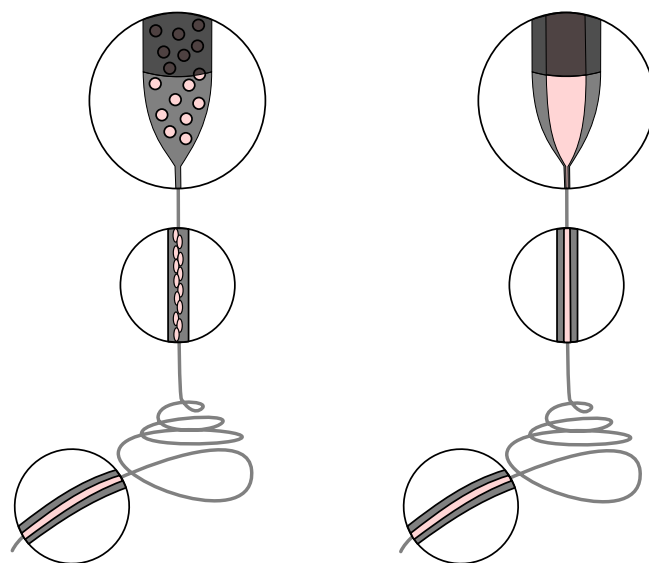

Figure 3.9: Schematic of (a) emulsion and (b) bicomponent electrospinning methods to obtain multicore fibres.
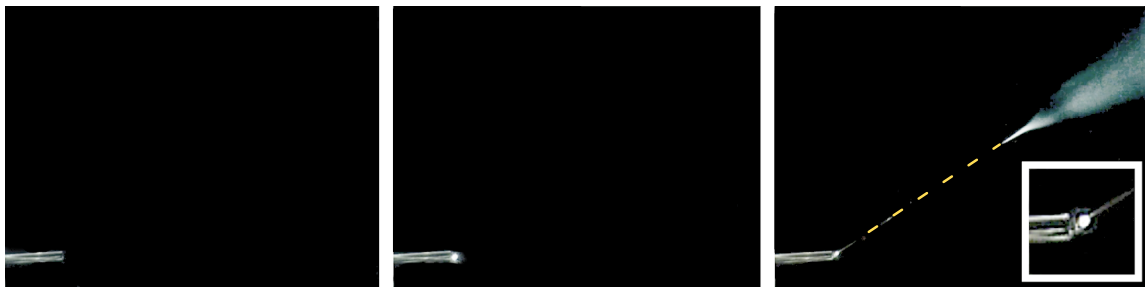
Figure 3.10: Homemade electrospinning equipment.

Figure 3.11: CCD images displaying three frames of a electrospinning run.

3.2.2 Collectors

In this thesis, several collectors were used to obtain aligned fibres, Figure 3.12. The main idea was to understand how fibres landed in the target and study the single fibre behaviour and then try to fabricate helical fibres. Additionally to those collectors represented in Figure 3.12, aluminium sheets were also used as a planar collector or to form two electrodes. However, in the planar configuration it was not possible to analyse the fibre deposition, since collection times were too short, to avoid having interaction between fibres, and did not allow to transfer the obtained fibres to a glass slide. In the case of electrodes made from aluminium sheets, fibres could be successfully collected and further analysed.

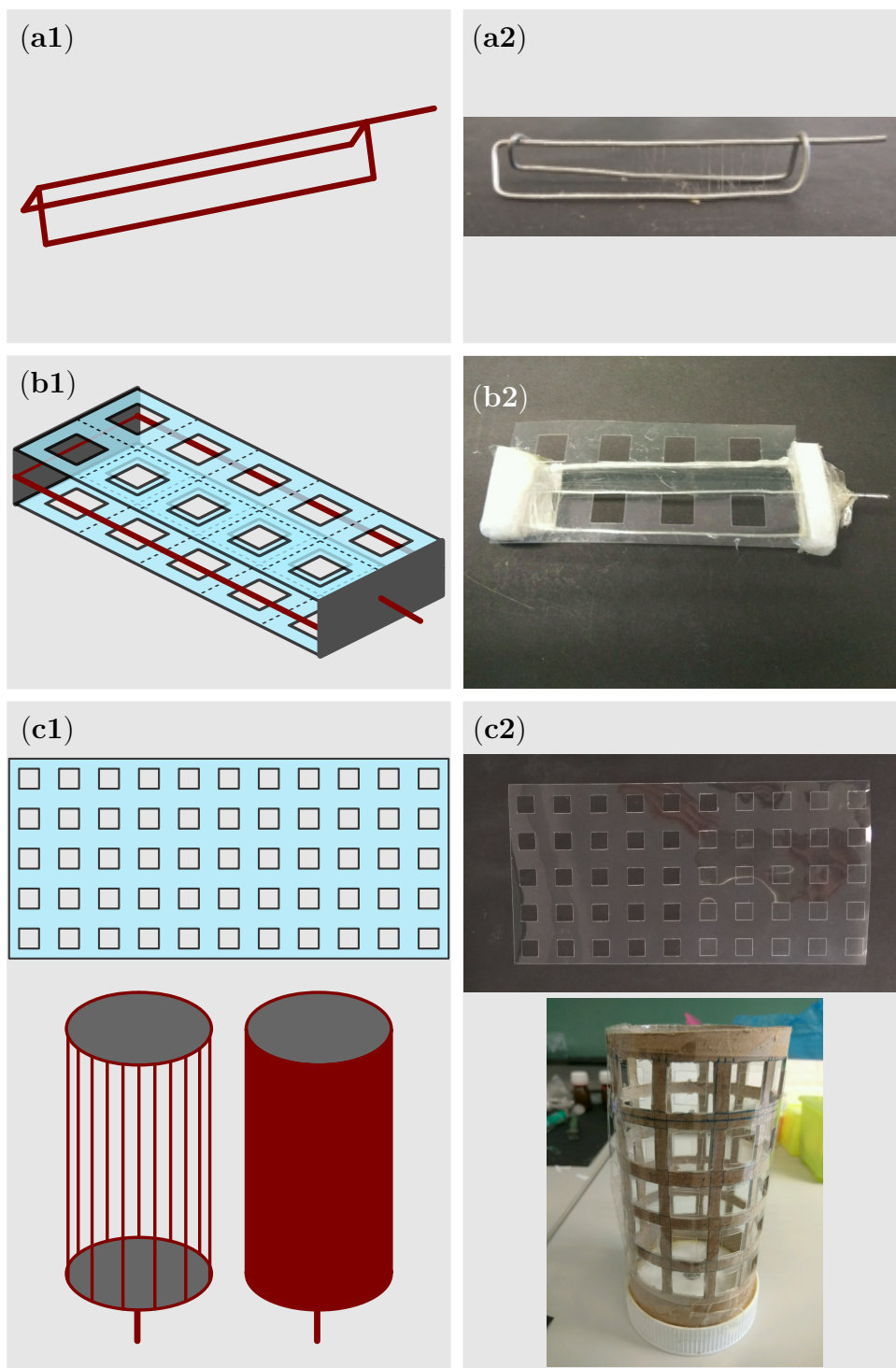Targets made from aluminium sheets are easy to made. However, if this kind

Figure 3.12: Different types of electrospinning collectors: **a** V-shape; **b** parallel sheets with two parallel electrodes; **c** cylindrical sheet wrapped around a wired drum.

of collectors are set to rotate, they become unstable. Another simple collector, but sturdy, was developed using an iron wire shaped with a *V* geometry, Figure 3.12(**a**). The *V*-shaped collector could be closed and opened up, allowing fibres to extend and contract. Also, the geometry of these collectors avoid fibres collected in different regions to interact with each other. These collectors were extremely light, which allowed to use high speed rotations, since the moment of inertia depends on the mass and the distance from rotational axis.

For PU/PBDO fibres, since only less than ten fibres were obtained on each batch, other targets were developed for producing a higher number of fibres. PU/PBDO fibre also had an important feature, not typical in electrospinning experiments: it does not undergo bending instabilities. Therefore, PU/PBDO fibres are less susceptible to become misaligned and also, in this specific case, depended on the rotation velocity for much lower values associated with the electrospinning technique. Figure 3.12(**b**) show the first developed target where two acetate sheets were settled on the top and in the bottom of a structure that had two electrodes in separating the sheets. It is worth to mention that the use of acetate sheets added other two improvements to the *V*-shaped collector: PU/PBDO fibres still had residual solvent (toluene) after landing the target, making the fibre ends to melt with the acetate sheet; acetate sheets are easy to cut and to handle, but remain robust to hold in the collection operation. A final optimization and improvement of the acetate sheets collector is shown in Figure 3.12(**c**). Initially, the collector was conceived as an acetate sheet wrapped around a wire drum. However, since previous results indicate a strong dependence of the alignment with the collector rotation, a cardboard frame was first tested to support the acetate sheets. Obtained fibres were still aligned and therefore there was no need to use the metallic rotating drum.

3.2.3 UV irradiation

PU/PBDO fibres after being electrospun were irradiated with UV light. Ultraviolet (UV) light is a electromagnetic radiation with lower wavelength than visible light. The energy of this type of radiation is enough to promote new crosslinkings in the copolymer. Used UV source had the wavelength $\lambda = 254\,\text{nm}$, Intensity $= 10^{-5}\,\text{mW}\,\text{cm}^{-1}$ and lamp to sample distance $L_{\text{UV}} = 20\,\text{cm}$), for times ranging from a few minutes to 24 h, depending if fibres were initially pre-strained or not.

Fibres were also irradiated in different regions. To produce symmetric perversions, fibres were irradiated with UV light on one side of the surface. Antisymmetric perversions were produced by irradiating two complementary sides of the fibre regions using two
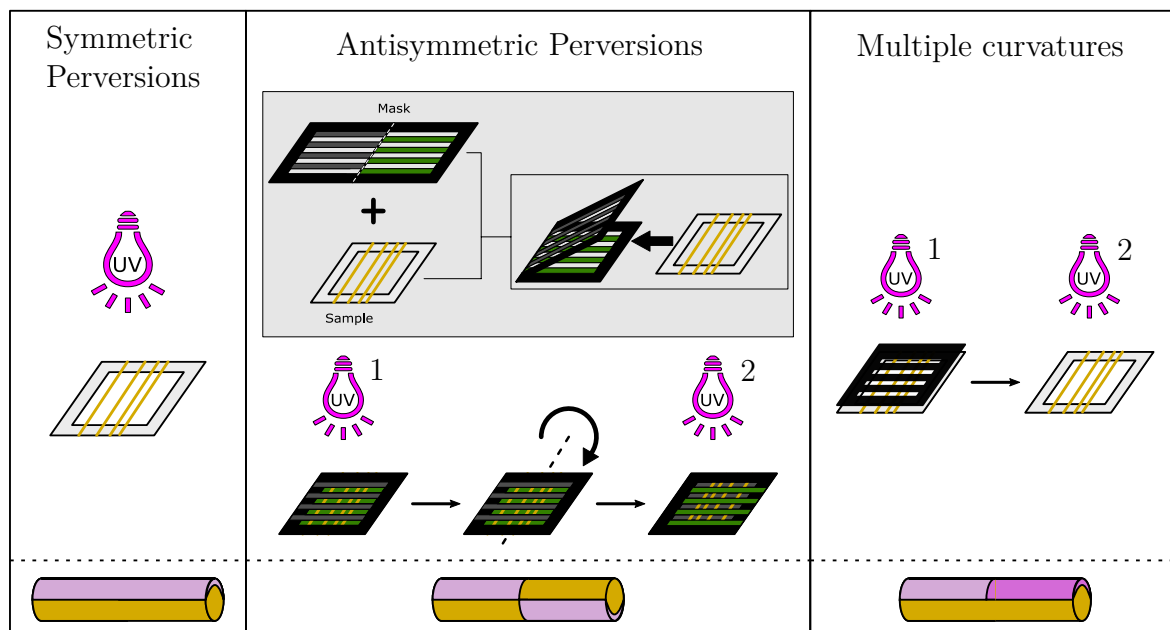
Figure 3.13: Schematic representation of the several experimental steps to produce polymeric fibres with symmetric, antisymmetric perversions and alternating intrinsic curvatures.

irradiation cycles. In the first cycle, a mask made with an opaque card protected sections of the fibre from UV light. In the second irradiation cycle, the sample was flipped and the complementary region were irradiated with the UV light, Figure 3.13. Fibres containing different intrinsic curvatures along their length were produced by irradiating parts of the fibre using also two irradiation cycles, but now in the same side, Figure 3.13. In the first cycle, a mask protected sections of the fibre from being irradiated with UV light. Next, the mask was removed and another cycle of UV irradiation was applied again.

The cardboard mask were cut with a precision cutting machine, a Silhouette Portrait. Different masks were used to obtain different schemes of UV irradiation. Some masks are shown in Figure 3.14.

3.3 Characterization

Obtained fibres had diameters from the order of the unit to the tenth of micrometers. Fibres could be observed at naked eye, with the right contrast of light. In the case of the PU/PBDO fibres, the releasing of the fibres were controlled by a DEVICE. Unfortunately, force-extension trials could not be performed because of the device could not perform measurements so low. The releasing of the fibres were recorded using a
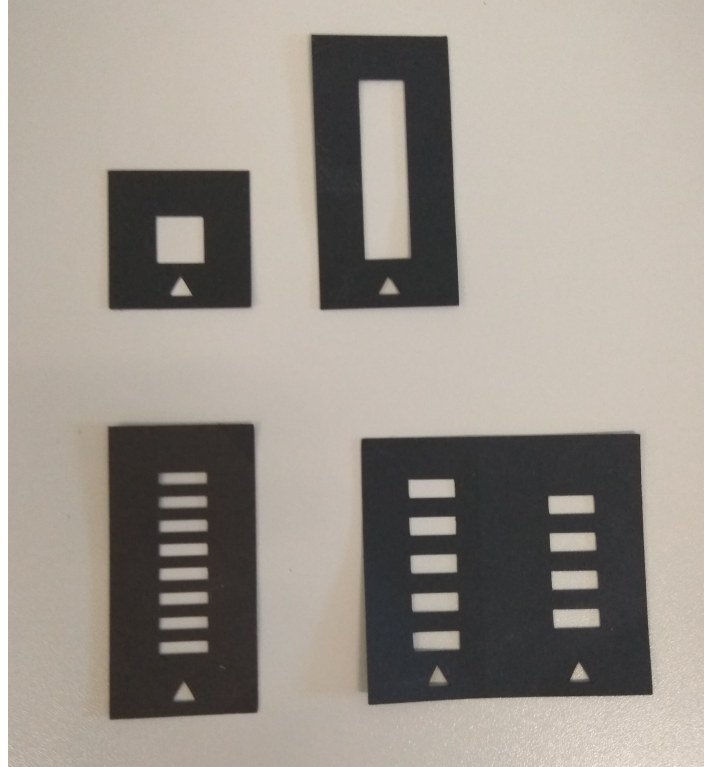
Figure 3.14: Examples of opaque masks used to protect the microfibres of being irradiated with UV light.

portable digital microscope, Veho VMS-004D, and a optical microscope. Wrinkles in the surface of the PU/PBDO fibres could be sometimes observed in the optical microscope, but a scanning electron microscope was used to observe more detailed information about the fibres morphology.

3.3.1 Polarizing Optical Microscopy (POM)

Samples were analysed by using an optical microscope to measure the helical quantities of the samples and to observe defects in the surface of the fibres. The optical observations were achieved by using a reflection and transmission mode Olympus BX51 microscope equipped with an Olympus DP73 camera.

3.3.2 Scanning Electron Microscopy (SEM) analysis

Before viewing fibres in the SEM, the substrates with filaments were glued onto aluminium stubs using a double-sided carbon tape and sputter coated using a Q300T

D Quorum target sequential sputtering system. Samples were sputter coated with a thin gold layer ($\leq 20\,\text{nm}$) to make their surfaces more conductive and therefore less susceptible to the accumulation of surface charge.

The samples were next introduced in a SEM equipment, a Zeiss DSM962. This is a conventional tungsten filament SEM equipment with secondary electron and backscattered electron modes. The SEM images under the in-lens mode have been carried out with an acceleration voltage of $2\,\text{kV}$ and aperture size of $30\,\mu\text{m}$.

References

[1]   V. A. Ganesh, H. K. Raut, A. S. Nair, and S. Ramakrishna, "A review on self-cleaning coatings," *Journal of Materials Chemistry*, vol. 21, no. 41, p. 16 304, 2011. DOI: 10.1039/c1jm12523k.

[2]   I. Sas, R. E. Gorga, J. A. Joines, and K. A. Thoney, "Literature review on superhydrophobic self-cleaning surfaces produced by electrospinning," *Journal of Polymer Science Part B: Polymer Physics*, vol. 50, no. 12, pp. 824–845, Jun. 15, 2012. DOI: 10.1002/polb.23070.

[3]   Y. H. Kim and G. Sun, "Durable Antimicrobial Finishing of Nylon Fabrics with Acid Dyes and a Quaternary Ammonium Salt," *Textile Research Journal*, vol. 71, no. 4, pp. 318–323, Apr. 2001. DOI: 10.1177/004051750107100407.

[4]   M. Faccini, C. Vaquero, and D. Amantia, "Development of Protective Clothing against Nanoparticle Based on Electrospun Nanofibers," *Journal of Nanomaterials*, vol. 2012, pp. 1–9, 2012. DOI: 10.1155/2012/892894.

[5]   B. Mahltig and H. Böttcher, "Modified Silica Sol Coatings for Water-Repellent Textiles," *Journal of Sol-Gel Science and Technology*, vol. 27, no. 1, pp. 43–52, May 1, 2003. DOI: 10.1023/A:1022627926243.

[6]   J. Zimmermann, F. A. Reifler, G. Fortunato, L.-C. Gerhardt, and S. Seeger, "A Simple, One-Step Approach to Durable and Robust Superhydrophobic Textiles," *Advanced Functional Materials*, vol. 18, no. 22, pp. 3662–3669, Nov. 24, 2008. DOI: 10.1002/adfm.200800755.

[7]   Yuan Gao and R. Cranston, "Recent Advances in Antimicrobial Treatments of Textiles," *Textile Research Journal*, vol. 78, no. 1, pp. 60–72, Jan. 2008. DOI: 10.1177/0040517507082332.

[8] B. Simoncic and B. Tomsic, "Structures of Novel Antimicrobial Agents for Textiles - A Review," *Textile Research Journal*, vol. 80, no. 16, pp. 1721–1737, Oct. 2010. DOI: 10.1177/0040517510363193.

[9] T. Textor and B. Mahltig, "A sol-gel based surface treatment for preparation of water repellent antistatic textiles," *Applied Surface Science*, vol. 256, no. 6, pp. 1668–1674, Jan. 2010. DOI: 10.1016/j.apsusc.2009.09.091.

[10] Q. Gao, H. Ma, W. Bao, C. Gao, and M. Ge, "Polyacrylonitrile/electroconductive TiO2 nanoparticles composite fibers via wet-spinning," *Fibers and Polymers*, vol. 17, no. 7, pp. 1048–1054, Jul. 2016. DOI: 10.1007/s12221-016-6314-1.

[11] J. Alongi, F. Carosio, and G. Malucelli, "Current emerging techniques to impart flame retardancy to fabrics: An overview," *Polymer Degradation and Stability*, vol. 106, pp. 138–149, Aug. 2014. DOI: 10.1016/j.polymdegradstab.2013.07. 012.

[12] C.-H. Xue, L. Zhang, P. Wei, and S.-T. Jia, "Fabrication of superhydrophobic cotton textiles with flame retardancy," *Cellulose*, vol. 23, no. 2, pp. 1471–1480, Apr. 2016. DOI: 10.1007/s10570-016-0885-2.

[13] F.-L. Zhou and R.-H. Gong, "Manufacturing technologies of polymeric nanofibres and nanofibre yarns," *Polymer International*, vol. 57, no. 6, pp. 837–845, Jun. 2008. DOI: 10.1002/pi.2395.

[14] L. S. Pinčuk and Springer-Verlag (Berlin), *Melt Blowing: Equipment, Technology, and Polymer Fibrous Materials*. Berlin; Heidelberg: Springer, 2002.

[15] D. Zhang, Ed., *Advances in Filament Yarn Spinning of Textiles and Polymers*, Woodhead Publishing series in textiles Number 150, Amsterdam: Elsevier/Woodhead Publishing, 2014, 210 pp.

[16] A. Haider, S. Haider, and I.-K. Kang, "A comprehensive review summarizing the effect of electrospinning parameters and potential applications of nanofibers in biomedical and biotechnology," *Arabian Journal of Chemistry*, Dec. 2015. DOI: 10.1016/j.arabjc.2015.11.015.

[17] W. Khoo and C. T. Koh, "A review of electrospinning process and microstructure morphology control," in *International Conference on Mechanical and Manufacturing Engineering (ICME2015)*, Oct. 4, 2015.

[18] M. H. Godinho, J. P. Canejo, G. Feio, and E. M. Terentjev, "Self-winding of helices in plant tendrils and cellulose liquid crystal fibers," *Soft Matter*, vol. 6, no. 23, pp. 5965–5970, Nov. 17, 2010. DOI: 10.1039/C0SM00427H.

[19] A. C. Trindade, J. P. Canejo, P. I. C. Teixeira, P. Patricio, and M. H. Godinho, "First Curl, Then Wrinkle," *Macromolecular Rapid Communications*, vol. 34, no. 20, pp. 1618–1622, Oct. 2013. DOI: 10.1002/marc.201300436.

[20] M. W. Frey, "Electrospinning Cellulose and Cellulose Derivatives," *Polymer Reviews*, vol. 48, no. 2, pp. 378–391, May 2008. DOI: 10.1080/15583720802022281.

[21] M. A. Hubbe, O. J. Rojas, L. A. Lucia, and M. Sain, "Cellulosic nanocomposites: A review," *BioResources; Vol 3, No 3 (2008)*, 2008.

[22] X. Cao, X. Wang, B. Ding, J. Yu, and G. Sun, "Novel spider-web-like nanoporous networks based on jute cellulose nanowhiskers," *Carbohydrate Polymers*, vol. 92, no. 2, pp. 2041–2047, Feb. 15, 2013. DOI: 10.1016/j.carbpol.2012.11.085.

[23] S. Suto, "Viscometric behavior of mesomorphic ethyl cellulose solution in chloroform," *Journal of Polymer Science: Polymer Physics Edition*, vol. 22, no. 4, pp. 637–646, Apr. 1984. DOI: 10.1002/pol.1984.180220407.

[24] Symposium on Polymeric Liquid Crystals, A. Blumstein, American Chemical Society, Division of Polymer Chemistry, American Chemical Society, and Meeting, *Polymeric Liquid Crystals*. New York: Plenum Press, 1985.

[25] W. P. Pawlowski, R. D. Gilbert, R. E. Fornes, and S. T. Purrington, "The liquid-crystalline properties of selected cellulose derivatives," *Journal of Polymer Science Part B: Polymer Physics*, vol. 26, no. 5, pp. 1101–1110, May 1988. DOI: 10.1002/polb.1988.090260514.

[26] J. P. Canejo, J. P. Borges, M. H. Godinho, P. Brogueira, P. I. C. Teixeira, and E. M. Terentjev, "Helical Twisting of Electrospun Liquid Crystalline Cellulose Micro- and Nanofibers," *Advanced Materials*, vol. 20, no. 24, pp. 4821–4825, Dec. 17, 2008. DOI: 10.1002/adma.200801008.

[27] M. Lewin, Ed., *Handbook of Fiber Chemistry*, 3rd ed, International fiber science and technology series 16, Boca Raton: CRC/Taylor & Francis, 2007, 1044 pp.

[28] S.-L. Tseng, A. Valente, and D. G. Gray, "Cholesteric liquid crystalline phases based on (acetoxypropyl)cellulose," *Macromolecules*, vol. 14, no. 3, pp. 715–719, May 1, 1981. DOI: 10.1021/ma50004a049.

[29] G. V. Laivins and D. G. Gray, "Liquid crystalline phase transition of a semiflexible polymer: Acetoxypropyl cellulose," *Macromolecules*, vol. 18, no. 9, pp. 1753–1759, Sep. 1985. DOI: 10.1021/ma00151a019.

[30] S. N. Fernandes, Y. Geng, S. Vignolini, B. J. Glover, A. C. Trindade, J. P. Canejo, P. L. Almeida, P. Brogueira, and M. H. Godinho, "Structural Color and Iridescence in Transparent Sheared Cellulosic Films," *Macromolecular Chemistry and Physics*, vol. 214, no. 1, pp. 25–32, Jan. 11, 2013. DOI: 10.1002/macp.201200351.

[31] L. van Langenhove, Ed., *Advances in Smart Medical Textiles: Treatments and Health Monitoring*, Woodhead publishing series in textiles number 173, Amsterdam Boston Cambridge Heidelberg London New York Oxford Paris San Francisco Singapore Sydney Tokyo: Elsevier/WP, Woodhead Publishing, 2016, 279 pp.

[32] A. K. Bhowmick and H. L. Stephens, Eds., *Handbook of Elastomers*, 2nd ed., rev. and expanded, Plastics engineering 61, New York: M. Dekker, 2001, 922 pp.

[33] C.-t. Zhao and M. Norberta de Pinho, "Design of polypropylene oxide/polybutadiene bi-soft segment urethane/urea polymer for pervaporation membranes," *Polymer*, vol. 40, no. 22, pp. 6089–6097, Oct. 1999. DOI: 10.1016/S0032-3861(98)00833-7.

[34] M. Godinho, L. Melo, and P. Brogueira, "Atomic force microscopy evidence of patterning urethane/urea copolymers," *Materials Science and Engineering: C*, vol. 23, pp. 919–922, 6-8 Dec. 2003. DOI: 10.1016/j.msec.2003.09.164.

[35] A. Trindade, M. Godinho, and J. Figueirinhas, "Shear induced finite orientational order in urethane/urea elastomers," *Polymer*, vol. 45, no. 16, pp. 5551–5555, Jul. 2004. DOI: 10.1016/j.polymer.2004.05.062.

[36] M. H. Godinho, A. C. Trindade, J. L. Figueirinhas, L. V. Melo, P. Brogueira, A. M. Deus, and P. I. C. Teixeira, "Tuneable micro- and nano-periodic structures in a free-standing flexible urethane/urea elastomer film," *The European Physical Journal E*, vol. 21, no. 4, pp. 319–330, Dec. 2006. DOI: 10.1140/epje/i2006-10070-8.

[37] M. Godinho, A. Trindade, J. Figueirinhas, L. Melo, and P. Brogueira, "Study of micro and nano surface structures from UV irradiated urethane/urea elastomers," *Biomolecular Engineering*, vol. 24, no. 1, pp. 97–101, Feb. 2007. DOI: 10.1016/j.bioeng.2006.05.028.

[38] P. Izak, M. Godinho, P. Brogueira, J. Figueirinhas, and J. Crespo, "3D topography design of membranes for enhanced mass transport," *Journal of Membrane Science*, vol. 321, no. 2, pp. 337–343, Aug. 2008. DOI: 10.1016/j.memsci.2008.05.014.

[39] A. C. Trindade, J. P. Canejo, L. F. V. Pinto, P. Patricio, P. Brogueira, P. I. C. Teixeira, and M. H. Godinho, "Wrinkling Labyrinth Patterns on Elastomeric Janus Particles," *Macromolecules*, vol. 44, no. 7, pp. 2220–2228, Apr. 12, 2011. DOI: 10.1021/ma1025169.

[40] A. C. Trindade, J. P. Canejo, P. Patricio, P. Brogueira, P. I. Teixeira, and M. H. Godinho, "Hierarchical wrinkling on elastomeric Janus spheres," *Journal of Materials Chemistry*, vol. 22, no. 41, p. 22 044, 2012. DOI: 10.1039/c2jm35018a.

[41] X. Xu, X. Zhuang, X. Chen, X. Wang, L. Yang, and X. Jing, "Preparation of Core-Sheath Composite Nanofibers by Emulsion Electrospinning," *Macromolecular Rapid Communications*, vol. 27, no. 19, pp. 1637–1642, Oct. 2, 2006. DOI: 10.1002/marc.200600384.

[42] J.-F. Zhang, D.-Z. Yang, F. Xu, Z.-P. Zhang, R.-X. Yin, and J. Nie, "Electrospun Core-Shell Structure Nanofibers from Homogeneous Solution of Poly(ethylene oxide)/Chitosan," *Macromolecules*, vol. 42, no. 14, pp. 5278–5284, Jul. 28, 2009. DOI: 10.1021/ma900657y.

[43] I. G. Loscertales, A. Barrero, I. Guerrero, R. Cortijo, M. Marquez, and A. M. Gañán-Calvo, "Micro/Nano Encapsulation via Electrified Coaxial Liquid Jets," *Science*, vol. 295, no. 5560, pp. 1695–1698, Mar. 1, 2002. DOI: 10.1126/science.1067595. pmid: 11872835.

[44] H. Jiang, Y. Hu, Y. Li, P. Zhao, K. Zhu, and W. Chen, "A facile technique to prepare biodegradable coaxial electrospun nanofibers for controlled release of bioactive agents," *Journal of Controlled Release*, vol. 108, pp. 237–243, 2–3 Nov. 28, 2005. DOI: 10.1016/j.jconrel.2005.08.006.

[45] H. Qu, S. Wei, and Z. Guo, "Coaxial electrospun nanostructures and their applications," vol. 1, no. 38, pp. 11 513–11 528, Sep. 10, 2013. DOI: 10.1039/C3TA12390A.

[46] G. H. Lee, J.-C. Song, and K.-B. Yoon, "Controlled wall thickness and porosity of polymeric hollow nanofibers by coaxial electrospinning," *Macromolecular Research*, vol. 18, no. 6, pp. 571–576, Jun. 25, 2010. DOI: 10.1007/s13233-010-0607-9.

[47] D. Li and Y. Xia, "Direct Fabrication of Composite and Ceramic Hollow Nanofibers by Electrospinning," *Nano Letters*, vol. 4, no. 5, pp. 933–938, May 1, 2004. DOI: 10.1021/nl049590f.

Chapter

4

Shaping helical electrospun filaments: a review
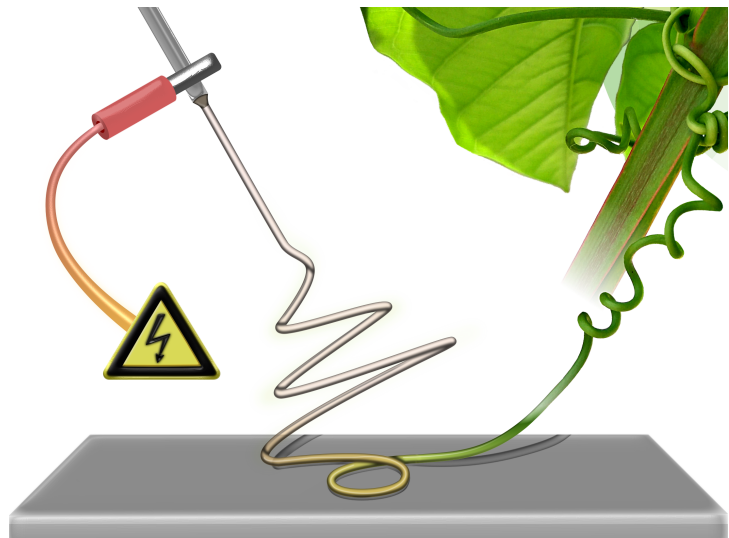
Adapted from:

P. E. S. Silva, F. Vistulo de Abreu, and M. H. Godinho, "Shaping helical electrospun filaments: A review," *Soft Matter*, 2017. DOI:

Abstract

Nature abounds with helical filaments designed for specific tasks. For instance, some plants use tendrils to coil and attach to the surroundings, while *Spiroplasma*, a helical bacterium, moves by inverting the helical handedness along the filament axis. Therefore, developing methods to shape filaments on demand to exhibit a diversity of physical properties and shapes could be of interest to many fields, such as the textile industry, biomedicine or nanotechnology. Electrospinning is a simple and versatile technique that allows the production of micro and nanofibres with many different helical shapes. In this work, we review the different electrospinning procedures that can be used to obtain helical shapes similar to those found in natural materials. These techniques also demonstrate that the creation of helical shapes at the micro/nanoscale is not limited by the chirality of the building blocks at the molecular level, a finding which opens new horizons on filament shaping.

4.1 Introduction

In nature, helices appear in a wide range of length scales, from the macroscale, as in plants and animals, to the microscale or even nanoscale as in biomolecules (Fig. 4.1 from a to e). They occur as a result of the forces imposed upon materials, as well as their properties. Helices often put in evidence a conferred functional advantage. For instance, *Passiflora edulis* uses straight tendrils to attach to surrounding structures, Fig. 4.1a, and coiling to create helical structures with helices with opposite handedness connected by an inversion (named a perversion).[2], [3] The helical tendrils are important because they help a delicate plant to grow upwards, better supporting itself to endure variable weather conditions. In tendrils, coiling is produced by the asymmetric contraction of cells on the fibre axis.[4]

In animals, some snakes coil to attack their preys by curling and squeezing their victims.[5] Some worms also contract into tight coils when they feel any kind of disturbance. These organisms use complex mechanisms of contraction and relaxation of muscles to generate coiling. While the helical shape appears to be of great importance for some organisms, on others its function remains uncertain. In the case of the marine worms *Carcinonemertes kurisi*, which live on pleopods on the abdominal surfaces of crabs, the advantage of their left-handed corkscrew-shape remains unclear (Fig. 4.1b).[6] Likewise, left-handed helices present in *xylem* microstructures vessels of vascular plants[7] (Fig. 4.1c) act as tube-containers to carry liquids to the leaves, via capillarity, and are vital to the survival of the plant.

The motility of some helical bacteria, for example *Spiroplasma*, a gram-positive microorganism with diameters of a few hundred nanometres and lengths in the micron range, which infects plants and animals,[9] was found to be generated by the propagation of a pair of perversions along its body axis, as shown in Fig. 4.1d. The inversion of the helical handedness allows these cells to travel at a velocity of a few microns per second in the direction opposite to that of the perversion movement.

At the nanoscale the double-helical DNA structure ensures the most efficient packing, accessibility and fidelity for replication of the information stored in the macromolecule.[11] Plenty of biophysical models have been developed to detail its functionality (Fig. 4.1e).

All these living organisms are a source of inspiration to produce synthetic helical shapes at different scales. In Fig. 4.2, some examples are given, showing macro to nano helices produced from diverse materials and techniques. Iamsaard et al.[12] used responsive liquid crystalline molecules associated to specific techniques of sample preparation to promote light-activated motion at the molecular level, leading to macroscopic
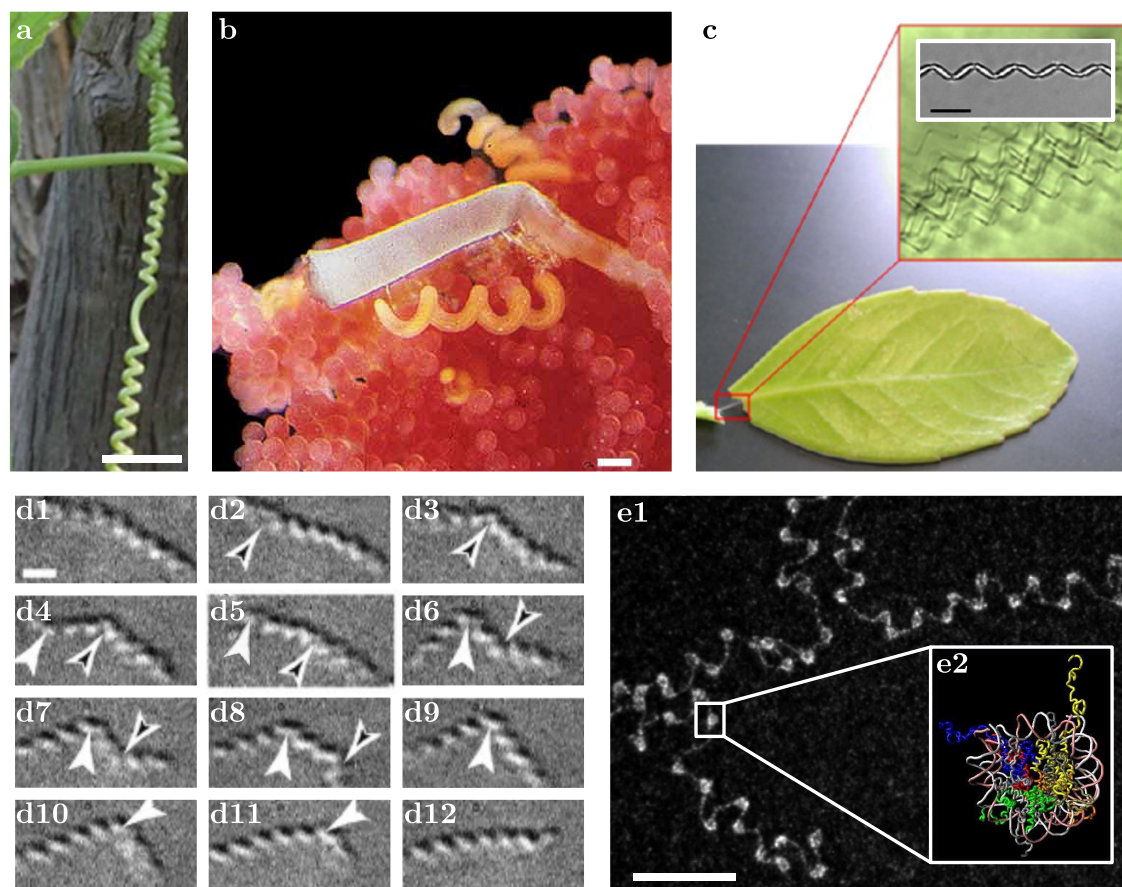
Figure 4.1: Helices in nature across different length scales. (a) *Passiflora edulis* tendrils forming left- and right-handed helical structures,[8] scale bar is 10 mm. (b) *Carcinonemertes kurisi* worms exhibiting left-handed helical shapes,[6] scale bar is 1 mm. (c) Image of stretched helical left-handed microstructures from xylem of *Rhaphiolepis indica*,[7] scale bar is 20 μm (d) Video frames of a *Spiroplasma*, a helical bacterium, that propels by moving a perversion (handedness inversion),[9] scale bar is 1 μm. (e1) TEM image from a nucleosomal array, extracted from chinese hamster ovary cells, scale bar is 100 nm. (e2) Biomolecular model.[10] Image (a) is reprinted from Godinho et al.[8] with permission from the Royal Society of Chemistry. Image (b) is reprinted from Sadeghian et al.[6] with permission from Taylor & Francis. Image (c) is reprinted from Gao et al.[7] with permission from the American Chemical Society. Image (d) is adapted from Shaevitz et al.[9] with permission from Elsevier. Image (e) is adapted from Moziconacci et al.[10] with permission from Nova Science Publishers, Inc..

twisting movements. Left- or right-handed programmed elastomeric helices are shown in Fig. 4.2a.

Spinning processes were also used to reproduce the helical structure of plant tendrils at the microscale, Fig. 4.2b.[13] A capillary instability of the viscous thread was found responsible for the as-spun helices produced from regenerated cellulose, with
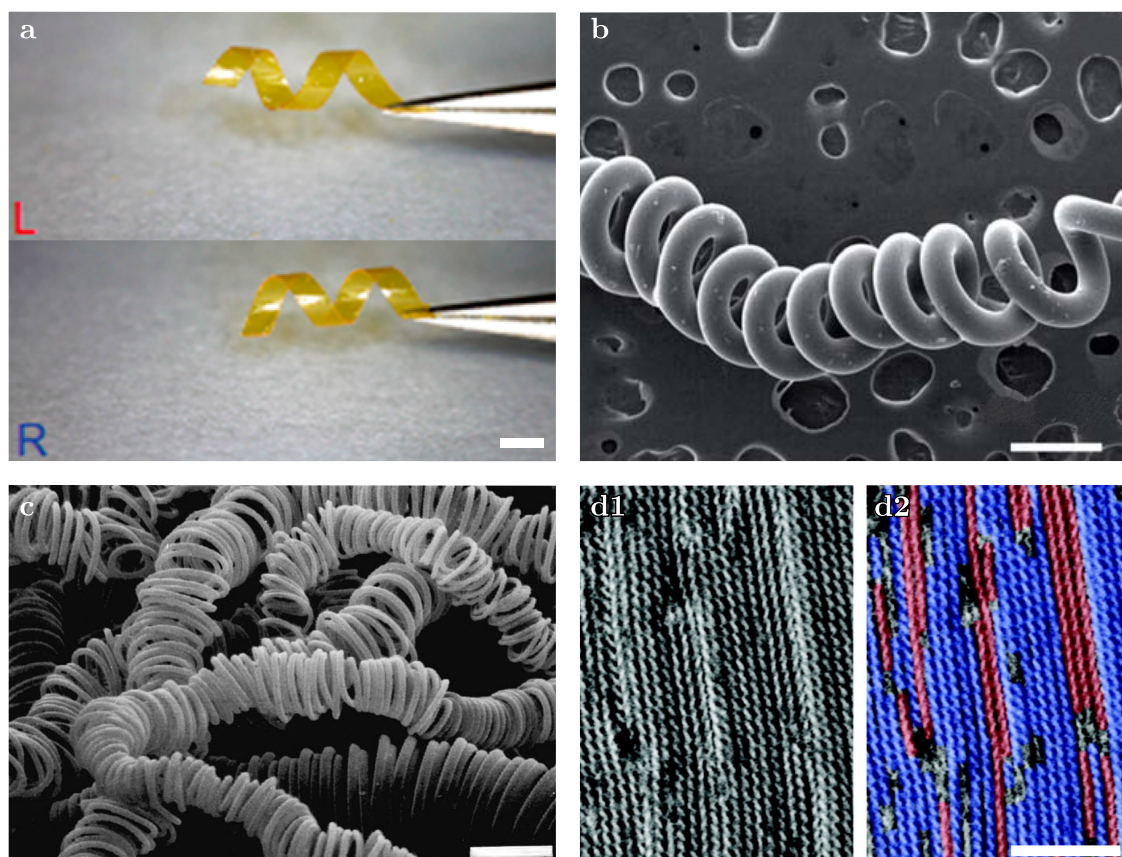
Figure 4.2: Helical synthetic systems. (a) Picture of a photoresponsive liquid-crystalline polymer ribbon. Depending on the director alignment and molecular photoisomerization, ribbons can deform into right- or left-handed helical shapes,[12] scale bar is 1 cm. (b) SEM image displaying a helical filament obtained by electrospinning,[13] scale bar is 400 μm. (c) SEM image of carbon coils obtained by the Ni catalysed pyrolysis of acetylene,[14] scale bar is 4 μm (d) AFM phase images of a helical poly(phenylacetylene)s mixture bearing optically active and achiral residues as the pendants groups in the cholesteric LC state and 2D crystals,[15] scale bar is 20 nm. Image (a) is reprinted from Iamsaard et al.[12] with permission from Nature Publishing Group. Image (b) is reprinted from Jia et al.[13] with permission from the Royal Society of Chemistry. Image (c) is reprinted from In-Hwang et al.[14] with permission from Elsevier. Image (d) is reprinted from Ohsawa et al.[15] with permission from the American Chemical Society.

their pitches and diameters dependent on the processing parameters. Both right and left-handed helices were obtained. The SEM picture shown in Fig. 4.2b illustrates of the helices produced at the microscale. Carbon micro right and left-handed helices were also obtained by using a rotating substrate and an anisotropic catalyst, Fig. 4.2c.[14] Hierarchical amplification from molecular to nanoscale helicity was demonstrated for

poly(phenylacetylene) copolymers.[15] AFM measurements revealed that right- and left-handed nano helices were produced from the same macromolecular system. The left-handed helicity is preponderant due to the precursor intrinsic macromolecular chirality.

This review is organized as follows. The next section introduces the electrospinning technique. There, the main ideas, procedures and apparatuses are presented. This introduction is useful for understanding the following sections, dedicated to the recent progress made in the production of helical filaments by electrospinning. Three sections then review three groups of strategies to obtain helices via electrospinning. The techniques have a different level of control over the geometrical parameters of the helices, such as the radius or pitch length. Handedness inversions (perversions) can also be observed and in some cases, produced on demand. This adds new degrees of freedom for shaping filaments. This is discussed at the end of this review, where a comparison between numerical modelling of filament shapes and experiments is also shown.

The chosen examples are intended to illustrate the opportunities that the electrospinning technique opens on the production of synthetic helices at the micro/nanoscale and do not represent an exhaustive list.

4.2 Electrospinning process

Electrospinning is a well-known technique that has been revived by Reneker,[16], [17] after the raising interest in nanotechnology: electrospinning allows the production of fibres with thickness under the micrometer range.[18]–[20] Electrospinning is a low-cost technique that has long been thought to be the future in the textile industry. It can be automated, is an easy and extremely flexible technique, and allows the production of non-woven fabrics with different textures and designs.

A variety of polymers have been electrospun into fibres with diameters ranging from the nano to the micrometer size.[21], [22] A solid polymer can be processed into a fibre if it can be dissolved or melted into a polymeric solution and the molecular weight is high enough to allow the intertwining between the polymeric chains.[23], [24]

A usual electrospinning experiment consists of ejecting a polymer solution using an electrostatic force, as shown in Fig. 4.3. When the electric field is applied to a liquid droplet, which can be formed when the solution is pumped through a tip of the needle, the accumulation of electrostatic charges causes the shape of the droplet to change from a sphere to an elongated cone shape (known as Taylor's Cone).[25] Once the threshold voltage is crossed, the electric field overcomes the surface tension of the polymer solution, a thin jet is released from the peak of the cone and begins to travel
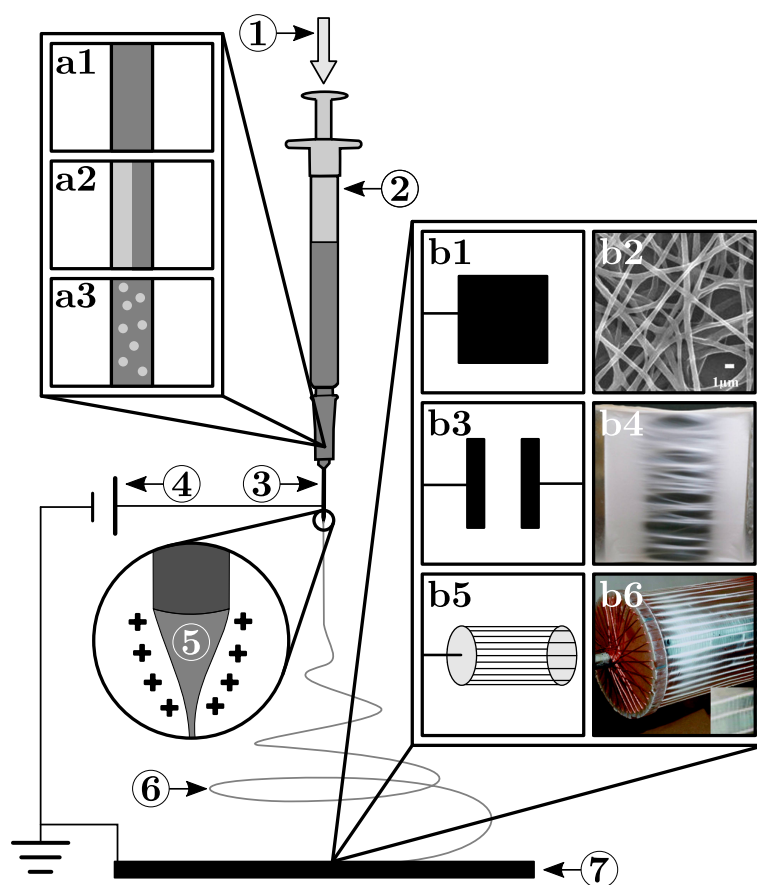
Figure 4.3: Scheme of basic electrospinning apparatus: ① Pump; ② Syringe; ③ Needle; ④ High-voltage power source; ⑤ Taylor's cone; ⑥ Jet; ⑦ Collector. (a) Types of precursor solutions (a1) single (a2) multi-core and (a3) emulsion. (b) Some examples of electrospinning collectors and images of fibres that can be obtained: (b1) and (b2) Plate collectors allow the collection of mostly randomly aligned fibres;[26] (b3) and (b4) Parallel electrodes are simple to set up and make it is easy to obtain aligned fibres;[27] (b5) and (b6) Rotating drum is a variation of the parallel electrodes and allows one to obtain larger areas of non-woven membranes;[28] Image (b2) is reprinted from Pal et al.[26] with permission from Elsevier. Image (b4) is reprinted from Jose et al.[27] with permission from Springer. Image (b6) is reprinted from Katta et al.[28] with permission from the American Chemical Society.

in a straight trajectory. After a few centimetres, the liquid solution may either undergo instabilities that produce a thin thread or is dispersed into tiny droplets (electrospraying technique), depending on the characteristics of the polymeric solution. The produced thread develops a whipping-like trajectory, which allows the solvent to be removed and promotes the elongation of the fibres. Fibres can then be easily collected in a sheet of aluminium foil or by more complex collectors, depending on the desired mat properties.

Electrical bending instabilities are a common occurrence in electrospinning experiments. Typically, they occur after a specific distance from the tip of the needle,

depending on the materials and experimental conditions. Multiple bending instabilities may occur during the jet flight and, every time a bending instability occurs, the path of the jet revolves in a trajectory with increasing radius around the previous jet axis until the thin jet is fully (or almost fully) solidified.[17] When the jet lands on the target, it can undergo a mechanical buckling instability due to compressive forces.[16], [29]

The diameter of the fibres and other properties of the mesh, like the presence of beads or pores, depend on several parameters, including the viscosity and conductivity of the solution, solution feed rate, applied voltage, tip-to-collector distance, temperature and humidity.[30], [31] For instance, solutions with higher polymer content have higher viscosity, which typically generates fibres with higher diameters. Solutions with a lower polymer content produce less uniform fibres and structures like beads and other defects can arise in the final electrospun fabric.[32] The increase of power voltage may reduce[33] or increase the diameter of the fibre.[34] The jet velocity increases with the applied voltage, which may also increase the whipping instabilities, generating thinner filaments. In contrast, larger quantities of solution can be ejected since electric forces will also be higher, generating thicker fibres. A short distance between the tip and the collector generally results in the formation of beads, due to insufficient time for the solvent to evaporate and for the filament to further elongate.[35] Increasing the spinning distance results in the reduction of the fibre diameter as well as better solvent evaporation.[36] However, with the increase of the distance between the tip and the collector, the reduction of the fibre diameter becomes less expressive since the jet is already solidified. Furthermore, an excessive distance can lead to a weaker field on the jet, which affects the collection of the fibres.[37]

Collectors also play an important role in the arrangement of electrospun fibres. If a grounded planar surface collector is used, like a metallic plate or an aluminium sheet, fibres will most likely be randomly oriented, Fig. 4.3b1 and b2.[26] The resulting fibre mesh is called a non-woven mat. By using collectors with other geometries or adding dynamics to the collection, it is possible to obtain other fibre assemblies. For instance, two parallel electrodes can be used to obtain uniaxially aligned fibres in the space between the electrodes, Fig. 4.3b3 and b4.[27], [38] This approach is simple, versatile and straightforward, not only for producing meshes of aligned fibres but also, if short collection times are used, to obtain single fibres. However, the lengths of the mats are limited by the distance between electrodes. Moreover, for large gaps or long collection times, fibres become misaligned. Using the same electrode methodology, it is possible to obtain sequences of aligned fibres along different directions if the electrodes are disposed in a circular disposition. In this case, different meshes can be obtained by alternately or simultaneously grounding the electrodes.[38] A different strategy was devised by

Kim et al.[39], by introducing a rotating drum in the system. In contrast with flat collectors or auxiliary electrodes, fibre collection is now dynamically assisted. Katta and co-workers [28] created copper-wire framed drums to collect well-oriented fibres. In fact, the wire-drum approach is a scale-up of the two-electrodes approach, where the sequence of electrodes continuously changes (see Fig.4.3b5 and b6). However, the mats thus obtained are still limited in thickness, an issue deriving from fibre conductivity effects. On the one hand, low conductivity causes charge accumulation on the surface of the mat and causes a deviation of the jet before landing. On the other hand, good conducting fibres may work as electrodes and the jet will effectively target the fibres instead of the array of copper wires. Larger mats are possible to be obtained, in comparison to the two-electrodes approach, but fibres may not be aligned along the drum axial direction.

Electrospinning also enables the manufacturing of micro and nano polymer helices in a controllable way. The subject is the focus of the next sections. In Table 4.1, a summary of works describing the use of electrospinning for the production of helical filaments is presented.

Method	Material	Solvent	Fibre diameter	Ref.
Tilted collector	Polycaprolactone (PCL)	Dimethyleformamide (DMF), Tetrahydrofuran (THF)	$1.2 - 2$ μm	[40]
Liquid-flow collector	Polystyrene (PS)	Dimethyleformamide (DMF)	$0.7 - 1.8$ μm	[41]
	Polyethylene oxide (PEO)	Water	10 μm	[42]
Nanopottery	Polyethylene oxide (PEO)	Water	50 nm	[43]
Rotating collector	Polyvinyl pyrrolidone (PVP)	Ethanol	2 μm	[44]
Bi-electrospinning	Polyvinyl pyrrolidone (PVP)	Ethanol	10 μm	[45]
Rotating electric field	Polyethylene oxide (PEO)	Dichloromethane	500 nm	[46]
Co-electrospinning	Polyethylene terephthalate (HSPET), Polytrimethylene terephthalate (PTT)	Trifluoroacetic acid (TFA), Methylene dichloride	800 nm	[47]
	Poly(m-phenylene isophthalamide) (Nomex), Thermoplastic polyurethane (TPU)	Dimethylacetamide (DMAc), Dimethylformamide (DMF), Lithium chloride (LiCl), Tetrahydrofuran (THF)	$100 - 500$ nm	[48]–[50]
	Polyethylene terephthalate (HSPET), Polytrimethylene terephthalate (PTT), Polyurethane (PU), Polyacrylonitrile (PAN)	Trifluoroacetate acid (TFA), Methylene dichloride (DCM), Dimethylformamide (DMF)	800 nm	[51]
Chiral solution	Acetoxypropyl cellulose (APC)	Dimethylacetamide (DMAc)	$1.5 - 2.75$ μm	[52], [53]
Surface modification (UV light)	Poly(propylene oxide)-based (PU) Hydroxyl-terminated polybutadiene (PBDO)	Toluene	$7 - 31$ μm	[54], [55]

Table 4.1: Main electrospun methodologies and materials used reported in literature to produce helical filaments.

4.3 Helices produced by buckling due to impingement on the collector

When a highly viscous jet lands on the target, it becomes unstable due to sudden compressive forces and buckles, similarly to a long bar under a load. This was first

realized by Taylor,[56] and since then numerous experiments have been performed and different patterns observed varying the solution, its physical properties, the distance from the nozzle, the collector type (liquid or solid), its movement and disposition.[29], [57], [58] In particular, spiral patterns were obtained using a static collector.[42] The same patterns have recently been obtained using elastic rods vertically dropped upon rigid substrates,[59] which shows that buckling at the collector is responsible for the emergence of the helical structures, and hence that these are not related to the bending instabilities taking place between the needle and the collector. This is also in agreement with the theoretical work by Yarin and collaborators[35], [58] who demonstrated that by integrating the buckling Euler equations with a clamped end, bending instabilities become spiral-like, in agreement with experiments.

Several other researchers developed methods to optimize helical production and to use different materials. Yu et al.[40] devised a method to create helical structures by adjusting the concentration of polycaprolactone (PCL) and the landing angle between the fibre and a tilted glass, Fig. 4.4a1. For concentrations as low as 3.5%, the jet was too fluid to generate enough stress for the occurrence of buckling instabilities and only sinuous structures were observed. For higher concentrations of the solution, jets became stiff enough for the occurrence of buckling instabilities led to the formation of flat coiled structures, which are often identified as helices, Fig. 4.4a2.[60] For even higher concentrations, around 10%, truly 3D helical filaments were obtained, Fig. 4.4a3. So, from these results it appears that helices require enough stiffness to support themselves. Moreover, fibres become considerably thicker for higher concentrations, since the diameter of the fibres increased from $150-250$ nm to $1.2-2$ μm. Furthermore, the concentration of the solution changed the loop diameter of the filaments, in a non-linear way. The diameter of the fibre loops displayed a maximum at 14.9 μm when the concentration was 5.8%. Helical fibres also required that the angle between the glass slide and the horizontal plane was between $10-30°$. Above 45° fibres tended to be straight.

Instead of a moving solid plate, Shariatpanahi and co-workers[41] used direct electrospinning to produce buckled helical fibres in a liquid collector with flow. The experimental setup can be observed in Fig. 4.4b1. A solution of polystyrene is ejected for 2.5 cm into a bath of gently flowing water. A high-voltage differential potential is applied between the needle tip and an electrode kept submerged but close to the surface of the water. The pitch length and the radius of the fibres were controlled by varying the applied DC voltage. Then, since different voltages can be used during a electrospinning run, fibres with multiple helical morphologies can be obtained, as shown in Fig. 4.4b2. Han et al.[42] obtained many other patterns, including sinuous, zigzag-
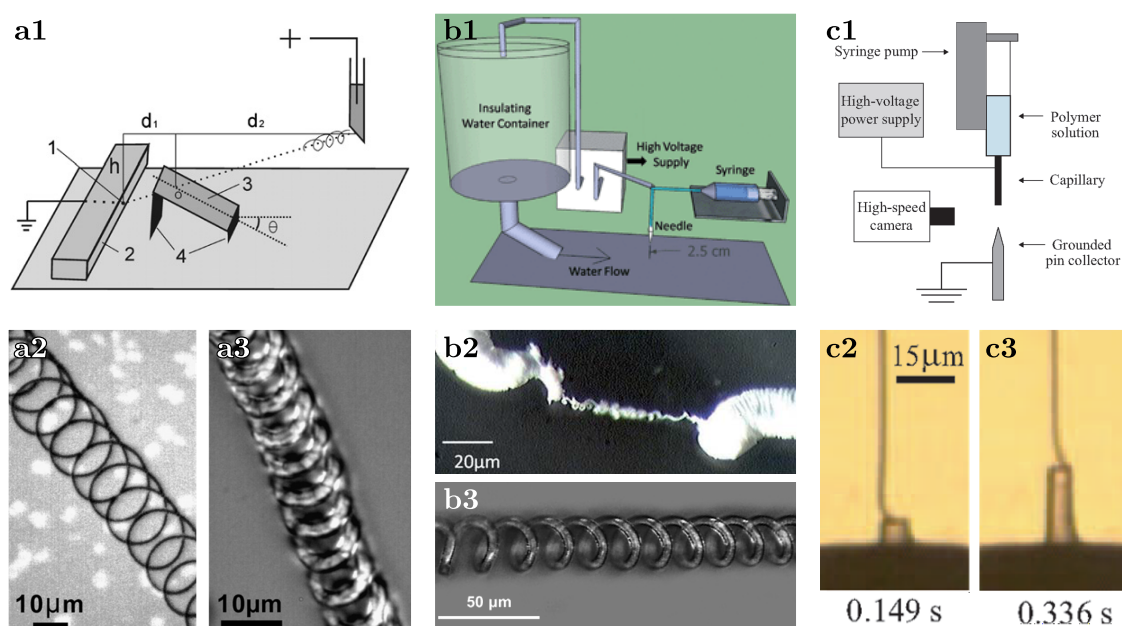
Figure 4.4: Electrospun helices obtained by buckling after impingement upon the collector. (a1) Schematic setup using an inclined collector: 1 – grounded electrode wire; 2 – wooden board; 3 – glass slide; 4 – supporter; h – height between the ground electrode and the syringe needle tip, θ – angle between the glass slide surface and the horizontal plane; O – intersecting point between the line defined by the needle tip and grounded wire end with the glass plane; d_1 and d_2 – horizontal distances from O to the landing place and to the needle tip, respectively.[40] (a2) Flat coiled and (a3) 3D helical structures. (b1) Scheme of a direct electrospinning experiment with a liquid collector. (b2) and (b3) Helical fibres with different morphologies.[41], [42] (c1) Scheme to obtain pottery helical fibres as shown for polyethylene oxide (PEO) fibres in (c2) and (c3)[43]. Image (a) is reprinted from Yu et al.[40] with permission from Elsevier. Images (b1) and (b2) are reprinted from Shariatpanahi et al.[41] with permission from the Royal Society of Chemistry. Image (b3) is reprinted from Han et al.[42] with permission from Elsevier. Image (c) is reprinted from Kim et al.[43] with permission from the American Chemical Society.

like, figures-of-eight, helical fibres as shown in Fig. 4.4b3, and other coiled structures, putting in evidence that electrospun fibres can be shaped with many morphologies in a reasonably controlled way.

Several experiments use a moving plate or a liquid medium to collect buckled filaments. A different strategy was devised by Kim et al.,[43] using a strong focused field to make the fibre fold and stack into a regular cylindrical spool on the top of a metallic tip, Fig. 4.4c1. By the time the polymer lands the grounded tip, the jet is already a solid and can be modelled as a thin elastic filament. Fig. 4.4c2 and c3 shows two instants of the formation of the coiled fibre, where the jets whirls at a rate

of 10000 rpm. The obtained fibres had typical diameters of 200 nm and coil radius ranging from $1 - 8$ μm. Moreover, it was found that helical radius increases with the fibre radius and with the applied electric field.

4.4 Helices obtained by twisting motion

The electrospun apparatus developed by Chang et al.[44], [61] allows the production of single helical microcoils and metallic ribbons. The usual electropsun setup was modified in order to accommodate metallic wires, which rotate at a constant speed, as targets. First, two copper needles, with a diameter of 50 μm, were placed on two motors and set to rotate at 2800 rpm, as shown in Fig. 4.5a1. Then, a positively charged jet of polyvinyl pyrrolidone (PVP) was collected between the two rotating metallic needles, forming a dense bundle, and dried for 5 min. A second negatively charged solution of PVP and copper nitrate was spun onto a parallel collector. The fibres of PVP and copper nitrate were then picked with a thin copper needle and placed on the rotating fibre bundle, forming fibres as shown in the Fig. 4.5a2. Afterwards, fibres were placed in a desiccator with controlled humidity for 2 h and 4 h, respectively, corresponding to fibres shown in Fig. 4.5a3 and a4. Afterwards, fibres were calcinated in air, at 823 K and for 1 h, burning the PVP from the samples. Finally, the coiled nanoribbons of copper oxide were reduced in hydrogen, at 573 K and for 2 h, Fig. 4.5a5. The handedness of the fibres is determined by the direction of the rotation of the targets, while the diameter and pitch were tuned by the diameter of the targets and helices treatments after deposition.

A rotating motor was also used to obtain double helical micro ropes as shown in Fig. 4.5b1. The electrospinning apparatus was modified in order to accommodate a motor to which a metallic needle was attached with the role of collecting and intertwining two electrospun fibres produced from two different spinnerets. The spinnerets were connected to a positive high-voltage supply, as shown in Fig. 4.5b1. Micro ropes with diameters of the order of tens of microns and lengths of centimetres were obtained from PVP solutions. SEM was used to confirm the manufacture of the micro ropes (Fig. 4.5b3). This mechanical method was named bi-electrospinning by the authors and can be adapted to produce ropes with more than one polymer per filament as well as more than two filaments per rope. The ability to produce ropes of almost arbitrary length is a big advantage of this method.

Electrospun twisted nanofibres were also obtained by controlling the trajectory of the jet using a rotating electric field as shown in Fig. 4.5c1.[46] Polyethyne oxide (PEO) solutions were used and twisted fibres with micrometric pitches were obtained as shown

in SEM and AFM pictures, Fig. 4.5c2 and c3. Precise tuning of the fibre pitch was achieved by controlling the rotation time of the electric field in the electrospinning system, as referred by Gu et al.[46] (delay time of 10 ms is at the origin of fibres with periodic twist of the order of 5 μm.

4.5 Helices produced by buckling due to asymmetric contraction

Inspired by asymmetric contraction mechanisms found in natural materials, co-electrospinning was used to produce helical nanofibres. Co-electrospinning uses two polymers and two main types of techniques are described in literature: coaxial and side-by-side systems. To produce helices, the polymers must have distinct mechanical behaviours, different shrinkages, and the coaxial system should be modified with an off-centred core-shell spinneret (see Fig. 4.6a1).[50]

Li et al.[51] reported the use of a microfluidic device as the spinneret to produce side-by-side nanofibres from two polymers with distinct mechanical behaviour, polyurethane (PU), and polyacrylonitrile (PAN). The authors obtained helical fibres with diameters of the order of 240 nm and helix diameters of 500 nm. Chen et al.[48], [49] generated nanosprings by using rigid (for example Nomex) and flexible (for example polyurethane (TPU)) polymers, and off-centred and side-by-side electrospinning techniques. The helices obtained had diameters, on average, similar to those reported by Li and collaborators.[51] Polyethylene terephthalate (HSPET) and polytrimethylene terephthalate (PTT) bi-component helices, produced by side-by-side electrospinning, with diameters of the order of the micron were also obtained by Zhang and co-workers[47] Nomex and TPU were used by Wu et al.[50], [63] to produce helices using a off-centred core-shell co-electrospinning technique. The authors found that the intrinsic curvature of the fibres appears when the jet forms and that the morphology of the fibres (see Fig. 4.6a2) was affected by the applied voltage, the conductivity of the system, and the relative amount of the bi-components present on the asymmetric filament. Helices were also produced by the usual electrospinning technique from liquid crystalline solutions.[52], [53], [62] In this case the intrinsic curvature of the system is acquired by an asymmetric contraction of an off-core internal disclination line, which promotes different shrinkages of the material along the main axis of the fibre (see Fig. 4.6b1 to b3). A circular trajectory was found for the jet as soon as it left the needle indicating that the high shear rate and the liquid crystalline characteristics of the solution are the main ingredients for the system to form micro helices.
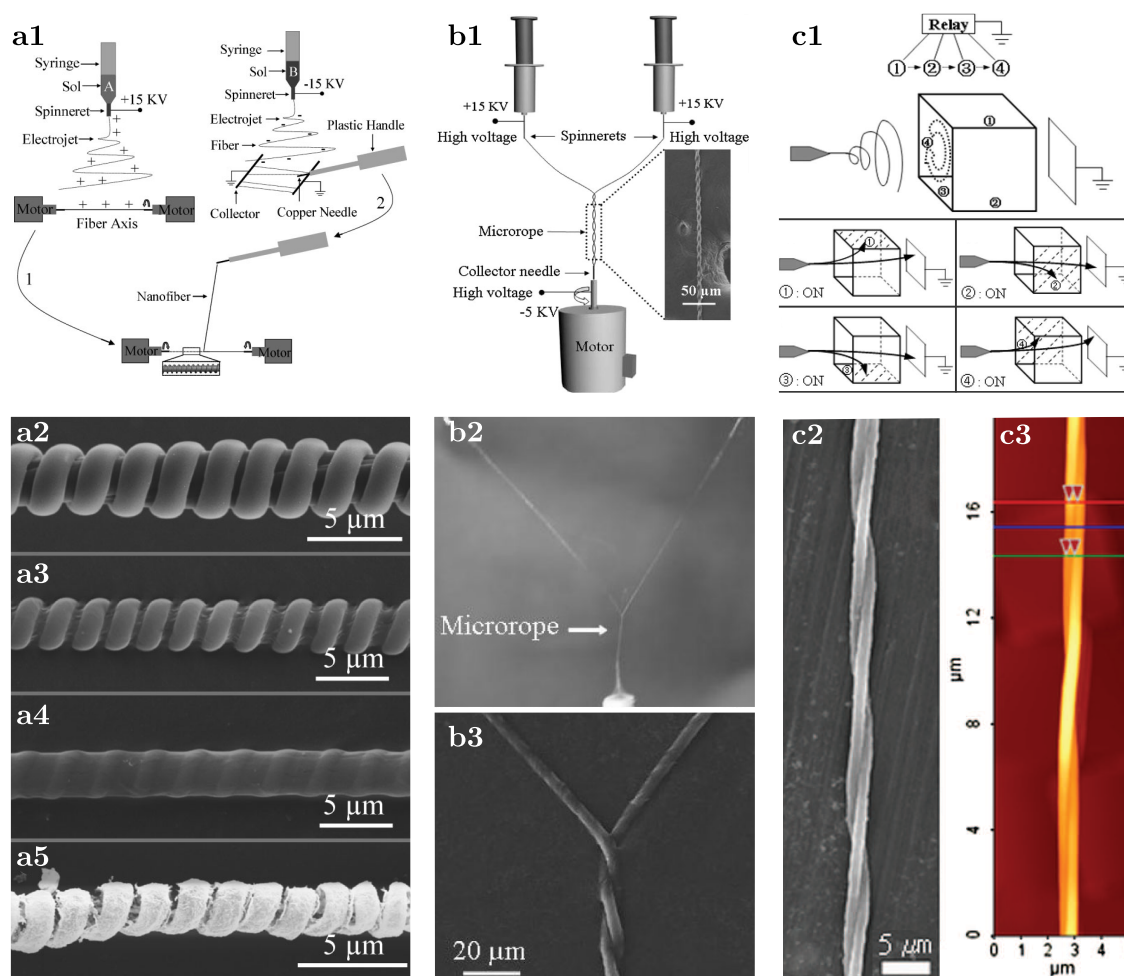
Figure 4.5: Helices obtained by filament twisting. **(a) and (b)** Rotating motors were used as represented in the schemes to produce electrospun helical filaments.[44], [45] (a1) Fibres from solution A were spun on two rotating copper needles, creating a dense bundle; fibres from solution B were spun onto parallel electrodes and, afterwards, transferred into the rotating bundle; (a2) to (a5) SEM images of the helical filaments (a2) after being collected by the target, after and subjected to different treatments are shown in (d). (b1) Micro rope production apparatus. (b2) Fibres are spun from two different spinnerets and collected by a rotating needle. (b3) SEM image showing the fibre.[45] (c1) Scheme showing the production of helical fibres using a rotating electric field. (c2) SEM and (c3) AFM pictures of the twisted fibres obtained.[46] Image (a) is reprinted from Chang et al.[44] with permission from Wiley. Image (b) is reprinted from Chang et al.[45] with permission from Wiley. Image (c) is reprinted from Gu et al. [46] with permission from Elsevier.

Another procedure used to obtain helices by electrospinning was proposed by Trindade et al.[54] in which electrospun straight fibres were obtained and then treated in order to acquire intrinsic curvature. Two reactive pre-polymers were mixed and
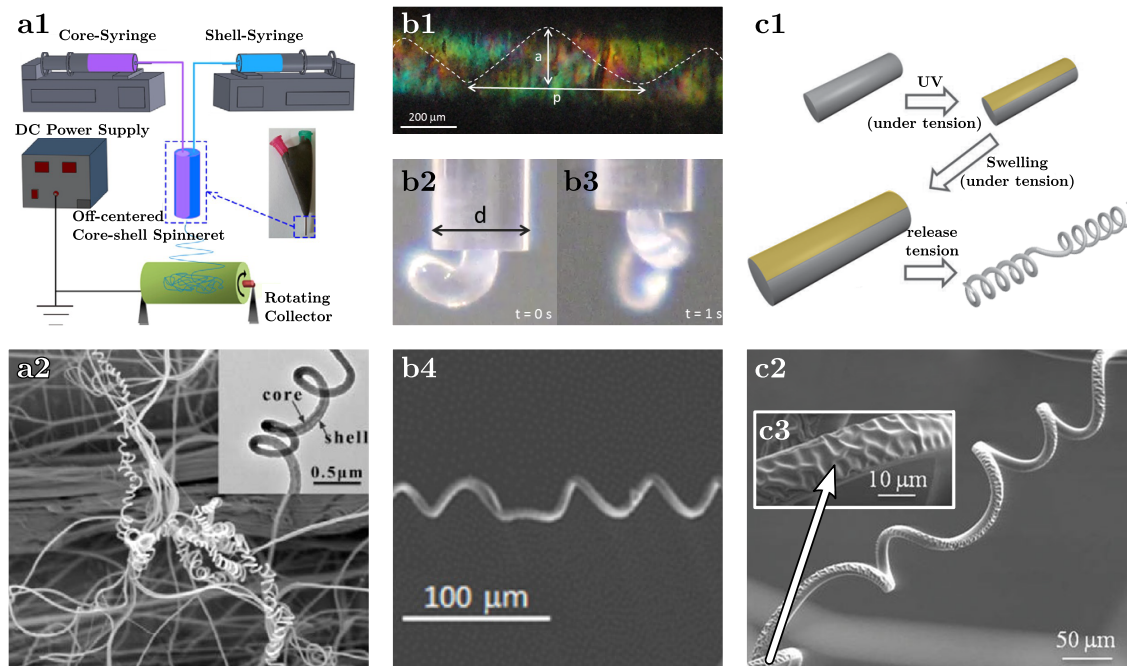
Figure 4.6: Helices obtained by asymmetric contraction in three different techniques. (a1) co-electrospinning scheme[50] used to obtain off centred fibres and (a2) meshes of helical fibres obtained; (b1) Optical microscope picture taken between cross polars of a sheared liquid crystalline cellulosic solution in a capillary glass tube showing an helical defect running along the main axis of the tube; (b2) and (b3) images capturing a time sequence of the jet escaping the capillary for solutions with the same shear rate;[62] (b4) single fibre obtained; (c1) Method involving UV irradation of electrospun fibres which curl and wrinkle, after swelling.[54] (c2) SEM images of the helical fibres with (c3) with wrinkles. Image (a) is reprinted from Wu et al.[50] with permission from the American Chemical Society. Image (b) is adapted from Canejo et al.[62] with permission from the Multidisciplinary Digital Publishing Institute. Image (c) is adapted from Trindade et al. [54] with permission from Wiley.

electrospun to generate straight elastic filaments onto a collector formed by two metallic parallel wires. The formed filaments need to have reactive sites, along their main axis, that can be activated to form a thin top layer with different mechanical properties from the bulk, as schematically shown in Fig. 4.6c1. For the system described in literature this requirement was achieved by the existence of double bonds that were activated by UV light. Releasing the stretched filaments generated helices. The filaments develop a half-wrinkled surface by swelling and drying, putting in evidence the existence of an imprinted UV layer (see Fig. 4.6c2 and c3).

4.5.1 Adding dimensions to the shaping of electrospun filaments

One common occurrence in the helical electrospun fibres obtained in the previously discussed techniques consists in the presence of regions with inversion of handedness. These regions are also known as perversions [2], [64], [65] and can be readily observed in Fig. 4.6b4 and c2. Perversions link helices with opposite directions of twisting. For instance, when straight fibres acquire intrinsic curvature and are allowed to relax, at a critical point they undergo a buckling instability due to the asymmetric contraction. This instability causes the fibre to coil into a helical shape, reducing the bending energy at the cost of increasing the torsion energy. If both fibre ends are fixed, the coiling of the fibre will generate a perversion to preserve the total twist constant, $\mathrm{Wr} + \mathrm{Tw} = \mathrm{constant}$, where Wr is the total writhe and Tw the total twist of the fibre.[66]

Recently, Huang et al.[67] and Liu et al.[68] demonstrated that helical structures containing multiple perversions can emerge in a strip by asymmetric contraction, using two elastomers of different lengths. This is illustrated in Fig. 4.7a. The shorter red strip was stretched to be the same length as the blue strip. While the stretching force P is maintained, the two strips were glued side-by-side. Then, as the force is slowly released, the bi-strip twists and bends to generate helices intercalated with perversions. They coined strips with these shapes as hemihelices.

Similar shapes can be reproduced with electrospun fibres. Moreover, with the selective irradiation with UV light of electrospun polymeric microfibres (Fig. 4.7b), it was possible to enlarge the diversity of possible shapes filaments can adopt Fig. 4.7c.[69] Indeed, Silva et al.[55] showed that by irradiating successive portions of a filament at different relative angles, a wider range of perversions exists which behave differently during coiling and after release. In Fig. 4.7b two extreme cases are presented. If the pre-straining is applied only in one side along the filament, when a perversion appears helices on the sides are mirror images of each other. By contrast, if instead of an uniform modification, the pre-strain is applied on alternate sides of the filament, as represented in Fig. 4.7b, the shape of the perversion and the relative symmetry of the helices is changed. These two extreme types of inversions where designated as symmetric and antisymmetric perversions. After being released, the shapes adopted by the filaments are also very different. In the first case, an angle appears between adjacent helices, while for antisymmetric perversions helices remain aligned.

The existence of perversions with this diversity, the possibility to "print" in specific positions and the impact they have on filament shapes, opens a wide range of possibilities
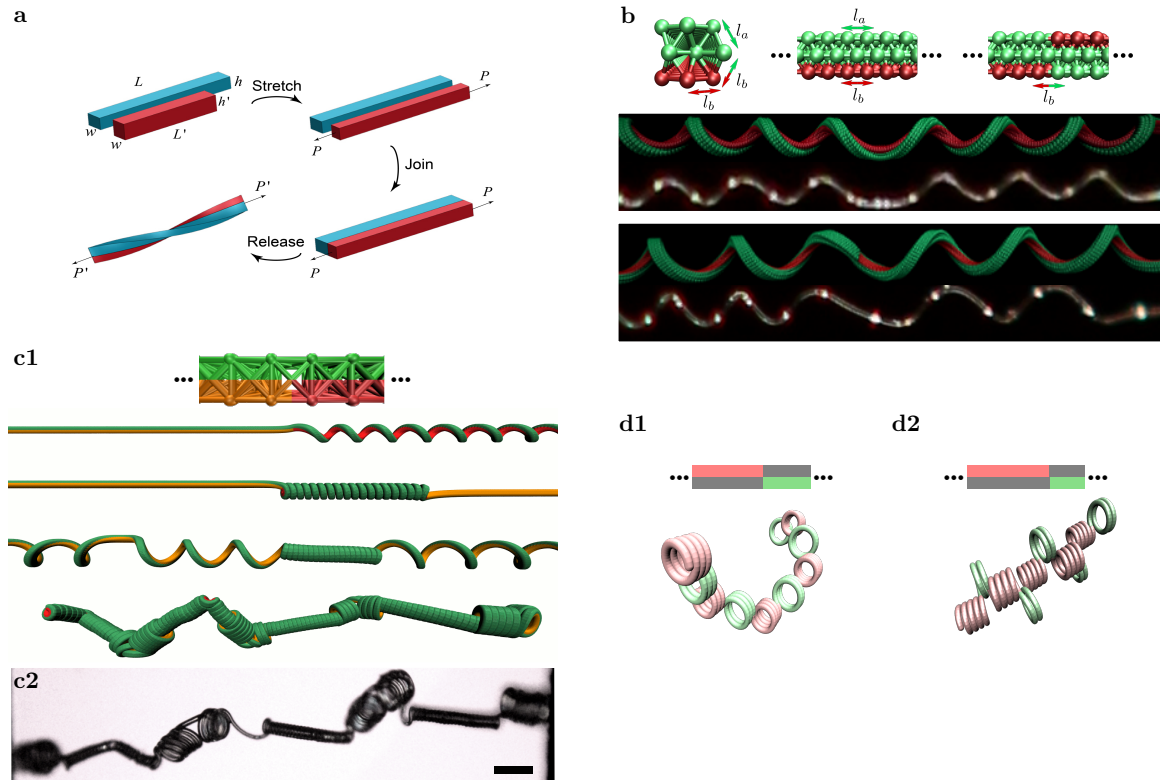
Figure 4.7: Simulation of helices with perversions . (a) Generation of twist from untwisted initial elastic blue and red strips.[68] The final intrinsic curvature of the filament results from gluing the two ribbons after stretching the red ribbon until it reaches the same length as the blue strip. (b1) Hexagonal beads arrangement used in simulations: the beads were connected by two harmonic potentials, denoted a (red) and b (green), with equilibrium bond distances, l_a and l_b.[55] (b2) Front view at the position where symmetric and (b3) antisymmetric perversions occur. (c1) Arrangement of the beads along the filament connected by three different harmonic potentials indicated by the colours. (c2) Optical microscope image of electrospun fibres with alternate exposure times.[69] (d1) and (d2) simulation of two fibres with the same intrinsic curvature but pre-strained on different places, as indicated by the colours. Image (a) is reprinted from Liu et al.[68] with permission from PLOS. Image (b) is reprinted from Silva et al.[55] with permission from Nature Publishing Group. Image (c) is reprinted from Silva et al.[69] with permission from Wiley.

for shaping single filaments. In this respect, computational modelling can be particularly useful since it allows studying, beforehand, the final design. In fact, Silva et al.[55] used molecular dynamics simulations to study the dynamics of elastic filaments and obtained good qualitative agreement between the filament shapes predicted by numerical simulations and observed experimentally (Fig. 4.7b andc). Silva et al. modelled elastic fibres by considering arrangements of beads bonded by harmonic potentials as shown in Fig. 4.7b and c. To generate filaments with intrinsic curvature, asymmetric contraction

was modelled by changing the equilibrium bond distances of the beads in one side of the filament. The intrinsic curvature was selected using a relation between the intrinsic curvature, K, and the pre-strain of the filament, χ:

$$K = \frac{1}{w}\frac{8\chi}{5(2+\chi)+1},\tag{4.1}$$

where w is the fibre cross-section width. In this study, simulations were deterministic and did not include temperature effects. Filaments were released at a constant rate, maintaining the ends fixed and for a high enough pre-strain, helical structures containing perversions were generated, as can be observed in Fig. 4.7b.

Silva and Godinho[69] obtained richer shapes with electrospun filaments. Now, shaping an electrospun filament gains extra dimensions because it becomes possible to change not only the helical radius, through the irradiation intensity, but also their length by selecting the irradiated portions, or the filament final shape, by choosing the type of perversion. In this sense it is possible to envisage the production of filaments with complex structures, for instance, helices made of helices Fig. 4.7d1, or wires made of misaligned helices Fig. 4.7d2.

4.6 Conclusions and Outlook

Inspiration from biological systems has been a fruitful approach to solve many technological problems. By combining the best of material science with an understanding of how nature solved similar problems, it has been possible to design new methodologies to produce materials with different properties. Helices are a smart shape commonly observed in nature. They offer additional flexibility and cohesion to materials and the possibility to develop motility strategies. Therefore, it is natural that researchers made an effort to tailor filaments with these shapes which could confer advantageous macroscopic properties to materials.

Electrospinning is a very versatile technique which allows the production of helical fibres by different methodologies. The examples highlighted here discuss the main procedures and mechanisms that can be used to synthetically shape helical microfibres. Here, we reviewed the progress made to produce different types of helical structures with electrospinning. Three main procedures were identified for the production of helices: (1) by mechanical buckling instabilities, when the fibres are impinged on the collectors and a high deformation occurs; (2) by twisting motion, when the fibres are twisted by the action of external mechanical or electric fields; (3) by asymmetric contraction, when the helices occur by the existence of a mismatch of the elastic properties between different

regions of the fibre. Unlike other techniques that require, for instance, the existence of molecular chirality to obtain helical structures, electrospinning can be adapted to use a wide range of different polymeric materials for the production of helical filaments.

Electrospun helical filaments are at the of non-woven membranes with enhanced permeation and mechanical characteristics, which is attributed to the high surface/volume ratio introduced by the helical filaments. These features can improve current applications such as the large-area sorption and reuse of crude oil from the ocean or industry. The outer side walls of helices can be activated with specific phobic materials and protecting the inner content and increase the efficiency on drug release of micro and nano assemblies.

References

[1] P. E. S. Silva, F. Vistulo de Abreu, and M. H. Godinho, "Shaping helical electrospun filaments: A review," *Soft Matter*, 2017. DOI: 10.1039/C7SM01280B.

[2] A. Goriely and M. Tabor, "Spontaneous Helix Hand Reversal and Tendril Perversion in Climbing Plants," *Physical Review Letters*, vol. 80, no. 7, pp. 1564–1567, Feb. 16, 1998. DOI: 10.1103/PhysRevLett.80.1564.

[3] McMillen and Goriely, "Tendril Perversion in Intrinsically Curved Rods," *Journal of Nonlinear Science*, vol. 12, no. 3, pp. 241–281, 2002. DOI: 10.1007/s00332-002-0493-1.

[4] S. J. Gerbode, J. R. Puzey, A. G. McCormick, and L. Mahadevan, "How the Cucumber Tendril Coils and Overwinds," *Science*, vol. 337, no. 6098, pp. 1087–1091, Aug. 31, 2012. DOI: 10.1126/science.1223304. pmid: 22936777.

[5] H. B. Lillywhite, *How Snakes Work: Structure, Function and Behavior of the World's Snakes.* Oxford ; New York: Oxford University Press, 2014, 241 pp.

[6] P. S. Sadeghian and C. Santos, "Two new species of *Carcinonemertes* (Hoplonemertea: Carcinonemertidae) living in association with leucosiid crabs from California and Tasmania," *Journal of Natural History*, vol. 44, pp. 2395–2409, 37-40 Sep. 22, 2010. DOI: 10.1080/00222933.2010.505014.

[7] W. Gao, X. Feng, A. Pei, C. R. Kane, R. Tam, C. Hennessy, and J. Wang, "Bioinspired Helical Microswimmers Based on Vascular Plants," *Nano Letters*, vol. 14, no. 1, pp. 305–310, Jan. 8, 2014. DOI: 10.1021/nl404044d.

[8] M. H. Godinho, J. P. Canejo, G. Feio, and E. M. Terentjev, "Self-winding of helices in plant tendrils and cellulose liquid crystal fibers," *Soft Matter*, vol. 6, no. 23, pp. 5965–5970, Nov. 17, 2010. DOI: 10.1039/C0SM00427H.

[9] J. W. Shaevitz, J. Y. Lee, and D. A. Fletcher, "Spiroplasma Swim by a Processive Change in Body Helicity," *Cell*, vol. 122, no. 6, pp. 941–945, Sep. 23, 2005. DOI: 10.1016/j.cell.2005.07.004. pmid: 16179261.

[10] J. Moziconacci and C. Lavelle, *Computational Biology: New Research*. New York: Nova Science Publishers, 2009, 441 pp.

[11] A. Travers and G. Muskhelishvili, "DNA structure and function," *FEBS Journal*, vol. 282, no. 12, pp. 2279–2295, Jun. 1, 2015. DOI: 10.1111/febs.13307.

[12] S. Iamsaard, S. J. Aßhoff, B. Matt, T. Kudernac, J. J. L. M. Cornelissen, S. P. Fletcher, and N. Katsonis, "Conversion of light into macroscopic helical motion," *Nature Chemistry*, vol. 6, no. 3, pp. 229–235, Feb. 9, 2014. DOI: 10.1038/nchem. 1859.

[13] B. Jia, L. Yu, F. Fu, L. Li, J. Zhou, and L. Zhang, "Preparation of helical fibers from cellulose–cuprammonium solution based on liquid rope coiling," *RSC Advances*, vol. 4, no. 18, p. 9112, 2014. DOI: 10.1039/c3ra47031h.

[14] W. In-Hwang, H. Yanagida, and S. Motojima, "Vapor growth of carbon micro-coils by the Ni catalyzed pyrolysis of acetylene using rotating substrate," *Materials Letters*, vol. 43, pp. 11–14, 1-2 Mar. 2000. DOI: 10.1016/S0167-577X(99)00220-7.

[15] S. Ohsawa, S.-i. Sakurai, K. Nagai, M. Banno, K. Maeda, J. Kumaki, and E. Yashima, "Hierarchical Amplification of Macromolecular Helicity of Dynamic Helical Poly(phenylacetylene)s Composed of Chiral and Achiral Phenylacetylenes in Dilute Solution, Liquid Crystal, and Two-Dimensional Crystal," *Journal of the American Chemical Society*, vol. 133, no. 1, pp. 108–114, Jan. 12, 2011. DOI: 10.1021/ja1087453.

[16] J. Doshi and D. H. Reneker, "Electrospinning process and applications of electrospun fibers," *Journal of Electrostatics*, Selected papers from the special technical session "Electrostatics in Polymer Processing and Charge Monitoring", 1993 IEEE Industry Applications Society Meeting, vol. 35, no. 2, pp. 151–160, Aug. 1, 1995. DOI: 10.1016/0304-3886(95)00041-8.

[17] D. H. Reneker and A. L. Yarin, "Electrospinning jets and polymer nanofibers," *Polymer*, vol. 49, no. 10, pp. 2387–2425, May 13, 2008. DOI: 10.1016/j.polymer. 2008.02.002.

[18] D. Li and Y. Xia, "Electrospinning of Nanofibers: Reinventing the Wheel?" *Advanced Materials*, vol. 16, no. 14, pp. 1151–1170, Jul. 19, 2004. DOI: 10.1002/adma.200400719.

[19] D. Li and Y. Xia, "Direct Fabrication of Composite and Ceramic Hollow Nanofibers by Electrospinning," *Nano Letters*, vol. 4, no. 5, pp. 933–938, May 1, 2004. DOI: 10.1021/nl049590f.

[20] G. Wang, D. Yu, R. V. Mohan, S. Gbewonyo, and L. Zhang, "A comparative study of nanoscale glass filler reinforced epoxy composites: Electrospun nanofiber vs nanoparticle," *Composites Science and Technology*, vol. 129, pp. 19–29, Jun. 6, 2016. DOI: 10.1016/j.compscitech.2016.04.006.

[21] Z.-M. Huang, Y.-Z. Zhang, M. Kotaki, and S. Ramakrishna, "A review on polymer nanofibers by electrospinning and their applications in nanocomposites," *Composites Science and Technology*, vol. 63, no. 15, pp. 2223–2253, Nov. 2003. DOI: 10.1016/S0266-3538(03)00178-7.

[22] G. R. Mitchell, Ed., *Electrospinning*, RSC Polymer Chemistry Series, Cambridge: Royal Society of Chemistry, 2015.

[23] M. G. McKee, G. L. Wilkes, R. H. Colby, and T. E. Long, "Correlations of Solution Rheology with Electrospun Fiber Formation of Linear and Branched Polyesters," *Macromolecules*, vol. 37, no. 5, pp. 1760–1767, Mar. 1, 2004. DOI: 10.1021/ma035689h.

[24] D. Hermida-Merino, M. Belal, B. Greenland, P. Woodward, A. Slark, F. Davis, G. Mitchell, I. Hamley, and W. Hayes, "Electrospun supramolecular polymer fibres," *European Polymer Journal*, vol. 48, no. 7, pp. 1249–1255, Jul. 2012. DOI: 10.1016/j.eurpolymj.2012.04.015.

[25] G. Taylor, "Electrically Driven Jets," *Proceedings of the Royal Society A: Mathematical, Physical and Engineering Sciences*, vol. 313, no. 1515, pp. 453–475, Dec. 2, 1969. DOI: 10.1098/rspa.1969.0205.

[26] J. Pal, S. Sharma, S. Sanwaria, R. Kulshreshtha, B. Nandan, and R. K. Srivastava, "Conducive 3D porous mesh of poly(?-caprolactone) made via emulsion electrospinning," *Polymer*, vol. 55, no. 16, pp. 3970–3979, Aug. 2014. DOI: 10.1016/j.polymer.2014.06.067.

[27] R. R. Jose, R. Elia, M. A. Firpo, D. L. Kaplan, and R. A. Peattie, "Seamless, axially aligned, fiber tubes, meshes, microbundles and gradient biomaterial constructs," *Journal of Materials Science: Materials in Medicine*, vol. 23, no. 11, pp. 2679–2695, Nov. 2012. DOI: 10.1007/s10856-012-4739-7.

References

[28]   P. Katta, M. Alessandro, R. D. Ramsier, and G. G. Chase, "Continuous Electrospinning of Aligned Polymer Nanofibers onto a Wire Drum Collector," *Nano Letters*, vol. 4, no. 11, pp. 2215–2218, Nov. 1, 2004. DOI: 10.1021/nl0486158.

[29]   J. O. Cruickshank and B. R. Munson, "Viscous fluid buckling of plane and axisymmetric jets," *Journal of Fluid Mechanics*, vol. 113, no. -1, p. 221, Dec. 1981. DOI: 10.1017/S0022112081003467.

[30]   A. L. Huebner and H. N. Chu, "Instability and breakup of charged liquid jets," *Journal of Fluid Mechanics*, vol. 49, p. 361, 02 Sep. 1971. DOI: 10.1017/S002211207100212X.

[31]   W. Khoo and C. T. Koh, "A review of electrospinning process and microstructure morphology control," in *International Conference on Mechanical and Manufacturing Engineering (ICME2015)*, Oct. 4, 2015.

[32]   S.-H. Tan, R. Inai, M. Kotaki, and S. Ramakrishna, "Systematic parameter study for ultra-fine fiber fabrication via electrospinning process," *Polymer*, vol. 46, no. 16, pp. 6128–6134, Jul. 25, 2005. DOI: 10.1016/j.polymer.2005.05.068.

[33]   S. Megelski, J. S. Stephens, D. B. Chase, and J. F. Rabolt, "Micro- and Nanostructured Surface Morphology on Electrospun Polymer Fibers," *Macromolecules*, vol. 35, no. 22, pp. 8456–8466, Oct. 1, 2002. DOI: 10.1021/ma020444a.

[34]   A. Gholipour Kanani and S. H. Bahrami, "Effect of Changing Solvents on Poly(-Caprolactone) Nanofibrous Webs Morphology," *Journal of Nanomaterials*, vol. 2011, pp. 1–10, 2011. DOI: 10.1155/2011/724153.

[35]   A. L. Yarin, S. Koombhongse, and D. H. Reneker, "Bending instability in electrospinning of nanofibers," *Journal of Applied Physics*, vol. 89, no. 5, pp. 3018–3026, Mar. 2001. DOI: 10.1063/1.1333035.

[36]   D. G. Yu, C. Branford-White, K. White, N. P. Chatterton, L. M. Zhu, L. Y. Huang, and B. Wang, "A modified coaxial electrospinning for preparing fibers from a high concentration polymer solution," *Express Polymer Letters*, vol. 5, no. 8, pp. 732–741, 2011. DOI: 10.3144/expresspolymlett.2011.71.

[37]   D. S. Gomes, A. N. R. da Silva, N. I. Morimoto, L. T. F. Mendes, R. Furlan, and I. Ramos, "Characterization of an electrospinning process using different PAN/DMF concentrations," *Polimeros*, vol. 17, no. 3, pp. 206–211, Sep. 2007. DOI: 10.1590/S0104-14282007000300009.

[38]   D. Li, Y. Wang, and Y. Xia, "Electrospinning Nanofibers as Uniaxially Aligned Arrays and Layer-by-Layer Stacked Films," *Advanced Materials*, vol. 16, no. 4, pp. 361–366, Feb. 17, 2004. DOI: 10.1002/adma.200306226.

[39] K. W. Kim, K. H. Lee, M. S. Khil, Y. S. Ho, and H. Y. Kim, "The effect of molecular weight and the linear velocity of drum surface on the properties of electrospun poly(ethylene terephthalate) nonwovens," *Fibers and Polymers*, vol. 5, no. 2, pp. 122–127, Jun. 2004. DOI: 10.1007/BF02902925.

[40] J. Yu, Y. Qiu, X. Zha, M. Yu, J. Yu, J. Rafique, and J. Yin, "Production of aligned helical polymer nanofibers by electrospinning," *European Polymer Journal*, vol. 44, no. 9, pp. 2838–2844, Sep. 2008. DOI: 10.1016/j.eurpolymj.2008.05.020.

[41] S. P. Shariatpanahi, A. Iraji zad, I. Abdollahzadeh, R. Shirsavar, D. Bonn, and R. Ejtehadi, "Micro helical polymeric structures produced by variable voltage direct electrospinning," *Soft Matter*, vol. 7, no. 22, p. 10 548, 2011. DOI: 10.1039/c1sm06009k.

[42] T. Han, D. H. Reneker, and A. L. Yarin, "Buckling of jets in electrospinning," *Polymer*, vol. 48, no. 20, pp. 6064–6076, Sep. 21, 2007. DOI: 10.1016/j.polymer.2007.08.002.

[43] H.-Y. Kim, M. Lee, K. J. Park, S. Kim, and L. Mahadevan, "Nanopottery: Coiling of Electrospun Polymer Nanofibers," *Nano Letters*, vol. 10, no. 6, pp. 2138–2140, Jun. 9, 2010. DOI: 10.1021/nl100824d.

[44] G. Chang and J. Shen, "Helical Nanoribbons Fabricated by Electrospinning," *Macromolecular Materials and Engineering*, vol. 296, no. 12, pp. 1071–1074, Dec. 12, 2011. DOI: 10.1002/mame.201100060.

[45] G. Chang and J. Shen, "Fabrication of Microropes via Bi-electrospinning with a Rotating Needle Collector," *Macromolecular Rapid Communications*, vol. 31, no. 24, pp. 2151–2154, Dec. 15, 2010. DOI: 10.1002/marc.201000463.

[46] B. K. Gu, M. K. Shin, K. W. Sohn, S. I. Kim, S. J. Kim, S.-K. Kim, H. Lee, and J. S. Park, "Direct fabrication of twisted nanofibers by electrospinning," *Applied Physics Letters*, vol. 90, no. 26, p. 263 902, Jun. 25, 2007. DOI: 10.1063/1.2753109.

[47] B. Zhang, C. Li, and M. Chang, "Curled Poly(ethylene glycol terephthalate)/Poly(ethylene propanediol terephthalate) Nanofibers Produced by Side-by-side Electrospinning," *Polymer Journal*, vol. 41, no. 4, pp. 252–253, 2009. DOI: 10.1295/polymj.PJ2008270.

[48] S. Chen, H. Hou, P. Hu, J. H. Wendorff, A. Greiner, and S. Agarwal, "Effect of Different Bicomponent Electrospinning Techniques on the Formation of Polymeric Nanosprings," *Macromolecular Materials and Engineering*, vol. 294, no. 11, pp. 781–786, Nov. 12, 2009. DOI: 10.1002/mame.200900139.

[49] S. Chen, H. Hou, P. Hu, J. H. Wendorff, A. Greiner, and S. Agarwal, "Polymeric Nanosprings by Bicomponent Electrospinning," *Macromolecular Materials and Engineering*, vol. 294, no. 4, pp. 265–271, Apr. 14, 2009. DOI: `10.1002/mame.200800342`.

[50] H. Wu, Y. Zheng, and Y. Zeng, "Fabrication of Helical Nanofibers via Co-Electrospinning," *Industrial & Engineering Chemistry Research*, vol. 54, no. 3, pp. 987–993, Jan. 28, 2015. DOI: `10.1021/ie504305s`.

[51] C. Li, J. Wang, and B. Zhang, "Direct formation of "artificial wool" nanofiber via two-spinneret electrospinning," *Journal of Applied Polymer Science*, vol. 123, no. 5, pp. 2992–2995, Mar. 5, 2012. DOI: `10.1002/app.34944`.

[52] J. P. Canejo, J. P. Borges, M. H. Godinho, P. Brogueira, P. I. C. Teixeira, and E. M. Terentjev, "Helical Twisting of Electrospun Liquid Crystalline Cellulose Micro- and Nanofibers," *Advanced Materials*, vol. 20, no. 24, pp. 4821–4825, Dec. 17, 2008. DOI: `10.1002/adma.200801008`.

[53] M. H. Godinho, J. P. Canejo, L. F. V. Pinto, J. P. Borges, and P. I. C. Teixeira, "How to mimic the shapes of plant tendrils on the nano and microscale: Spirals and helices of electrospun liquid crystalline cellulose derivatives," *Soft Matter*, vol. 5, no. 14, pp. 2772–2776, Jul. 7, 2009. DOI: `10.1039/B821631B`.

[54] A. C. Trindade, J. P. Canejo, P. I. C. Teixeira, P. Patricio, and M. H. Godinho, "First Curl, Then Wrinkle," *Macromolecular Rapid Communications*, vol. 34, no. 20, pp. 1618–1622, Oct. 1, 2013. DOI: `10.1002/marc.201300436`.

[55] P. E. S. Silva, J. L. Trigueiros, A. C. Trindade, R. Simoes, R. G. Dias, M. H. Godinho, and F. V. de Abreu, "Perversions with a twist," *Scientific Reports*, vol. 6, p. 23 413, Mar. 30, 2016. DOI: `10.1038/srep23413`.

[56] G. I. Taylor, "Instability of jets, threads, and sheets of viscous fluid," in *Applied Mechanics*, M. Hetényi and W. G. Vincenti, Eds., Berlin, Heidelberg: Springer Berlin Heidelberg, 1969, pp. 382–388. DOI: `10.1007/978-3-642-85640-2_30`.

[57] B. Tchavdarov, A. L. Yarin, and S. Radev, "Buckling of thin liquid jets," *Journal of Fluid Mechanics*, vol. 253, no. -1, p. 593, Aug. 1993. DOI: `10.1017/S0022112093001910`.

[58] A. L. Yarin, *Free Liquid Jets and Films: Hydrodynamics and Rheology*, ser. Interaction of mechanics and mathematics series. Harlow, Essex: Longman Scientific & Technical, 1993, 446 pp.

[59] M. K. Jawed, F. Da, J. Joo, E. Grinspun, and P. M. Reis, "Coiling of elastic rods on rigid substrates," *Proceedings of the National Academy of Sciences*, vol. 111, no. 41, pp. 14 663–14 668, Oct. 14, 2014. DOI: 10.1073/pnas.1409118111.

[60] R. Kessick and G. Tepper, "Microscale polymeric helical structures produced by electrospinning," *Applied Physics Letters*, vol. 84, no. 23, pp. 4807–4809, Jun. 7, 2004. DOI: 10.1063/1.1762704.

[61] G. Chang, G. Song, J. Yang, R. Huang, A. Kozinda, and J. Shen, "Morphology control of nanohelix by electrospinning," *Applied Physics Letters*, vol. 101, no. 26, p. 263 505, Dec. 24, 2012. DOI: 10.1063/1.4773365.

[62] J. Canejo and M. Godinho, "Cellulose Perversions," *Materials*, vol. 6, no. 4, pp. 1377–1390, Mar. 28, 2013. DOI: 10.3390/ma6041377.

[63] J. Wu, S. Liu, L. He, H. Wang, C. He, C. Fan, and X. Mo, "Electrospun nanoyarn scaffold and its application in tissue engineering," *Materials Letters*, vol. 89, pp. 146–149, Dec. 15, 2012. DOI: 10.1016/j.matlet.2012.08.141.

[64] G. Domokos and T. J. Healey, "Multiple helical perversions of finite, intristically cuverd rods," *International Journal of Bifurcation and Chaos*, vol. 15, pp. 871–890, 03 Mar. 2005. DOI: 10.1142/S0218127405012430.

[65] A. Lazarus, J. T. Miller, M. M. Metlitz, and P. M. Reis, "Contorting a heavy and naturally curved elastic rod," *Soft Matter*, vol. 9, no. 34, pp. 8274–8281, Aug. 7, 2013. DOI: 10.1039/C3SM50873K.

[66] P. Pieranski, J. Baranska, and A. Skjeltorp, "Tendril perversion—a physical implication of the topological conservation law," *European Journal of Physics*, vol. 25, no. 5, p. 613, 2004. DOI: 10.1088/0143-0807/25/5/004.

[67] J. Huang, J. Liu, B. Kroll, K. Bertoldi, and D. R. Clarke, "Spontaneous and deterministic three-dimensional curling of pre-strained elastomeric bi-strips," *Soft Matter*, vol. 8, no. 23, p. 6291, 2012. DOI: 10.1039/c2sm25278c.

[68] J. Liu, J. Huang, T. Su, K. Bertoldi, and D. R. Clarke, "Structural Transition from Helices to Hemihelices," *PLOS ONE*, vol. 9, no. 4, e93183, 2014. DOI: 10.1371/journal.pone.0093183.

[69] P. E. S. Silva and M. H. Godinho, "Helical Microfilaments with Alternating Imprinted Intrinsic Curvatures," *Macromolecular Rapid Communications*, vol. 38, no. 5, p. 1 600 700, Mar. 2017. DOI: 10.1002/marc.201600700.

Chapter

5

Perversion with a twist
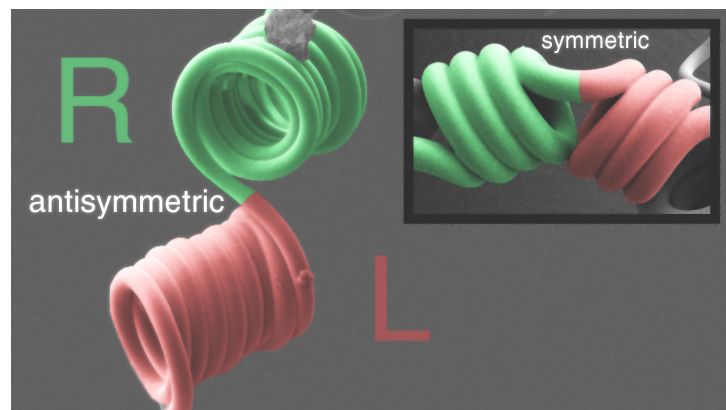
Abstract

Perversions connecting two helices with symmetric handedness are a common occurrence in nature, for example in tendrils. These defects can be found in our day life decorating ribbon gifts or when plants use tendrils to attach to a support. Perversions arise when clamped elastic filaments coil into a helical shape but have to conserve zero overall twist. We investigate whether other types of perversions exist and if they display different properties. Here we show mathematically and experimentally that a continuous range of different perversions can exist and present different geometries. Experimentally, different perversions were generated using micro electrospun fibres. Our experimental results also confirm that these perversions behave differently upon release and adopt different final configurations. These results demonstrate that it is possible to control on demand the formation and shape of microfilaments, in particular, of electrospun fibres by using ultraviolet light.

5.1 Introduction

The physical mechanisms controlling the shape of elastic filaments are still a matter of intense debate and new findings[2], [3]. Understanding the elastic behaviour of filamentary materials is very important given the observed diversity in nature[4], [5], the mounting interest in the context of nanotechnology[6]–[9] and the need to find simple mechanisms to produce and control the shape of filaments[10]–[13].

In particular, helical structures have drawn considerable attention. First, several different mechanisms have been proposed to explain their ubiquitous occurrence in nature. They could be formed by entropic forces [14], due to intrinsic torsion [15], [16] or buckling induced instabilities[17], [18]. Helical structures can also appear in different arrangements. For instance, proteins are well known for having complex structures, with helices intertwined with beta sheets or other less regular but equally well defined structures. Their organization is crucial for establishing protein function [19]. In polymer science, it is always a challenge to tune the shape of filaments. This can be accomplished by the action of diverse external stimuli such as temperature, polarity or metal ions[20].

Helical structures have been also obtained with a variety of techniques in nanotechnology. Helices in carbon nano-materials were first observed and reported as "an unusual occurrence" by Davis et. al[21] in 1953. Since then, many strategies have been devised to produce materials with different coiling. Chemical vapour deposition allows the production of high quantities of helices. The strategy consists in using an unequal extrusion of carbon from a catalyst surface[22]–[24]. This technique allows producing helical structures with different shapes simply by changing the catalyst grain morphology. Helices can also be grown by considering that catalyst particles are affected by van der Waals forces between the fibre and the surroundings, as in the work of Zhang et al.[25]. It has been advocated that these structures can find a wide range of applications, such as nanosprings[26], [27], electronic circuit components[28], [29] and in reinforcement composites[30].

Considerable work has also been done to obtain helical filaments by electrospinning. However, in many cases the helical structures become flattened as they land on the target[31]–[33]. This is not the case reported by Chen et al.[34], who produced coiled core-shell fibres by coaxial electrospinning. A simpler technique has been proposed by Trindade et al.[35], using ultraviolet (UV) irradiation upon the fibres. In both techniques it is the differential shrinkage of the elastomeric polymer that induces coiling due to buckling. In this work we will use a procedure adapted from the latter technique.

An interesting feature that can be observed in all these helical structures is the

inversion of the twisting direction, known as a perversion. Perversions appear also in plants when tendrils attach to a support and shorten to direct the plant towards the attachment point. Perversions arise when filaments curl having both ends clamped. In simple terms, perversions can be seen as structures connecting helices with opposite handedness.

Considerable work has been devoted to better understand perversions and its relevance. On the mathematical side, Goriely and Tabor [17] discussed the formation of a perversion in the presence of intrinsic curvature using Kirchhoff equations. Later, Domokos and Healey[36] obtained solutions in the presence of multiple perversions. The occurrence of multiple perversions was also studied both theoretically and experimentally by Huang et al.[37], who showed that a helical filament could display an arbitrary number of perversions depending on the pre-strain imposed on one side of a filament. Perversions arise also when torsion is externally applied on an elastic filament, as discussed by Lazarus et al.[3]. Finally, Gerbode et al.[2] used a simple experimental set-up to demonstrate the ubiquitously presence of perversions in tendril coiling. In all these works, perversions are described as having the same geometries and impinging the same elastic properties to the elastic filaments. Next, we will show that this view can be considerably enlarged.

5.2 Motivation

In this work we questioned whether tendril perversions are the only structures linking helices with opposite handedness. A simple theoretical argument suggests that other possibilities exist. Consider the example in Figure 5.1, where two helices with opposite handedness are linked by a perversion at the centre and the ends are held so that they do not rotate. Our analysis consists in reducing the complexity of the system to a set of two helices with opposite handedness linked at a single point. This linking point represents a region of the curve equidistant relatively to the centre of the perversion, perturbed by the presence of the perversion. Thus, outside this region the curve behaves approximately as two perfect helices. A simple way of describing helical curves uses the Frenet-Serret (FS) frame, $Q = [\mathbf{T}, \mathbf{N}, \mathbf{B}]$, where $\mathbf{T}$ is the unit vector tangent to the curve, $\mathbf{N}$ is the normal vector and $\mathbf{B}$ is the binormal vector given by the cross product of $\mathbf{T}$ and $\mathbf{N}$. The evolution of the FS frame along the curve can be written in terms of the Darboux vector, $\boldsymbol{\Omega}$, through the continuous differential equations $Q'_i = \boldsymbol{\Omega} \times Q_i$. Left and right handed helices have constant curvature, κ, and torsion, τ. They differ only on the Darboux vector, through a sign change in the torsion factor: $\boldsymbol{\Omega} = \kappa \mathbf{B} \pm \tau \mathbf{T}$.
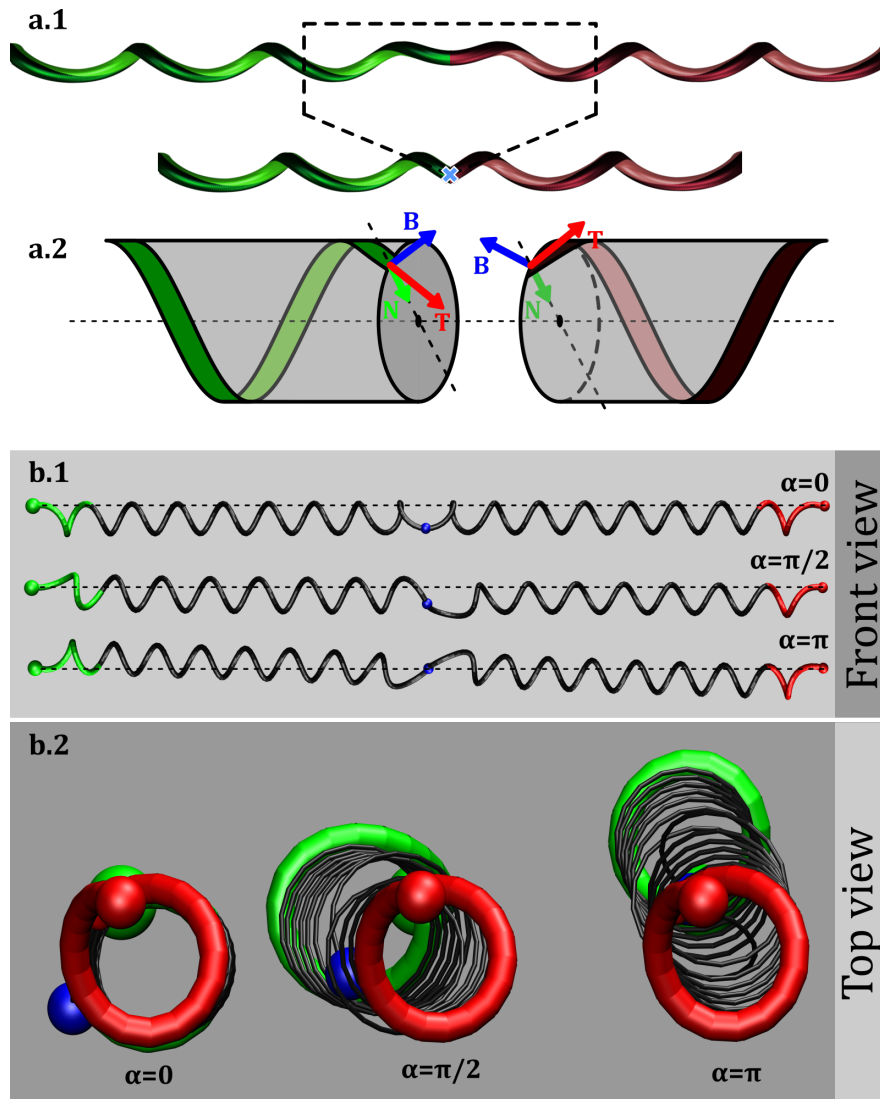
Figure 5.1: **Generalized perversions in helical filaments. a.1** Illustration of the simplification introduced in the model: the initial filament is reduced to three elements, two perfect helices with opposite handedness (right and left handed depicted in green and red respectively) and a perversion point (blue cross). **a.2** FS frames at the points connecting the perversion for a symmetric perversion, $\alpha = 0$. Front **b.1** and top **b.2** views of 3 types of perversions, with $\alpha = 0, \pi/2$ and π. In the front view, it is clear that symmetric perversions display an M shape and the filament is symmetric relatively to the axial plane passing through the perversion centre. By contrast, antisymmetric perversions, $\alpha = \pi$, display an N shape and are antisymmetric instead. The top view clearly shows that symmetric perversions keep the two helices axis remain steady while for antisymmetric perversions helices axis tilt relatively to the direction of release. For other perversions (for instance, with $\alpha = \pi/2$), a combination of the two effects occurs.

In our simplified model, these equations must be discontinuous at the linking point, and be capable of relating Darboux vectors and FS frames of the two helices, as illustrated in the example in Figure 5.1**a.2**. Since in any helix, normal vectors always point towards the centreline, the normal vector is perpendicular to the twisting vector which is always directed along the helix axis. In this particular case, the left helix tangent vector can be obtained from the right helix tangent vector by a rotation around the normal by 2θ, where θ is the angle between the tangent and the twisting vector. As a result, in the simplified model, the FS equations can be rewritten as:

$$Q_i' = (S\mathbf{\Omega}) \times (R_{\mathbf{N}, -2\theta} Q_i). \tag{5.1}$$

The only difference between this equation and the conventional FS equations is the application of the two transformations, $R_{\mathbf{N}, -2\theta}$ and S, at the perversion point. $R_{\mathbf{N}, -2\theta}$ denotes a rotation of the FS frame around the normal and S changes the handedness of the helix, $S\mathbf{\Omega} = S(\kappa\mathbf{B} + \tau\mathbf{T}) = \kappa\mathbf{B} - \tau\mathbf{T}$.

The important observation made in this work is that any further rotation of the FS frame around $\mathbf{\Omega}$ is still compatible with existence of a right helix with the opposite handedness. That is, we can generalize the previous equation to:

$$Q_i' = (S\mathbf{\Omega}) \times (R_{\mathbf{\Omega}, \alpha} R_{\mathbf{N}, -2\theta} Q_i). \tag{5.2}$$

Thus, $\alpha = 0$ corresponds to the description of perversions as are usually described. However, this equation suggests that other types of perversions can also exist. After the second rotation operating on the FS frame, the right helix conserves the same direction of the rotation axis but its position can change. On Figure 5.1**b** we illustrate filaments with different types of perversions. Different perversions induce different symmetry properties and different shapes (Figure 5.1**b**). For $\alpha = 0$ and $\alpha = \pi$, filaments are respectively symmetric and antisymmetric relatively to the axial plane passing through the perversion centre. For this reason, we named perversions with $\alpha = 0$ and $\alpha = \pi$ as symmetric and antisymmetric perversions.

Importantly, these symmetry properties are maintained also during force-extension experiments, as long as helices are aligned along the extensional axis. As a result, symmetric perversions will keep both helices axis aligned and the perversion rotates around the axis while the number of loops changes. By contrast, for antisymmetric perversions, the helices axis tilt relatively to the direction of release (see Figure 5.1**b.2** and supplementary materials **SM1**). When the number of loops in the helices changes during elongation, the perversion rotates around itself while its location remains static for antisymmetry to be maintained. More complex dynamics and configurations take place
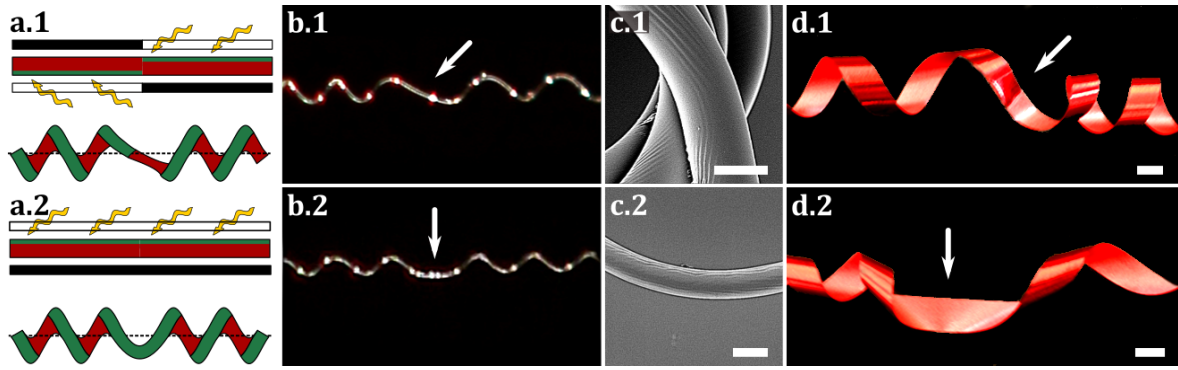
Figure 5.2: **Generation of antisymmetric and symmetric perversions.** **a** Sketches illustrating UV writing on fibres, for generation of **a.1** antisymmetric and **a.2** symmetric perversions. Elastic electrospun filaments after UV light exposition and fibre relaxation for **b.1** antisymmetric and **b.2** symmetric perversions. White arrows point to the perversion centres. **c** SEM pictures for the two perversion types. **c.1** In antisymmetric perversions wrinkles induced by UV light on the outer surface of the fibre changes side while **c.2** in symmetric perversions they remain on the same side. **d** The two types of perversions can be observed in gift-wrap ribbons. The antisymmetric perversion is obtained by glueing the opposite sides of two ribbon halves. Scale bar represent 5μm in **c** and 1cm in **d**.

for perversions with other α values. Nevertheless, in general terms, for $\alpha \neq 0$ helices axis are tilted and their axis locations are related by α. This can be understood taking into account that the total twist does not change during force-extension experiments since a moment is applied at both clamped ends [38]. Given that the twist developed by the two helices is symmetric, they cancel each other, and consequently the total twist of the filament, equal to α, remains for the total twist of the filament. This implies that FS frames at the ends of the filament are rotated by α around $\mathbf{\Omega}$, which establishes the different orientation of the helices.

The challenge reported in this paper has been to reproduce these generalized type of perversions. We focused on generating perversions with $\alpha = 0$ and $\alpha = \pi$, the two most distinctive types of perversions. Symmetric perversions appear naturally when filaments held on both ends twist to adopt a helical shape, as reported in [18], [38]. To generate antisymmetric perversions we noted, that after the $\alpha = \pi$ rotation, the normal vector switches direction. This implies that the bending of a filament at this point must change abruptly. This consideration offered a perspective on how to make materials with these properties: by intrinsically changing the curvature of filaments in specific regions. In the next section we describe how microfilaments with the two types of perversions were created. Afterwards we will further discuss the physical behaviour of these filaments.

5.3 Results

5.3.1 Writing the intrinsic curvature on microfilaments

Elastic microfilaments, with intrinsic curvature, were obtained from electrospun fibres produced from two pre-polymers with different functionalities (see Materials), which generate a crosslinking network after formation of the fibres. Two flat parallel electrodes were used to collect stretched fibres. If fibres are released at this point, no coiling is observed, but only bending due to gravity (see supplementary video **SV9**). Application of UV light established an asymmetry between the two sides of a filament by further crosslinking of the outer surface of the fibres double bonds, existing along one of the repetitive units[39]. In Figure 5.2**a**, sketches represent stretched fibres irradiated on opposite alternate sides (**a.1**) or on the same side (**a.2**) along the main axis of the filament. The higher crosslinking density at the top layer of the fibre relatively to the remaining soft material creates a differential shrinkage. This is responsible for the intrinsic curvature of the filament. This way we can write the outer surfaces of the stretched filaments with UV. Upon relaxation of the fibres clamped at both ends, coiling of the filaments creates helical structures separated by perversions which can exhibit different symmetries depending on the UV writing. In Figure 5.2**b.1** a spontaneous antisymmetric perversion appears in an elastic filament, treated as described in (**a.1**), after being released. The *N* shape of this antisymmetric perversion is clearly different from *M* of the (conventional) symmetric perversion in Figure 5.2**b.2**, for a filament irradiated only on one side (**a.2**).

The UV writing wrinkles the fibres surfaces as can be observed in Scanning Electron Microscopy (SEM) images (see Figure 5.2**c**). In filaments with antisymmetric perversions wrinkles switch side at the middle of the perversion, (**c.1**), while in filaments with symmetric perversions wrinkles are always on the same side (**c.2**). The same kind of antisymmetric perversions can be observed in gift ribbons (Figure 5.2**d**). After sweeping the dull side of the stripe with a scissors blade the ribbon acquires intrinsic curvature and forms a helix. Stretching while removing the loops of the strip, will lead to a straight configuration. The release of the ribbon with both ends clamped creates perversions with a visible switch of the helical handedness[40]. If the fibre is cut in two halves and glued together switching the two sides, an antisymmetric perversion appears as shown in Figure 5.2**d.1**. For a matter of comparison, a ribbon with a symmetric perversion is
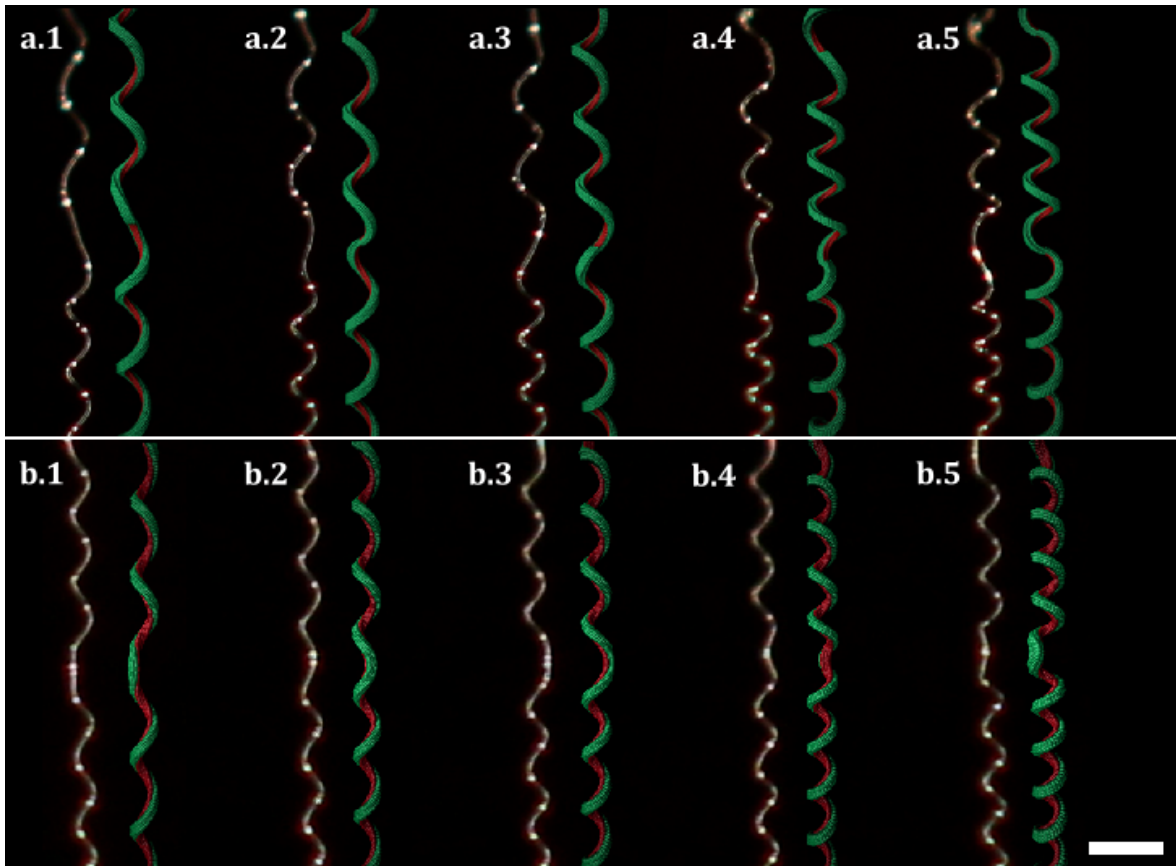
Figure 5.3: **Evolution of the shape of elastic filaments with intrinsic curvature upon release.** Photos taken from experimental fibres (left filaments) and from molecular dynamics simulations (right filaments), displaying how **a** antisymmetric and **b** symmetric perversions curl during release. Simulations describe qualitatively well the experimental behaviour of both fibres.

shown in Figure 5.2**d.2**.

5.3.2 Release of filaments with intrinsic curvature

Antisymmetric and symmetric perversions were 'printed' in the elastic stretched filaments as described in the methods section. Fibres were released at a controlled rate, with both ends constrained from rotating. In Figure 5.3, results obtained with a filament irradiated for 24h, initial length $L = 1$cm and diameter $D = 7\mu$m, are shown as well as results obtained with numerical simulations with physically plausible parameters. As shown in Figure 5.3, simulations reproduce well the coiling of the fibre in the presence of the perversion when the load decreases (see videos **SV2** and **SV5** in supplementary materials).

The movement of the filament during unloading must be compatible with the

symmetry of the perversion. Antisymmetric links force right and left helices to rotate in antiphase around the line connecting the two ends (Figure 5.3**a**). By contrast, the symmetric perversion promotes the rotation in phase of the two helices (Figure 5.3**b**). To further enlighten the difference in the movements in the presence of the two types of perversions, numerical simulations were performed leading to the detailed analysis in Figure 5.4. In this figure, the movement of two points, symmetrically disposed relatively to the perversion centre, is depicted and clearly shows that the two points move around the axis, defined by the two ends, either symmetrically or
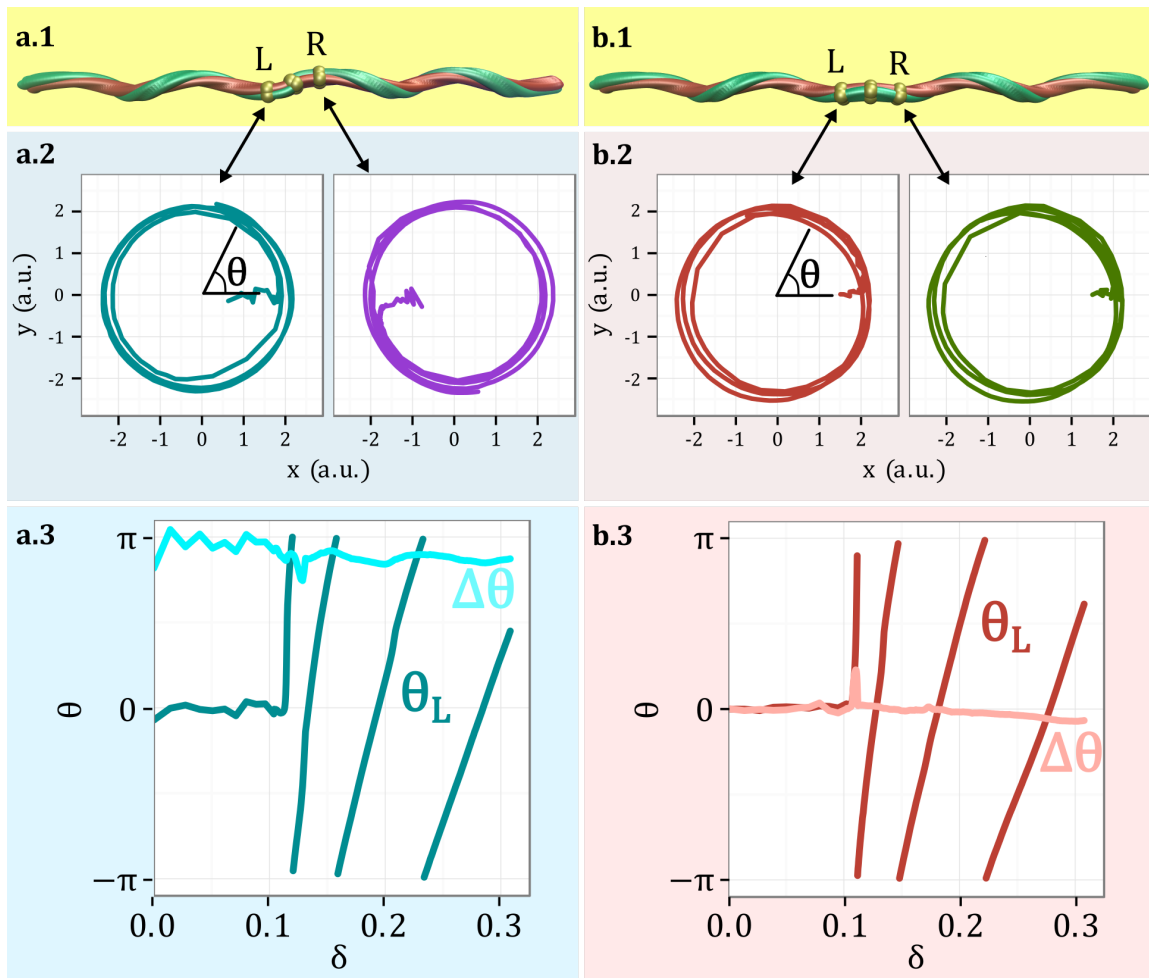
Figure 5.4: **Detailed analysis of the movement of two symmetric points close to the perversions centres during unloading. a** In antisymmetric perversions, the two points, designated by L (Left) and R (Right), move in opposite directions while **b** they move in the same direction in the symmetric perversion. Here θ represents the angular position in polar coordinates. These numerical results were obtained during fibre release, here parametrised by $\delta = \frac{L_0 - L_e}{L_0}$, where L_0 represents the initial fibre elongation and L_e the end-to-end distance. From **a.3** and **b.3** it is clear that upon release the phase difference, $\Delta\theta$, between the two points is approximately constant and equal to π or 0 for the antisymmetric or symmetric perversions, respectively.

antisymmetrically, in accordance with the perversion name. An interesting consequence of the antisymmetry property of the antisymmetric perversion, is that the point at the centre does not change position. This is also in agreement with our experimental observations and with the simplified model. Another interesting result, which is also in agreement with our experimental observations, is that the curling speed decreases with the unloading.

The dynamics observed in fibres with perversions is not the only distinctive feature. Equilibrium configurations are also conspicuously different. In Figure 5.5**a**, SEM pictures of unstrechted microfilaments written with the two types of perversion are shown. Symmetric and antisymmetric perversions are clearly different, a result that can also be readily observed either with ribbon strips or in numerical simulations. This shows that the difference between the two types of perversion is a robust result observable at different scales. In antisymmetric perversions helices remain aligned as a result of the fact that there is no bending at antisymmetric perversion centre. By contrast, symmetric perversions tend to bend the link between the two helices, creating an angle between them.

Finally, as antisymmetric perversions require a switch of the intrinsic bending properties, the perversion can only occur at specific locations. This also means that they should not be expected to be as ubiquitous in nature, but, on the other side, they can be engineered on demand. This contrasts with symmetric perversions which can travel along the material during their formation and hence have a more delocalised nature.

5.4 Materials and Methods

5.4.1 Materials

The elastic filaments were obtained from electrospinning by using a methodology similar to the one described previously in literature[35]. The elastic behaviour of the filaments was controlled by the relative amount of the pre-polymers used for preparing the starting solution. The first network was prepared from the reaction of poly(propylene oxide)-based triisocyanate-terminated prepolymer (PU) and hydroxyl-terminated polybutadiene (PBDO), the second crosslinking reaction on the top of the filaments was promoted by UV irradiation, according to the procedure and details described previously, for 40%w/w of PU and 60%w/w of PBDO[35]. The completion of the first reaction was achieved after the formation of the PU/PBDO electrospun fibres. The precursor solution with the two prepolymers, dissolved in toluene, was poured
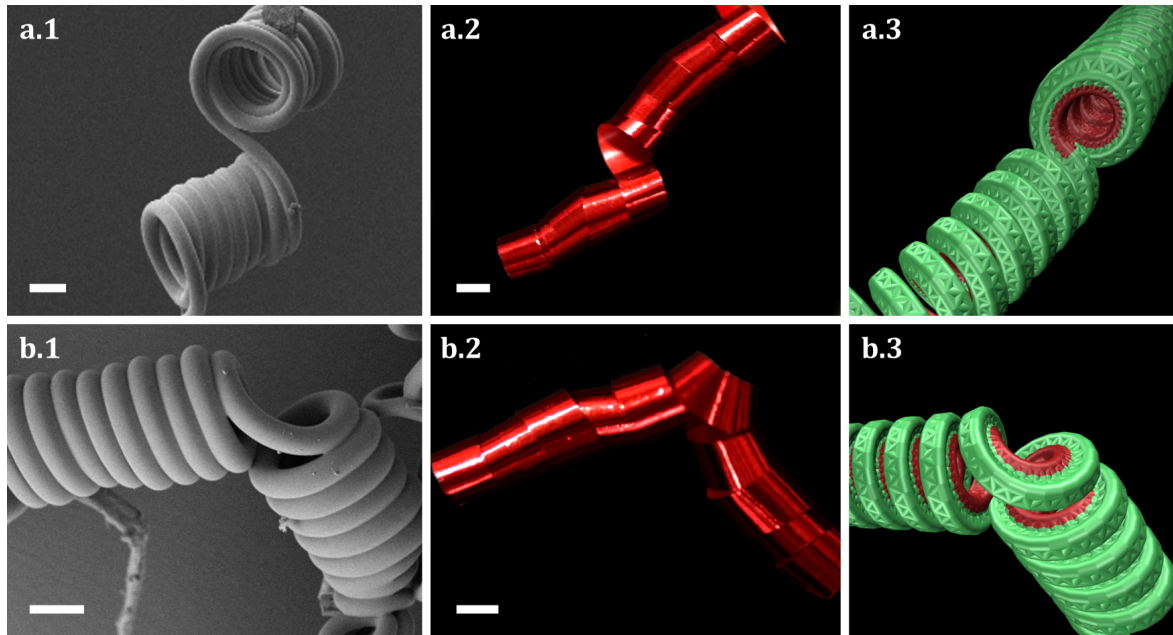
Figure 5.5: **Final configuration for helices connected by antisymmetric and symmetric perversions.** After complete relaxation of the elastic filament, the filaments adopt distinctive shapes. For antisymmetric perversions (top figures) helices remain aligned while they bend for symmetric perversions (bottom figures). Scale bar represent 10μm in **a** and 1cm in **b**.

into a 1ml syringe fitted with a 25-gauge needle and an infusion syringe pump (model KDS100) was used to control the solution feed rate (0.8ml h^{-1}). A conducting ring of 15cm diameter was held coaxially with the needle tip at its centre, and electrically connected to it and to the positive output of a high-voltage power supply (Glassman EL 30kV). The solution was accelerated towards a suspended collector target consisting of two parallel, flat metallic bars, by the action of an electric field applied between the syringe tip and the rotating target. A sample holder, made using acetate sheets cut with a precision cutting machine (Silhouette Portrait) was placed between the metallic bars. Optimal electrospinning conditions for this system were found to be: voltage at 14kV for a syringe tip-target separation of 15cm, relative humidity 70%. The filaments were UV irradiated ($\lambda = 254$nm, Intensity$=10^{-5}$mW/cm^2, lamp to sample distance $L_{UV} = 20$cm) during 24h and extracted for 24h (T=50° C) (Soxhlet extractor) in toluene, to remove the sol fraction, followed by drying in an oven for 48h at 50°, before being observed by SEM and POM (Polarized Light Microscopy). To produce symmetric perversions, fibres were irradiated with UV light only on one side of the surface. Antisymmetric perversions were produced irradiating the two sides of the fibre but on complementary regions using two irradiation cycles. In the first cycle, a mask made with an opaque card, cut with the precision cutting machine, protected sections

of the fibre from UV light. For the second irradiation cycle the sample was flipped and the complementary mask was used to apply UV light to the other side (see Figure 5.2**a** and illustration in supplementary materials **SM2**)

5.4.2 Unloading procedure and characterization of the microfilaments

The experimental observations of the unstretching of the filaments were made under axial loading. This was accomplished by using an extensometer from Rheometric Scientific (Minimat Firmware Version 3.1) coupled to a Canon EOS550D Camera equipped with a macro lens (EFS 60 mm). The lengths and diameters of individual filaments visible in these SEM images were measured with ImageJ software (version 1.48, http://imagej.nih.gov/ij/) and scaled according to the magnification quoted by the microscope software. Optical observations were achieved by using a reflection and transmission mode Olympus BX51 microscope equipped with an Olympus DP73 camera. SEM was used to image the morphology features of the elastic filaments with an Auriga crossbeam (SEM-FIB) workstation instrument (Carl Zeiss) equipped with an Oxford energy dispersive X-Ray spectrometer. The SEM images under the in-lens mode have been carried out with an acceleration voltage of 2kV and aperture size of 30μm. The substrates with filaments were glued on to aluminium stubs using a double-sided carbon tape and coated with a thin carbon layer (< 20nm) using a Q300T D Quorum sputter coater.

5.4.3 MD simulation

To study the dynamics of elastic filaments we developed molecular dynamics simulations using LAMMPS (Large-scale Atomic/Molecular Massively Parallel Simulator, http://lammps.sandia.gov) platform[41]–[43]. Elastic fibres were modelled by arranging beads in hexagonal close packed lattices (see SFig. 9 in supplementary materials **SM3**) bonded by harmonic potentials, $V_i = k_h/2(l - l_i)^2$, where k_h is the elastic constant and l_i the equilibrium bond distances. Filaments had initial length $L = 1200\sigma$ (LJ units, see http://lammps.sandia.gov/doc/units.html) and $\sqrt{3}$ by $\sqrt{3}\sigma$ of cross-section. Intrinsic curvature was produced by pre-straining one side of the rod. This was accomplished by changing the equilibrium bond distances as shown in supplementary materials **SM3**. Different helical curvatures were obtained by controlling the pre-strain amplitude. The intrinsic curvature was selected using the relation $K = \frac{1}{w}\frac{8\chi}{5(2+\chi)+1}$ (as discussed in Sup-

plementary Materials **SM3**), where w is the fibre cross-section width and χ is the initial pre-strain. Simulations were deterministic and did not include temperature effects. The integration of the equations of motion used a NVE integrator (Verlet/Leap-frog method) to update beads positions and velocities on each timestep (stepsize of $1 \times 10^{-3} \tau$). Helical structures were formed by releasing the filament at constant rate and with the ends set to not rotate. Different helical curvatures were established by controlling the pre-strain amplitude. To generate antisymmetric perversions the pre-strained side of the filament was changed at specific regions.

5.5 Conclusions

In this work we have proposed that a whole range of perversion geometries can exist in elastic filaments. We have given special attention to the demonstration that two extreme types of perversions, denominated symmetric and antisymmetric, exist in practice, and in particular at the microscale. These two perversion types exhibit distinct properties. Symmetric and antisymmetric perversions have different shapes (M or N), upon release they rotate around the centreline in or out of phase relatively to their centres and adopt different final configurations (bent or aligned). These properties were put in evidence through numerical and experimental work and are summarized in the supplementary video **SV1**.

Both types of perversions were reproduced with PU/PBDO electrospun filaments using irradiation with UV light. Irradiation with UV light was crucial to create an asymmetric contraction of the fibre relaxation through a higher crosslinking of the elastomer network. Irradiation of UV light on selected areas worked as a printing tool allowing to create antisymmetric perversions on demand. Our methodology can be applied to other type of elastic fibres only by playing selectively on the crosslink density across the filament. In this way, threads can be self-shaped to spontaneously produce symmetric or antisymmetric perversions linking right and left handed helices. Since linked helices adopt different configurations for the different perversions, perversions can be used to assemble fibres in different types of structures, which could find applications in nanotechnology or in the textile industry.

The study presented here focused on describing the new symmetry properties of these generalized type of perversions. Further studies are still necessary to describe their shape in detail, to enlighten how the different type of perversions appear, how they can coexist and interact, to analyse how stresses are distributed in fibres and how perversions may lend materials with new properties. Some of these issues we will pursue in future studies.

5.6 Supplementary Materials

SM1: Videos Overview and Legends

For a clearer understanding of the phenomena reported in this work we display a set of figures from accompanying videos and respective video legends.

Video **SV1**: Comparative overview of symmetric and antisymmetric perversions obtained in computer simulations, experiments with electrospun fibres and gift ribbons.
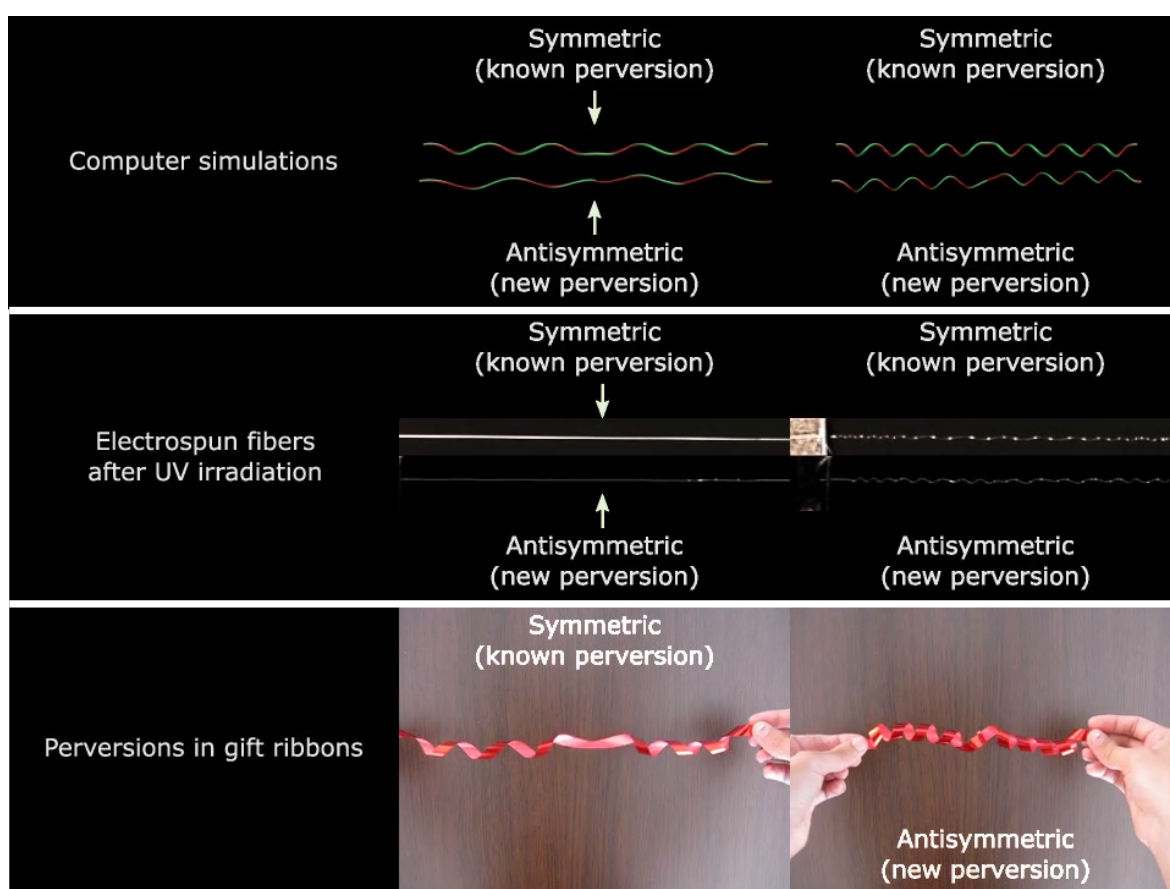

Figure 5.6: Snapshots from the video overviewing symmetric and antisymmetric perversions.

Video **SV2**: Simulations obtained releasing a pre-strained fibre with both ends fixed.
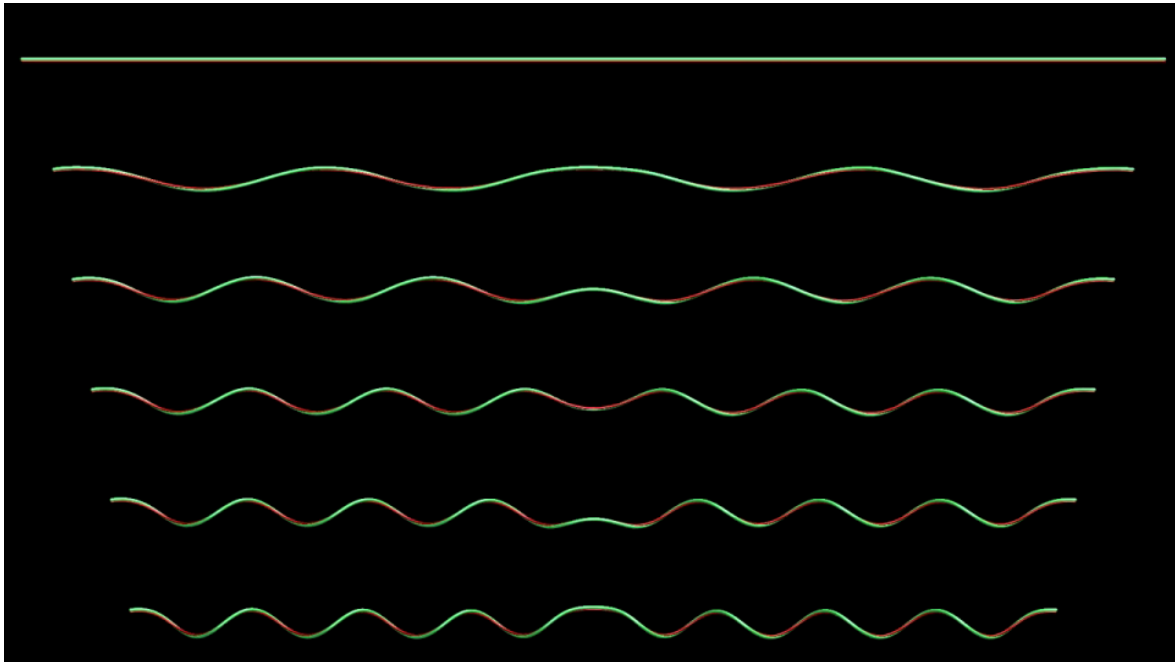
Figure 5.7: Sequence of images from supplementary video **SV2**. A symmetric perversion appears in the centre of the filament. Pre-straining is depicted in red.

Video **SV3**: Top view of the previous simulation **SV2**.
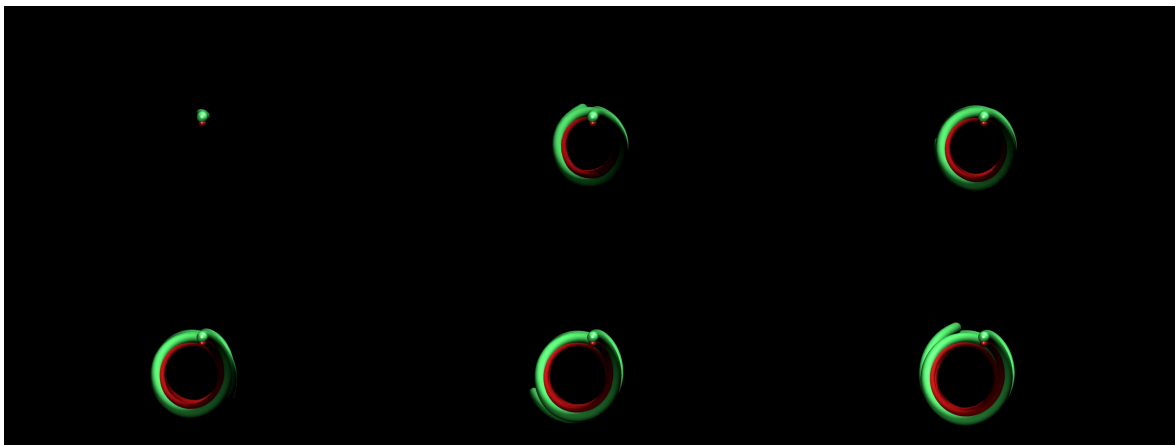
Figure 5.8: The top view shows the symmetric perversion revolving around the centreline of the filament (supplementary video **SV3**).
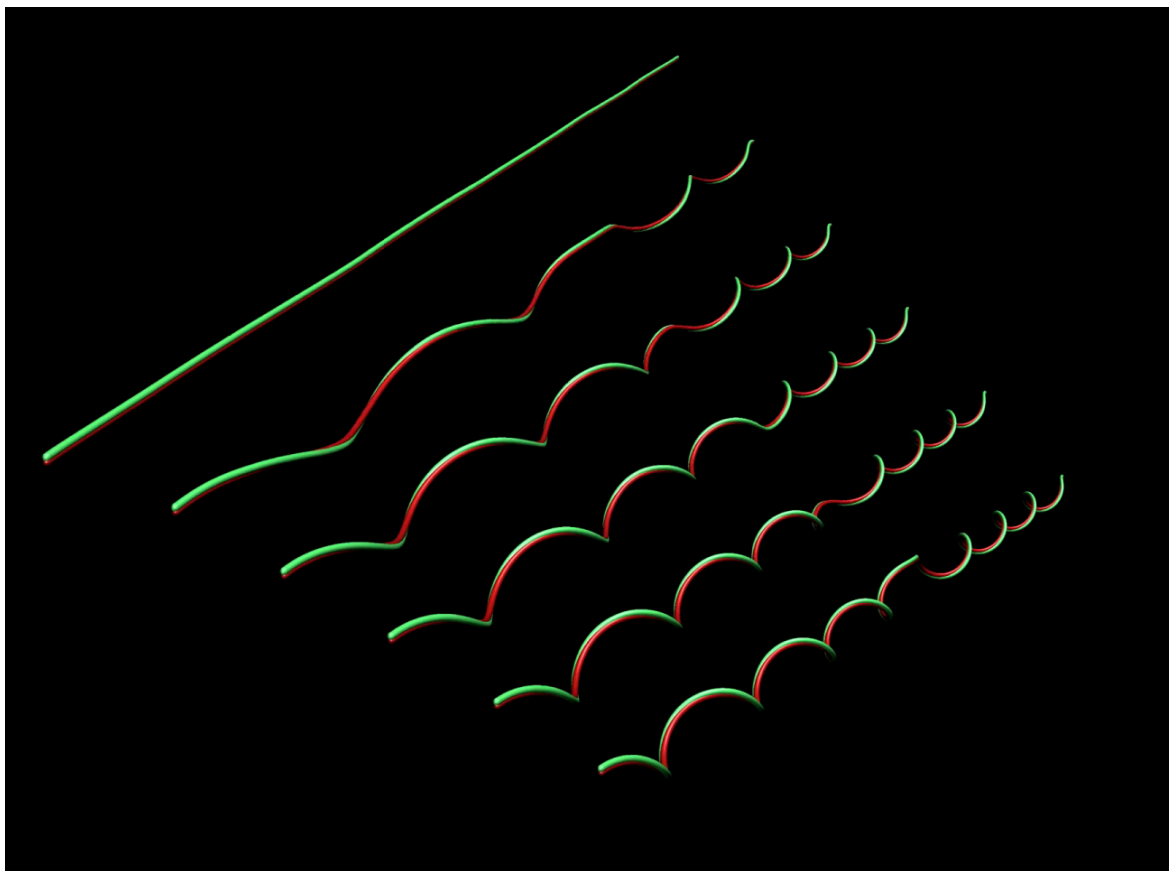
Video **SV4**: Another view of simulation **SV2**.

Figure 5.9: View from another angle of the same simulation steps illustrated in SFig. 5.7 (supplementary video **SV4**).

Video **SV5**: Simulations obtained releasing a pre-strained fibre with both ends fixed, but with a change in pre-straining in the middle of the fibre.
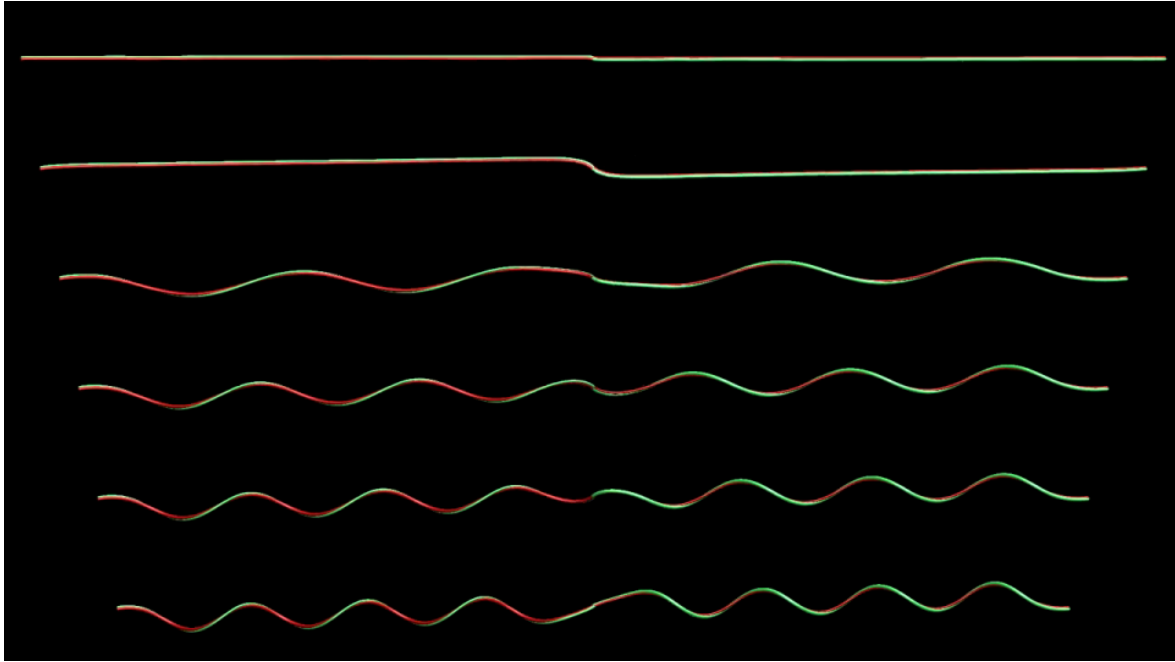

Figure 5.10: Sequence of images from supplementary video **SV5**. An antisymmetric perversion arises at the centre of the filament. In contrast to the symmetric case, the centre of the antisymmetric perversion remains aligned with the filament ends.

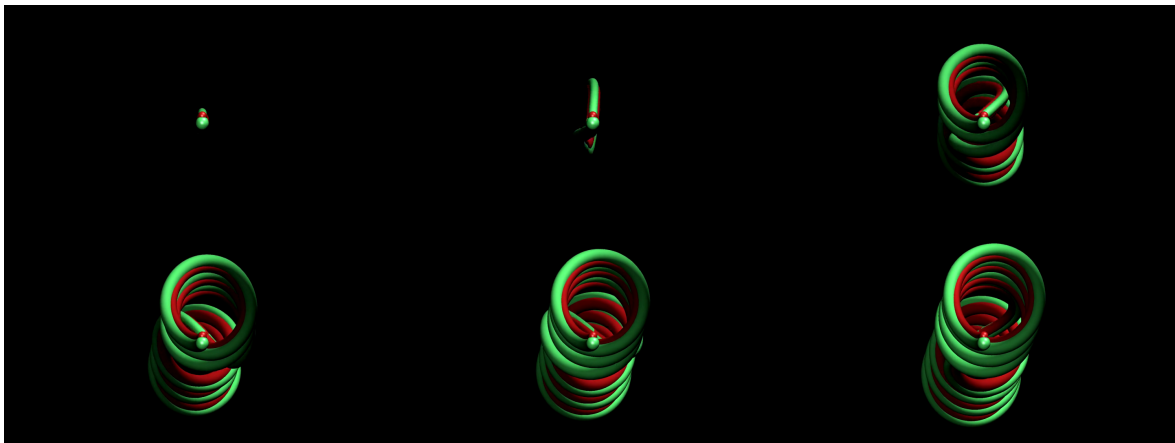Video **SV6**: Top view of the previous simulation **SV5**.

Figure 5.11: In antisymmetric perversions, helices centrelines on the two sides of the perversion are uncentred (supplementary video **SV6**).

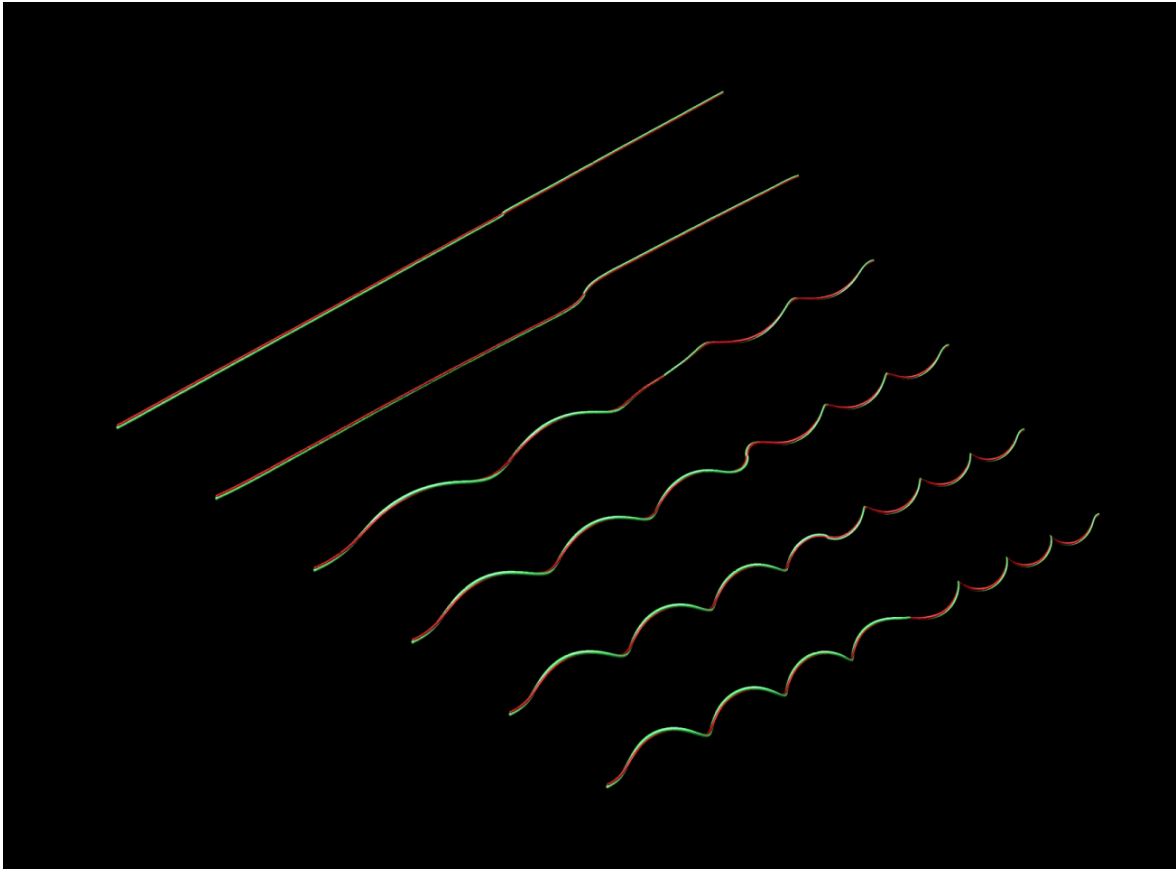Video **SV7**: Another view of simulation **SV5**.

Figure 5.12: View from another angle of the same simulation steps illustrated in SFig. 5.10 (supplementary video **SV7**).

Video **SV8**: View along helices centreline of simulation **SV5**.
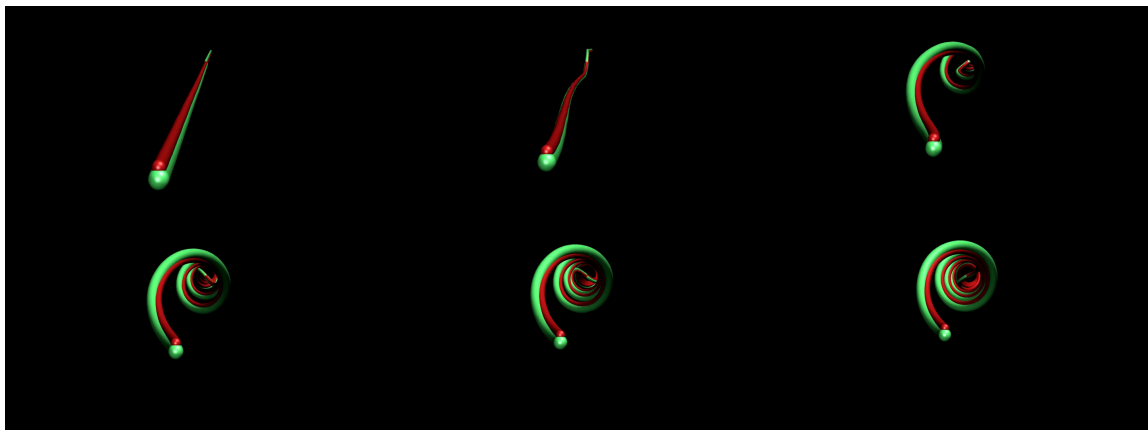

Figure 5.13: View along helices centreline of the same simulation steps illustrated in SFig. 5.10 (supplementary video **SV8**).

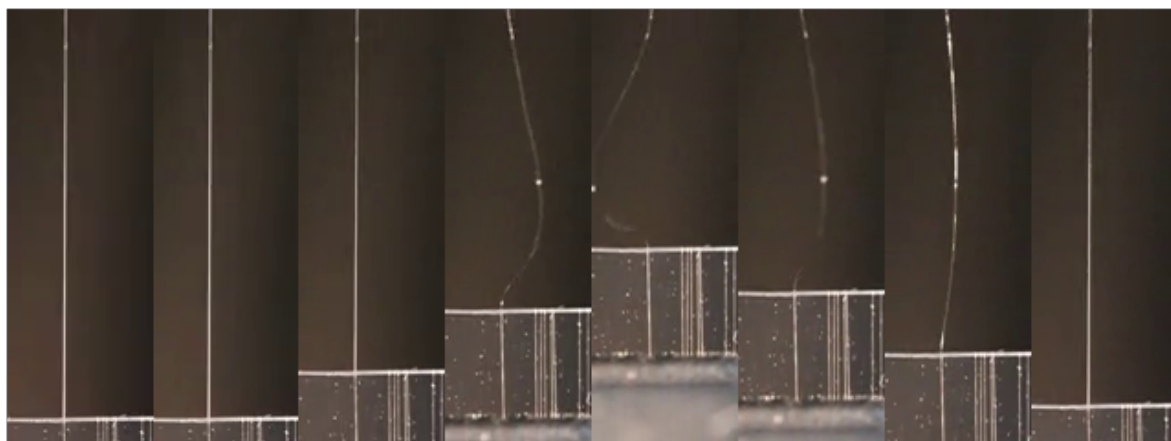Video **SV9**: Release and extension of a electrospun fibre with no UV irradiation.

Figure 5.14: Release of a polymeric fibre without UV irradiation. The fibre bends due to gravity but shows no sign of intrinsic curvature.

SM2: Experimental procedure

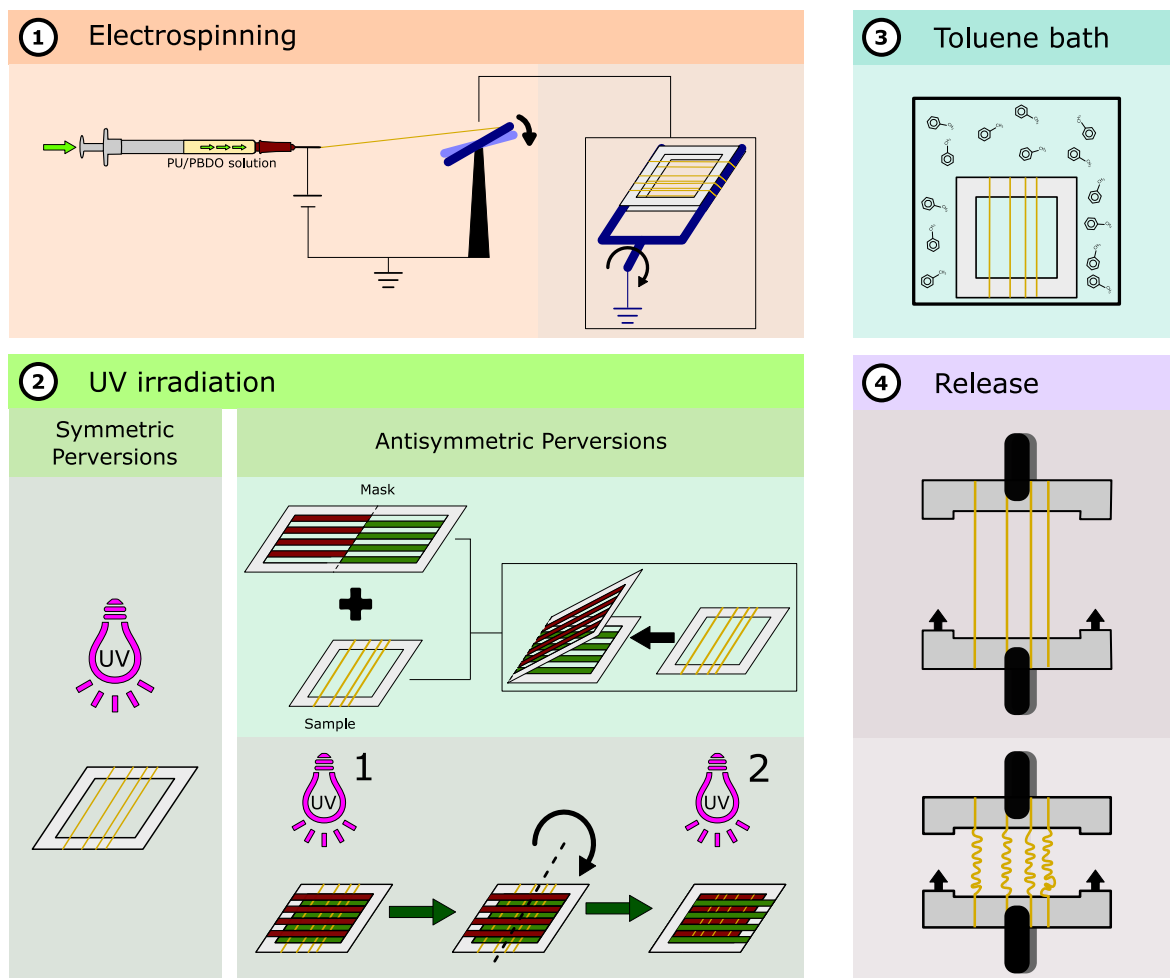In SFig. 5.15 the several steps involved in sample preparation are depicted.

Figure 5.15: **Schematic representation of the several experimental steps to produce polymeric fibres with symmetric and antisymmetric perversions.** ① A solution of PU/PBDO dissolved in toluene is accelerated towards a suspended collector target consisting of two parallel metallic bars by action of an electric field applied between the syringe tip and the rotating target. The gel point is achieved after the deposition of the fibres. ② To produce symmetric perversions, fibres are irradiated during 24h on one side with UV light. To produce antisymmetric perversions, two cycles of UV irradiation are applied sequentially on each side; masks protect complementary regions of the fibre from the irradiation. By the action of UV light in the presence of the air oxygen the double bonds of the PBDO were allowed to open and form an additional network on the top of the fibre. ③ UV-irradiated fibres are swollen in toluene for 24h (Soxhlet extractor) to remove the sol fraction. ④ After being dried, fibres are released at a controlled rate, with both ends constrained from rotating.

SM3: Simulations of perversions and relation to experiments

The model described in this paper provides a simple description of the different types of perversions. In order to provide additional evidence for the mechanism proposed to observe the different types of perversions we used LAMMPS (Large-scale Atomic/Molecular Massively Parallel Simulator) to model the dynamics of elastic filaments.

Microfilaments were formed using structures with cross-sections made of $N_w = 3$ by $N_h = 3$ beads along the width and height, respectively (see SFig. 5.16**a**). Beads were connected by two harmonic potentials, denoted a and b, with equilibrium bond distances, l_a and l_b, and illustrated in different colours in SFig. 5.16. For sufficiently unmatched bond distances (in our case, with $l_b < l_a$), one side of the filament becomes stretched relatively to the other, and upon release the filament gains a helical shape with an intrinsic curvature K, as well discussed in Liu et al.[18].
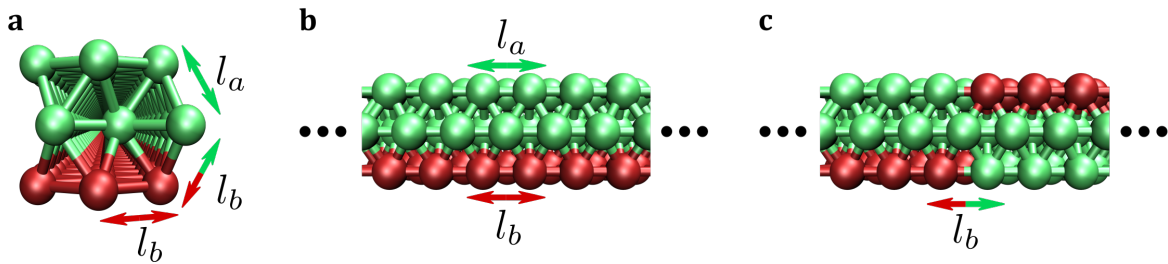

Figure 5.16: **Beads arrangement used in simulations. a** Arrangement of beads in a section displaying in different colors the different types of bonds. **b** and **c** Front view at the position where symmetric or antisymmetric perversions occur, respectively.

To create perversions, filaments were released starting with the initial length $L = L_a = (N-1)l_a$. This means that in the initial configuration only b bonds were pre-stretched, which agrees with the experimental set-up since only one side of the filament is irradiated with UV light. During release, ends are approached at constant rate along the same direction and without allowing rotations. For sufficiently large mismatches between l_a and l_b, one or more symmetric perversions appear as discussed previously[18]. To obtain antisymmetric perversions, a and b bonds alternate positions as shown in SFig. 5.16**c**. The same release procedure is used. Simulations were performed with time steps of $dt = 1 \times 10^{-3}$ in lj units.

In order to match the results obtained in simulations with the release experiments in **Fig. 3**, it was necessary to select three parameters as shown in Liu et al.[18]: the

appropriate mismatch between l_a and l_b, the filament length L_* and the cross-section width, $w = \sqrt{3}/2(N_w - 1)l_a$. According to elastic beam theory, the longitudinal strain ϵ at an arbitrary point on the cross section of two strips is given by:

$$\epsilon = \begin{cases} \dfrac{L_* + y\theta}{L_a} - 1, y > 0 \text{ for strip } a \\[3mm] \dfrac{L_* + y\theta}{L_b} - 1, y < 0 \text{ for strip } b \end{cases} \tag{5.3}$$

where $L_* = \theta/K$ and θ are the length and angle of the curve, respectively. Mechanical equilibrium of forces and momenta requires:

$$\int \sigma dA = \int_0^{w_a} \sigma_a h_a dy + \int_{-w_b}^0 \sigma_b h_b dy = 0 \tag{5.4}$$

$$\int \sigma y dA = \int_0^{w_a} \sigma_a y h_a dy + \int_{-w_b}^0 \sigma_b y h_b dy = 0 \tag{5.5}$$

In a linear elastic material the axial stress is given by $\sigma = E\epsilon$. In computational simulations we used $h_a = 2h$ and $h_b = h$, thus equations 5.4 and 5.5 become:

$$\int_0^{w_a} 2\left(\frac{L_* + y\theta}{L_a} - 1\right) dy + \int_{-w_b}^0 \left(\frac{L_* + \theta}{L_b} - 1\right) dy \tag{5.6}$$

$$\int_0^{w_a} 2\left(\frac{L_* + y\theta}{L_a} - 1\right) y dy + \int_{-w_b}^0 \left(\frac{L_* + y\theta}{L_b} - 1\right) y dy \tag{5.7}$$

$$\tag{5.8}$$

Neglecting the effect of the pre-strain on the width of fibres, then $w_a = w_b = w$, and hence we can write:

$$L_*\left(\frac{4}{L_a} + \frac{2}{L_b}\right) + \theta\left(\frac{2w}{L_a} - \frac{w}{L_b}\right) - 6 = 0 \tag{5.9}$$

$$L_*\left(\frac{6}{L_a} - \frac{3}{L_b}\right) + \theta\left(\frac{4w}{L_a} + \frac{2w}{L_b}\right) - 3 = 0 \tag{5.10}$$

Solving for L_* and θ, $K = \theta/L_*$ can be obtained giving:

$$K = \frac{1}{w}\frac{8\chi}{5(2 + \chi) + 1} \tag{5.11}$$

Intrinsic curvature is controlled by the pre-strain $\chi = L_a/L_b - 1$ applied to one side of the simulated fibre. SFig. 5.17 shows the variation of the curvature K with the pre-strain χ. Hence, for a given fibre of length L_* the number of loops can be selected by increasing or decreasing the curvature value matching experimental observations.
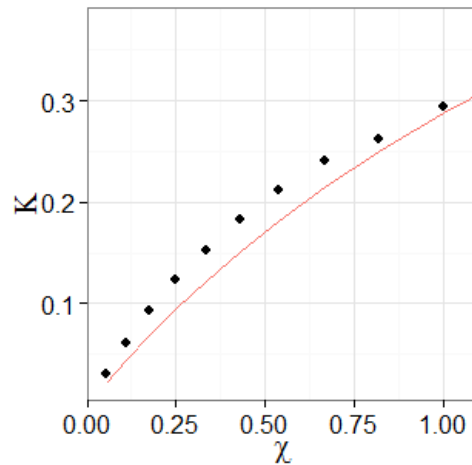
Figure 5.17: **Curvature K as a function of pre-strain χ.** Elastic filaments were simulated by using pre-strained layers with $\chi = L_a/L_b - 1$. Black markers represent the curvature obtained in numerical simulations. The red line corresponds to the prediction obtained from the linear model.

References

[1] P. E. S. Silva, J. L. Trigueiros, A. C. Trindade, R. Simoes, R. G. Dias, M. H. Godinho, and F. V. de Abreu, "Perversions with a twist," *Scientific Reports*, vol. 6, p. 23 413, Mar. 30, 2016. DOI: 10.1038/srep23413.

[2] S. J. Gerbode, J. R. Puzey, A. G. McCormick, and L. Mahadevan, "How the Cucumber Tendril Coils and Overwinds," *Science*, vol. 337, no. 6098, pp. 1087–1091, Aug. 31, 2012. DOI: 10.1126/science.1223304. pmid: 22936777.

[3] A. Lazarus, J. T. Miller, M. M. Metlitz, and P. M. Reis, "Contorting a heavy and naturally curved elastic rod," *Soft Matter*, vol. 9, no. 34, pp. 8274–8281, Aug. 7, 2013. DOI: 10.1039/C3SM50873K.

[4] Y. Forterre and J. Dumais, "Generating Helices in Nature," *Science*, vol. 333, no. 6050, pp. 1715–1716, Sep. 23, 2011. DOI: 10.1126/science.1210734.

[5] J.-S. Wang, G. Wang, X.-Q. Feng, T. Kitamura, Y.-L. Kang, S.-W. Yu, and Q.-H. Qin, "Hierarchical chirality transfer in the growth of Towel Gourd tendrils," *Scientific Reports*, vol. 3, no. 1, Dec. 2013. DOI: 10.1038/srep03102.

[6] Y. Sun, W. M. Choi, H. Jiang, Y. Y. Huang, and J. A. Rogers, "Controlled buckling of semiconductor nanoribbons for stretchable electronics," *Nature Nanotechnology*, vol. 1, no. 3, pp. 201–207, Dec. 2006. DOI: 10.1038/nnano.2006.131.

[7] N. Clauvelin, B. Audoly, and S. Neukirch, "Mechanical Response of Plectonemic DNA: An Analytical Solution," *Macromolecules*, vol. 41, no. 12, pp. 4479–4483, Jun. 2008. DOI: 10.1021/ma702713x.

[8] S. Singamaneni and V. V. Tsukruk, "Buckling instabilities in periodic composite polymeric materials," *Soft Matter*, vol. 6, no. 22, p. 5681, 2010. DOI: 10.1039/c0sm00374c.

[9] M. Yang and N. A. Kotov, "Nanoscale helices from inorganic materials," *Journal of Materials Chemistry*, vol. 21, no. 19, p. 6775, 2011. DOI: 10.1039/c0jm03028g.

[10] R. Dreyfus, J. Baudry, M. L. Roper, M. Fermigier, H. A. Stone, and J. Bibette, "Microscopic artificial swimmers," *Nature*, vol. 437, no. 7060, pp. 862–865, Oct. 6, 2005. DOI: 10.1038/nature04090.

[11] F. Vistulo de Abreu, R. G. Dias, and C. von Ferber, "Pseudo-knots in helical structures," *Soft Matter*, vol. 4, no. 4, p. 731, 2008. DOI: 10.1039/b719234g.

[12] W. Guo, M. Li, and J. Zhou, "Modeling programmable deformation of self-folding all-polymer structures with temperature-sensitive hydrogels," *Smart Materials and Structures*, vol. 22, no. 11, p. 115 028, Nov. 1, 2013. DOI: 10.1088/0964-1726/22/11/115028.

[13] S. Tibbits, "4D Printing: Multi-Material Shape Change," *Architectural Design*, vol. 84, no. 1, pp. 116–121, Jan. 2014. DOI: 10.1002/ad.1710.

[14] P. R. Bandaru, C. Daraio, K. Yang, and A. M. Rao, "A plausible mechanism for the evolution of helical forms in nanostructure growth," *Journal of Applied Physics*, vol. 101, no. 9, p. 094 307, May 2007. DOI: 10.1063/1.2723189.

[15] S. Armon, E. Efrati, R. Kupferman, and E. Sharon, "Geometry and Mechanics in the Opening of Chiral Seed Pods," *Science*, vol. 333, no. 6050, pp. 1726–1730, Sep. 23, 2011. DOI: 10.1126/science.1203874.

[16] Z. L. Wu, M. Moshe, J. Greener, H. Therien-Aubin, Z. Nie, E. Sharon, and E. Kumacheva, "Three-dimensional shape transformations of hydrogel sheets induced by small-scale modulation of internal stresses," *Nature Communications*, vol. 4, p. 1586, Mar. 12, 2013. DOI: 10.1038/ncomms2549.

[17] A. Goriely and M. Tabor, "Spontaneous Helix Hand Reversal and Tendril Perversion in Climbing Plants," *Physical Review Letters*, vol. 80, no. 7, pp. 1564–1567, Feb. 16, 1998. DOI: 10.1103/PhysRevLett.80.1564.

[18] J. Liu, J. Huang, T. Su, K. Bertoldi, and D. R. Clarke, "Structural Transition from Helices to Hemihelices," *PLOS ONE*, vol. 9, no. 4, e93183, 2014. DOI: 10.1371/journal.pone.0093183.

[19] F. A. Carey, *Organic Chemistry*. Boston [Mass.]; Montreal: McGraw-Hill Higher Education, 2008.

[20] S. Leiras, F. Freire, J. M. Seco, E. Quiñoá, and R. Riguera, "Controlled modulation of the helical sense and the elongation of poly(phenylacetylene)s by polar and donor effects," *Chemical Science*, vol. 4, no. 7, p. 2735, 2013. DOI: 10.1039/c3sc50835h.

[21] W. R. Davis, R. J. Slawson, and G. R. Rigby, "An Unusual Form of Carbon," *Nature*, vol. 171, no. 4356, pp. 756–756, Apr. 1953. DOI: 10.1038/171756a0.

[22] W. Wang and A. M. Rao, "Bulk Synthesis of Helical Coiled Carbon Nanostructures," *MRS Proceedings*, vol. 858, Jan. 2004. DOI: 10.1557/PROC-858-HH2.8.

[23] A. Shaikjee and N. Coville, "The effect of copper catalyst reducibility on low temperature carbon fiber synthesis," *Materials Chemistry and Physics*, vol. 125, no. 3, pp. 899–907, Feb. 2011. DOI: 10.1016/j.matchemphys.2010.09.009.

[24] Y. Wang, J. Xu, Y. Wang, and H. Chen, "Emerging chirality in nanoscience," *Chem. Soc. Rev.*, vol. 42, no. 7, pp. 2930–2962, 2013. DOI: 10.1039/C2CS35332F.

[25] L. Zhang, Y. Zhu, C. Ge, C. Wei, and Q. Wang, "The synthesis of carbon coils using catalyst arc discharge in an acetylene atmosphere," *Solid State Communications*, vol. 142, no. 9, pp. 541–544, Jun. 2007. DOI: 10.1016/j.ssc.2007.03.009.

[26] X. Chen, S. Zhang, D. A. Dikin, W. Ding, R. S. Ruoff, L. Pan, and Y. Nakayama, "Mechanics of a Carbon Nanocoil," *Nano Letters*, vol. 3, no. 9, pp. 1299–1304, Sep. 2003. DOI: 10.1021/nl034367o.

[27] H. Bi, K. C. Kou, K. (Ostrikov, J. Q. Zhang, and Z. C. Wang, "Mechanical model and superelastic properties of carbon microcoils with circular cross-section," *Journal of Applied Physics*, vol. 106, no. 2, p. 023 520, Jul. 15, 2009. DOI: 10.1063/1.3177324.

[28] G. Seifert, T. Köhler, and T. Frauenheim, "Molecular wires, solenoids, and capacitors by sidewall functionalization of carbon nanotubes," *Applied Physics Letters*, vol. 77, no. 9, pp. 1313–1315, Aug. 28, 2000. DOI: 10.1063/1.1289263.

[29] W. Jin, T. Fukushima, M. Niki, A. Kosaka, N. Ishii, and T. Aida, "Self-assembled graphitic nanotubes with one-handed helical arrays of a chiral amphiphilic molecular graphene," *Proceedings of the National Academy of Sciences*, vol. 102, no. 31, pp. 10 801–10 806, Aug. 2, 2005. DOI: 10.1073/pnas.0500852102.

[30] K.-t. Lau, M. Lu, and K. Liao, "Improved mechanical properties of coiled carbon nanotubes reinforced epoxy nanocomposites," *Composites Part A: Applied Science and Manufacturing*, vol. 37, no. 10, pp. 1837–1840, Oct. 2006. DOI: 10.1016/j.compositesa.2005.09.019.

[31] Y. Xin, Z. H. Huang, E. Y. Yan, W. Zhang, and Q. Zhao, "Controlling poly(p-phenylene vinylene)/poly(vinyl pyrrolidone) composite nanofibers in different morphologies by electrospinning," *Applied Physics Letters*, vol. 89, no. 5, p. 053 101, Jul. 31, 2006. DOI: 10.1063/1.2236382.

[32] M. K. Shin, S. I. Kim, and S. J. Kim, "Controlled assembly of polymer nanofibers: From helical springs to fully extended," *Applied Physics Letters*, vol. 88, no. 22, p. 223 109, May 29, 2006. DOI: 10.1063/1.2208689.

[33] J. Yu, Y. Qiu, X. Zha, M. Yu, J. Yu, J. Rafique, and J. Yin, "Production of aligned helical polymer nanofibers by electrospinning," *European Polymer Journal*, vol. 44, no. 9, pp. 2838–2844, Sep. 2008. DOI: 10.1016/j.eurpolymj.2008.05.020.

[34] S. Chen, H. Hou, P. Hu, J. H. Wendorff, A. Greiner, and S. Agarwal, "Polymeric Nanosprings by Bicomponent Electrospinning," *Macromolecular Materials and Engineering*, vol. 294, no. 4, pp. 265–271, Apr. 14, 2009. DOI: 10.1002/mame.200800342.

[35] A. C. Trindade, J. P. Canejo, P. I. C. Teixeira, P. Patricio, and M. H. Godinho, "First Curl, Then Wrinkle," *Macromolecular Rapid Communications*, vol. 34, no. 20, pp. 1618–1622, Oct. 1, 2013. DOI: 10.1002/marc.201300436.

[36] G. Domokos and T. J. Healey, "Multiple helical perversions of finite, intristically cuverd rods," *International Journal of Bifurcation and Chaos*, vol. 15, pp. 871–890, 03 Mar. 2005. DOI: 10.1142/S0218127405012430.

[37] J. Huang, J. Liu, B. Kroll, K. Bertoldi, and D. R. Clarke, "Spontaneous and deterministic three-dimensional curling of pre-strained elastomeric bi-strips," *Soft Matter*, vol. 8, no. 23, p. 6291, 2012. DOI: 10.1039/c2sm25278c.

[38] McMillen and Goriely, "Tendril Perversion in Intrinsically Curved Rods," *Journal of Nonlinear Science*, vol. 12, no. 3, pp. 241–281, 2002. DOI: 10.1007/s00332-002-0493-1.

[39] A. C. Trindade, J. P. Canejo, P. Patricio, P. Brogueira, P. I. Teixeira, and M. H. Godinho, "Hierarchical wrinkling on elastomeric Janus spheres," *Journal of Materials Chemistry*, vol. 22, no. 41, p. 22 044, 2012. DOI: 10.1039/c2jm35018a.

[40] P. Pieranski, J. Baranska, and A. Skjeltorp, "Tendril perversion—a physical implication of the topological conservation law," *European Journal of Physics*, vol. 25, no. 5, p. 613, 2004. DOI: 10.1088/0143-0807/25/5/004.

[41] S. Plimpton, "Fast Parallel Algorithms for Short-Range Molecular Dynamics," *Journal of Computational Physics*, vol. 117, no. 1, pp. 1–19, Mar. 1, 1995. DOI: 10.1006/jcph.1995.1039.

[42] W. M. Brown, P. Wang, S. J. Plimpton, and A. N. Tharrington, "Implementing molecular dynamics on hybrid high performance computers – short range forces," *Computer Physics Communications*, vol. 182, no. 4, pp. 898–911, Apr. 2011. DOI: 10.1016/j.cpc.2010.12.021.

[43] W. M. Brown, A. Kohlmeyer, S. J. Plimpton, and A. N. Tharrington, "Implementing molecular dynamics on hybrid high performance computers – Particle–particle particle-mesh," *Computer Physics Communications*, vol. 183, no. 3, pp. 449–459, Mar. 2012. DOI: 10.1016/j.cpc.2011.10.012.

Chapter

6

Helical Microfilaments with Alternating Imprinted Intrinsic Curvatures
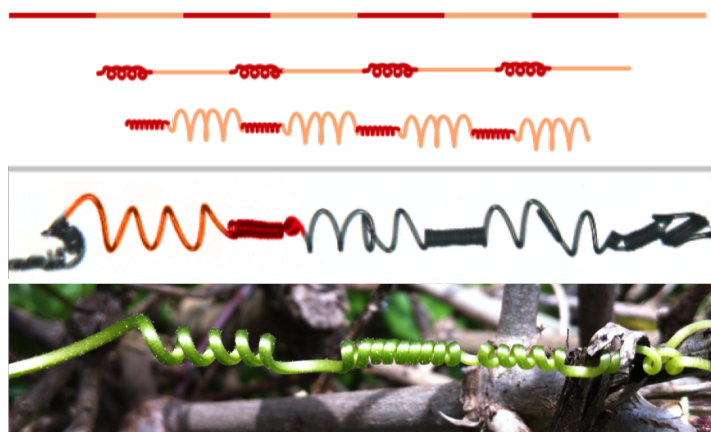
Abstract

There has been an intense research for developing techniques that can produce filaments with helical shapes, given the widespread of potential applications. In this work, how helices with different curvatures can be precisely imprinted in microfilaments is shown. It is also shown that using this technique, it is possible to produce, in a single fibre, helices with different curvatures. This striking and innovative behaviour is observed when one side of the stretched filaments is irradiated with UV light, modifying the mechanical properties at surface. Upon release, the regions with higher curvature start to curl first, while regions with lower intrinsic curvature remain stretched until start to curl later. The results presented here can be important to understand why structures adopt a helical shape in general, which can be of interest in nanotechnology, biomolecular science, or even to understand why plant filaments curl.

6.1 Introduction

Helical-shaped filaments are ubiquitous in nature at various scales ranging from tendrils with millimetric diameters to micrometric plant petiole tracheary elements[2]. The understanding of the mechanisms that lead elastic nature and manmade filaments, such as plant stems and polymer networks, to adopt a helical configuration is crucial to produce structures with specific helical geometries. In the case of plant tendrils, the helical pitch as well as the radius is not constant indicating the variation of the intrinsic curvature along the stem. In this work, we address the question: how would the response to stretch of a filament with different intrinsic curvatures along its length be changed in comparison with another with constant intrinsic curvature.

Configurable and adaptive fibres that can be tailored for specific materials and devices are desired for a variety of applications in many fields, such as textiles[3], [4], tissue engineering[5], [6], and nanotechnology[7], [8]. Given their dimensionality, fibres can adopt different configurations, such as straight or coiled, they can undergo large deformations[9], exhibit complex phenomena, like buckling leading to the formation of helices[10] or plectonemes[11], and be used as single fibres[12] or as complex meshes[13].

The helical configuration is, in numerous situations, a very good way of packing linear structures giving additional strength and flexibility to the fibres. Many natural structures adapted the helical form in different contexts and scales, from plant tendrils or seed pods[14]–[16] to macromolecules (DNA[17], [18] and proteins[19]–[21]). For instance, the seeds developed by filaree, a flowering plant, possess the ability to drill and bury themselves into the soil. The plant starts by projecting the seeds up to half a meter away. When the seeds reach the soil, their awns twist and untwist as a response to the variation of humidity, improving the chance of germination and survival[22], [23]. In this case, not only does the helical structure arises as a consequence of the twist of the awn, but it also allows the whole structure to be compact enough for the seed to bury itself in the ground. Frirdich et al.[24] removed one major component gene of the bacterial cell wall from the *Campylobacter jejuni*, a major cause of diseases in chickens, and observed the loss of helicity of the bacteria. Resulting mutant bacteria were about three orders of magnitude less effective in contaminating chick cells when compared to the wild type. The motility of the bacteria and other pathogenic attributes were negatively modified by the shape shifting, which may explain why some bacteria evolved to adopt more complex shapes besides spheres or rods. *Spiroplasmas* are bacteria that infect plants and insects and use their helical shape to move. However, the contraction and expansion of a helical filament is not enough to create translation in a microscopic environment. Additionally, the bacteria change their helical handedness spontaneously,

creating a region that inverts the helical twist, known as a perversion or a kink. This perversion can travel along the cell, breaking the symmetry of the movement and propelling the bacteria in a variety of environments with different viscosities[25], [26].

The occurrence of helicity may have different origins. Filaments with constant intrinsic bending and torsion are expected to adopt a helical shape, for instance, when a metallic spring is produced by applying a constant deformation to a straight wire on a lathe[27] or when a nylon thread is heated with a helical configuration, it will keep the same configuration after cooling[28]. Another less obvious case happens when plant tendrils attach to a support, one part of the tendril contracts asymmetrically along the filament and the different elastic properties between the tendril sides give rise to an intrinsic curvature that coils the filament[15]. In this case, fibres have no intrinsic torsion but, due to a constraint between the ends or due to self-contact, they form helical structures[10], [29]. Another example where helicity might occur is suggested by Kamien and co-worker[30] where a purely entropic approach is used to understand the occurrence of helical conformations in long molecular chains. In this case, filaments do not coil due to intrinsic properties of the material, but instead due to the surroundings of the filament. In this work, we use the properties of urethane/urea elastomers to produce helical microfilaments[31]. These elastomers contain functional carbon–carbon double bonds groups that open by UV light selective exposure creating a stiffer elastic surface. Similar to what happens in nature with plant tendrils, when these polymeric fibres are irradiated with UV light, the asymmetric contraction between the different regions of the filaments leads to the rise of helicity.

To produce thin micro and nanostructures, electrospinning is a simple and versatile technique. Electrospinning techniques do not require an expensive setup and basic setup includes a charged polymeric solution being ejected through a syringe by a pump in a high voltage differential. The electrostatic effects make it possible to obtain fibres with diameters several orders lower than the tip diameter, as well as different morphologies and arrangements of electrospun fibres. A looping behaviour typically occurs during the solution ejection due to bending instabilities[32]. However, the helical shape is generally not kept after fibres land the target. Using collectors with different configurations, such as a disk or a wire drum, fibres can be reorganized during the flight and aligned meshes are obtained[33], [34]. To achieve nonflat electrospun helical structures, one needs to create an intrinsic curvature along the fibre. For instance, Chen and co-workers[35] used coaxial tips to produce core–shell fibres that, due to the differential shrinkage between the layers, produced helices. A different strategy was used in this work. Fibres were irradiated with UV light to create a mismatch of elastic properties that lead fibres to coil.

Many works were dedicated to the study of elastic filaments and the generation of right- and left-handed helices connected by different kinds of perversions. In this work, we address the imprinting of different intrinsic curvatures not only in different filaments but also along the same filament. To perform this work, electrospun elastic microfilaments were obtained and computational simulations were used to understand the helical shapes of the filaments made experimentally.

6.2 Experimental Section

6.2.1 Materials

The electrospun fibres were obtained from a solution of poly(propylene oxide)-based triisocyanate-terminated prepolymer (PU) and hydroxyl-terminated polybutadiene (PBDO) in toluene, according to the procedure and details described previously, with a 40% w/w PU/60% w/w PBDO ratio[36]. The PU and PBDO prepolymers were dissolved in toluene, solid content 40%w/w, one drop of dibutyltin dilauryate catalyst was added, and the chemical reaction was allowed to occur during 1 h before inserting the reactive mixture in the syringe.

6.2.2 Electrospinning Experiment

The PU/PBDO microfibres were obtained from electrospinning by using a methodology similar to the one described previously in the literature[31]. The solution was poured into a 1 milliliter syringe fitted with a 25-gauge needle and an infusion syringe pump (model KDS100) was used to control the solution feed rate ($0.8 \, \text{mL} \, \text{h}^{-1}$). The syringe was connected to the positive output of a high-voltage power supply (Glassman EL 30 kV). A conducting ring with a radius of 15 cm was placed concentric with the needle tip and the solution was accelerated to a collector. The collector consisted of an acetate sheet placed in a cylindrical frame with a concentric metallic rod connected to the ground. Since the used solution displayed no chaotic behaviour, there was no need to use more complex collector geometry. A grid of squares with a width of 1 cm was cut in the acetate sheet using a precision cutting machine (Silhouette Portrait). The acetate sheets are flexible and easy to cut, and since there is residual toluene in the fibres when they are deposited in the sheet, both ends of the fibre merge and fix on the acetate. While the solution was being ejected, the suspended collector was rotating around its centreline (Figure 6.1**a**). The electrospinning conditions used for this system were: voltage at 14 kV, syringe tip-target separation of 15 cm, and relative humidity
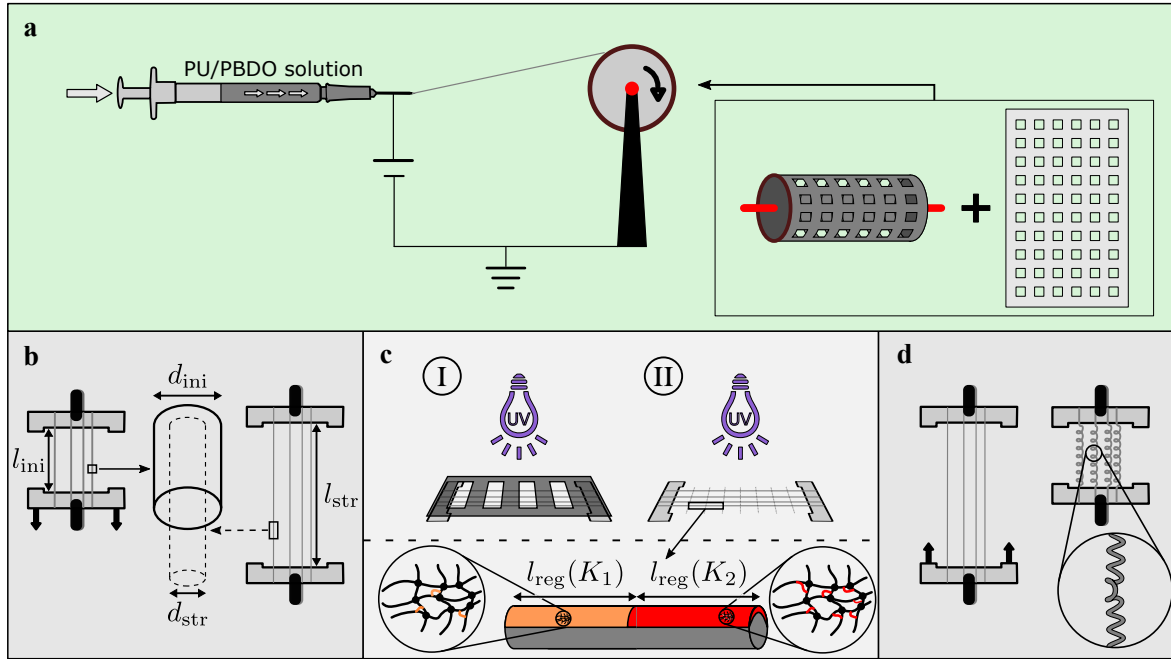
Figure 6.1: **Schematic representation of the experimental steps to produce helical fibres. a** PU/PBDO were dissolved in toluene and electrospun to a target consisting of an acetate sheet with a grid of squared holes cells supported by a cylindrical cardboard with a concentric metallic rod. **b** Cells with suspended fibres are stretched, decreasing filament radius and increasing contact area. **c** Fibres are irradiated with UV light, promoting a second crosslinking in the exposed area. To create alternated regions with different intrinsic curvatures, a first irradiation step is applied using a mask to partially cover the fibres (I) and afterwards all the top fibres are irradiated (II). **d** When cells are released, filaments start to coil due to the asymmetric contraction between irradiated and non irradiated parts.

50%.

6.2.3 UV Irradiation

A squared cell was cut from the target and stretched to three times the original size ($l_{\text{str}} = 3l_{\text{ini}}$) (Figure 6.1**b**). Thenceforth, the filaments were UV irradiated in one half of the surface ($\lambda = 254\,\text{nm}$, intensity $I = 10^{-5}\,\text{mW cm}^{-2}$, and lamp to sample distance $L_{\text{UV}} = 20\,\text{cm}$) for a range of times between 2 and 10 min. Fibres containing different intrinsic curvatures along their length were produced by irradiating parts of the fibre using two irradiation cycles (Figure 6.1**c**). In the first cycle, a mask made with an opaque card, cut with a precision cutting machine, protected sections of the fibre from UV light. For the second irradiation cycle, the mask was removed. Fibres were released and let to relax before being observed by scanning electron microscopy (SEM) and

polarized light microscopy (POM) (Figure 6.1**d**).

6.2.4 Scanning Electron Microscopy and Polarized Light Microscopy

The morphology of the filaments was investigated by means of SEM and POM. A Carl Zeiss Auriga crossbeam (SEM-FIB) workstation instrument and a Q150T ES Quorum sputter coater were used to obtain SEM images and to coat the samples with a carbon layer, respectively. The acquisition of the data was performed using an accelerating voltage of $2\,\mathrm{kV}$ and aperture size of $30\,\mathrm{\mu m}$ or $5\,\mathrm{kV}$ with $5.6 - 7.2\,\mathrm{mm}$ as working distance. The fibres were supported by and observed on the electrospun collectors. POM pictures and videos were acquired with an Olympus BX51 microscope working in transmission mode between parallel polars, coupled to an Olympus DP73 Charged-Coupled Detector camera and to the Stream Basic v.1.9 Olympus software.

6.2.5 Molecular Dynamics Simulations

The impact of the intrinsic curvature on the fibre conformation was studied by performing molecular dynamics simulations using the Large-scale Atomic / Molecular Massively Parallel Simulator (LAMMPS) platform[37]–[39]. In the simulations, a single fibre was constructed using a cubic network of interconnected beads. Each bead was connected to its nearest and next-nearest neighbours, bonded by harmonic potentials $V_i = k_\mathrm{h}/2(r - r_i)^2$, where k_h is the elastic constant and r_i is the equilibrium bond distances. Different filaments were simulated with initial length $L_0 = 300$ and 2400σ (LJ unitis; see http://lammps.sandia.goc/doc/units.html) and $\sigma \times \sigma$ of cross-section. To simulate the mismatch between the two sides of the polymeric fibre, different equilibrium bond distances were used to generate an intrinsic curvature. The elastic properties were set by adjusting the intrinsic curvature to match the experimental data (see Section SM3 in the Supporting Information). Filaments were released at constant velocity and with the ends set to not rotate. Simulations used an NVE integrator (Verlet/leapfrog method) to update beads positions and velocities on each time step, with a step size of $1 \times 10^{-3}\tau$.

6.3 Results and Discussion

A low number of fibres were collected in order to avoid interaction between them and to analyse their individual behaviours. Each collecting cell contained one to five suspended straight fibres with no initial curvature. The fibres were stretched to three times their initial length and then irradiated by UV light, in one side of the fibre. Two main procedures were followed, (I) different fibres were irradiated for different times and (II) the same fibre was selectively irradiated for different times, along its length (masks were used; see Section 2.1). Upon relaxation, the fibres clamped at both ends started to coil, creating helical structures separated by perversions. Fibres were released at the same controlled rate. Although the number of perversions might depend on releasing rate[40], in this work it was not observed a dependence of the fibres geometry with the used releasing rate.

By following procedure (I), helices with different pitches were obtained by changing the irradiation time. In Figure 6.2, we show the results obtained with filaments irradiated for $2 - 10$ min, with initial length $l_{ini} = 1$ cm, stretching length $l_{str} = 3$ cm, and initial fibre diameter $d_{ini} = 16$ µm for $\mathbf{a}-\mathbf{e}$ and $d_{ini} = 8$ µm for $\mathbf{f}$, and the respective numerical simulations adjusted to match the different fibres configurations. As the UV light exposure time increases, the helical radius decreases and the number of loops N_{loops} increases, for fibres with the same average diameter ($d_{ini} = 16$ µm). When the straight fibres were released, at a critical point they started to coil. Since the fibre ends were fixed and could not rotate for accommodating the twisting that arises from the coiling, the total twist must remain constant by the topological conservation law $\mathrm{Wr} + \mathrm{Tw} = \mathrm{constant}$[41], where Wr and Tw are the fibre total writhe and twist. The occurrence of helices with opposite handedness linked by perversions was observed.

The differences between the filaments from Figure 6.2 $\mathbf{a}-\mathbf{e}$ can be verified by relating the curvature $\kappa = R/(R^2 + H^2)$, where H is the vertical separation between loops and R is the radius of the helix, with the UV exposure time (Figure 6.2$\mathbf{g}$). The curvature increases with the time of UV irradiation. The number of perversions that arises along the filament also increases with the time of irradiation.

In previous works[31], [42], PU/PBDO electrospun fibres were not prestrained when irradiated for 24 h; no helices were produced unless further mechanical treatment was applied. In comparison with this work, prestrained fibres only required a few minutes of UV light irradiation and no toluene extraction to produce helical fibres, after being released. The main mechanism behind the helical shape of the obtained fibres relies in the strain difference between the two layers, UV irradiated, and non irradiated, that upon release of the asymmetric contraction leads to an intrinsic curvature. The greater
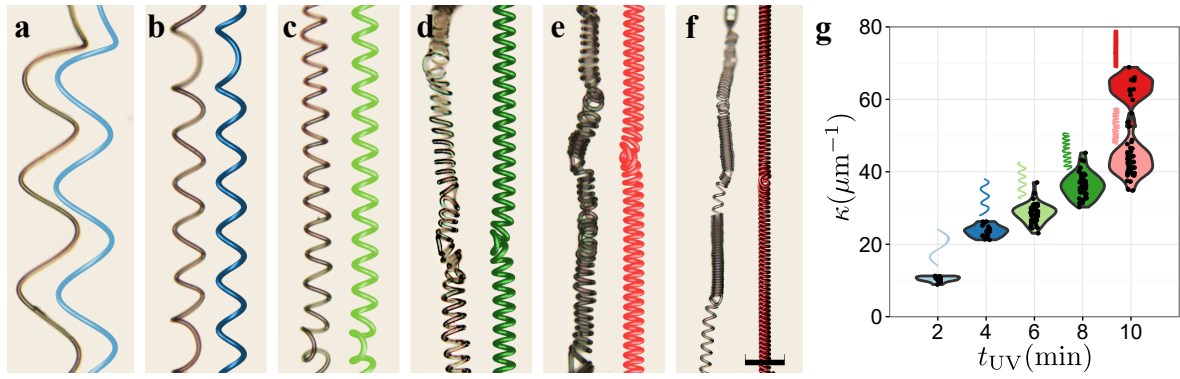
Figure 6.2: **POM images of electrospun fibres (left filaments) and from molecular dynamics simulations (right vivid coloured filaments). a−e** Fibres are exposed to UV for $2-10\,\mathrm{min}$, with $2\,\mathrm{min}$ of timestep, and fibre diameter $d_{\mathrm{ini}} = 16\,\mu\mathrm{m}$; **f** fibre exposed for $10\,\mathrm{min}$, fibre diameter $d_{\mathrm{ini}} = 8\,\mu\mathrm{m}$. Simulations correctly reproduce the geometric behaviour of the helical radius and vertical separation of polymeric fibres. **g** Statistical analysis of curvature κ as a function of UV exposure time t_{UV}. The violin plots represent the distribution of the data points. Jitter was added to time variable in order to evidence the density of points.

the difference between the mechanical properties of the top layer surface created and enhanced by UV and the rest of the filament, the higher the intrinsic curvature. By stretching the fibre before being irradiated, the diameter of the stretched filament will be $d_{\mathrm{str}} = l_{\mathrm{ini}}/l_{\sim\approx\searrow} d_{\mathrm{ini}}$ and the effective irradiation area $S_{\mathrm{str}}/S_{\mathrm{ini}} = l_{\mathrm{str}}/l_{\mathrm{ini}}$, where d_{ini} is the diameter of unextended filament, S is the filament surface, and l is the length of the filament. Then, stretching the elastic fibres decreased the fibre radius and increased the irradiation area. This change dramatically decreases the time needed to create an anisotropy along the fibre. Therefore, the higher the initial stretch, the lower irradiation time is needed for the fibres to acquire an intrinsic curvature.

In Figure 6.3**a**, a typical SEM picture showing a released electrospun microfibre after being stretched and exposed to UV radiation for $10\,\mathrm{min}$ can be observed. Right- and left-handed helices connected by perversions can be observed and wrinkles can be generated in the irradiated surface by sol/gel extraction of the fibre in a good solvent[31]. In fact, a closer look into the fibre cross-section (6.3**b**) reveals a wrinkling pattern only on the irradiated half of the surface.

The most interesting results are related to microfilaments exposed alternately along their length to different UV exposure times. In Figure 6.3c, the regions of the fibre with helices with smaller curvature were irradiated for a UV exposure time $t_{\mathrm{UV}} = 1\,\mathrm{min}$ while the counterpart regions were irradiated for $t_{\mathrm{UV}} = 4\,\mathrm{min}$. The resulting shape, after releasing the fibre, is a set of alternated helices with two distinct curvatures with unevenly distributed perversions. Despite the perversions occurring in a larger number,
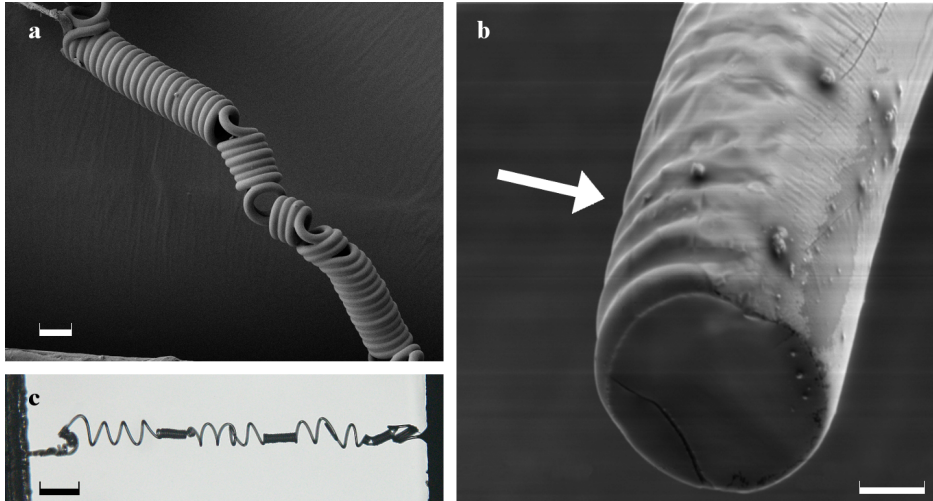
Figure 6.3: **SEM images of electrospun fibres with uniform and multiple irradiated regions. a** SEM image showing a helical filament with some defects. **b** SEM image evidencing the formation of a wrinkling pattern in one side of the microfilament surface, indicated by the white arrow. **c** POM image of electrospun fibres irradiated with two different UV exposure times in alternate areas. Regions of the fibre exposed for longer times have a higher number of loops and smaller helical radius. Scale bar represents $20\,\mu m$ in (a), $5\,\mu m$ in (b), and $200\,\mu m$ in (c).

there were regions with no perversions (see also other examples in the Supporting Information). Computational simulations of filaments with similar characteristics display the same behaviour (see Videos SV1 and SV2, Supporting Information). Further analysis on the release of polymeric fibres also displayed another interesting feature: regions with higher intrinsic curvatures curl first (Figure 6.4**a,b**). This led us to the following conjecture: when one releases filaments with a constant intrinsic curvature, with their ends fixed, perversions arise to counterbalance the total twist being constant (zero, if no initial twisting); if the intrinsic curvature of the filament is not constant and instead alternates, as discussed here, curling of the regions with high intrinsic curvature reflects high elastic energy gain, hence they curl up first; these regions have no restriction on the twist in their boundaries, therefore they can choose the handedness to avoid perversions locally (although the total twist along the filament must remain constant); afterwards, regions with lower intrinsic curvature start to rotate.

From the experimental and computational observations, the transition from straight to helical conformations occurs at a critical point during the releasing of the fibres. Mathematically, a helix with curvature κ and torsion τ can be defined by the position vector $r(s) = 1/\gamma^2(\kappa\cos(\gamma s), \kappa\sin(\gamma s), \tau\gamma s)$. If a force of magnitude F is applied at the
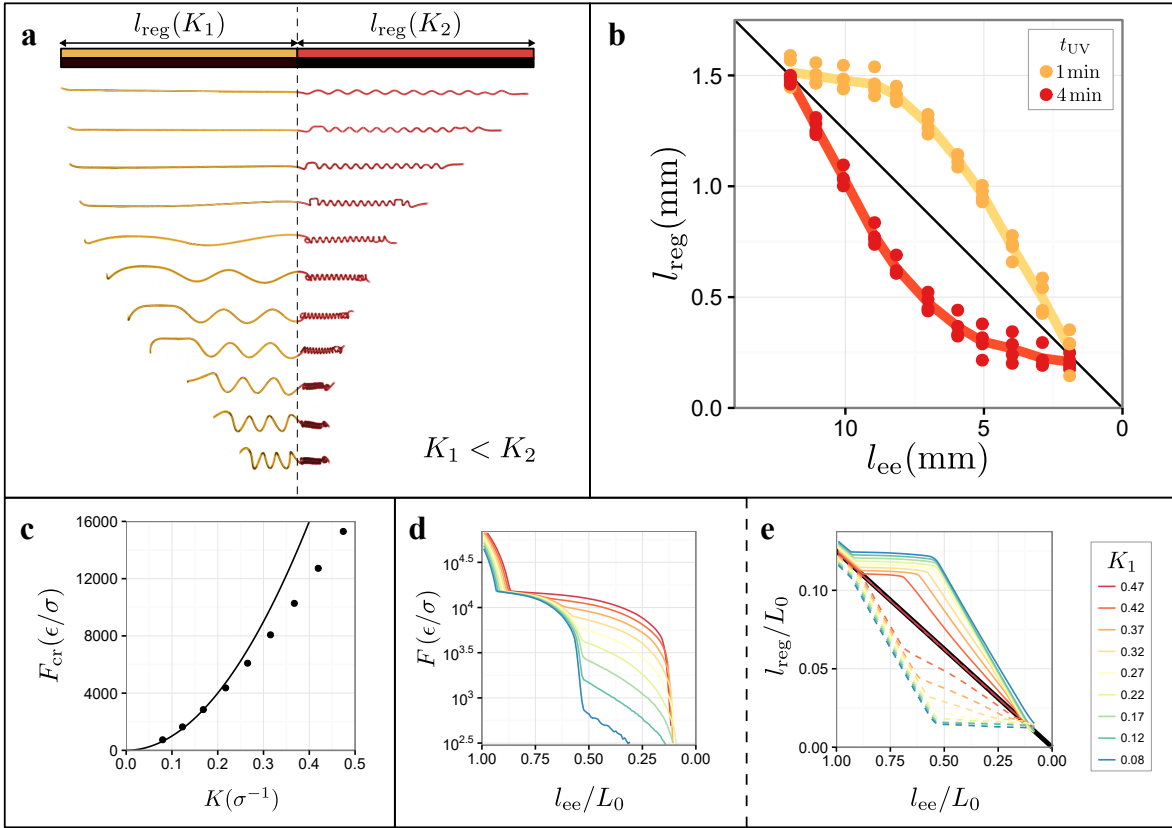
Figure 6.4: **a,b** Release of one experimental fibre with eight regions (only two are shown; see complete fibre sequence in the Supporting Information) irradiated alternately with 1 and 4 min, generating intrinsic curvatures K_1 and K_2, respectively. The fibre in **a** was coloured to match the colour in **b**. **a** Depending on the irradiation times, regions start to coil in different moments after the fibre release. **b** Length of the regions l_{reg} with intrinsic curvature K_1 (yellow dots) and K_2 (red dots). Coloured lines correspond to length averages of the regions with the same intrinsic curvature and black line to $l_{\mathrm{reg}} = l_{\mathrm{ee}}/8$. **c** The critical force F_{cr} as a function of intrinsic curvature K for a filament with $L_0 = 300\sigma$. The black line and markers correspond to the prediction from the theoretical model and data from simulations. **d** Force-extension of filaments with $L_0 = 2400\sigma$ (eight regions with length $l_{\mathrm{reg}} = L_0/8 = 300\sigma$ and alternate intrinsic curvatures K_1 ranging from 0.08 to 0.47 and $K_2 = 0.47$). **e** Average length of the regions l_reg, with intrinsic curvature K_1 (dashed lines) and K_2 (continuous lines) as a function of the end-to-end distance l_{ee}. For $K_1 = K_2 = 0.47$, there is a single transition in the force-extension corresponding to when fibres start coiling and all regions retract with the same displacement (red lines are over black thick line $l_{\mathrm{reg}} = l_{ee}/8$). For fibres with different intrinsic curvature, $K_1 \neq K_2$, regions with K_2 start coiling for $F = F_{\mathrm{cr}}(K_2)$ and $l_{\mathrm{reg}}(K_2)$ has almost no retraction. When $F = F_{\mathrm{cr}}(K_1)$, region $l_{\mathrm{reg}}(K_1)$ begins to coil.

ends, the total energy density of the helix is given by[43]

$$\mathcal{E} = \frac{1}{2}EI(\kappa - K)^2 + \frac{1}{2}GJ\tau^2 - \frac{F\tau}{\gamma} \tag{6.1}$$

where E is the Young's modulus, G is the shear modulus, I is the cross-sectional moment of inertia, K is the intrinsic curvature, J is the torsion constant, and $\gamma = \sqrt{\kappa^2 + \tau^2}$. For a stable configuration, $\frac{\partial\mathcal{E}}{\partial\kappa} = EI(\kappa - K) + \frac{F\kappa\tau}{\gamma^3} = 0$ and $\frac{\partial\mathcal{E}}{\partial\tau} = GJ\tau - \frac{F\kappa^2}{\gamma^3} = 0$. By combining both equations, the applied force can be written in function of κ:

$$F = EI(K - \kappa)\frac{(\kappa^2 - \alpha\kappa(K - \kappa))^{3/2}}{\kappa\left(\alpha\kappa(K - \kappa)\right)^{1/2}}, \quad \alpha = \frac{EI}{GJ}. \tag{6.2}$$

When the filament goes from the helical to the straight configuration, the critical force can be obtained by taking the limit $\kappa \to 0$:

$$F_{\mathrm{cr}} = \frac{E^2 I^2}{GJ}K^2. \tag{6.3}$$

For a simulation of a filament with initial length $L_0 = 300\sigma$, $k_{\mathrm{h}} = 2\times 10^4$ and intrinsic curvature K varying from 0.08 to 0.47, the relationship between intrinsic curvature and the critical force for the theoretical model and computational simulations is shown in Figure 6.4**c**. For low values of curvature, theoretical predictions show a good agreement with the computational simulations values and, despite theoretical prediction failing for higher values of curvature, the critical force still increases with the intrinsic curvature. In fact, when a stretched fibre with different curvatures is released, the regions with higher curvature will start to coil first. Figure 6.4**d** shows several force-extension curves for fibres with regions with two alternated different intrinsic curvatures $l_{\mathrm{reg}}(K_1)$ and $l_{\mathrm{reg}}(K_2)$, with $K_1 = 0.08$ to 0.47 and a fixed $K_2 = 0.47$ ($K1 \leq K2$). When $K_1 = K_2 = 0.47$, there is a single transition in the force-extension corresponding to when fibres start coiling and all regions shrink with the same displacement (Figure 6.4**d,e**. For fibres with alternated intrinsic curvatures, $K_1 \neq K_2$, $l_{\mathrm{reg}}(K_2)$ start coiling after reaching the critical force $F = F_{\mathrm{cr}}(K_2)$ and the length of the regions with lower intrinsic curvature $l_{\mathrm{reg}}(K_1)$ remains almost constant. After the applied force decreases enough until $F = F_{\mathrm{cr}}(K_1)$, the region $l_{\mathrm{reg}}(K1)$ begins to coil and $l_{\mathrm{reg}}(K_1)$ decreases at higher rate than $l_{\mathrm{reg}}(K2)$. It should be noted that, despite the difference between $l_{\mathrm{reg}}(K_1)$ and $l_{\mathrm{reg}}(K_2)$ in Figure 6.4**a** being higher than the difference between the average values displayed in Figure 6.4**b**, after the fibres being completely released, the regions with lower curvatures have lower values of l_{reg} than the regions with higher curvatures. Two additional examples showing this behaviour are provided in the Supplementary Materials. Considering the self-contact of the fibres and ignoring the effects introduced by perversions in the helical

geometry, the theoretical minimal value of $l_{\text{reg}}(K) = d_{\text{ini}}N_{\text{loops}}$. Then, $l_{\text{reg}}(K_1)$ would retract to a value lower than $l_{\text{reg}}(K_2)$. However, when $l_{\text{reg}}(K_1)$ is close to $l_{\text{reg}}(K_2)$, fibres start to bend in the perversions and this analysis requires the fibre to be aligned along the axis of release.

When filaments with different intrinsic curvatures are released (or stretched) different parts of the filament curl (or unwind) depending on the applied force. The intrinsic curvature imprinted allows the precise design of the filaments at the microscale.

6.4 Conclusions

Our experiments demonstrated for the first time how to produce microfilaments composed by segments with different curvatures and how their shapes changed under tension. Besides displaying different helical morphologies, these filaments started to coil in distinct stages when released. Regions with higher intrinsic curvature curl first and the shrinkage of the regions length is not constant along the filament. Computational simulations correctly capture the experimental observations. Although the force-extension curves were not experimentally obtained, both theoretical model and computational simulations predict a dependence of the critical force to the fibre start coiling with its intrinsic curvature.

Moreover, a facile strategy to produce microfilaments with different helical geometries has been reported. The intrinsic curvature of PU/PBDO microfilaments was tuned by applying different exposure times to UV light. Irradiating fibres while being stretched decreased the required time for generating a layer with different physical properties from 24 h to a few minutes. The same strategy can be applied to other elastic filaments, provided that their structures can be fairly stretched and an asymmetry between two regions of the filament can be created when tension is applied, which could find applications in nanotechnology or in the textile industry.

The work presented here is a first study on how the presence of a nonconstant intrinsic curvature changes the elastic properties of the filaments. Due to the generality of used computational simulations, our study can also enlighten the analysis of filaments containing a multiplicity of helical shapes. A deeper study is required to the outcome of using fibres: with three or more regions having three or more intrinsic curvature constants, with alternated intrinsic curvatures in meshes of filaments.

6.5 Supplementary Materials

6.5.1 SM1: Videos overview

For a clear visualization of the phenomena reported in this work, a set of figures containing a few frames from supplementary videos are shown.

Video **SV1**: Comparative overview of symmetric and antisymmetric perversions obtained in computer simulations, experiments with electrospun fibres and gift ribbons.
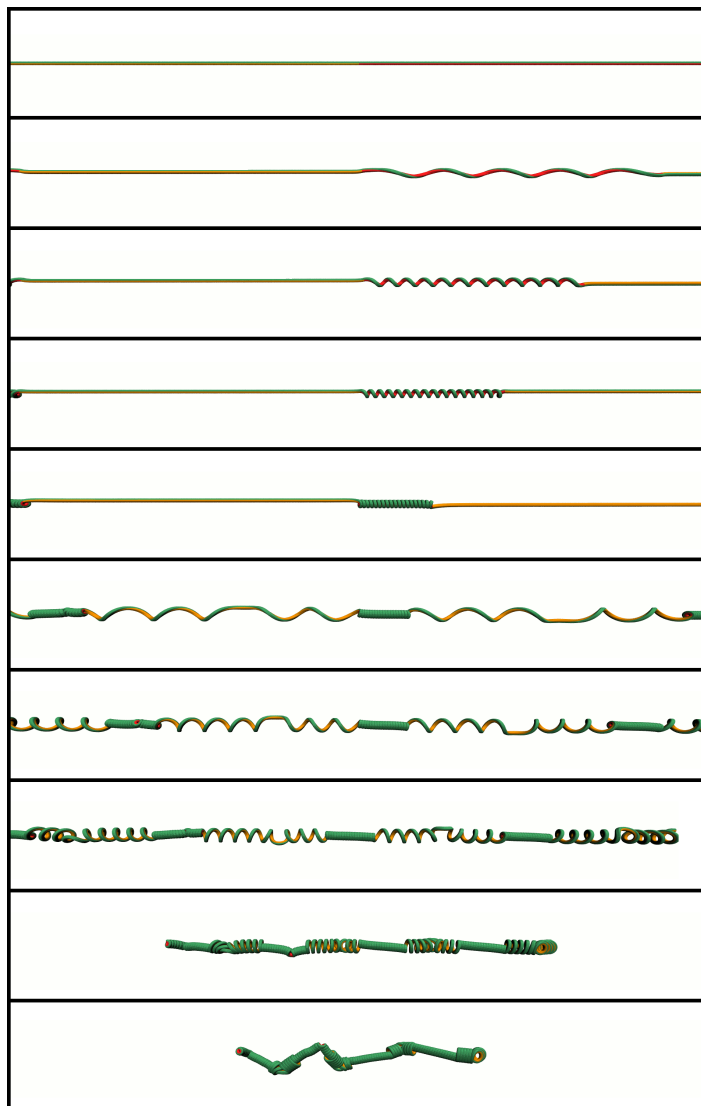

Figure 6.5: Snapshots from the supplementary video SV1. Two different pre-strains are depicted in yellow ($\chi = 1/3$) and in red ($\chi = 1$).
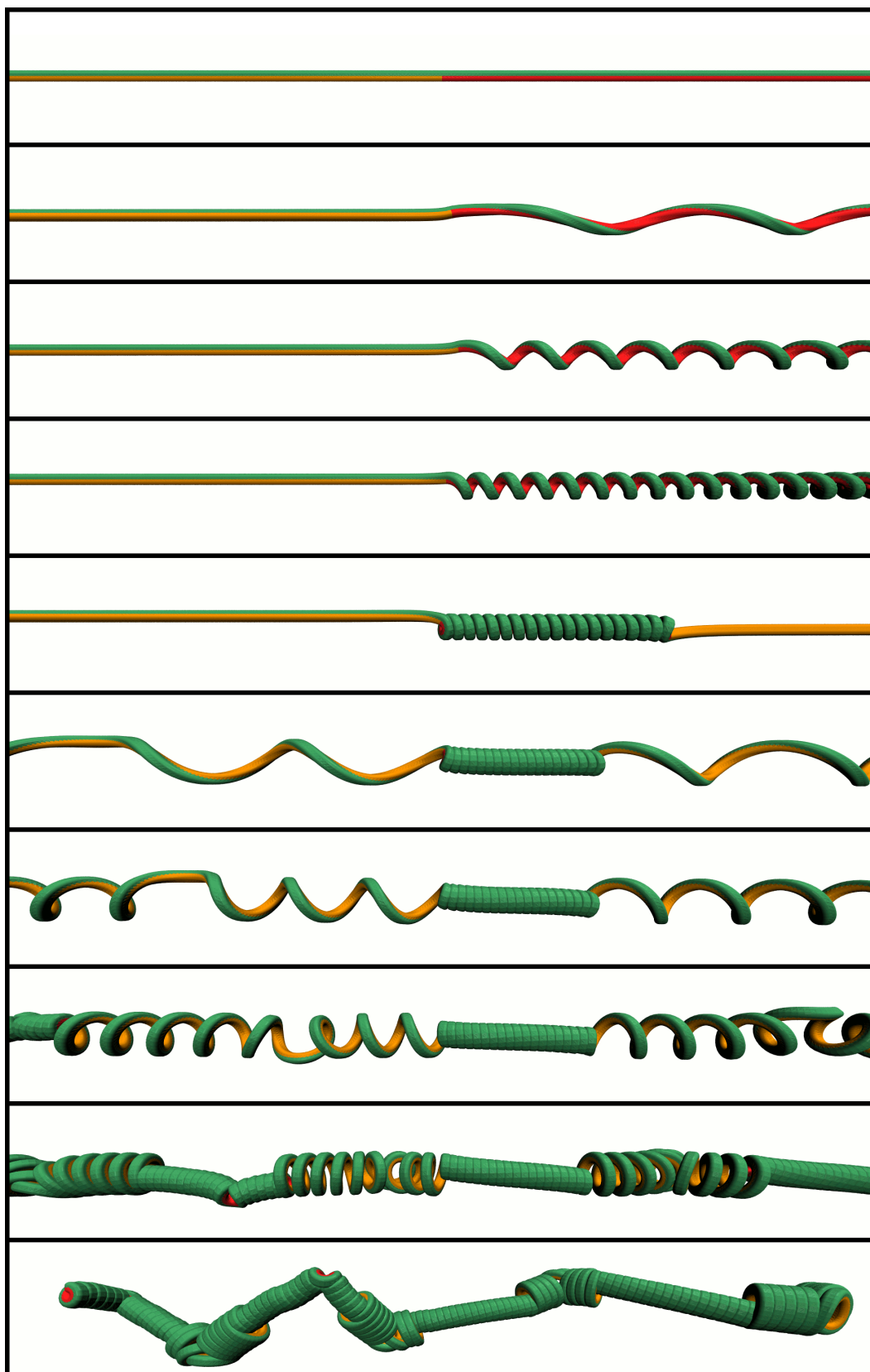
Figure 6.6: Snapshots from the supplementary video SV2 where a close up of SV1 is displayed.

6.5.2 SM2: Molecular dynamics simulations of filaments with multiple intrinsic curvature and relationship between pre-strain with intrinsic curvature

The microfilaments behaviour reported in this work can be complex, not easy to handle due to their dimensions and the dynamics of the fibres release might be hard to observe since the ratio between the length and the fibres diameter is enormous (in the order of the 10^3). LAMMPS (Large-scale Atomic/Molecular Massively Parallel Simulator) was used to simulate the dynamics of elastic filaments. A similar approach and considerations were taken into account as in the model used here, with the change of used type of network to form the filaments. Despite being used a simple model, it can successfully exhibit the complex phenomena that occurred on obtained experimental microfibres. The microfilaments were formed using structures with cross-sections made of $N_w = 2$ by $N_h = 2$ beads along the width and height, respectively (see S. Fig. 3). Beads were connected by three harmonic potentials, bonds a, b and c, with equilibrium bond distances (r_a, r_b and r_c) as illustrated in different colouring in S. Fig. 3.
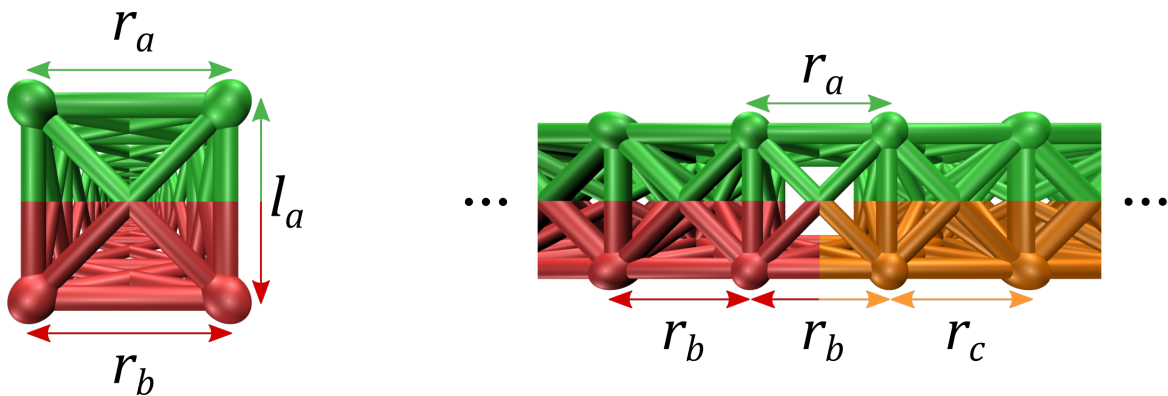

Figure 6.7: Beads arrangement used to form the elastic filaments in simulations. (a) Front and (b) side views of beads and bonds displaying in different colours according to the used potential.

In the experimental set-up, fibres were irradiated with (I) the same time along the fibre to create a constant intrinsic curvature and with (II) two different times alternately along the fibre to create regions with different intrinsic curvature (see Figure 1). To model fibres in the case (I), filaments were pre-strained with $r_b = r_c$ and for enough

unmatched $r_b < r_a$, one side of the filament becomes stretched relatively to the other, and upon release the filament gains a helical shape with an intrinsic curvature K. For the filaments with multiple intrinsic curvature (II), $r_b \neq r_c$ generating filaments with intrinsic curvature K_1 and K_2. In order to match the computational simulations with the experimental fibres it was necessary to relate the pre-strain $\chi = r_a/r_b - 1$ with the intrinsic curvature, S. Fig. 4.
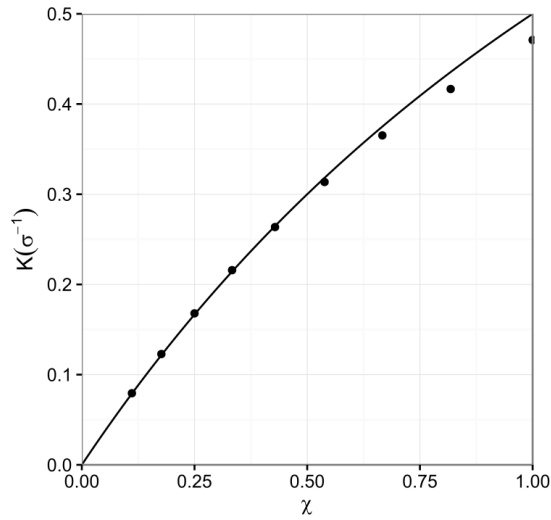

Figure 6.8: Curvature K as a function of pre-strain χ. Black markers represent the curvature obtained in numerical simulations. The black line corresponds to the prediction obtained from the linear model.

6.5.3 SM3: Release of an electrospun fibre irradiated with UV light for different exposing times
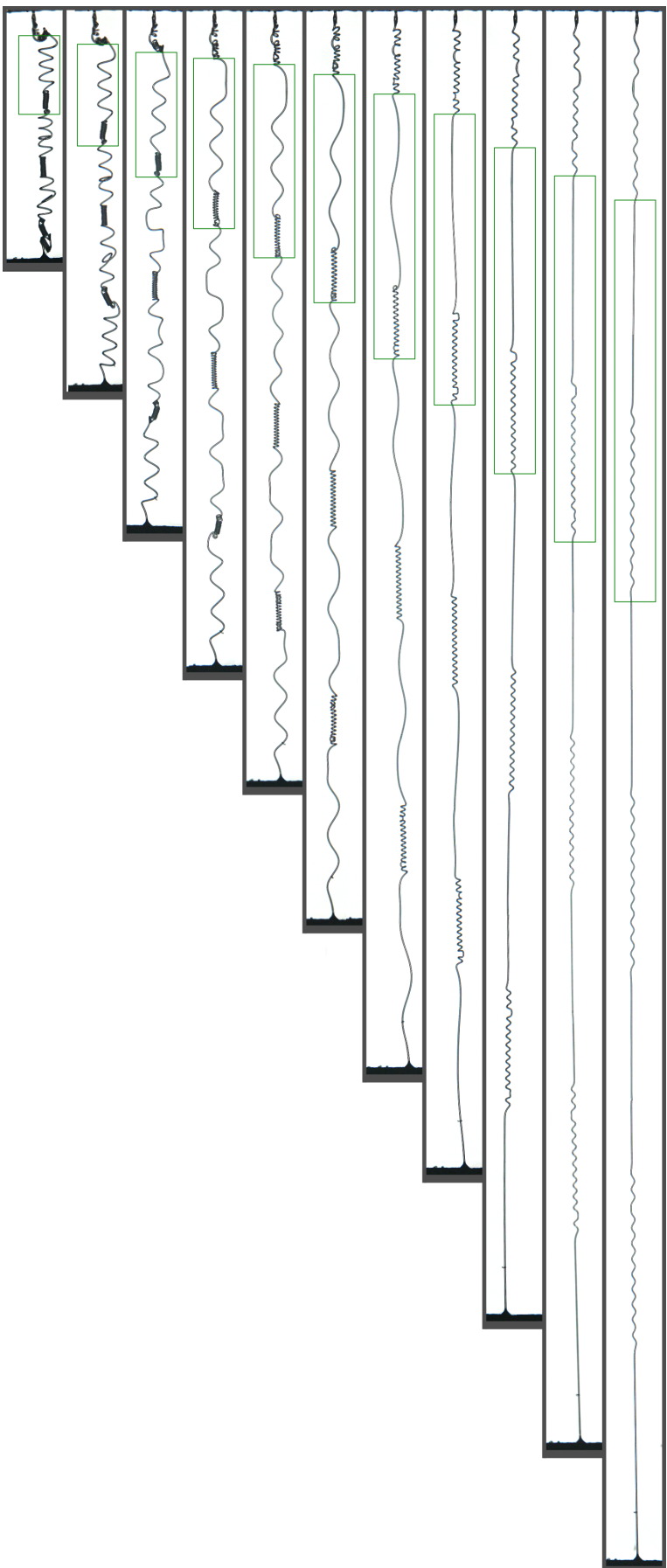
Figure 6.9: A sequence of experimental images illustrating the release of a microfilament with multiple intrinsic curvatures. The fibres were alternately irradiated, as the colour scheme indicates in top, for 4 min (red region) and 1 min (orange region). Regions irradiated for longer times have higher curvature and start to curl first at the 12mm.The two regions used in the main manuscript (Figure 4a) are highlighted by the green boxes.
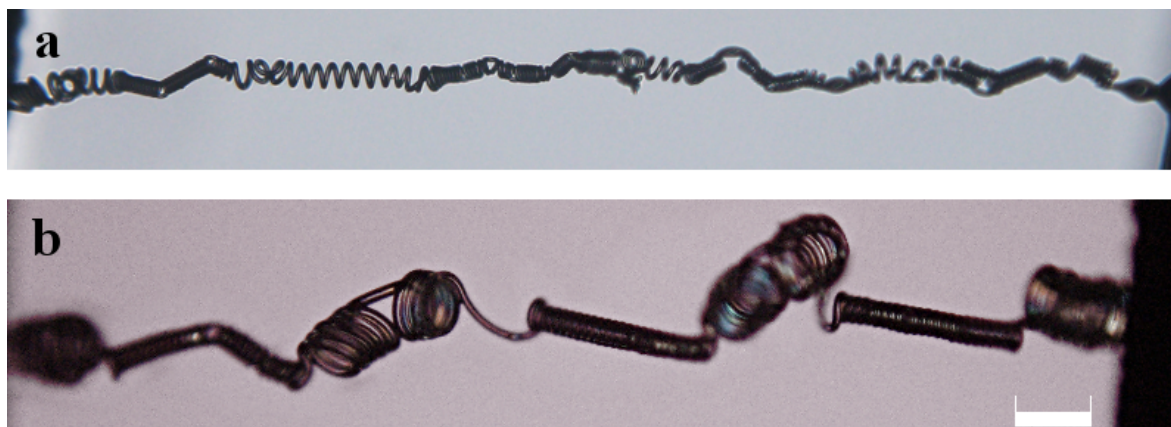
Figure 6.10: POM images of electrospun fibres irradiated with alternate UV exposure times. Fibres were exposed for 4 and 8 min and the fibres diameter is (a) $d_ini = 8\,\mu m$ and (b) $d_ini = 16\,\mu m$. Scale bar represent $d_ini = 200\,\mu m$.

References

[1]   P. E. S. Silva and M. H. Godinho, "Helical Microfilaments with Alternating Imprinted Intrinsic Curvatures," *Macromolecular Rapid Communications*, vol. 38, no. 5, p. 1 600 700, Mar. 2017. DOI: 10.1002/marc.201600700.

[2]   D. G. Gray, "Isolation and handedness of helical coiled cellulosic thickenings from plant petiole tracheary elements," *Cellulose*, vol. 21, no. 5, pp. 3181–3191, Aug. 3, 2014. DOI: 10.1007/s10570-014-0382-4.

[3]   M. Stoppa and A. Chiolerio, "Wearable Electronics and Smart Textiles: A Critical Review," *Sensors*, vol. 14, no. 7, pp. 11 957–11 992, Jul. 7, 2014. DOI: 10.3390/s140711957.

[4]   Z. Xia, "Adaptive and Self-shaping Materials," in *Biomimetic Principles and Design of Advanced Engineering Materials*, John Wiley & Sons, Ltd, 2016, pp. 79–100.

[5]   X. Li, Y. Yang, Y. Fan, Q. Feng, F.-z. Cui, and F. Watari, "Biocomposites reinforced by fibers or tubes as scaffolds for tissue engineering or regenerative medicine," *Journal of Biomedical Materials Research Part A*, vol. 102, no. 5, pp. 1580–1594, May 1, 2014. DOI: 10.1002/jbm.a.34801.

[6]   A. H. Rajabi, M. Jaffe, and T. L. Arinzeh, "Piezoelectric materials for tissue regeneration: A review," *Acta Biomaterialia*, vol. 24, pp. 12–23, Sep. 15, 2015. DOI: 10.1016/j.actbio.2015.07.010.

[7]   A. Agarwal and H. Hess, "Biomolecular motors at the intersection of nanotechnology and polymer science," *Progress in Polymer Science*, Special Issue on Stimuli-Responsive Materials, vol. 35, pp. 252–277, 1–2 Jan. 2010. DOI: 10.1016/j.progpolymsci.2009.10.007.

[8]   H.-W. Huang, M. S. Sakar, A. J. Petruska, S. Pané, and B. J. Nelson, "Soft micromachines with programmable motility and morphology," *Nature Communications*, vol. 7, p. 12 263, Jul. 22, 2016. DOI: 10.1038/ncomms12263.

[9]   T. Strick, J.-F. Allemand, V. Croquette, and D. Bensimon, "Twisting and stretching single DNA molecules," *Progress in Biophysics and Molecular Biology*, Single Molecule Biochemistry and Molecular Biology, vol. 74, pp. 115–140, 1–2 Jul. 2000. DOI: 10.1016/S0079-6107(00)00018-3.

[10] A. Goriely and M. Tabor, "Spontaneous Helix Hand Reversal and Tendril Perversion in Climbing Plants," *Physical Review Letters*, vol. 80, no. 7, pp. 1564–1567, Feb. 16, 1998. DOI: 10.1103/PhysRevLett.80.1564.

[11] A. Lazarus, J. T. Miller, M. M. Metlitz, and P. M. Reis, "Contorting a heavy and naturally curved elastic rod," *Soft Matter*, vol. 9, no. 34, pp. 8274–8281, Aug. 7, 2013. DOI: 10.1039/C3SM50873K.

[12] U. Yogeswaran and S.-M. Chen, "A Review on the Electrochemical Sensors and Biosensors Composed of Nanowires as Sensing Material," *Sensors*, vol. 8, no. 1, pp. 290–313, Jan. 21, 2008. DOI: 10.3390/s8010290.

[13] J. Wu, S. Liu, L. He, H. Wang, C. He, C. Fan, and X. Mo, "Electrospun nanoyarn scaffold and its application in tissue engineering," *Materials Letters*, vol. 89, pp. 146–149, Dec. 15, 2012. DOI: 10.1016/j.matlet.2012.08.141.

[14] M. H. Godinho, J. P. Canejo, L. F. V. Pinto, J. P. Borges, and P. I. C. Teixeira, "How to mimic the shapes of plant tendrils on the nano and microscale: Spirals and helices of electrospun liquid crystalline cellulose derivatives," *Soft Matter*, vol. 5, no. 14, pp. 2772–2776, Jul. 7, 2009. DOI: 10.1039/B821631B.

[15] S. J. Gerbode, J. R. Puzey, A. G. McCormick, and L. Mahadevan, "How the Cucumber Tendril Coils and Overwinds," *Science*, vol. 337, no. 6098, pp. 1087–1091, Aug. 31, 2012. DOI: 10.1126/science.1223304. pmid: 22936777.

[16] S. Armon, H. Aharoni, M. Moshe, and E. Sharon, "Shape selection in chiral ribbons: From seed pods to supramolecular assemblies," *Soft Matter*, vol. 10, no. 16, p. 2733, 2014. DOI: 10.1039/c3sm52313f.

[17] A. Travers and G. Muskhelishvili, "DNA structure and function," *FEBS Journal*, vol. 282, no. 12, pp. 2279–2295, Jun. 1, 2015. DOI: 10.1111/febs.13307.

[18] R.-H. Pusarla and P. Bhargava, "Histones in functional diversification," *FEBS Journal*, vol. 272, no. 20, pp. 5149–5168, Oct. 1, 2005. DOI: 10.1111/j.1742-4658.2005.04930.x.

[19] P. C. Weber and F. R. Salemme, "Structural and functional diversity in 4-alpha-helical proteins," *Nature*, vol. 287, no. 5777, pp. 82–84, Sep. 4, 1980. PMID: 6251384.

[20] Y. Timsit and P. Várnai, "Helical Chirality: A Link between Local Interactions and Global Topology in DNA," *PLOS ONE*, vol. 5, no. 2, e9326, 2010. DOI: 10.1371/journal.pone.0009326.

[21] B. Singh, C. Fleury, F. Jalalvand, and K. Riesbeck, "Human pathogens utilize host extracellular matrix proteins laminin and collagen for adhesion and invasion of the host," *FEMS Microbiology Reviews*, vol. 36, no. 6, pp. 1122–1180, Nov. 1, 2012. DOI: 10.1111/j.1574-6976.2012.00340.x. PMID: 22537156.

[22] N. E. Stamp, "Self-Burial Behaviour of Erodium Cicutarium Seeds," *Journal of Ecology*, vol. 72, no. 2, pp. 611–620, 1984. DOI: 10.2307/2260070. JSTOR: 2260070.

[23] D. Evangelista, S. Hotton, and J. Dumais, "The mechanics of explosive dispersal and self-burial in the seeds of the filaree, Erodium cicutarium (Geraniaceae)," *Journal of Experimental Biology*, vol. 214, no. 4, pp. 521–529, Feb. 15, 2011. DOI: 10.1242/jeb.050567. PMID: 21270299.

[24] E. Frirdich, J. Biboy, C. Adams, J. Lee, J. Ellermeier, L. D. Gielda, V. J. DiRita, S. E. Girardin, W. Vollmer, and E. C. Gaynor, "Peptidoglycan-Modifying Enzyme Pgp1 Is Required for Helical Cell Shape and Pathogenicity Traits in Campylobacter jejuni," *PLOS Pathog*, vol. 8, no. 3, e1002602, 2012. DOI: 10.1371/journal.ppat.1002602.

[25] R. Gilad, A. Porat, and S. Trachtenberg, "Motility modes of Spiroplasma melliferum BC3: A helical, wall-less bacterium driven by a linear motor," *Molecular Microbiology*, vol. 47, no. 3, pp. 657–669, Feb. 1, 2003. DOI: 10.1046/j.1365-2958.2003.03200.x.

References

[26] J. W. Shaevitz, J. Y. Lee, and D. A. Fletcher, "Spiroplasma Swim by a Processive Change in Body Helicity," *Cell*, vol. 122, no. 6, pp. 941–945, Sep. 23, 2005. DOI: `10.1016/j.cell.2005.07.004`. pmid: `16179261`.

[27] "Apparatus for winding wire into a helix," US3039707 A, 1959.

[28] M. K. S. Verma, A. Majumder, and A. Ghatak, "Embedded Template-Assisted Fabrication of Complex Microchannels in PDMS and Design of a Microfluidic Adhesive," *Langmuir*, vol. 22, no. 24, pp. 10 291–10 295, Nov. 2006. DOI: `10.1021/la062516n`.

[29] McMillen and Goriely, "Tendril Perversion in Intrinsically Curved Rods," *Journal of Nonlinear Science*, vol. 12, no. 3, pp. 241–281, 2002. DOI: `10.1007/s00332-002-0493-1`.

[30] Y. Snir and R. D. Kamien, "Entropically Driven Helix Formation," *Science*, vol. 307, no. 5712, pp. 1067–1067, Feb. 18, 2005. DOI: `10.1126/science.1106243`. pmid: `15718461`.

[31] A. C. Trindade, J. P. Canejo, P. I. C. Teixeira, P. Patricio, and M. H. Godinho, "First Curl, Then Wrinkle," *Macromolecular Rapid Communications*, vol. 34, no. 20, pp. 1618–1622, Oct. 1, 2013. DOI: `10.1002/marc.201300436`.

[32] D. H. Reneker, A. L. Yarin, H. Fong, and S. Koombhongse, "Bending instability of electrically charged liquid jets of polymer solutions in electrospinning," *Journal of Applied Physics*, vol. 87, no. 9, pp. 4531–4547, May 1, 2000. DOI: `10.1063/1.373532`.

[33] P. Kiselev and J. Rosell-Llompart, "Highly aligned electrospun nanofibers by elimination of the whipping motion," *Journal of Applied Polymer Science*, vol. 125, no. 3, pp. 2433–2441, Aug. 5, 2012. DOI: `10.1002/app.36519`.

[34] P. Katta, M. Alessandro, R. D. Ramsier, and G. G. Chase, "Continuous Electrospinning of Aligned Polymer Nanofibers onto a Wire Drum Collector," *Nano Letters*, vol. 4, no. 11, pp. 2215–2218, Nov. 1, 2004. DOI: `10.1021/nl0486158`.

[35] H. Jiang, Y. Hu, Y. Li, P. Zhao, K. Zhu, and W. Chen, "A facile technique to prepare biodegradable coaxial electrospun nanofibers for controlled release of bioactive agents," *Journal of Controlled Release*, vol. 108, pp. 237–243, 2–3 Nov. 28, 2005. DOI: `10.1016/j.jconrel.2005.08.006`.

[36] M. H. Godinho, A. C. Trindade, J. L. Figueirinhas, L. V. Melo, P. Brogueira, A. M. Deus, and P. I. C. Teixeira, "Tuneable micro- and nano-periodic structures in a free-standing flexible urethane/urea elastomer film," *The European Physical Journal E*, vol. 21, no. 4, pp. 319–330, Dec. 2006. DOI: 10.1140/epje/i2006-10070-8.

[37] S. Plimpton, "Fast Parallel Algorithms for Short-Range Molecular Dynamics," *Journal of Computational Physics*, vol. 117, no. 1, pp. 1–19, Mar. 1, 1995. DOI: 10.1006/jcph.1995.1039.

[38] W. M. Brown, P. Wang, S. J. Plimpton, and A. N. Tharrington, "Implementing molecular dynamics on hybrid high performance computers – short range forces," *Computer Physics Communications*, vol. 182, no. 4, pp. 898–911, Apr. 2011. DOI: 10.1016/j.cpc.2010.12.021.

[39] W. M. Brown, A. Kohlmeyer, S. J. Plimpton, and A. N. Tharrington, "Implementing molecular dynamics on hybrid high performance computers – Particle–particle particle-mesh," *Computer Physics Communications*, vol. 183, no. 3, pp. 449–459, Mar. 2012. DOI: 10.1016/j.cpc.2011.10.012.

[40] S. Liu, Z. Yao, K. Chiou, S. I. Stupp, and M. O. de la Cruz, "Emergent perversions in the buckling of heterogeneous elastic strips," *Proceedings of the National Academy of Sciences*, vol. 113, no. 26, pp. 7100–7105, Jun. 28, 2016. DOI: 10.1073/pnas.1605621113. pmid: 27303040.

[41] P. Pieranski, J. Baranska, and A. Skjeltorp, "Tendril perversion—a physical implication of the topological conservation law," *European Journal of Physics*, vol. 25, no. 5, p. 613, 2004. DOI: 10.1088/0143-0807/25/5/004.

[42] P. E. S. Silva, J. L. Trigueiros, A. C. Trindade, R. Simoes, R. G. Dias, M. H. Godinho, and F. V. de Abreu, "Perversions with a twist," *Scientific Reports*, vol. 6, p. 23 413, Mar. 30, 2016. DOI: 10.1038/srep23413.

[43] J. Liu, J. Huang, T. Su, K. Bertoldi, and D. R. Clarke, "Structural Transition from Helices to Hemihelices," *PLOS ONE*, vol. 9, no. 4, e93183, 2014. DOI: 10.1371/journal.pone.0093183.

Chapter

7

Entanglements using physical pseudoknots and perversions

Active and smart materials have recently received attention in numerous fields, such as in robotics, electronics[1], polymer science[2] and nanotechnology[3]. For instance, the development of instrumentation incorporating components with mechanical flexibility represents a current challenge to semiconductor technologies. For this purpose, several stress-induced bending approaches are being tested to create structures with a wide range of geometries that can adapt their shape without losing their operability[4], [5]. Shape-memory materials can also undergo big deformations and still recover the original shape by using different kinds of external stimuli, such as light[6], temperature[7], [8], electrical[9] or magnetic fields[10]. More recently, due to advances in 3D printing, instead of developing materials with new chemistries, composite materials

can be designed and fabricated to precisely acquire complex geometries. In this way, knowledge from the diverse active soft materials allows combining them in different arrangements resulting in a technology known as 4D printing[11]. Conceptually, 4D printing could already be found in past technologies, like on rapid prototyping processes, where the distribution of different materials results in an active response along either distance or direction[12], [13] and in deployable structures, like origami constructions where the patterned disposition of ridges assists the packaging rigid frameworks[14] and other transformable structures capable of performing large configuration changes[15]. For instance, Lessinnes and Goriely[16] conceived a family of two deployable elastic rods connected by rigid segments by looking at the Bristol ladder. The Bristol ladder is a ladder that can be folded by rotating the ends, forming a double helical structure. The helical pitch decreases, with the increase of the rotation, until being completely folded. In nature, many examples of this kind of structures can be found in insects, like in the case of the wings of beetles where the number of foldings can reach up to ten times along the span direction[17]. In plants, one obvious example is the opening and closure of the flowers, which is crucial to the reproductive cycle, that usually is regulated by the changes in light intensity[18]. Carnivorous plants possess an active trapping mechanism to capture insects. The trap consists in a pair of leaves that, when triggered, have a rapid movement to entrap the prey. After digestion, the leaves slowly return to the previous state and remain in a silent state ready to snap again[19]. Plant tendrils revolve around until attaching to a support. Afterwards, tendrils start to wind, generating helical structures with both handednesses separated by inversion regions, also known as perversions[20]. Nature has many self-organizing systems. The mimicry of these systems armed with the recent advances in polymer science and 4D printing, opens a vast potential for improving or creating new applications.

Smart and active materials are also highly desirable in the textile industry. Fabrics have been produced by humankind since the ancient times. People wear all kinds of garments depending on the climacteric conditions or fashion, use bandages to protect a wound and prevent infections or other kind of fabrics in numerous situations. The inclusion of sensing and actuation in fabrics has the potential of improving comfort by self-adapting fabrics to the people needs, during activities, changes in the environment, and also actively monitoring mundane habits or preventing serious health issues[21], [22].

In general, fabrics can be of three categories: knits, wovens and nonwovens. In knitted fabrics filaments are linked with knots. The yarn in knitted fabrics follows a meandering path, on which loops are successively crossed with others loops. Woven fabrics go through a process known as weaving. Weaving consists in disposing perpendicular

threads that are interlaced following a patterned movement or precise intertwining to form the fabric. Nonwoven materials do not use organized interlacing or looping of the yarns for internal cohesion as in a woven fabric but, instead, the linking of the fibres is accomplished by mechanical, chemical, thermal or other types of bonding.

Inspired by the idea of shaping structures using self-organization, in this chapter two descriptions creating entanglements using exclusively mechanical interactions will be presented. In the first case, braids are produced by using the winding behaviour of the perversions. Therefore, a small introduction to braid theory will be introduced to classify the types of entanglements obtained. In the second approach, fabrics are produced by using links known as physical pseudoknots (PPKs).

7.1 Winding number

An important achievement in braid theory is the description of the number of different configurations a group of strands can adopt. This has practical relevance in material science since the mechanical properties of each filament and the way fibres are disposed can generate mats with higher or lower flexibility, durability, strength, and with different responses to movements of traction, compression, bending or torsion.

In topology, strands are characterized by geometrical quantities that are preserved under homeomorphisms (continuous deformations of the object without breaking its shape). For instance, the linking number measures how much two curves wind around each other. The linking number was first used by Gauss, in the 19th century, even if, its derivation is attributed to Maxwell, in relation to studies on electromagnetic induction[23]. Considering two closed nonintersecting curves, C and C^*, parametrized by s and s^*, and with the three coordinate functions, $(x(s), y(s), z(s))$, a pointing unit vector $\mathbf{U}$ can be defined by the difference between the positions vectors $\mathbf{r}$ and $\mathbf{r}^*$:

$$\mathbf{U}(s, s^*) = \frac{\mathbf{r}(s) - \mathbf{r}^*(s^*)}{\|\mathbf{r}(s) - \mathbf{r}^*(s^*)\|}. \tag{7.1}$$

The linking number, Lk, between the two curves can be defined by taking the integer result of the following double integral:

$$\mathrm{Lk}_{C,C^*} \equiv \frac{1}{4\pi} \oint_C \oint_{C^*} \mathbf{T}(s) \times \mathbf{T}(s^*) \cdot \frac{\mathbf{r}(s) - \mathbf{r}^*(s^*)}{\|\mathbf{r}(s) - \mathbf{r}^*(s^*)\|^3} \, \mathrm{d}s \, \mathrm{d}s^* \tag{7.2}$$

$$= \frac{1}{4\pi} \oint_C \oint_{C^*} \frac{\mathbf{T}(s) \times \mathbf{T}(s^*) \cdot \mathbf{U}(s, s^*)}{\|\mathbf{r}(s) - \mathbf{r}^*(s^*)\|^2} \, \mathrm{d}s \, \mathrm{d}s^*, \tag{7.3}$$

where $\mathbf{T}$ and $\mathbf{T}^*$ are the unit tangent vectors of C and C^*, respectively. Lk is independent

of the direction of $\mathbf{U}$ and to a change of both curve directions ($\mathbf{T} \to -\mathbf{T}$ and $\mathbf{T}^* \to -\mathbf{T}^*$), which means $\mathrm{Lk}(C, C^*) = \mathrm{Lk}(C^*, C)$, but changes its sign if the direction of one of the curves is reversed. Lk can also be calculated by taking the half of signed numbers of crossings of the two curve, seen in any plane projection. The sign of the crossing can be determined according to the right-hand rule applied on how the top strand rotates relatively to the other[24], as shown in Figure 7.1.
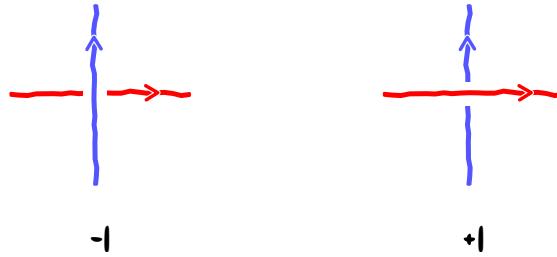

Figure 7.1: Positive and negative crossings are determined by the right-hand rule.

Călugăreanu showed in the 1960s that the linking number could be decomposed into two quantities, the twist number, Tw, and the writhe number, Wr:

$$\mathrm{Tw} + \mathrm{Wr} = \mathrm{Lk}. \tag{7.4}$$

In a rough description, the twist measures how much the secondary curve revolves around the axis curve, while writhe measures how much the curve kinks and coils[25]. If the curves are separated by a large distance, for instance in the order, or bigger, of the radius of curvature, the description of both quantities might be hard to visualize. For this reason, curves close to each other are usually considered, like the boundaries of a ribbon or the double chains of the DNA molecule. Defining a unit vector $\mathbf{U}$ normal to $\mathbf{T}$ and pointing to curve C^*, then

$$\mathbf{r}^*(s) = \mathbf{r}(s) + \epsilon(s)\mathbf{U}(s). \tag{7.5}$$

The twist number of a close ribbon is given by

$$\mathrm{Tw}_{C,C^*} \equiv \frac{1}{2\pi} \oint_{\mathbf{r}} \mathbf{U}(s) \times \frac{\mathrm{d}\mathbf{U}(s)}{\mathrm{d}s} \cdot \mathbf{T}(s)\,\mathrm{d}s, \tag{7.6}$$

while the writhe is the integral when both line integrals go along the axis curve

$$\mathrm{Wr}_{C,C^*} \equiv \frac{1}{4\pi} \oint_{\mathbf{r}} \oint_{\mathbf{r}} \mathbf{T}(s) \times \mathbf{T}(s^*) \cdot \frac{\mathbf{r}(s) - \mathbf{r}(s^*)}{\|\mathbf{r}(s) - \mathbf{r}(s^*)\|^3}\,\mathrm{d}s\,\mathrm{d}s^*. \tag{7.7}$$

A special case occurs when $\mathbf{U} = \mathbf{N}$ where the total twist is the same as the total

geometric torsion of the axis curve. Recovering the Darboux vector, $\mathbf{\Omega}_{\mathrm{FS}} = \kappa\mathbf{B} + \tau\mathbf{T}$, derived in the Chapter 1, we can rewrite equation 7.6:

$$\mathrm{Tw}_{\mathrm{FS}} = \frac{1}{2\pi} \oint_{\mathbf{r}} \mathbf{N} \times \frac{\mathrm{d}\mathbf{N}}{\mathrm{d}s} \cdot \mathbf{T}\,\mathrm{d}s \tag{7.8}$$

$$= \frac{1}{2\pi} \oint_{\mathbf{r}} \mathbf{N} \times (\mathbf{\Omega}_{\mathrm{FS}} \times \mathbf{N}) \cdot \mathbf{T}\,\mathrm{d}s \tag{7.9}$$

$$= \frac{1}{2\pi} \oint_{\mathbf{r}} \mathbf{\Omega}_{\mathrm{FS}} \cdot \mathbf{T}\,\mathrm{d}s \tag{7.10}$$

$$= \frac{1}{2\pi} \oint_{\mathbf{r}} \tau\,\mathrm{d}s. \tag{7.11}$$

All these quantities are based on how closed curves wind and unwind.

In the following we will be concerned with sets of curves with both ends fixed as those represented in Figure 7.2**a**, where a red, green and blue curves are constrained at the ends ($z = a$ and $z = b$). These curves are monotonic in the z direction, i.e., their tangent vectors have always a positive z-component. These curves are of interest since they model our experimental conditions when fibres are released. In this case, the position vector can be mapped in terms of the z coordinate. The angular variation of the relative position between two curves can be written as:

$$\frac{\mathrm{d}\theta(z)}{\mathrm{d}z} = \frac{(\mathbf{U}(z) \times \mathrm{d}\mathbf{U}(z)/\mathrm{d}z)_z}{\|\mathbf{U}(z)\|^2}. \tag{7.12}$$

The angle θ can be calculated, for instance, with respect to the x axis, so $\mathbf{U}(z) = \|\mathbf{U}(z)\|(\cos\theta(z), \sin\theta(z), 0)$. The net winding number, w, counts the number of times that the vector $\mathbf{U}(z)$ twists in the $x - y$ plane, from the point a to the point b:

$$w_{C,C^*} = \frac{1}{2\pi} \int_a^b \frac{\mathrm{d}\theta}{\mathrm{d}z}\,\mathrm{d}z \tag{7.13}$$

$$= \frac{\Delta\theta_{ab}}{2\pi} + n, \tag{7.14}$$

where $\theta(z = i) = \theta_i$, with $i = a, b$, and n is the number of times the angle θ crosses the negative x axis in the anti-clockwise direction. The net winding number is invariant relatively to the choice of the x axis. So, the x axis can be defined to be in the same direction of $\mathbf{U}(z = a)$, which further simplifies the equation 7.14, $w_{C,C^*} = \theta_b/2\pi + n$. Another consequence is that n can be counted as the half of the number of crossings, similarly to what was described above for the linking number. In this way, w_{C,C^*} can be calculated without integrating $\mathrm{d}\theta/\mathrm{d}z$.

The winding number can be useful, for instance, to estimate the degree of braiding of the coronal field of the sun[26] or to study the magneto-rheological properties of
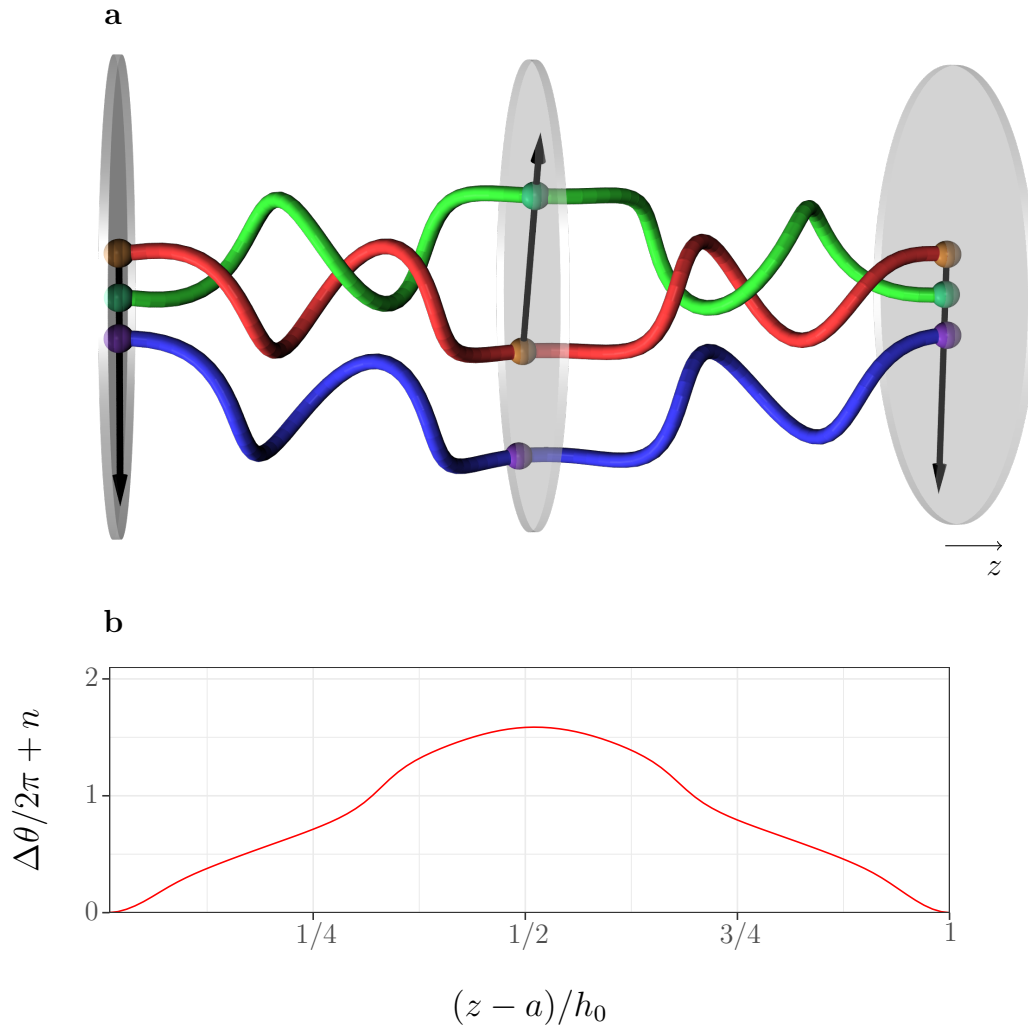
a

b

Figure 7.2: **a** Three filaments containing perversions, constrained at the ends ($z = a$ and $z = b$). The net winding number, which counts the number of times a vector that points from one curve to another winds from a to b. In the case of red and green curves, the vector depicted by a black arrow winds in the clockwise direction from $z = a$ to $z \approx (a + b)/2$ and then winds in the anticlockwise direction until $z = b$, so $w_{\text{red,green}} = 0$. **b** Evolution of the net winding number for red and green curves, where $h_0 = b - a$.

ferrofluids[27], [28]. In this chapter, the winding number will be used to measure how strands become entangled upon release. In this case, since strands are released with no initial twist and their ends are not allowed to rotate, handedness should be conserved when strands curl, i.e., upon release there can only be formed the same amount of loops with opposite handedness. As a result, the total winding number will always be equal

to zero. Figure 7.2**b** shows the evolution of the path integral in equation 7.13 for the curves red and green.

Both curves revolve around each other up increasing the winding number to a maximum near the middle of the strands. This point corresponds to the inversion of handedness in both strands, after which, the winding number decreases to zero. From a topological point of view, and imagining that one would tie both ends before release, then it is clear that the strands in Figure 7.2**a** cannot be knotted since all the process involves continuous deformations. However, from the point of view of the response to physical forces, the green and the red strands will behave much differently to the blue strand because of the physical constraints created by the presence of one strand on the movements of the other. This effect can even be amplified if one includes the impact of friction[29].

Therefore, the winding number can have the merits of capturing the degree of entanglement between strands. Nevertheless, if between two points, $\mathbf{r}_i$ and $\mathbf{r}_j$, $|w_{ij}| \geq 1$, then any translational movement of one strand forces the contact on the other. Therefore, it is important to develop a quantity that has the simplicity and properties of the net winding number, but produces a nonzero result when strands are locally linked, as the green and red strands in Figure 7.2**a**. We can define the partial winding number, $\bar{w}_{C,C^*}$, which registers the maxima and minima. In the previous case, red and blue curves have a partial winding number $\bar{w}_{\text{red,green}} \approx 1.59$, which means that the red and blue strand are linked once at the left and at the right of the perversions.

Figure 7.3 shows a more complex case where two strands are linked with the winding of two perversions. In this case, the evolution of the winding number has two relevant extrema, Figure 7.3**b**. From left to right in Figure 7.3**a**, the two filaments revolve around each other from one of the ends until reach a region with a symmetric perversion, the first extremum in Figure 7.3**b**, and then revolve in the opposite direction until reach another region with a symmetric perversion, the second extremum. Afterwards, the two filaments revolve in the opposite (original) direction until reaching the other end. For instance, if one considers the revolution between one of the ends and the closest perversion, the result of the winding number is nonzero. Therefore, the net winding number registers all the revolutions of the strands around the perversions by keeping the set of all extrema, $\bar{w}_{C,C^*} = \{e_1, e_2, ..., e_n\}$. In the case presented in Figure 7.3 $\bar{w}_{\text{red,green}} \approx \{1.36, -2.75\}$. Besides the maximum and the minimum at $z \approx a + (1/4)h_0$ and $z \approx a + (3/4)h_0$, respectively, there are other local maxima and minima. All these points have a value inferior to the unit, corresponding to loops that did not link. The the partial winding number registers all the extrema with a value superior to the unit.
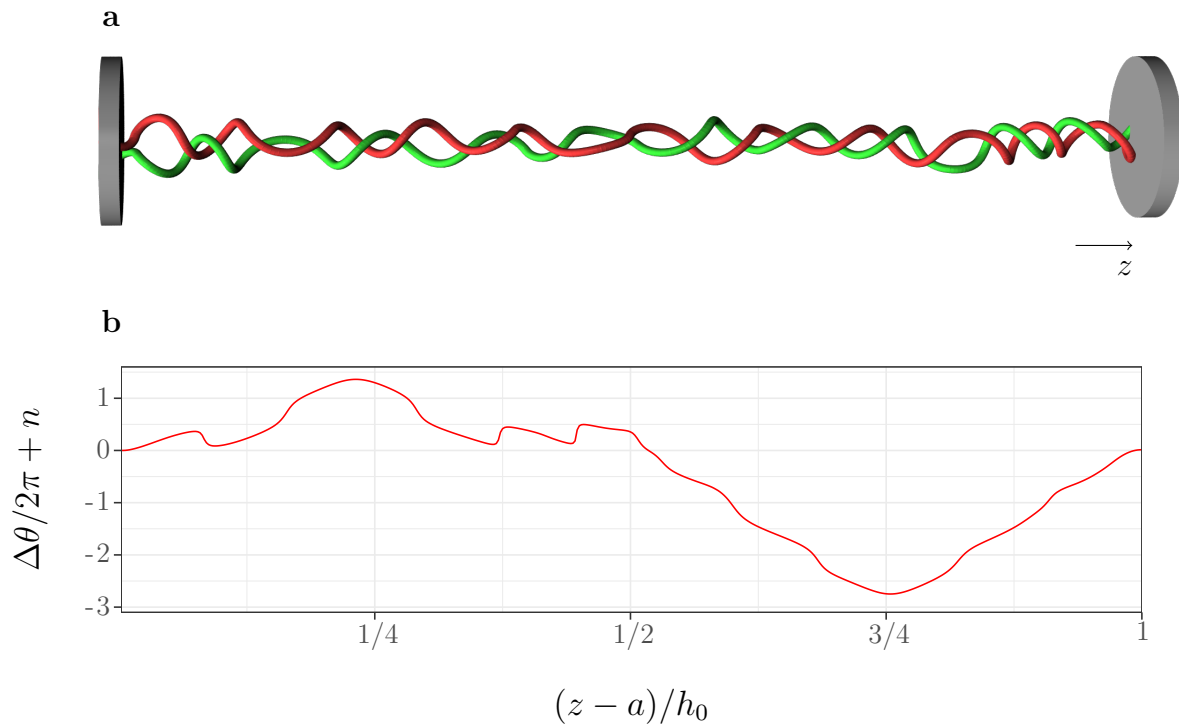
a

b

$$(z - a)/h_0$$

Figure 7.3: **a** Two filaments constrained by the winding of two perversions, with both ends fixed ($z = a$ and $z = b$). **b** Evolution of the net winding number for red and green curves, where $h_0 = b - a$. The linkage of both filaments from a to $z \approx (a + b)/2$ is similar to the example shown in Figure 7.2: the vector **U** rotates in the clockwise direction and then, after reaching the perversion centre, it inverts its rotation. However, in this case, the regions near the limits are not linked, which produces a wavy behaviour in the plot shown in **b**. From $z \approx (a + b)/2$ to b there is a perversion that rotates in the opposite direction, which results in the rotation of **U** in the anticlockwise direction and then, after reaching near the perversion region, **U** inverts its direction of rotation.

7.2 Braid diagrams

Objects like knots, weaves or other kinds of structures that contain entanglements are three-dimensional. However, it is possible to use simpler two dimensional representations, called braids diagrams, to register information concerning all crossings and, therefore, generate an alternative representation for the entanglements.

Braid diagrams consist in the projected lines of strands arranged from a top segment to a bottom segment and in such a way that when strands cross, the line of the strand on the top is drawn while the line of the strand lying on the bottom is interrupted. Lines cannot reverse their vertical direction, they should always move downwards (top-bottom diagrams are typically used in braid theory). Furthermore, projections in braid diagrams are merely indicative of the entanglements, so quantities like length, fibre diameter

or other physical properties are not represented to scale. Therefore, strands can be deformed and moved to different places if they do not intersect other strands. This deformation is called an elementary move. When a finite number of elementary moves is applied to a braid β and produces a different braid β', the two braids are said to be equivalent (or equal), which is denoted by $\beta \sim \beta'$. Figure 7.4 shows an example of two equivalent braid diagrams. In these braids, a number of allowed movements, transformed the crossings order of the left diagram – (1) red-blue, (2) red-green and (3) blue-green – in the equivalent right diagram – (1) blue-green, (2) red-green and (3) red-blue.
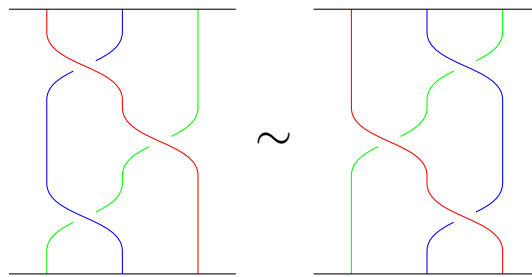

Figure 7.4: Two equivalent braids containing three strands.

Mathematicians have developed a formal approach to classify all types of braids and simple ways of classifying equivalent braids. This can be non trivial specially for braids with a large number of strands. Considering that a n-braid is a braid containing n strands, a n-braid β cannot be equivalent to a m-braid β', for $n \neq m$. By establishing the definition of equivalent braids, the next important step is to understand what happens when two braids are merged. The set of non-equivalent n-braids forms the n-braid group, $\mathbf{B}_n$, also known as Artin's n-braid group, since it was Artin who first in-depth investigated this group in 1925[30] and 1947[31]. The product of two n-braids, β and β', results in a new n-braid, $\beta\beta'$. An example of the product of two 3-braids is shown in Figure 7.5.
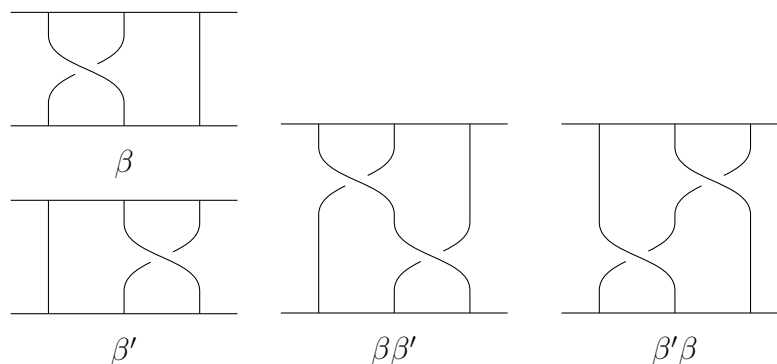

Figure 7.5: Two 3-braids, β and β', and their products, $\beta\beta'$ and $\beta'\beta$.

The product of braids have several properties (the proof of the following propositions can be found in [32], [33]). Considering β, β', β^* and $\beta^\dagger$ are n-braids:

- if $\beta \sim \beta'$ and $\beta^* \sim \beta^\dagger$, then $\beta\beta^* \sim \beta'\beta^\dagger$;

- braid product is associative, $(\beta\beta')\beta^* \sim \beta(\beta'\beta^*)$, but not necessarily commutative, $(\beta\beta')$ need not be equivalent to $(\beta'\beta)$;

- the simplest n-braid joins the n ends via straight lines, the identity or trivial braid, $\mathbf{1}_n$;

- the product of a braid with the identity is commutative, $\beta\mathbf{1}_n \sim \mathbf{1}_n\beta \sim \beta$;

- for any β, there is a β' such that $\beta\beta' \sim \mathbf{1}_n$; this braid β' is called the inverse of β and can be denoted as β^{-1};

- the set of equivalence classes forms the Artin's n-braid group, $\mathbf{B}_n = \mathcal{B}_{n/\sim}$, where $\mathcal{B}_n$ is the set of all n-braids.

The product of braids shown in Figure 7.5 puts in evidence that a braid might be segmented into smaller braids containing only a single crossing. These smaller braids have the same number of strands and positions, $i = 1, 2, \ldots n$, as the original braid, and are denoted by σ_i^ξ, where i stands for the crossing between braids in positions i and $i+1$ and ξ give the information of the crossing of the strand in i over, $\xi = 1$, or under, $\xi = -1$, the strand $i+1$. Then,

$$\beta = \sigma_{i_1}^{\xi_1}\sigma_{i_2}^{\xi_2}\ldots\sigma_{i_k}^{\xi_k}, \tag{7.15}$$

where $1 \leq i_1, i_2, \ldots, i_k \leq n-1$ and $\xi_i = \pm 1$. Any ordered combination of a set of σ constitutes a braid word and different relations in a presentation can be derived for $\mathbf{B}_n$. For instance, the following relations hold in $\mathbf{B}_n$:

$$\sigma_i\sigma_j = \sigma_j\sigma_i, \qquad \text{for any } 1 \leq i, j \leq n-1, \text{ with } |i - j| \geq 2 \tag{7.16}$$

$$\sigma_i\sigma_{i+1}\sigma_i = \sigma_{i+1}\sigma_i\sigma_{i+1}, \qquad \text{for any } 1 \leq i \leq n-2 \tag{7.17}$$

In fact, any other relation is a result from the above relations[32].

An important remark results from the product of a braid with its inverse, Figure 7.6, which results in a braid equivalent to a trivial braid. This result is also related with the total winding number of entangled filaments using perversions being zero. Once again, although topologically different braids can be equivalent, the energy to perform deformations of the filament are relevant. Using perversions to create entanglements
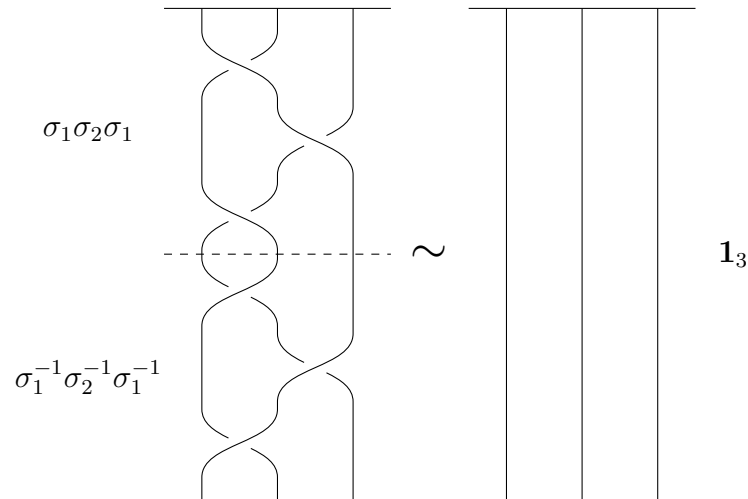
Figure 7.6: Product of a braid β with its inverse. The result is equivalent to the trivial braid $\mathbf{1}_3$.

will always result in a final braid equivalent to the trivial braid, topologically, but the number of crosses between perversions are relevant, physically.

7.3 Winding filaments using perversions

Perversions occur in a range of contexts in elastic structures, from the climbing plants to the DNA. Rather than being specific of a molecular orientation or from a complex pattern of forces distributions, perversions arise essentially from topological constraints and the need to coil to reach configurations with lower energies. Despite the existence of plenty of works discussing theoretical models and simulations to predict the behaviour that leads filaments to kink, there are not as many on how perversions can be used for real applications. Iamsaard et at.[34], developed a proof of concept of a structure capable of converting molecular movement into macroscopic work. Inspired by the movement and structure of tendrils, the group created a helical strip with both handednesses, with a perversion located at the middle of the structure, and observed a winding and unwinding behaviour of the strip by applying alternate cycles of irradiation of UV and visible light. Since both ends were clamped, the perversion junction produced a motion similar to the piston motion that can be found in classical mechanical motors.

There are several steps that are required to transform a bundle of fibres to a fabric. In the case of knitted fabrics, as the name mentions, yarns need to be knotted to each other, which require bending the filament into loops and move other strands (or the same) inside the loops. In woven fabrics, yarns are weaved one set between the other. Typically, the two sets, the warp and the weft (the filling), are interlaced at the right

angles using a loom. In a different type of technique, linking of fibres can be achieved by mechanical bonding, chemical bonding or thermal bonding. These kind of fabrics are known as nonwoven since, as the name indicates, they do not require weaving. The mechanical bonding in nonwoven fabrics is usually achieved by the entwining of fibres. These kind of entanglements use high pressures streams of water, hydroentanglement or spunlace, or by using the reciprocation of barbed needles through the filaments, needlepunching. In the specific case of helical structures, PPKs can be used to create entanglements between filaments.

In this section, we suggest another way to obtain fabrics by only using physical interactions and without the need of knitting or weaving the filaments: fabrics generated using perversions to entangle the filaments.

7.3.1 Winding two filaments

Perversions are structures that connect helices with different handednesses. As explained in the Chapter 5, a range of perversions with different shapes can be observed by twisting the filament in the middle of the perversion by an angle α. Two distinctive cases occur when the filament is not additionally twisted – symmetric perversions (tendril perversion) – and when the filament is twisted by π – antisymmetric perversions. In Figure 7.7, two filaments have the same intrinsic curvature (**a** and **b**), but swap the side where strained layers lay, as shown by the colours (in yellow are represented the most strained bonds).

When both filaments have strained bonds on the same sides, perversions wind in a similar movement, Figure 7.7**a1-b1**. The filaments do not touch each other until the end of the release, when loops start to tighten. For simulations where filaments have strained bonds on the opposite sides (filament at right is rotated by π, in the filament axis, relatively to the filament at left), perversions revolve around the helical axis and become linked, Figure **a3-b3**. For the other cases, where the strained bonds of the filament at right is rotated by $\pi/2$ and $3\pi/2$ as to the strained bonds of the filament at left, Figure **a2-b2** and **a4-b4**, strands linked when the perversions rotated on the same direction and did not link when the perversions rotated in opposite directions. In these last cases, perversions rotated in different directions, which highlights the importance of controlling the rotation direction of the perversions. In fact, similarly to the buckling instabilities of rods, that can bend in any direction right before the bending, there is also a bifurcation of solutions when a filament with intrinsic curvature curl. The winding of the perversion has equal chance of rotating in the clockwise and in the anticlockwise directions. It should also be noted that simulations do not include Brownian effects
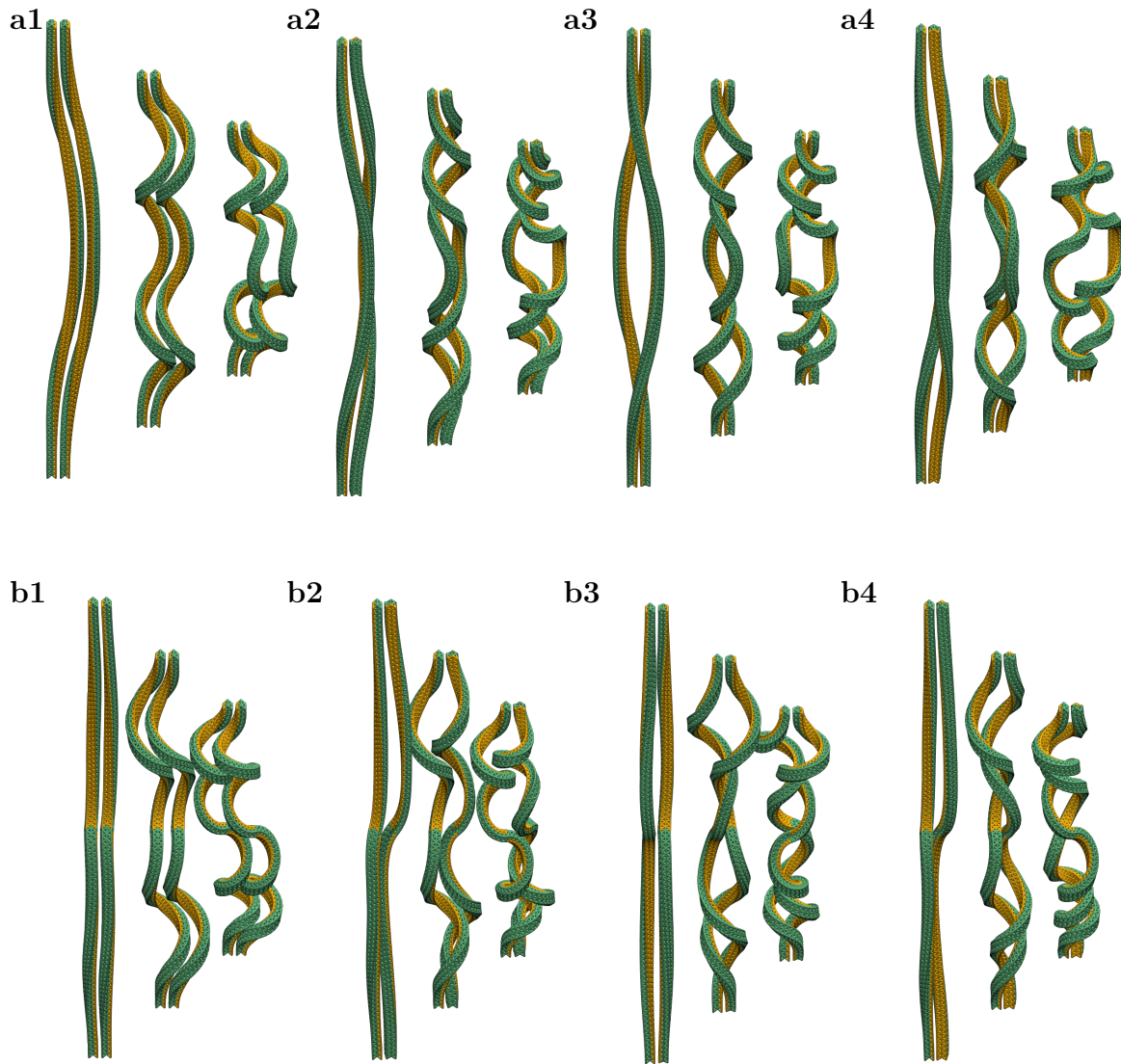
Figure 7.7: Filaments containing **a** symmetric and **b** antisymmetric perversions. From **1** to **4** one filament is rotated with respect to the other by 0, $\pi/2$, π and $3\pi/2$.

and filaments initial conditions and positions are replicated, which might have cause both perversions to rotate in the same direction in simulations of Figure **a1-b1** and **a3-b3**, since there is no contact between the filaments in the beginning of the coiling. In theory, it should be expected that arising perversions have the same probability of rotating in the clockwise or in the anticlockwise directions. However, the same does not happen in the other cases, where filaments make contact, which might induce a perturbation big enough to the filaments coil in a different fashion.

In the simulations where the filaments become intertwined, links start to be formed near the perversions region. In the case of the symmetric perversions, the central region of the perversions forms a hook-like structure, which, once attached, brings closer both

filaments while they wind during the release. In the case of antisymmetric perversions, the central point of the perversions remains aligned along the line connecting the endpoints. As a result, central points in antisymmetric perversions cannot initially attach. However, a link is formed by the surrounding loops in a similar way as the symmetric perversions do. In these simulations, it is also possible to observe that the link between the filaments must be formed in the first revolution of the winding as otherwise loops hinder linking the two filaments.

Another factor determining the ability to entangle two parallel filaments is the distance between them. Indeed, if filaments are too far away, they will not interact, as they need to be closer than the twice of the helical radius, $l_{i,j} < 2R$, to interact. The closer the filaments are, the easier it will be to wind one around another. Furthermore, it is expected to the higher number of linked loops, the more the filaments will be entangled. However, for a fixed filament length, L, if the intrinsic curvature is increased, in order to increase the number of loops, the helix radius will decrease. If the filament diameter, d, is about the same order of helical radius, the filaments may have not enough available space to wind, so $R > d$ reflects the upper limit of the intrinsic curvature. A simple diagram resuming the basic requirements for entangle filaments using perversions is shown in Figure 7.8.

After the analysis on the displacement of the filaments, it is important to solve the control over the direction of winding. By observing the pull and release of gift ribbons containing perversions, usually, it is possible to see that ribbons wind always in the same directions. Although gift ribbons may be considered twistless structures, intrinsic torsion is zero or much lower than the intrinsic curvature, the transition from straight to coiled is susceptible to small modifications in the morphology of the ribbon. Then, if the intrinsic torsion is changed by a small amount up to the middle of the filament and changed in a reverse direction, it might be enough to control on which direction the perversion will rotate. In theory, it should be easy enough to change the intrinsic torsion of the filaments. However, the same is not necessarily true for the electrospun fibres discussed in the Chapters 5 and 6. Recovering the generalization of perversions, a local change of the intrinsic torsion by changing the side where the pre-strain is applied. In the case of antisymmetric perversions, the symmetry of the transformation does not remove the uncertainty of the direction. But, for the remaining rotations, the symmetry is broken for all remaining twists. Experimentally, the local change of the intrinsic curvature in the polymeric fibres, described in Chapters 5 and 6, can be achieved by irradiating the fibres in different sides. Several simulations were performed so study the control of the winding by changing the intrinsic curvature on specific locations.

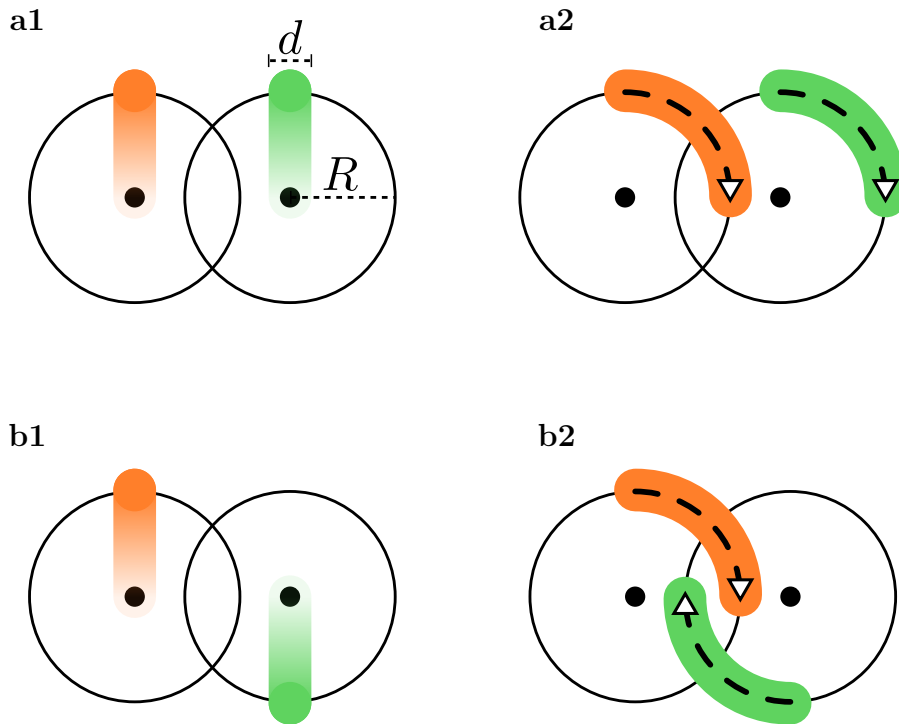In Figure 7.9 the release of three filaments containing specific different sides of

Figure 7.8: Diagram explaining the mechanism of entanglements using perversions. **a** If initially both perversion wind the same way, the filaments will not attach to each other. **b** If perversions are out of phase, here by π, and rotate in the same direction the perversions wind around each other and create intertwined loops.

pre-strained bonds is shown. Consider that filaments ($L = 400\sigma$) are a composition of four smaller primary sections, s_i, for $i = 1$ to 4, with equal lengths $L_s = 100\sigma$, and those smaller sections are composed by three other secondary sections, $s_{i,1}$, $s_{i,2}$ and $s_{i,3}$, with the lengths $L_{s_{i,1}} = 40\sigma$, $L_{s_{i,2}} = 20\sigma$ and $L_{s_{i,3}} = 40\sigma$. Also, consider that the leftmost pre-strained layer is in the east side of the filament. In all simulations, regions $s_{i,1}$ and $s_{i,3}$ have the east side pre-strained and the only changing feature between the simulations is which sides of $s_{i,2}$ are pre-strained. To simplify the description, if $s_{i,2}$ have the layer pre-strained at north (N) it will be designated by a N-region and at south (S) by S-region. For instance, in the case illustrated in Figure 7.9**a**, the filament have a NSNS configuration. In the N-regions, the pre-strained side rotates by $\pi/2$, in the anticlockwise direction, between $s_{i,1}$ and $s_{i,2}$ and rotates by the same amount, but in the clockwise direction, between $s_{i,2}$ and $s_{i,3}$. Upon release, the winding direction is in agreement with the two previous modifications. For S-regions, the analysis is the same but with a swap in the order of rotations, which leads to the formation of perversions winding in the opposite direction. In the simulation of Figure 7.9**b**, all regions s_i have the same configuration, NNNN. In this case, all perversions generated by the local torsion wind in the same direction. This generates three adjacent perversions
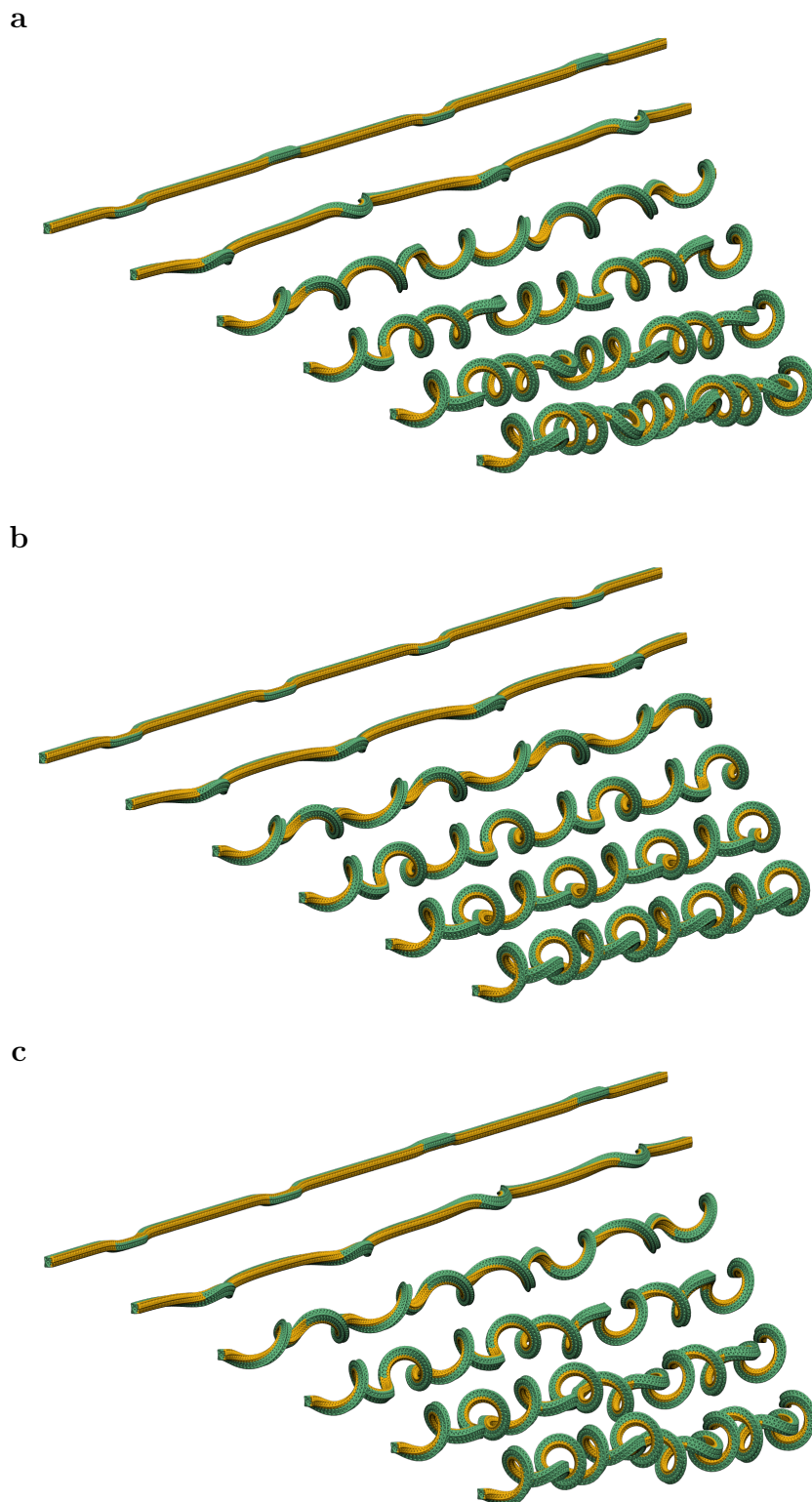
a

b

c

Figure 7.9: Simulations of the release of filaments containing specific pre-strained regions that generate perversions rotating **a** in alternated directions, **b** in the same directions; in **c** the first two perversions rotate in the opposite direction of the last two perversions.

due to the fact that helices at right and left of the main perversions have different handednesses. These additional perversions do not rotate during the release of the filament. In the previous case perversions rotate in opposite directions, which generates helices with a matching handedness, Figure 7.9**a**. In the last simulation, the filament have a NNSS configuration, Figure 7.9**c**. In this case, the winding behaviour of the filament is a combination of the two previous simulations, where two supplementary perversions appear between the main perversions rotating in the same direction. Then, it will be optimal to use NS(NS) configurations to prevent the formation of additional perversions.

We can conclude that perversions can be used to entangle two filaments. With higher intrinsic curvatures, the filaments will wind more but with the cost of decreasing the radius of curvature, which for a too high amount it can interfere with the interaction between the filaments. Also, winding direction can be controlled by changing locally the intrinsic curvature.

7.3.2 Winding filaments with multiple perversions

Demonstrating the entanglements of two perversions are encouraging because it suggests an idea to produce fabrics using a similar strategy. However, including one or more filaments, it requires improving the previous described strategy. In order to obtain a mesh of entangled filaments, we found inspiration in the structures devised for the metallic net fences that use zigzag-patterned wires, as represented in Figure 7.10. It is clear that the green wire crosses alternately the red wire and the blue wire. We sought producing a similar entangled effect, however our goal is to produce it without interlooping the wires. Our strategy had in mind the, on one side, the initially straight filaments will invade their neighbours space during the winding process upon release; on the other side, perversions can work to hook neighbouring filaments. In this way, we found that it is possible to entangle one filament with those immediately on its side. Curiously, locally, the effects are similar to the metallic net fences entanglement process.

By using the approach of the simulation using a NS(NS) configuration, as shown in Figure 7.9**a**, it was hard to generate nets with filaments connecting more than one neighbour filament. Therefore, between the primary sections, which in this case are the N- and S-regions, an additional rotation of π of the pre-stained side was introduced. This way, right after starting the release, and before the coiling due to the buckling instability, the N-regions get to one adjacent filament and the S-regions get closer to the other filament, as shown in Figure 7.11**a**.

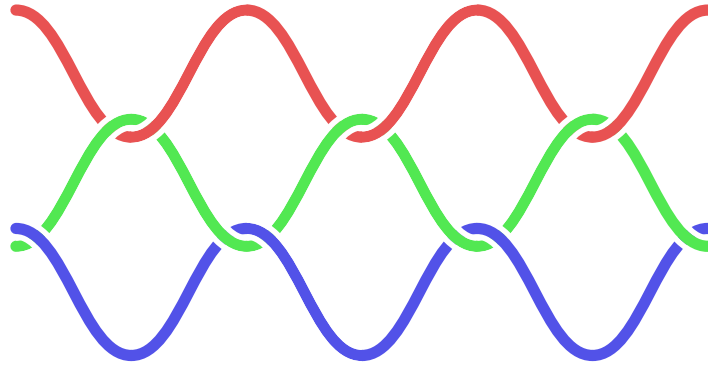The simulation shown in the Figure 7.11 has twenty five filaments with $L = 820\sigma$,

Figure 7.10: Depiction of a metallic net fence using zigzag wires.

2σ by 2σ of cross-section, σ bead-to-bead initial separation, 0.6σ of pre-strained bond, and with four N-regions intercalated with four S-regions. The filaments are separated by 2.5σ and even filaments are rotated by π in respect with odd filaments.

Although in this simulation filaments were set with perversions to interact alternately with the neighbouring filaments, due the closeness of the filaments and a suitable intrinsic curvature, after the first half rotation of the perversions, a second link also formed in the following half rotation. In this case, perversions can interact with more than one filament. The interaction between neighbouring filaments can be controlled by setting up different initial separations between the filaments. This can be important because it allows to draw patterns in which perversions are made to interact (or not) with neighbouring filaments and, in this way, create fabrics with different patterns and mechanical properties. From the total extension to the fabric at rest there is a difference of ≈ 4.5 times. So, the final mesh should have a good elasticity. However, one important difference can be readily inspected by observing the release instant shown in Figure 7.9**b**: the elastic behaviours in the y-direction and in the z-direction are likely to be different. Another important characteristic of fabrics is how they behave near the edges. For instance, weaved filaments require a different termination at the borders to keep the fabric from unravelling or fraying. In the case of meshes linked by perversions there might be some issues on the ends. In the simulation of Figure 7.11, the ending segments have no intrinsic curvature to form a clasp-like structure and prevent the fabric of fraying.

Figures 7.12 and 7.13 show two examples of simulations where one point at the middle of a filament is pulled in the y-direction, perpendicular to the direction of release, z, and in the plane of the fabric, and in the x-direction, perpendicular to y and z, respectively. All ends of the fabric, except the ones which filament is being pulled, are kept fix. There are differences between the two computational experiments on how much the filament is stretched until coming out of the fabric. This difference can be
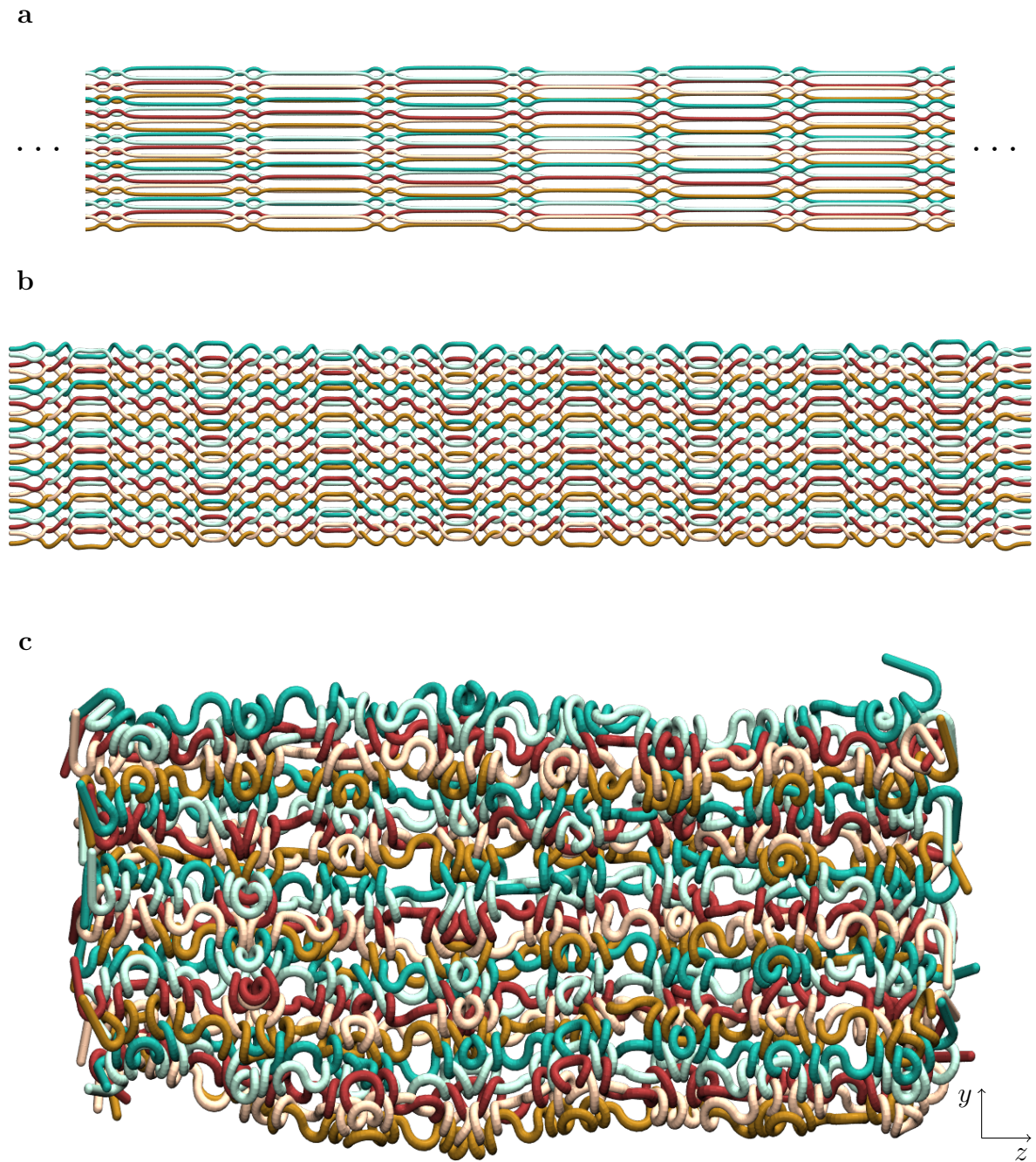
a

b

c

Figure 7.11: Formation of a fabric by winding twenty five filaments with perversions.

explained by how the fabrics responds to the extension in each direction. Another justification might be the global winding of the filaments around each other.

7.3.3 Fast unwinding

In general, knitted fabrics have good flexibility, are durable and resistant to friction and other mechanical agents. By contrast, nonwoven fabrics might not perform as good as knitted fabrics. Nevertheless, they have features more suitable for technical tasks, like for filtration, ventilation, insulation, liquid absorption or other purposes, and since they are, usually, cheaper and more eco-friendly they are more appropriate for disposable applications. In the case of filaments with intrinsic curvature, the occurrence of single or multiple perversions in one filament is already mathematically well understood. The number of perversions and their location depend on the length of the filament and on the amount of the intrinsic curvature. However, perversions are not static and there are few works about the dynamics of perversions. For instance, by twisting one of the ends, the perversion can move along the helical structure. When two perversions meet in the same region they can also disappear. The dynamics of perversions is rich in different kinds of phenomena. In this subsection, an interesting occurrence will be presented when pulling apart two linked filaments.

Figure 7.14 shows two intertwined filaments with a single perversion each in the middle being pulled by one of the perversions when the other is kept fixed. The remaining parts of the filaments are free to move. In the beginning of the draw, perversions start to stretch until both filaments start to curling around themselves. In the meanwhile, the still linked filaments revolve around the axis of the pulling direction, until all loops are untangled and the filaments become separated. Most of both filaments have now a double helix structure and they have opposite handednesses. Apart the direction of the handednesses, the result is somewhat expected, considering filaments are being stretched and their stretched half parts have enough space to wind and form helical joint structures.

Using the same simulation but now, instead of pulling both filaments by the perversions, all ends of the filaments are pulled out in a direction perpendicular to the release, as shown in Figure 7.15. The filaments start to unwind but with the pulled ends getting straight while the rest of the coils, between the ends and the perversions, do not change considerably their shape. At some point, both filaments undergo in an instability that untangles most part of the filaments.
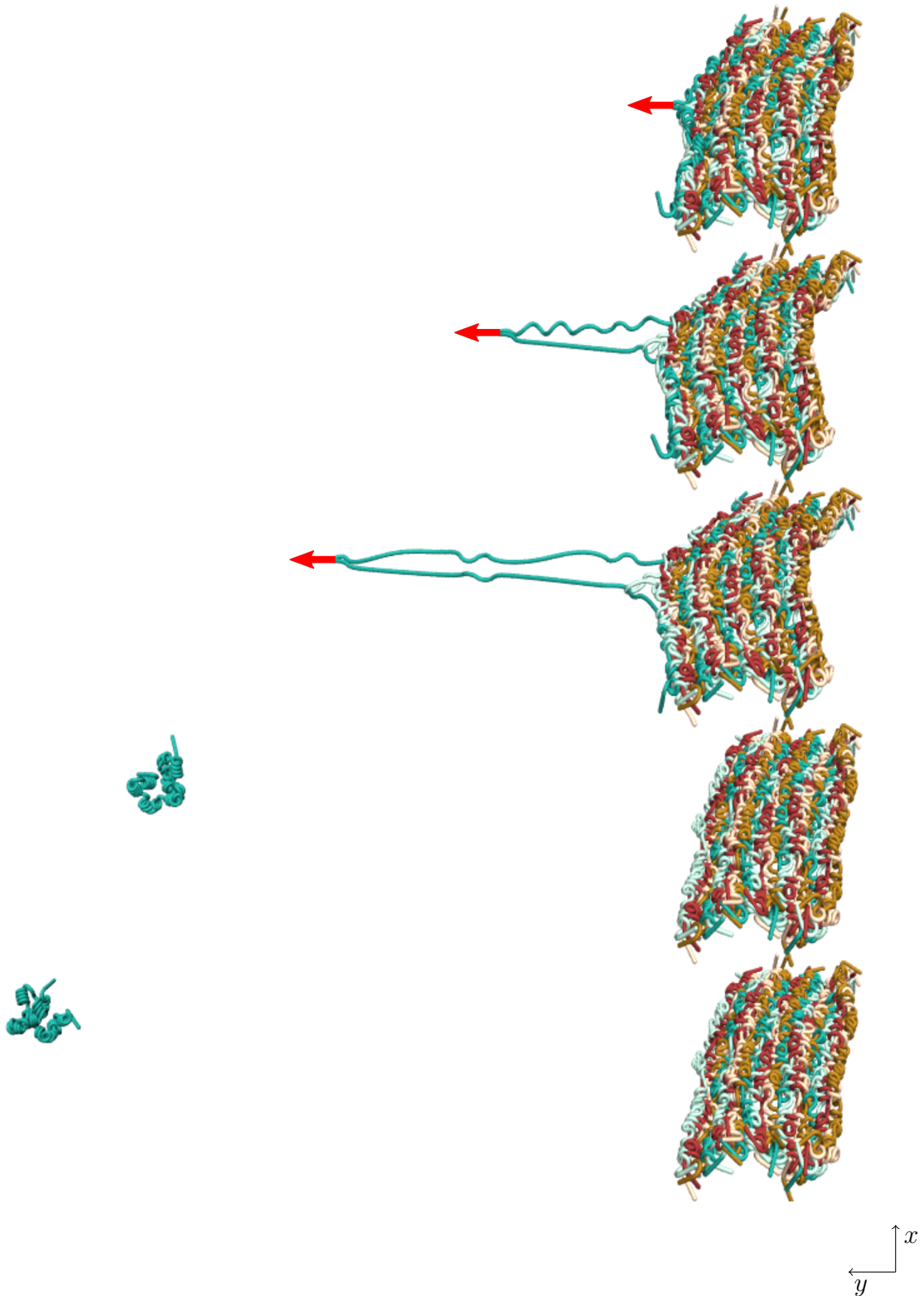
Figure 7.12: Pulling of a filament in the y direction. The dragging force is represented by the red arrow. All filaments have both ends fixed, with the exception of the filament that is being removed.
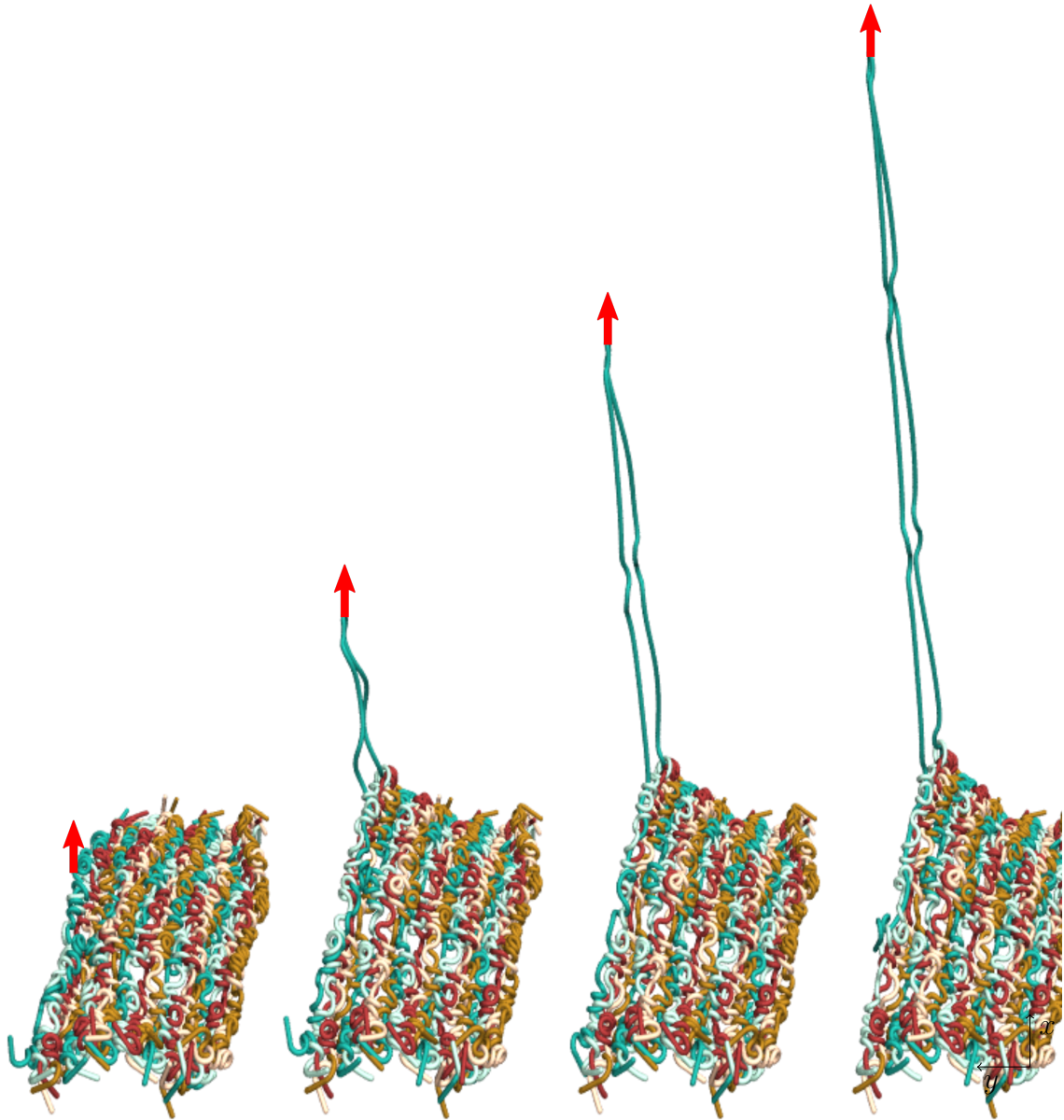
Figure 7.13: Pulling of a filament in the x direction. The dragging force is represented by the red arrow. All filaments have both ends fixed, with the exception of the filament that is being removed.
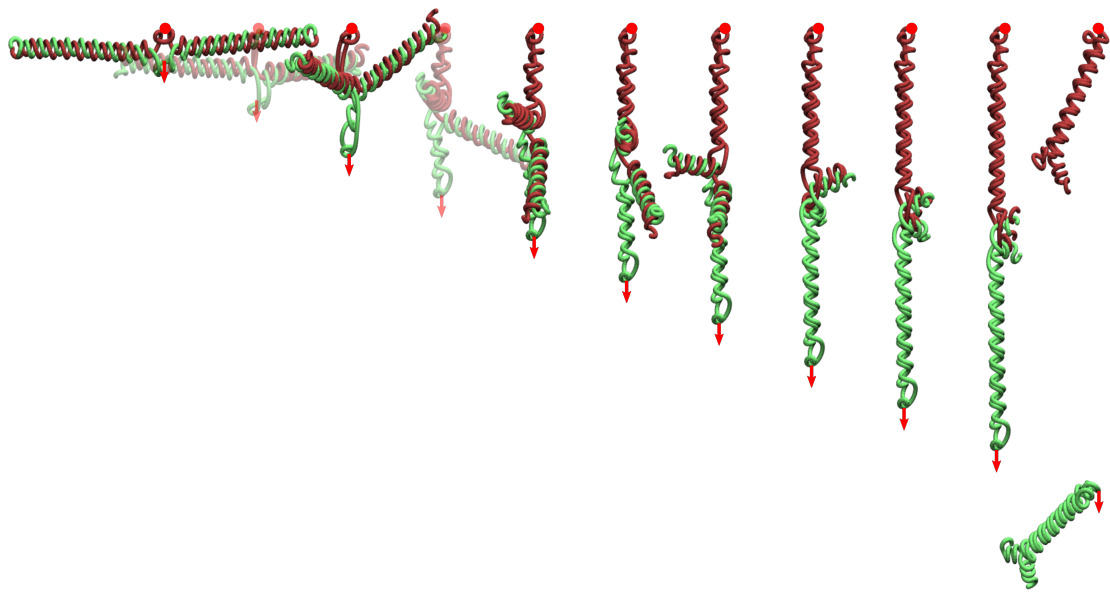
Figure 7.14: Separation of two filaments linked by a perversion: red filament is fixed at the point indicated with a red dot while green filament is dragged by a force represented with a red arrow. For the sake of visualization, some instants have transparency effects.
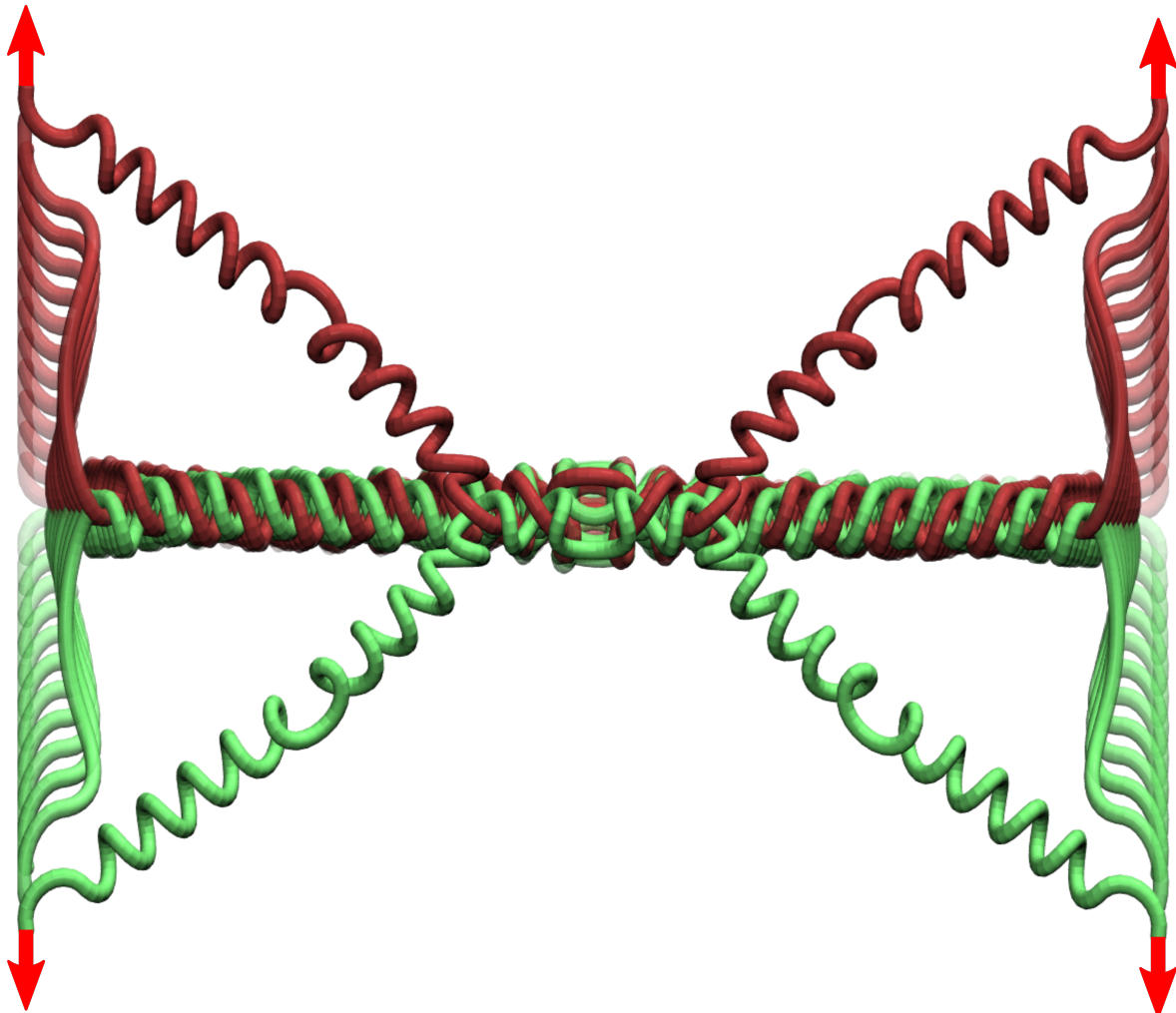
Figure 7.15: Separation of two filaments linked by a perversion: all ends of the filaments are dragged by forces represented with red arrows. To emphasize the fast unlooping, that occurs between the two instants where the ends are farther from the helical centreline, all instants are overlaid with the increasing opaqueness. For the sake of visualization, the red arrows are shown only in the last instant.

7.4 Entanglements of helices with PPKs

The mechanical bonding in nonwoven fabrics is usually achieved by entwining fibres. These kind of entanglements can be achieved by using high pressures streams of water, hydroentanglement or spunlace, or by using the reciprocation of barbed needles through the filaments, needlepunching. An alternative method was put forward by Abreu[35], when helical structures are present. In this case, local and stable links that can be formed when one loop of one helix forces inside another helix until becomes trapped, creating what was called a physical pseudoknot (PPK). Howerer, it was unclear what kind of strategies could be used to create systems with many PPKs. In this section, computer simulations will be used to model the behaviour of many helical chains. As we will see, there are several factors that might restrict the formation of PPKs, such as the geometry of the helix or the interaction dynamics between the helices.

Our simulations allow considering the formation of multiple pseudoknots, in order to identify the best strategies to produce non-woven fabrics. Given the size of the systems involved, simulations are lengthy (one run takes typically two to three days, depending on the size of the system). Several strategies have been studied. These were, in chronological order: a) relaxation of two sets of helical fibres; b) release of an helix over a mat of helices using well defined movement paths of a throwing nozzle

7.4.1 Release of stretched helices

Concerning the properties of systems with many PPKs, multiple simulations were performed to study the dynamics of the release of stretched helices. Different angles of release were simulated. Results revealed less formation of PPKs than expected. During relaxation, due to the helix geometry, filaments tend to either align or force apart.

For instance, some of the helices in the Figure 7.16 come out of the plane of release, preventing helices to become constrained to each other in a early stage of the simulation.

7.4.2 Entangling helices using a deposited single helix

Another strategy conceived to form PPKs consisted on a controlled releasing of a coil over a mat of helices, Figure 7.17.

Different velocities releases and paths were tested. Although multiple PPKs could be formed using this method, the strategy was not as simple and efficient enough to be
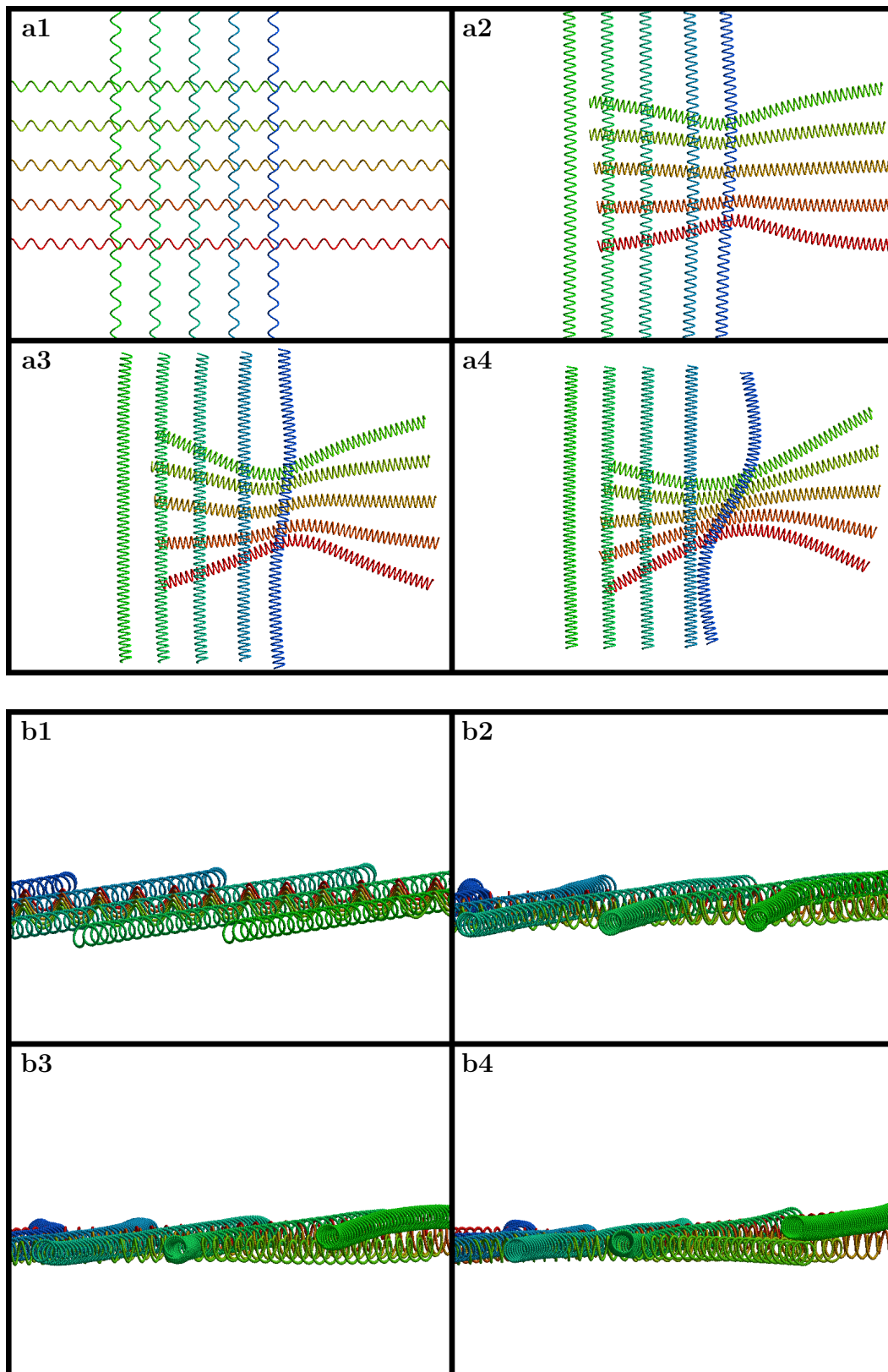
Figure 7.16: **a** top and (b) side views of a simulation showing the release of stretched helices. The filaments are displaced as a quadrangular grid and released at constant rate with the ends fixed. During the release some helices become out of plane, as can observed in **b**.

implemented in a practical experiment. Create a first PPK is easy because the helix is rather small and thus the filament movement can be controlled. After a first link being created, deposited helix movement becomes more restricted, disabling certain moves that promoted the formation of next PPKs.

The first strategy did not produce results as good as expected, as simulations showed that frequently helices repelled each other and did not produce physical pseudoknots. Interestingly, however, an old patent that we found in the meantime, proposed a similar strategy to produce entanglements[36]. This patent, however, was not aware of the physical pseudoknot effect, and followed a different motivation, not requiring a robust entanglement to be established. Indeed, our simulations showed that this patent could not be claiming a robust mechanism for producing entanglements. This motivated us further on the search of mechanisms promptly producing pseudoknots on a large scale.

As a result, a second strategy was conceived consisting of releasing helical fibres over a mat of helices through a nozzle. The nozzle would move according to either a random path or a well-defined trajectory, Figure 7.17. Although it was shown that more than one PPK could be produced in this way, the strategy did not seem to be robust enough for practical industrial applications.

Currently, we are improving a mechanism of entangling filaments using helical loops by considering other approaches. For instance, one idea consists in using two sets of fibres in different states. One set is made of helices, while a second set consists of straight fibres, matched within the first set, and which when released gain a helical conformation. Results seem more robust relatively to those using the former strategies, although considerable work is still required to completely clarify whether this new strategy can be promising from a practical point of view, in which case posting a patent is still under consideration.
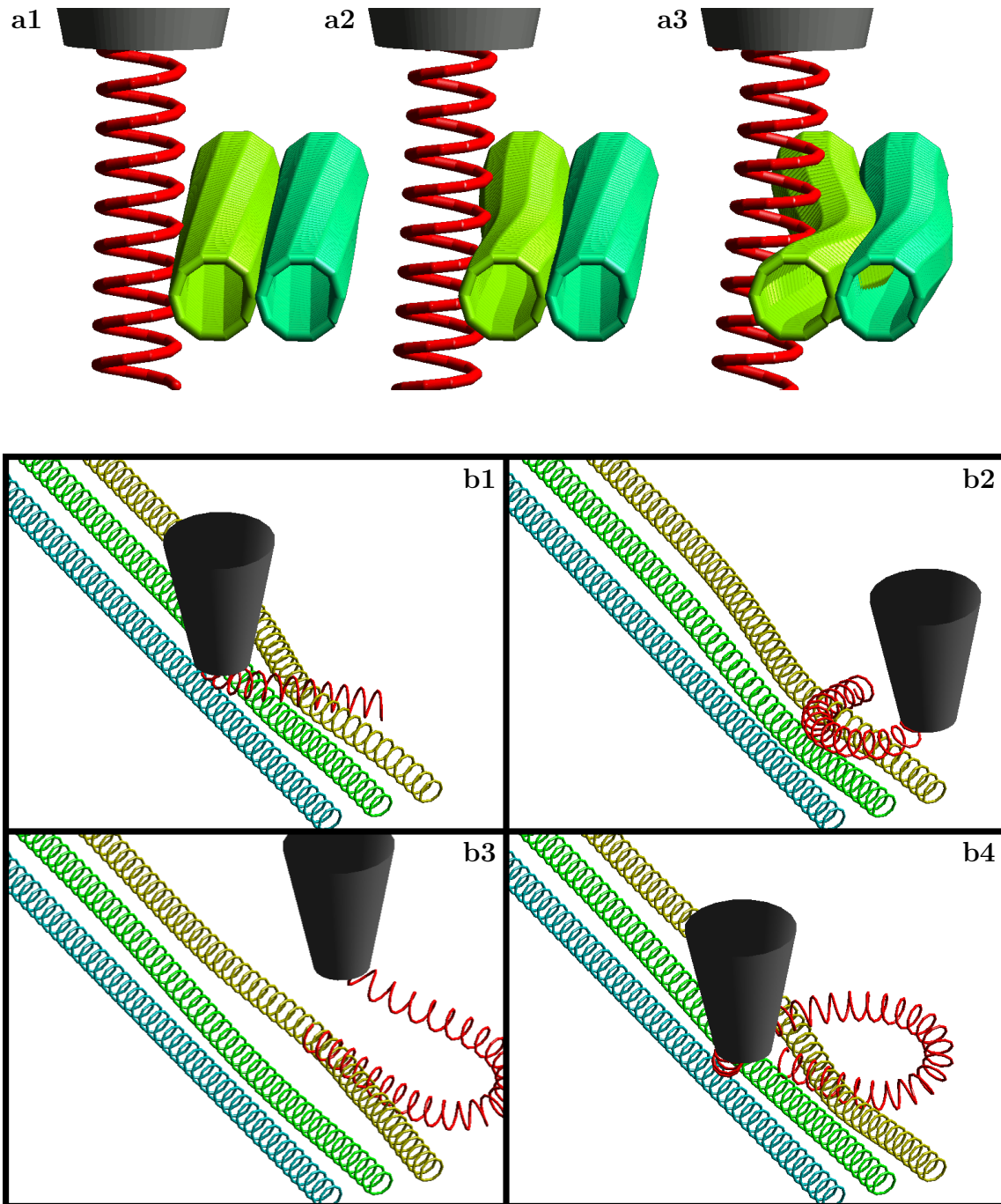
Figure 7.17: Simulations of a nozzle ejecting a red helix and moving through a mesh of helices. From **a1** to **a3** the side view of a case when the movement of the nozzle makes the red helix to be pushed into the green helix. Instead of getting intertwined, both helices behave as two elastic cylinders. From **b1** to **b4**, the red helix gets intertwined with the yellow helix, however it cannot make a second link.

References

[1] R. Vidoni, T. Mimmo, and C. Pandolfi, "Tendril-Based Climbing Plants to Model, Simulate and Create Bio-Inspired Robotic Systems," *Journal of Bionic Engineering*, vol. 12, no. 2, pp. 250–262, Apr. 2015. DOI: 10.1016/S1672-6529(14)60117-7.

[2] Y. Zhao and T. Ikeda, Eds., *Smart Light-Responsive Materials: Azobenzene-Containing Polymers and Liquid Crystals*, Hoboken, N.J: Wiley, 2009, 514 pp.

[3] M. A. Ratner and D. Ratner, *Nanotechnology: A Gentle Introduction to the next Big Idea.* Upper Saddle River, NJ: Prentice Hall, 2003, 188 pp.

[4] S. Xu, Z. Yan, K.-I. Jang, W. Huang, H. Fu, J. Kim, Z. Wei, M. Flavin, J. McCracken, R. Wang, A. Badea, Y. Liu, D. Xiao, G. Zhou, J. Lee, H. U. Chung, H. Cheng, W. Ren, A. Banks, X. Li, U. Paik, R. G. Nuzzo, Y. Huang, Y. Zhang, and J. A. Rogers, "Assembly of micro/nanomaterials into complex, three-dimensional architectures by compressive buckling," *Science*, vol. 347, no. 6218, pp. 154–159, Jan. 9, 2015. DOI: 10.1126/science.1260960.

[5] K.-I. Jang, K. Li, H. U. Chung, S. Xu, H. N. Jung, Y. Yang, J. W. Kwak, H. H. Jung, J. Song, C. Yang, A. Wang, Z. Liu, J. Y. Lee, B. H. Kim, J.-H. Kim, J. Lee, Y. Yu, B. J. Kim, H. Jang, K. J. Yu, J. Kim, J. W. Lee, J.-W. Jeong, Y. M. Song, Y. Huang, Y. Zhang, and J. A. Rogers, "Self-assembled three dimensional network designs for soft electronics," *Nature Communications*, vol. 8, p. 15 894, Jun. 21, 2017. DOI: 10.1038/ncomms15894.

[6] A. Lendlein, H. Jiang, O. Jünger, and R. Langer, "Light-induced shape-memory polymers," *Nature*, vol. 434, no. 7035, pp. 879–882, Apr. 14, 2005. DOI: 10.1038/nature03496.

[7] D. Ratna and J. Karger-Kocsis, "Recent advances in shape memory polymers and composites: A review," *Journal of Materials Science*, vol. 43, no. 1, pp. 254–269, Jan. 2008. DOI: 10.1007/s10853-007-2176-7.

[8] S. T. Ly and J. Y. Kim, "4D printing – fused deposition modeling printing with thermal-responsive shape memory polymers," *International Journal of Precision Engineering and Manufacturing-Green Technology*, vol. 4, no. 3, pp. 267–272, Jul. 2017. DOI: 10.1007/s40684-017-0032-z.

[9]   Y. Liu, H. Lv, X. Lan, J. Leng, and S. Du, "Review of electro-active shape-memory polymer composite," *Composites Science and Technology*, vol. 69, no. 13, pp. 2064–2068, Oct. 2009. DOI: 10.1016/j.compscitech.2008.08.016.

[10] A. N. Vasil'ev, V. D. Buchel'nikov, T. Takagi, V. V. Khovailo, and E. I. Estrin, "Shape memory ferromagnets," *Physics-Uspekhi*, vol. 46, no. 6, pp. 559–588, Jun. 30, 2003. DOI: 10.1070/PU2003v046n06ABEH001339.

[11] S. Tibbits, "4D Printing: Multi-Material Shape Change," *Architectural Design*, vol. 84, no. 1, pp. 116–121, Jan. 2014. DOI: 10.1002/ad.1710.

[12] X. Yan and P. Gu, "A review of rapid prototyping technologies and systems," *Computer-Aided Design*, vol. 28, no. 4, pp. 307–318, Apr. 1996. DOI: 10.1016/0010-4485(95)00035-6.

[13] N. Oxman, S. Keating, and E. Tsai, *Functionally Graded Rapid Prototyping*. Sep. 16, 2011, 483 pp. DOI: 10.1201/b11341-78.

[14] T. Tachi, "Geometric Considerations for the Design of Rigid Origami Structures," *Proceedings of the International Association for Shell and Spatial Structures (IASS) Symposium*, vol. 12, no. 2, pp. 458–460, 2010.

[15] S. Pellegrino and C. D. Structures, Eds., *Deployable Structures*, Courses and lectures / International Centre for Mechanical Sciences 412, Wien: Springer, 2001, 360 pp.

[16] T. Lessinnes and A. Goriely, "Design and Stability of a Family of Deployable Structures," *SIAM Journal on Applied Mathematics*, vol. 76, no. 5, pp. 1920–1941, Jan. 2016. DOI: 10.1137/16M1070293.

[17] M. C. Natori, N. Katsumata, H. Yamakawa, H. Sakamoto, and N. Kishimoto, "Conceptual Model Study Using Origami for Membrane Space Structures," ASME, Aug. 4, 2013, V06BT07A047. DOI: 10.1115/DETC2013-13490.

[18] W. G. van Doorn, "Flower opening and closure: A review," *Journal of Experimental Botany*, vol. 54, no. 389, pp. 1801–1812, Aug. 1, 2003. DOI: 10.1093/jxb/erg213.

[19] A. G. Volkov, T. Adesina, V. S. Markin, and E. Jovanov, "Kinetics and Mechanism of Dionaea muscipula Trap Closing," *PLANT PHYSIOLOGY*, vol. 146, no. 2, pp. 694–702, Dec. 7, 2007. DOI: 10.1104/pp.107.108241.

[20] A. Goriely and M. Tabor, "Spontaneous Helix Hand Reversal and Tendril Perversion in Climbing Plants," *Physical Review Letters*, vol. 80, no. 7, pp. 1564–1567, Feb. 16, 1998. DOI: 10.1103/PhysRevLett.80.1564.

[21]   M. Stoppa and A. Chiolerio, "Wearable Electronics and Smart Textiles: A Critical Review," *Sensors*, vol. 14, no. 7, pp. 11 957–11 992, Jul. 7, 2014. DOI: `10.3390/s140711957`.

[22]   M. Parvinzadeh Gashti, E. Pakdel, and F. Alimohammadi, "Nanotechnology-based coating techniques for smart textiles," in *Active Coatings for Smart Textiles*, Elsevier, 2016, pp. 243–268. DOI: `10.1016/B978-0-08-100263-6.00011-3`.

[23]   R. L. Ricca and B. Nipoti, "GAUSS' LINKING NUMBER REVISITED," *Journal of Knot Theory and Its Ramifications*, vol. 20, no. 10, pp. 1325–1343, Oct. 2011. DOI: `10.1142/S0218216511009261`.

[24]   Orlandini, E, Tesi, M. C., Whittington, S. G., Sumners, D. W., and Janse van Rensburg, E. J., "The writhe of a self-avoiding walk," *Journal of Physics A: Mathematical and General*, vol. 27, no. 10, p. L333, 1994.

[25]   M. A. Berger, L. H. Kauffman, B. Khesin, H. K. Moffatt, R. L. Ricca, and D. W. Sumners, *Lectures on Topological Fluid Mechanics*, R. L. Ricca, Ed., ser. Lecture Notes in Mathematics. Berlin, Heidelberg: Springer Berlin Heidelberg, 2009, vol. 1973. DOI: `10.1007/978-3-642-00837-5`.

[26]   M. A. Berger, "The Development of Structure in Coronal Magnetic Fields," in *Activity in Cool Star Envelopes*, O. Havnes, B. R. Pettersen, J. H. M. M. Schmitt, and J. E. Solheim, Eds., Dordrecht: Springer Netherlands, 1988, pp. 21–24. DOI: `10.1007/978-94-009-2951-7_3`.

[27]   P. Pieranski, S. Clausen, G. Helgesen, and A. T. Skjeltorp, "Braids Plaited by Magnetic Holes," *Physical Review Letters*, vol. 77, no. 8, pp. 1620–1623, Aug. 19, 1996. DOI: `10.1103/PhysRevLett.77.1620`.

[28]   K. de Lange Kristiansen, G. Helgesen, and A. T. Skjeltorp, "Braid theory and Zipf-Mandelbrot relation used in microparticle dynamics," *The European Physical Journal B*, vol. 51, no. 3, pp. 363–371, Jun. 2006. DOI: `10.1140/epjb/e2006-00241-7`.

[29]   M. K. Jawed, P. Dieleman, B. Audoly, and P. M. Reis, "Untangling the Mechanics and Topology in the Frictional Response of Long Overhand Elastic Knots," *Physical Review Letters*, vol. 115, no. 11, Sep. 11, 2015. DOI: `10.1103/PhysRevLett.115.118302`.

[30]   E. Artin, "Theorie der Zöpfe," *Abhandlungen aus dem Mathematischen Seminar der Universität Hamburg*, vol. 4, no. 1, pp. 47–72, Dec. 1, 1925. DOI: `10.1007/BF02950718`.

References

[31] E. Artin, "Theory of Braids," *The Annals of Mathematics*, vol. 48, no. 1, p. 101, Jan. 1947. DOI: 10.2307/1969218. JSTOR: 1969218?origin=crossref.

[32] K. Murasugi and B. I. Kurpita, *A Study of Braids*, ser. Mathematics and its applications v. 484. Dordrecht ; Boston: Kluwer Academic Publishers, 1999, 272 pp.

[33] M. Chiodo, "An introduction to braid theory," Msc, University of Melbourne, 2005.

[34] S. Iamsaard, S. J. Aßhoff, B. Matt, T. Kudernac, J. J. L. M. Cornelissen, S. P. Fletcher, and N. Katsonis, "Conversion of light into macroscopic helical motion," *Nature Chemistry*, vol. 6, no. 3, pp. 229–235, Feb. 9, 2014. DOI: 10.1038/nchem. 1859.

[35] F. Vistulo de Abreu, R. G. Dias, and C. von Ferber, "Pseudo-knots in helical structures," *Soft Matter*, vol. 4, no. 4, p. 731, 2008. DOI: 10.1039/b719234g.

[36] R. Steel, "Coiled-filament non-woven fabrics," 2 9 1971.

Chapter

8

Conclusions and Recommendations

This thesis presents the results of research performed from January 2012 to October 2017, at the Physics Department of the University of Aveiro and at the Department of Materials Science of the Faculty of Science and Technology of New University of Lisbon. The subject under consideration was structures with helical filaments. The research was done in collaboration with my supervisors, Professor Fernão Vístulo de Abreu and Professor Maria Helena Godinho.

We began the manuscript (Chapter 2) by providing some insights about the dynamics of elastic filaments using molecular dynamics simulations. Two different algorithms, Filament Simulator (FS) and Large-scale Atomic/Molecular Massively Parallel Simulator (LAMMPS), were presented. FS algorithm was used to generate linear chains with helical topologies for studying the dynamics of physical pseudoknots (PPKs). In LAMMPS, filaments chains were generated by using the bead-springs model.

In Chapter 3, a description of the properties of the materials used to produce electrospun microfibres was introduced. Some details about the electrospinning set up, focusing on the equipment, the operation

and used collectors, was next presented. In addition to the equipment to produce microfibres, it was explained how the coiling in specific locations of the polyurethane fibres was generated by using UV light and opaque masks. Technical details of the used characterization techniques were given in the end of the chapter.

Electrospinning technique and the strategies to produce synthetic electrospun helical fibres was reviewed in Chapter 4. The main procedures to produce helical microfibres were categorized by the origin of the coiling in fibres: (1) due to mechanical buckling instabilities, when the fibres are impinged on the collectors and a high deformation occurs; (2) due to twisting motion, when the fibres are twisted by the action of external mechanical or electric fields; (3) due to asymmetric contraction, when the helices occur by the existence of a mismatch of the elastic properties between different regions of the fibre.

In Chapter 5, we have proposed a range of new geometries in perversions. The description of the properties of the perversions focused in the demonstration of the occurrence of two extreme types of perversions, denominated symmetric and antisymmetric, depending on how intrinsic curvature is generated in filaments, and was computationally and experimentally observed. Symmetric and antisymmetric perversions have different shapes, upon release they rotate around the centreline in or out of phase relatively to their centres and adopt different final configurations. The results presented in Chapter 5 focused on describing the generalization of the concept of perversions and have the purpose to instigate a new attention in a phenomenon that was observed, at least, for more than two centuries.

In Chapter 6 we reported an improvement of the methodology to obtain helical electrospun filaments, by modifying the properties of the fibres while being stretched. Irradiating the fibres with UV while being stretched decreased the required time for generating a layer with different physical properties from 24 h to a few minutes. We proposed also a simple strategy to obtain experimentally microfilaments composed by segments with different curvatures. Besides displaying different helical properties, fibres also displayed different critical points of when the regions started coiling, upon release. We inferred that the critical points depend on a critical tension to curl dependant on the intrinsic curvature of the filament, as expected theoretically and confirmed computationally.

Further studies are still necessary to explain in depth the phenomenons reported in Chapter 5 and Chapter 6. Considering the results reported in this thesis, we propose some recommendation for future investigation:

- use finite element method to study the dynamics of filaments with more complex and realistic geometries;

- further investigate theoretically how the additional twist change in the perversions modifies the mathematical treatment reported by McMillen and Goriely[1];

- if we artificially force one (symmetric) perversion to travel in a filament until find another perversion, they undo both inversions; understand what happens when both types of perversions occur and how they interact can also be important for future applications;

- perversions have a huge potential for applications; there are many fields, such as nanotechnology and robotics, interested in the creation of nano and microrobots; as reported in this thesis, some structures in nature use perversions as an advantage to perform non-trivial movements[2], which can be further explored by, first, reproducing the same types of movements and, second, exploring the inclusion of different types of shapes;

- flexible electronic devices already include helical topologies to accommodate displacements[3]; however, helices without perversions are usually considered; by only including perversions the same applications would be able to extend beyond the current limit, since the existence of perversions makes easier to wind and unwind the structures and reach longer strains, in comparison to the same helix without perversions; therefore, a simple and straightforward, but effective, application would be the inclusion of perversions in electronics that use helical filaments to accommodate strains.

Lastly, in Chapter 7 we described two possible approaches to obtain entanglements using helical structures. In both approaches, only the physical interactions were considered. In the first case, the winding of the perversions was specifically controlled to clamp and revolve around, linking at least one filament to another. In the second case, the filaments are linked by creating constraints using the loops of helices (physical pseudoknots). So far, fabrics using both kind of approaches were explored only computationally. We propose some recommendation for future investigation:

- the simulations presented in this thesis serve as a first study to produce fabrics using entanglements subsequent of the helicity of filaments; a more realistic model needs to be considered, such as friction and irregularities in filaments; moreover, the connection between braid and knots theories still needs to be developed; for instance, how can the physical properties of different fabrics relate with net winding numbers;

- produce real fabrics that use one of the two mechanisms of linkage, by using perversions and physical pseudoknots; experiments have additional difficulties that

sometimes are not predicted by the computational simulations, so the experimental reproduction might give new insights on both effects;

- physical pseudoknots were already observed experimentally in metallic springs; it still remains unclear how this type of linkage changes when helical soft structures are used instead; then, it would be important, besides knowing the helical features of the filaments, understand how the mechanical attributes are important to obtain fabrics with physical pseudoknots.

References

[1]   McMillen and Goriely, "Tendril Perversion in Intrinsically Curved Rods," *Journal of Nonlinear Science*, vol. 12, no. 3, pp. 241–281, 2002. DOI: 10.1007/s00332-002-0493-1.

[2]   J. W. Shaevitz, J. Y. Lee, and D. A. Fletcher, "Spiroplasma Swim by a Processive Change in Body Helicity," *Cell*, vol. 122, no. 6, pp. 941–945, Sep. 23, 2005. DOI: 10.1016/j.cell.2005.07.004. pmid: 16179261.

[3]   K.-I. Jang, K. Li, H. U. Chung, S. Xu, H. N. Jung, Y. Yang, J. W. Kwak, H. H. Jung, J. Song, C. Yang, A. Wang, Z. Liu, J. Y. Lee, B. H. Kim, J.-H. Kim, J. Lee, Y. Yu, B. J. Kim, H. Jang, K. J. Yu, J. Kim, J. W. Lee, J.-W. Jeong, Y. M. Song, Y. Huang, Y. Zhang, and J. A. Rogers, "Self-assembled three dimensional network designs for soft electronics," *Nature Communications*, vol. 8, p. 15 894, Jun. 21, 2017. DOI: 10.1038/ncomms15894.